International Journal of

Thermodynamics

Editor-in-Chief
L. Kuddusi

Honorary Editors
A. Bejan
M. J. Moran
J. Szargut
G. Tsatsaronis
A. Valero
M. R. von Spakovsky

CONTENTS

Thermodynamic Bases for Obtaining Crystalline Perfect Silicon from Tin-silicon Solution

Alijon Razzokov Shonazarovich[1*], Khushnudbek Eshchanov Odilbekovich[2]

[1]Department of Physics, Urgench State University, Urgench, Uzbekistan
[2]Department of Chemistry, Urgench State University, Urgench, Uzbekistan
E-mail: [1]razzokov.a@bk.ru

Abstract

Silicon epitaxial layers were grown on a silicon (Si<111>) substrate in the range of 1323÷1073 K with initial crystallization temperatures from the silicon-tin (Si-Sn) solution. To determine the forces acting between the silicon nanoclusters in solution and the tin (Sn) particles and the silicon (Si) surface, the dielectric constant values of silicon, tin at selected temperatures were found experimentally. Given the Gibbs energy of the system to obtain the perfect epitaxial layers and structures of the crystal, optimal technological growth conditions are given.

Keywords: Epitaxy, nanocluster, crystallization, solution-melt, dislocation, dielectric constant.

1. Introduction

Semiconductor materials CdTe, CdS, GaAs, GaP, GaSb, GaN, InSb, InP, InAs, ZnSe, ZnS and solid solutions obtained on their basis $Al_xGa_{1-x}As$, $Al_xGa_{1-x}P$, $GaAs_{1-x}P_x$, $Ga_xIn_{1-x}As$, although they have high photoelectric parameters and are used as active elements in the development of optoelectronic devices, however, the synthesis of high-quality crystals of binary compounds is a technologically difficult task, therefore they are expensive materials. The manufacture of massive elements based on binary compounds is impractical. However, the possibility of obtaining a relatively low temperature of epitaxial silicon films from a solution-melt on relatively cheap silicon substrates makes them widely used materials. Therefore, the elucidation of the physicochemical features, i.e. The thermodynamic foundations of growing epitaxial Si films from a solution-melt remain one of the urgent problems of modern semiconductor physics. Using the literary known parameters, as well as conducting an experimental study to determine some constants and quantities, it is shown that crystalline perfect silicon grows under optimal conditions. It has been established that the optimal technological growth mode with the lowest energy costs.

The authors of [1, 2] attempted to obtain structurally perfect silicon epitaxial layers from a tin solution-melt. To accomplish this, they investigated the technological growth modes, electrical, photoelectric properties of epitaxial silicon layers.

However, those modes of technological growth, which are associated with the physical and chemical properties of the grown solution-melt of such a system, have not been thoroughly researched too far.

2. Theoretical Part

In a metastable system, crystallization occurs in two stages: a forced stage of nucleation—the formation of an interface, and the second spontaneous stage—growth on a seed. As a result, at the growth stage, the following main processes and related stages can be differentiated: delivery of a substance to a growing crystal (transport processes in the environment) and its attachment (kinetic phenomena on the surface).

During the forced growth of epitaxial layers at the crystal-liquid boundary, the isobaric-isothermal potential of the system ($\Delta G_{cr}>0$) increases. The free energy varies depending on the surface size and its surface energy σ.

A very important factor in the binding growth of silicon is the solvent and the substrate material, which has a specific orientation (In our study, the solvent was tin or gallium, and the substrate was oriented silicon <111>).

Despite $\Delta G_{cr}>0$, epitaxial silicon layers grow on the substrate due to surface energy in diffusion-kinetic or mixed mode. It should also be noted that the fact that the size of the crystal-forming nanoclusters in the system is in a critical state ($\Delta G_{cr}>0$) causes the crystallization process to begin. When nanoclusters of critical size are placed on the substrate, a $\Delta G_{cr}<0$ condition occurs when new 2D-sized primary centres larger than the critical size begin to appear (Figure 1). This condition is energetically preferred for the growth of epitaxial layers on the substrate surface.
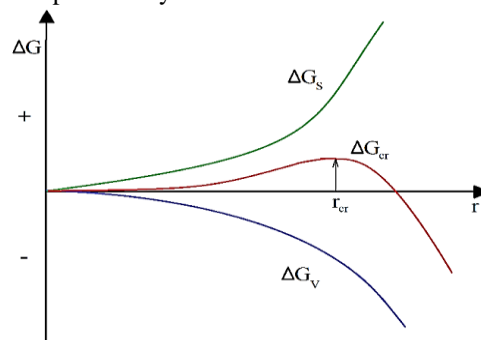

Figure 1. Volumetric Gibbs energy-G_v, surface Gibbs energy-ΔG_s and total Gibbs energy representing cluster formation-ΔG_{cr}, dependence on cluster radius.

When a substrate isn't available (solid surface), self-formation of nanoparticles occurs during cooling, however, this interferes with getting a single crystal from a homogeneous solution melt. As a result, a silicon substrate is used, which shares the same atomic radius of the crystallized film and substrate, as well as the coefficient of thermal expansion of the materials. All of these processes, however, are always specified by technological parameters, such as temperature, cooling rate, solvent type, and so on. Therefore, we will provide novel theoretical calculations for obtaining a film of a silicon single crystal on a silicon substrate with the lowest energy consumption and dislocation density. This is very important in production. For the ideal case of a silicon system dissolved in a tin liquid, the mixing Gibbs energy is as follows [3, 4, 5].

$$\Delta G_{mix} = RT(X_1 \ln X_1 + X_2 \ln X_2) \tag{1}$$

In real systems, the activity must be used instead of the moles of the solution's components. In this example, in contrast to formula (1), the Gibbs energy of the interference is given in the form below [3, 4].

$$\Delta G_{mix} = RT(X_1 \ln a_1 + X_2 \ln a_2) \tag{2}$$

The following expression can be used to determine the activity in formula [4, 5, 6]:

$$a = \gamma \cdot X \tag{3}$$

Here, X-mole fraction, γ -activity coefficient.

On the other hand, the determination of the magnitude of the expression γ is based on experimental results. The formula (4) was used to calculate the activity coefficient for the silicon component.

$$\lg \gamma_{Si} = \frac{a' - b' T_{(s)(Si)}}{RT_{(s)(Si)}} (1 - X_{Sn})^2 \tag{4}$$

The values of the constants a' and b' in the formula are determined experimentally. For the Si–Sn system, a'=31162 and b'=4.0289 are found [7, 8, 9].

The detected activities of silicon and tin in the Si-Sn system (a) are given in the following table (Table 1).

Table 1. Silicon and tin activity values.

№	T	a(Sn)	a(Si)
1	1373 K	0.8785675	0.5857100
2	1323 K	0.914285	0.4285700
3	1273 K	0.942855	0.3047617
4	1223 K	0.961000	0.2071425
5	1173 K	0.975285	0.1571400
6	1123 K	0.989570	0.1328555
7	1073 K	0.999000	0.0142850

Using the data in the table, the interference of the Si-Sn system was determined by the Gibbs energy (Figure 2).

The graph depicts how the Gibbs energy values of the system's mixing drop as the temperature rises. This shows that the system's silicon solubility in the tin solution is increasing.
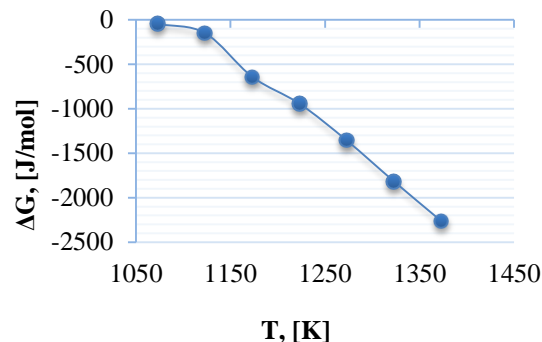
Figure 2. Gibbs temperature dependence graph of system interference

Silicon crystals occur during the cooling of the Si-Sn system. Formula (1) is used to calculate the total Gibbs energy for the crystallization process in the system (formula (5)) [3, 10].

$$\Delta G_{system} = \Delta G_{cr} + \Delta G_{mix.then} - \Delta G_{mix.first} \tag{5}$$

Silicon nanoclusters were considered to be formed during the cooling of the system. The formation of silicon nanoclusters can be seen as the beginning of the primary crystallization process in the system [11, 12, 13, 14, 15]. The Gibbs (ΔG_{cr}) energy for the formation of silicon nanocrystals in a liquid tin medium was calculated using the following formulas [16]. The results of the calculation are shown in Figure 3.

$$r_c = \frac{2\sigma_{s-l}V_m}{\mu_1 - \mu_2} = \frac{2\sigma_{s-l} \cdot V_m \cdot T_l}{L \cdot \Delta T} \tag{6}$$

$$\mu_1 - \mu_2 = \Delta G_v = L\frac{\Delta T}{T_l} \tag{7}$$

$$\Delta G_{cr} = \frac{16\pi\sigma_{s-l}^3 V_m^2}{3(\Delta G_v)^2} \tag{8}$$

Here, μ_1 and μ_2 -chemical potential of liquid and solid silicon, V_m-molar volume of silicon, L -the heat of fusion of silicon, σ_{s-l} -solid-liquid interface surface tension of silicon.
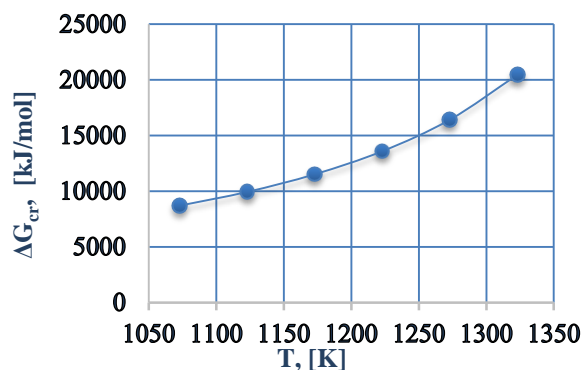
Figure 3. Formation of silicon nanocrystals Gibbs temperature dependence graph.

The silicon nanoclusters generated in the system settle on the surface of the silicon embedded in the system, forming a macro-sized single crystal. For each temperature,

the total Gibbs energy of the system was calculated using the formula (5) (Figure 4).
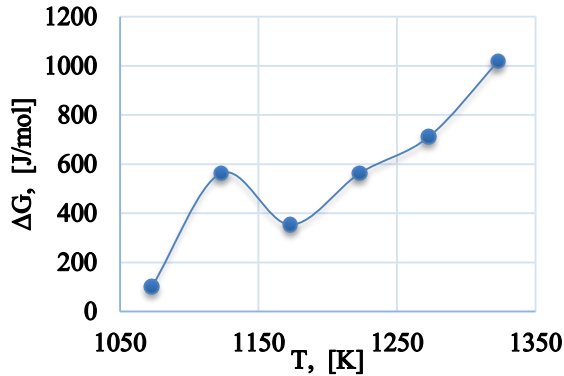
Figure 4. Gibbs energy in the formation of silicon crystals in the system temperature dependence graph.
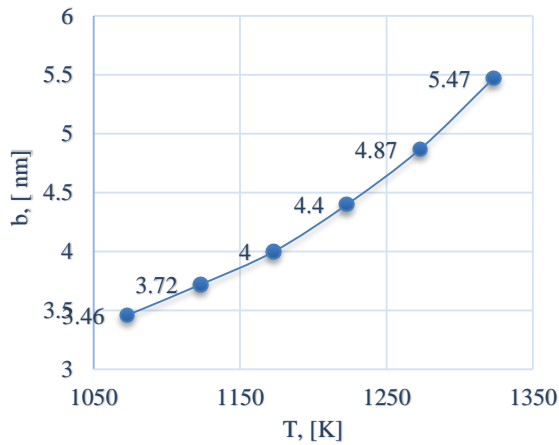
Figure 5. Temperature dependence of different sizes of dislocation centers relative to the growing surface.

Examination of the formation of silicon crystals at different temperatures revealed that the different sizes of the dislocation centres on the crystal-forming surface (base) decreased with decreasing temperature (Figure 5) [16]. However, as can be seen from the graph in Figure 4, during crystallization at 1173 K, the Gibbs energy of the system has a specific decrease, while the Gibbs energy of the system has increased again at 1123 K. This reduces the probability of the formation of silicon crystals from 1173 K to 1123 K. Even at temperatures below 1123 K, a decrease in the Gibbs energy of the system is observed during crystallization. However, the amount of silicon in the Si-Sn system remains very low at temperatures below 1123 K (0.001 mole fraction).

3. Method and Materials

Chemically pure samples of tin and silicon were used for the experiment. Silicon plate in the <111> direction was used as the substrate.

The experiment was carried out in an EPOS-type device (Pd-15T purifier) and in a hydrogen atmosphere at a temperature of 333-1323 K. The LVT 9/11-Nabertherm heater was used for heat transfer. A 4-Channel Type-K thermometer was used to check the temperature.

4. Experimental Part

Epitaxial layers of a silicon single crystal were grown from a tin and gallium solution-melt on single-crystal Si substrates with (<111>) p and n-type conductive liquid-phase epitaxy according to the technology described in [17]. The substrates were 20 mm in diameter and ~400 μm in thickness.

The composition of the solution-melt, consisting of silicon and tin, as well as silicon and tin, was determined from the phase diagram of the Sn–Si and Ga–Si binary alloy. The solubility of silicon in the tin was investigated at temperatures ranging from 1073 to 1373 K in order to create a liquid solution melt. Epitaxial silicon films were grown at temperatures of the onset (T_{oc}) and end of crystallization (T_{ec}), respectively, in the range 1323÷1073 K. The samples were grown at different values of the technological parameters of liquid epitaxy. A high-quality silicon single crystal with a dislocation density of $5 \cdot 10^4 \div 9 \cdot 10^3$ cm^{-2} was obtained.

The interaction forces of the particles in the system have been studied in the nanoscale explanation of the growth of low-defect and dislocated silicon epitaxial layers from the Si-Sn liquid solution to the Si surface. Here, silicon nanoclusters interact with the growing surface to participate in the formation of silicon single crystals on the surface [16]. The forces of interaction of the formed silicon nanoclusters with the solvent tin particles in the system, as well as with the particles on the surface of the growing silicon substrate (Lennard-Jones forces) were calculated [18, 19, 20].

$$U_{L-J} = \frac{A}{r_{AB}^{12}} - \frac{B}{r_{AB}^{6}} \tag{9}$$

$$B = \frac{3 \cdot \alpha_{Si} \cdot \alpha_{Sn} \cdot I_{Si} \cdot I_{Sn}}{2 \cdot (4\pi\varepsilon_0)^2 \cdot (I_{Si} + I_{Sn})} \tag{10}$$

$$\alpha = 4\pi\varepsilon_0 R_p^{3} \frac{\varepsilon - 1}{\varepsilon + 2} \tag{11}$$

$$\sigma = \frac{r}{2^{1/6}} \tag{12}$$

$$A = B \cdot \sigma^{6} \tag{13}$$

Where σ is the distance at which the intermolecular potential between the two particles is zero. A and B are constants, which depend on the type and particle composition. r- is the contact distance of the particles, I-ionization potential of the particle, α-polarity, R_p-particle radius, ε-dielectric constant, $\varepsilon_0 = 8,85 \cdot 10^{-12}$ F/m.

To determine the Lennard-Jones forces from formula (7), it is necessary to determine the quantities A and B. Formula (8) is used to determine the magnitude of B [21, 22]. The quantities α_{Si} and α_{Sn} in formula (8) are the polarity of silicon and tin in solution. As the crystallization process in the system took place at different high temperatures, it became necessary to determine the dielectric constant of the particles to know the polarity values at the same temperatures (polarity was determined using the formula (11)).

Since there is almost no data on the dielectric constant of silicon and tin in the scientific literature, we determined the parameters experimentally (Figures 6-7) [23, 24].

The dielectric constant of silicon was determined in a parallel-plate capacitor, while that of a tin metal was

determined in a hemispherical capacitor chain. The detection process was carried out in a hydrogen atmosphere.
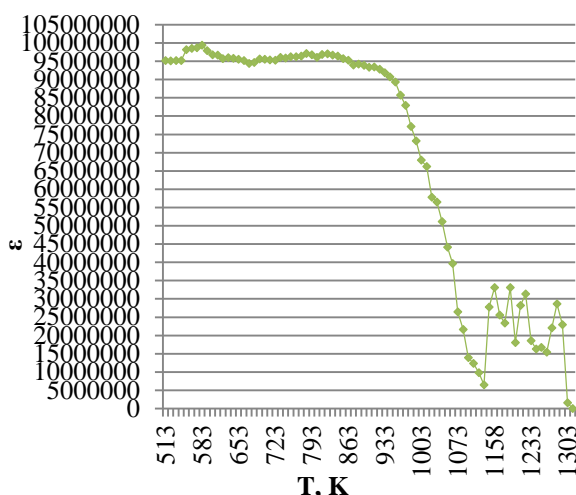
Figure 6. Dielectric constant values of tin metal at different temperatures.

According to the scientific literature [25, 26], the dielectric constant of metals is very high at room temperature, as shown in Figure 6. Experiments have shown that the dielectric constant of tin averages $9.6 \cdot 10^7$ from 513 K to 883 K. There was a decrease in dielectric constant from 883 K to 1133 K, an increase and decrease from 1133 K to 1283 K, and a sharp decrease from 1283 K to 1323 K.

Based on the experimental results, it can be said that the change in the metallic properties of tin is observed when the temperature exceeds 883 K. It can be assumed that the structure (chemical bonds, shape) in the liquid medium is unstable when the values of dielectric refractive index in the range of 1133÷1323 K are not regulated.
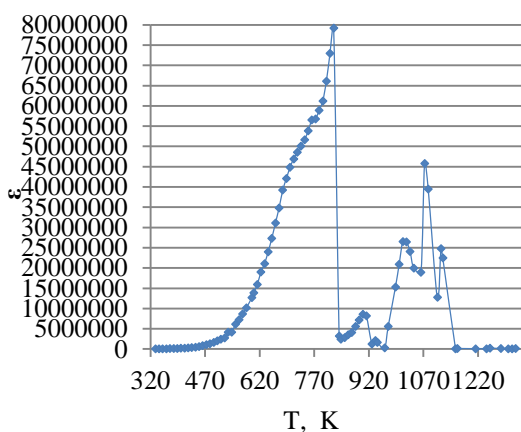
Figure 7. Dielectric constant values of silicon at different temperatures.

In the experiment, we determined the values of dielectric constant of silicon at temperatures of 333÷1323 K. It can be seen that the values of dielectric constant increase in the temperature range of 333÷823 K, and sharply decrease from 823 K to 843 K. It was observed that the dielectric constant values from 843 K to 1158 K were in the form of irregular increase and decrease. Differences in the dielectric constant of silicon decreased from 1158 K to 1323 K (Figure 7).

Based on the dielectric constant values determined experimentally at the selected appropriate crystallization temperatures of silicon and tin, the Lennard-Jones interaction forces of the tin solvent particles and the growing surface of silicon nanoclusters were calculated using formulas (9)-(13) (Table 2, Figure 8).

Table 2. Temperature dependence of Lennard-Jones force values between silicon surface and silicon nanoclusters.

T_{cr}	Cluster radius	$B \cdot 10^{-74}$	$A \cdot 10^{-127}$	$U_{L-J} \cdot 10^{-22}$ J (Si_{nano}-$Si_{surface}$)
1323 K	2.60 nm	3.7517	5.6185	-901.857
1273 K	2.33 nm	2.700	3.155	-670.132
1223 K	2.10 nm	1.9769	1.6459	-557.980
1173 K	1.90 nm	1.4638	0.769	-536.382
1123 K	1.77 nm	1.1836	0.5677	-413.300
1073 K	1.65 nm	0.959	0.3986	-334.544
1023 K	1.54 nm	0.779	0.2758	-275.000
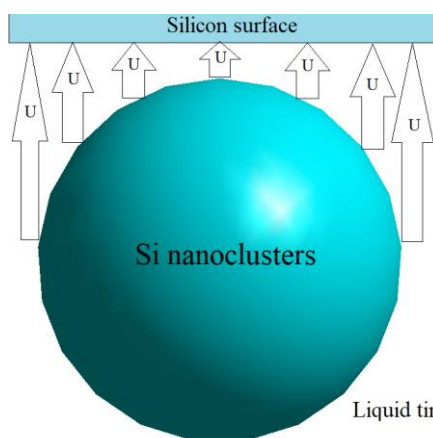
Figure 8. Scheme of the interaction between the substrate surface and the silicon nanocluster in the liquid tin medium.

In a silicon-tin solution, the strengths of silicon nanoclusters forming silicon single crystals on the silicon surface increase with increasing temperature. Consequently, the probability of a covalent bond between the surface and the silicon nanocluster increases due to an increase in the Lennard-Jones forces. This process leads to the formation of a single crystal on the surface on which it grows.
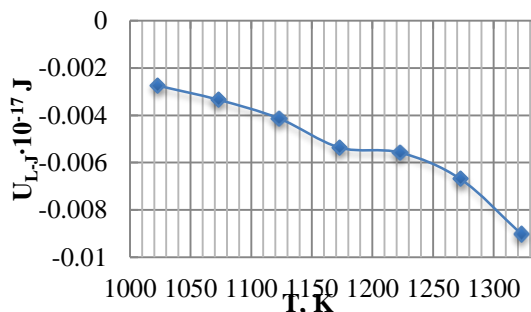
Figure 9. Lennard-Jones forces between silicon nanoclusters, which form silicon single crystals, and crystallization at different temperatures.

In a silicon-tin solution, the interaction potential between the silicon nanocluster and tin particles also increases in the arc direction with decreasing temperature (Table 3).

Table 3. Temperature dependence of Lennard-Jones force values between tin particles and silicon nanoclusters.

T_{cr}	Cluster radius	$B \cdot 10^{-74}$	$A \cdot 10^{-131}$	$U_{L-J} \cdot 10^{-22}$ J (Si_{nano}-Sn_m)
1323 K	2.60 nm	4.4697	3.2584	-39635570
1273 K	2.33 nm	3.2165	2.3448	-23666760
1223 K	2.10 nm	2.3557	1.7179	-14564514
1173 K	1.90 nm	1.9383	1.4130	-10151320
1123 K	1.77 nm	1.4105	1.0280	- 6578138
1073 K	1.65 nm	1.1440	0.8340	-4630000
1023 K	1.54 nm	0.9300	0.6779	-3482447.8

It was found that the interaction potential values of tin particles with silicon nanoclusters change from a temperature of 1323 K to a temperature of 1073 K on a curved line, and at temperatures below 1073 K on a straight line (Figure 10-11).
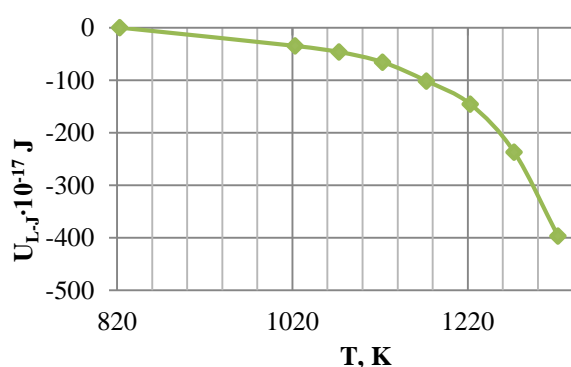
Figure 10. Lennard-Jones interaction forces between silicon nanoclusters and tin particles that form silicon single crystals during crystallization at different temperatures.
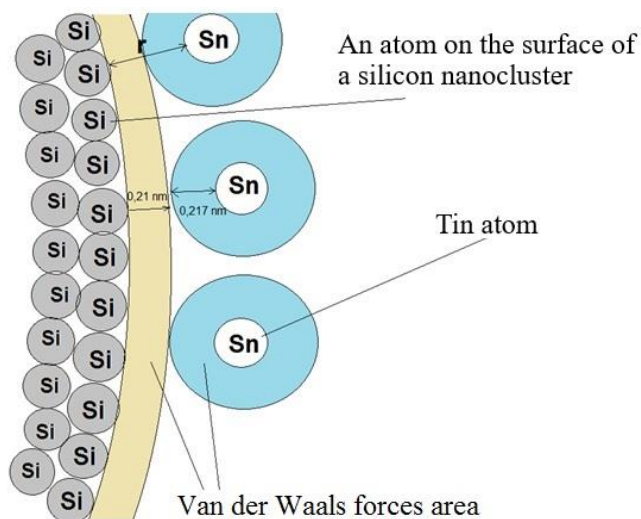
Figure 11. Scheme of the interaction of silicon nanoclusters and tin particles.

From experiments and theoretically determined indicators, it can be concluded that as the initial temperatures of single crystal growth decrease, the Si-Si impact forces increase. However, at the film-base boundary, the dislocation density increases exponentially when the temperature is high at the beginning of the growth process. This can be explained by the relatively large size of the initial nanocluster in the formation of the single crystal

(Table 2). Therefore, the conditions are chosen to grow crystalline perfect epitaxial layers with relatively low dislocation density of the required thickness in accordance with the Si base orientation. This is based on the above experimental and theoretical measurement calculations performed by us.

5. Conclusion

The energy and technological conditions for the growth of silicon epitaxial layers from the liquid Si-Sn system to the silicon surface to crystalline perfect, ie low dislocation, were investigated. The optimal energy conditions for the growth of silicon single crystals were calculated theoretically, the Gibbs energy of the system, the size of the silicon nanocluster forming the single crystal, the size of the dislocation centres relative to the surface were calculated, and a temperature of 1173 K was chosen for growing the silicon single crystal from Si-Sn. The experiment was carried out based on these theoretical results, and a high-quality silicon single crystal with a dislocation density of $5 \cdot 10^{4} \div 9 \cdot 10^{3}$ cm^{-2} was obtained.

Nomenclature

|	
a	Activity
γ	Activity coefficient
ΔG	Changes in Gibbs energy, J/mol
R	Universal gas constant, 8,314 $J \cdot K^{-1} \cdot mol^{-1}$
T	Temperature, K
X	Mole fraction
r_c	Critical radius of the particle, m
σ_{s-l}	solid-liquid surface tension, J/m^2
V_m	Molar volume, m^3
μ	Chemical potential, J/mol
L	Heat of fusion, J/mol
b	Size of dislocation centers, nm
U_{L-J}	Lennard-Jones forces, J
r	Distance between particles, m
σ	Distance at which the intermolecular potential between the two particles is zero, m
ε	Dielectric constant
ε_0	Electric constant, $8,85 \cdot 10^{-12}$ F/m
α	Polarity
I	Ionization potential, J
R_p	The radius of the polar particle, m

References:

[1] A. Nikiforov, V. Timofeev, V. Mashanov, T. Gavrilova and D. Gulyaev, "Elastically stressed pseudomorphic SiSn island array formation with a pedestal on the Si(100) substrate using Sn as a growth catalyst", *Journal of Crystal Growth*, vol. 518, pp. 103-107, 2019. Available: https://doi.org/10.1016/j.jcrysgro.2019.04.021.

[2] K. Fujiwara, "Crystal Growth Behaviors of Silicon during Melt Growth Processes", *International Journal of Photoenergy*, pp. 1-16, 2012. Available: https://doi.org/10.1155/2012/169829.

[3] Gaskell, D.R., & Laughlin, D.E. *Introduction to the Thermodynamics of Materials*, 6th Ed. CRC Press, 2017. Available: https://doi.org/10.1201/9781315119038.

[4] Arthur D. Pelton. *Phase Diagrams and Thermodynamic Modeling of Solutions,* Elsevier. 2019. Available: https://doi.org/10.1016/C2013-0-19504-9.

[5] Kaufman Myron, *Principles of Thermodynamics*, CRC Press, p. 213, 2002. ISBN 978-0-8247-0692-0

[6] Guggenheim, E.A. "The Conceptions of Electrical Potential Difference between Two Phases and the Individual Activities of Ions". *Journal Physcal Chemistry*, vol. 33, (6), pp. 842–849, 1929. Available: https://doi.org/10.1021/j150300a003.

[7] J. Safarian, L. Kolbeinsen, and M. Tangstad, "Thermodynamic activities in silicon binary melts," *Journal of Materials Science*, vol. 47, no. 14, pp. 5561–5580, 2012. Available: https://doi.org/10.1007/s10853-012-6449-4.

[8] Michael J. Moran, Howard N. Shapiro, Daisie D. Boettner, Margaret B. Bailey. *Fundamentals of Engineering Thermodynamics*, 3rd Ed. Michael J., Wiley –Interscience, 2010. ISBN 0-471-07681-3

[9] L. S. Darken, "Application of the Gibbs-duhem equation to ternary and multicomponent systems," *Journal of the American Chemical Society*, vol. 72, no. 7, pp. 2909–2914, 1950. Available: https://doi.org/10.1021/ja01163a030.

[10] S. Uda, X. Huang, S.Koh. *Journal of Crystal Growth*, vol. 281, pp. 481–491, 2005.

[11] P. Rudolph, in: *Crystal growth Technology*, H.J. Scheel and T. fukuda (eds.) Wiley –Interscience, 2003.

[12] E. D. Shukin, A. V. Persov, E.A. Ameline. *Colloid chemistry*, -M.: Higher. sch., 2004.

[13] Ivan Markov. *Crystal Growth For Beginners: Fundamentals of Nucleation, Crystal Growth And Epitaxy*, 3th Ed. Singapore: World Scientific, 2016. Available: https://doi.org/10.1142/10127.

[14] Burton, W. K.; Cabrera, N. *"Crystal growth and surface structure. Part I".* Discussions of the Faraday Society, 1949. Available: https://doi.org/10.1039/DF9490500033.

[15] Burton, W.K.; Cabrera, N. *"Crystal growth and surface structure. Part II".* Discussions of the Faraday Society, 1949. Available: https://doi.org/10.1039/DF9490500040.

[16] Razzokov, A.Sh., Khakimov, N.Z., Davletov, I.Y., Eshchanov, Kh.O. and Matnazarov, A.R. "Obtaining a structurally perfect semiconductor solid solution $Si_{1-x}Ge_x$ with electrophysical and photoelectric properties," *Scientific-technical journal*, vol. 24, iss. 5, pp. 11, 2020. Available: https://uzjournals.edu.uz/ferpi/vol24/iss5/11.

[17] Saidov, A.S., Razzokov, A. Sh. "Obtaining and morphological studies of epitaxial layers of the $Si_{1-x}Ge_x$ solid solution", *Siberian Physical Journal,* vol. 15, no. 2, pp. 84–91, 2020. Available: https://doi.org/10.25205/2541-9447-2020-15-2-84-91.

[18] Lennard-Jones, J.E. "Cohesion". *Proceedings of the Physical Society*, vol. 43 no. 5, pp. 461–482, 1931. Available: https://doi.org/10.1088/0959-5309/43/5/301.

[19] Simon Stephan, Martin T. Horsch, Jadran Vrabec & Hans Hasse. MolMod–an open access database of force fields for molecular simulations of fluids, *Molecular Simulation*, vol. 45, no. 10, pp. 806-814, 2019. Available: https://doi.org/10.1080/08927022.2019.1601191.

[20] N. Tchipev, S. Seckler, M. Heinen, J. Vrabec, F. Gratl, M. Horsch, M. Bernreuther, C. W. Glass, C. Niethammer, N. Hammer, B. Krischok, M. Resch, D. Kranzlmüller, H. Hasse, H.-J. Bungartz, and P. Neumann, "Twetris: Twenty trillion-atom simulation," *The International Journal of High Performance Computing* Applications, vol. 33, no. 5, pp. 838–854, 2019. Available: https://doi.org/10.1177/1094342018819741.

[21] Jones, J. E. "On the determination of molecular fields. —II. From the equation of state of a gas". *Proceedings of the Royal Society of London. Series A, Containing Papers of a Mathematical and Physical Character,* vol. 106 no. 738, pp. 463–477, 1924. Available: https://doi.org/10.1098/rspa.1924.0082.

[22] Wood, W. W.; Parker, F. R. "Monte Carlo Equation of State of Molecules Interacting with the Lennard-Jones Potential. I. A Supercritical Isotherm at about Twice the Critical Temperature". *The Journal of Chemical Physics*, vol. 27, no. 3, pp. 720–733, 1957. Available: https://doi.org/10.1063/1.1743822.

[23] S. Dubrovskiy and K. Gareev, "Measurement method for detecting magnetic and dielectric properties of composite materials at microwave frequencies", *2015 IEEE NW Russia Young Researchers in Electrical and Electronic Engineering Conference*, St. Petersburg, pp. 24-26, 2015. Available: https://doi.org/10.1109/EIConRusNW.2015.7102223.

[24] Grove, Timothy & Masters, Mark & Meirs, Richard. *Determining Dielectric Constants Using a Parallel Plate Capacitor.* Physics Faculty Publications, 2005. Available: https://doi.org/10.1119/1.1794757.

[25] Boltaev, A.P., Pudonin, F.A. & Sherstnev, I.A. "Low-frequency giant effective permittivity of island metal films", *Physics of the Solid State*, vol. 57, pp. 2099–2105, 2015. Available: https://doi.org/10.1134/S1063783415100066.

[26] Costa, F., Amabile, C., Monorchio, A., Prati, E. "Waveguide Dielectric Permittivity Measurement Technique Based on Resonant FSS Filters", *IEEE Microwave and Wireless Components Letters*. vol. 21, no. 5, pp. 273, 2011. Available: https://doi.org/10.1109/LMWC.2011.2122303.

Maximum Liquefaction of Gases Revisited

R. Pitanga Marques[1*], P.R.G. Bordoni[2], M. O. Pinho[3]

[1] Department of Mechanical Engineering, CEFET-RJ
[2] Department of Computer Science, Universidade Federal do Rio de Janeiro (UFRJ)
[3] Department of Mathematics, CEFET-RJ
E-mail: [1]rupitanga@hotmail.com

Abstract

Joule-Thomson liquefiers are the commonest machines to liquefy gases. Over the years, countless number of articles have been published on the subject. Dozens of 1st and 2nd law analyses were carried out on Joule-Thomson liquefaction cycles. And yet an aspect of purely theoretical interest seems to have passed unnoticed, namely: for a given volume of gas, what conditions should be fulfilled to achieve maximum liquefaction without considering engineering details of design equipment and the highly irreversible character of work-consuming devices, heat exchangers, heat leaks and the throttling process. This work addressed this issue by applying the 1st law analysis and elementary calculus prescriptions to a simple Linde-Hampson liquefying process. The same approach could be applied to other liquefying cycles. As is well-known, for a given mass flow rate of a gas, maximum fraction liquefied occurs when the pre-cooling temperature, T_i, and initial pressure, P_i, lie on the inversion curve. It has been proved that this is only true if an additional condition is fulfilled. Expressions for it were derived for the van der Waals, RKS and PR equations of state.

Keywords: Liquefaction of gases; Joule-Thomson effect; maximum fraction liquefied; inversion curves; liquefier.

1.Introduction

Commercial liquefaction of gases is a century-old technology. The pioneering work of Carl von Linde in Germany, William Hampson in England and Georges Claude in France opened a new branch of science and technology: cryogenics [1]. From biological research, where liquid nitrogen is used to freeze blood cells, tissues, and similar, to space flight, where liquid oxygen is used in combination with liquid hydrogen to propel rockets, liquefied gases have found a variety of applications in modern industrial societies [2].

In throttling processes, fluids flow through a restriction which can be an orifice, a valve or a porous plug. They undergo, in general, an increase or a decrease in temperature. The Joule-Thomson (or Kelvin) coefficient is a measure of the change in temperature which results from a drop in pressure across the constriction. And is defined by

$$\mu = \left(\frac{\partial T}{\partial P}\right)_h \tag{1}$$

A throttling process does not necessarily entail cooling or heating. An isenthalpic expansion of ideal gases results in no temperature change. From this point of view, the Joule-Thomson coefficient can be seen as a measure of departure from ideal-gas behaviour.

Joule-Thomson coefficients may be positive, zero (as in the case of ideal gases) or negative. Fig. 1 below illustrates, μ, for different gases as a function of the temperature.

For most real gases, the Joule-Thomson coefficient gives rise to a decrease of temperature within only a certain domain of temperature and pressure. At room temperatures (see Fig. 1), the coefficient is positive for nearly all gases. Thus, if a gas undergoes an isothermal compression, and is allowed to expand to low pressures, part of it will be liquefied. The higher the pressure or lower the temperature, the higher the non-ideality is to produce enough cooling to liquefy the gas [4].
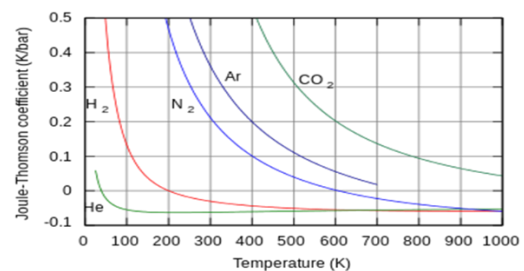
Figure 1. Joule-Thomson coefficients as a function of the temperature for different gases [3].

Most liquefaction cycles use the Joule-Thomson effect to attain a certain level of non-ideality in the cryogenic gas. In the Linde-Hampson liquefier, a nozzle is used to produce the Joule-Thomson effect to cool the gas to become a liquid. The incoming gas is compressed in a multistage compressor to high pressure before delivery to the cooler, which is a recuperative heat exchanger. This counter-flow heat exchanger cools down the incoming gas to a temperature below the inversion temperature by exchanging heat with chilled water available. The cold gas is constantly recycled to cool more incoming compressed gas. Because of the cumulative cooling effect, the gas gradually becomes cold enough until liquefaction occurs after expansion at the

throttle. In the Claude liquefier, part of the gas from the multistage compressor goes to the expander where it does work. The expansion engine operates adiabatically to lower the temperature of part of the high pressure gas. The work of the expander partially compensates for the work of compression and reduces the requirement for very high pressures in the liquifier. The gas cooled down in the process is used to cool the incoming compressed gas in the cooler. As in the Linde liquefier, the continuing flow of gas will decrease the temperature at a point where part of the gas will be liquefied by the Joule-Thomson effect. For gases with a negative Joule-Thomson coefficient, near-standard conditions (hydrogen, helium, neon), the Claude should be replaced by the Collins liquefier — an extension of the Claude liquefaction process with a sophisticated mechanical design of reciprocating expanders and heat exchangers. This is because the cooling duty required is the highest among cryogens for the removal of the sensible heat. The incoming gas from the compressor is cooled by liquid nitrogen in the cooler. For a detailed exposition of all cryogenic liquefaction processes and liquefiers, the interested reader should consult Mukhopadhyay [5].

The performance of liquefiers can be assessed by means of the concept of the figure of merit (FOM). A very good description of FOM and the thermodynamics associated with cryogenic plants may be found in references [6,7]. FOM is defined by the ratio of the ideal work, $-W_i$ for a thermodynamically ideal liquefaction process to the actual work required to liquify the cryogenic gas, $-W_l$. Thus,

$$FOM = \frac{-W_i}{-W_l} \qquad (2)$$

Table.1 illustrates the performance of a simple Linde-Hampson liquefier for different gases.

Table 1. Work of liquefaction and FOM of a simple Linde-Hampson process[*] for different cryogens(reproduced under permission from Mukhopadhyay [4]) *P₁= 1 atm, P₂= 200 atm, T₁ = T₂ = 300 K, 100% efficiency of isothermal compressor and 100% effectiveness of the main heat exchanger with no temperature difference between the incoming and outgoing streams at the inlet.

Cryogen	Normal boiling point (K)	% Liquefied	Work of liquefaction (kJ/kg)	FOM
N₂	77.4	7.08	6673	0.115
Air	78.8	8.08	5621	0.131
Ar	87.3	11.83	2750	0.174
O₂	90.2	10.65	3804	0.167
CH₄	111.7	19.77	3957	0.276
C₂H₆	184.5	52.57	611	0.588

Like all cyclic machines, liquefiers depend on components performance to maximise the liquid yield. The highly irreversible character of work-consuming devices, heat exchangers, heat leaks and the throttling process do reduce the fraction liquefied. In a very interesting study, B.-Z. Maytal [8] showed that for any real Linde–Hampson machine of finite size, the recuperator can be optimized to reach extreme rates of performance. For a similar group of liquefiers an optimal flow rate was found to maximize the rate of production of liquid cryogen. A study by M. Kanoglu et al [9] based on 1st and 2nd law analyses of a simple Linde–

Hampson cycle established the minimum work requirement, applicable to any cryogen to enhance the performance of the liquefier. More recently, C. Yilmaz et al. [10] carried out a comprehensive thermodynamic analysis of the simple Linde-Hampson, precooled Linde-Hampson, Claude, and Kapitza cycles. They were model in the computer environment and analyzed with Engineering Equation Solver (EES) software program. The authors concluded that the Claude cycle delivers the largest liquid yield while the Kapitza cycle, the best exergy efficiency. Nontheless, they pondered that despite their low efficiencies, the simple Linde-Hampson and precooled Linde-Hampson cycles offer the simplicity of their setup.

To the best of the authors' knowledge, the only work found in the literature related to this was published by A. T. A. M. de Waele [11]. The author carried out a 1st law analysis of a simple Linde-Hampson machine and obtained, as expected, the expression for the liquefied fraction exactly the same as ours. However, de Waele did not investigate the (thermodynamic) pre-requisites for it to achieve maximum liquefaction.

This work aims to discuss a question raised by Zemansky and Dittman [12] on the optimal theoretical conditions to liquefy common gases.

2. Thermodynamic Model

Consider the steady-state liquefying system shown pictorially in Fig. 2 and corresponding T-s diagram .

For simplicity, engineering details of the system components are omitted. The objective is to determine the maximum fraction liquefied from first principals. Zemansky and Dittman's analysis captures enough of the physics of liquefaction by identifying the states visited by the stream of gas. This paper followed Zemansky and Dittman's reasoning and kept their notation.

At steady state, liquid is formed at a constant rate: a certain mass flow rate fraction, **y,** is liquefied and stored in a vessel for later use, and 1— **y** of mass flow rate fraction of low-pressure gas pre-cools the incoming high-pressure gas in a counter-flow heat exchanger. A fresh stream of makeup gas at room temperature joins the low-pressure stream of gas before entering the compressor to replenish the cycle. Considering there are no pressure drops, no heat leaks, no temperature of approach at the warm end of the heat exchanger, a simple first law analysis yields

$$h_i = y\, h_L + (1-y)h_f. \qquad (3)$$

This shows the enthalpy of the incoming gas equals the enthalpy of **y** units of mass flow rate in liquid form plus the enthalpy of 1— **y** units of mass flow rate of the outgoing gas. Or:

$$y = \frac{h_f - h_i}{h_f - h_L} \qquad (4)$$

Where:
h_i is the enthalpy of the incoming gas at (T_i, P_i)
h_L is the enthalpy of the fraction liquefied at (T_L, P_L)
h_f is the enthalpy of the outgoing gas at (T_f, P_f)
if the heat exchanger and throttling valve are thermally insulated (schematically shown by the dotted lines in the figure).
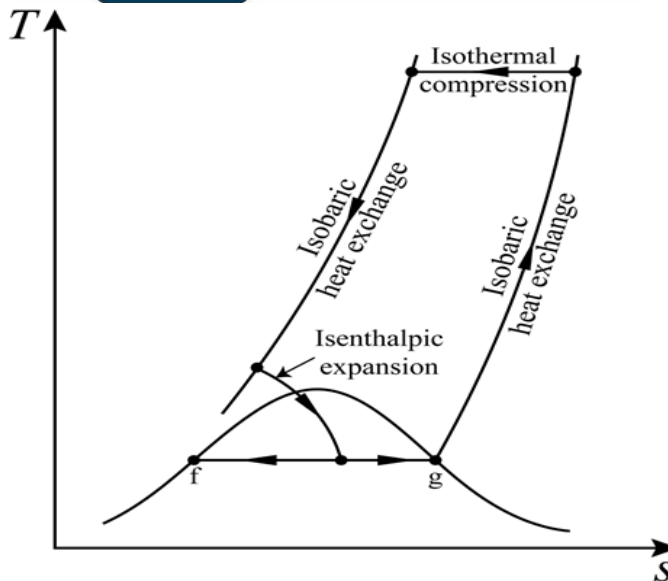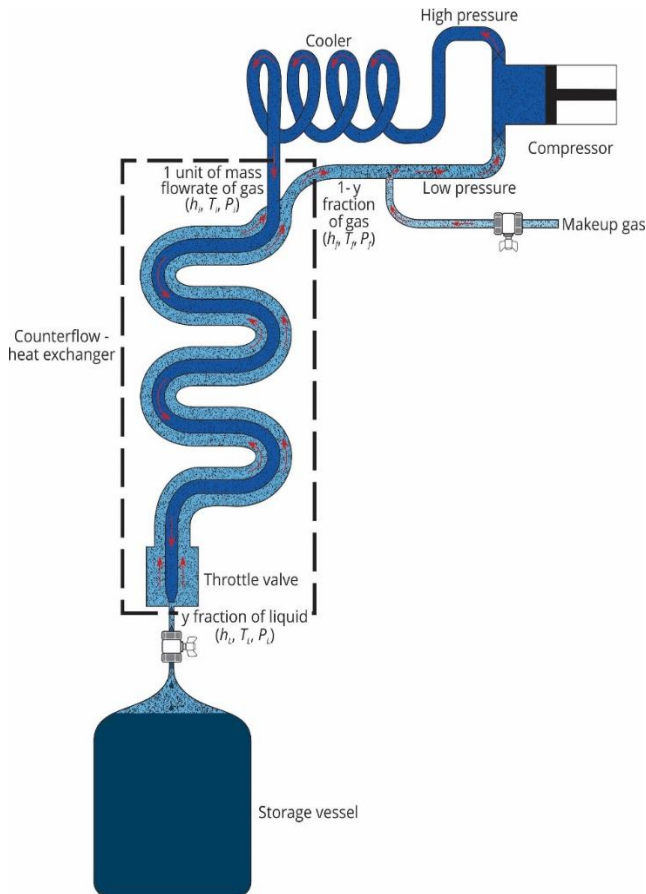
Figure 2. Pictorial view of a simple Linde-Hampson liquefier (inspired on a figure of the book of Zemansky and Dittman [12]) and correspondingT-s diagram drawn by Mrs. Isabel Menezes.

The enthalpy of the incoming gas, h_i , is a function of pressure that may be chosen at will (the optimum pressure to start throttling corresponds to a point on the inversion curve) at a fixed T_i ; h_L , the enthalpy of the fraction liquefied at the entry of the storage vessel, is independent of both pressure and temperature, and therefore, constant. h_f ,the enthalpy of the outgoing gas, despite the pressure drop in the return pipe, remains nearly constant. Therefore, the fraction liquefied, y , is a function of, h_i , only. For maximum liquefaction (highest possible value of y), h_i ought to be a minimum, i.e.:

$$\left(\frac{\partial h_i}{\partial P}\right)_{T=T_i} = -\left(\frac{\partial h_i}{\partial T}\right)_P \left(\frac{\partial T}{\partial P}\right)_{h_i} = -c_p \mu = 0 \qquad (5)$$

Zemansky and Dittman posited on page 284 of their book that y to be a maximum, $\mu = 0$ at $T = T_i$ since c_p cannot be zero except at the absolute zero. But they did not carry their analysis any further and promptly concluded that "…*the point (T_i, P_i) must lie on the inversion curve in order to maximize the fraction y of the liquid* ".

Elementary calculus shows that after establishing the critical points of a function by setting $f'(x) = 0$, we need to calculate the second order derivative to determine whether such points are a local maximum or a local minimum. If the function $f(x)$ is twice differentiable at a critical point, x, then:

if $f''(x) < 0$ then $f(x)$ has a local maximum at x .
if $f''(x) = 0$ then the test is inconclusive.
if $f''(x) > 0$ then $f(x)$ has a local minimum at x .

In brief, the sign of the second order derivative should be studied, $\left(\frac{\partial^2 h_i}{\partial P^2}\right)_T$, in order to decide whether the point (T_i, P_i) lies on the inversion curve.

2.1 The Joule-Thomson Inversion Curve

The locus of all points at which the Joule-Thomson coefficient, μ , is zero is called the inversion curve, shown schematically in red in Fig.3 (a P-T diagram in reduced coordinates, $T_r = T/T_c$ and $P_r = P/P_c$). The locus is a collection of points of maximum values of curves of equal enthalpy. The inversion curve joins together points at which the slope $\left(\frac{\partial T}{\partial P}\right)_H$ changes from positive to negative according to elementary calculus prescriptions $\left(\frac{\partial T}{\partial P}\right)_h = 0$ and $\left(\frac{\partial^2 T}{\partial P^2}\right)_h < 0$. The inversion curve, which is parabolic in shape, is a boundary between two regions: the region of cooling where $\mu > 0$, and the region of heating where $\mu < 0$. The upper part cuts the T-axis at the maximum inversion temperature while the lower part ends, abruptly, at the vapour pressure curve (Fig.3) [13-14]. An isobar drawn on the diagram intersects several isenthalps (shown in black) at a number of points at which μ is calculated by measuring the slope.
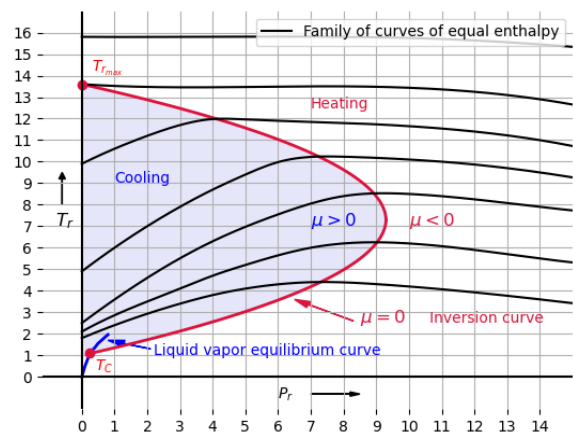
Figure 3. Joule-Thomson inversion curve drawn by one of the authors.

To draw the inversion curve, experimental points for which $\mu = 0$ are required. Since volumetric data of sufficient accuracy for gases are rare at highly reduced temperatures, the upper part is either determined by a least-square fit or by an equation of state (EoS) [13].

Over the years, several authors have calculated the Joule-Thomson inversion curve by making use of equations of state, [13-22]. The calculation of the Joule-Thomson inversion curve for each new EoS provides a severe test for its predictive capability. A better agreement with experimental inversion curves of different substances is a clear indication of its superiority.

Written in reduced coordinates, the predictive inversion curve (for an equation of state) is given by,

$$T_r \left(\frac{\partial P_r}{\partial T_r}\right)_{V_r} + V_r \left(\frac{\partial P_r}{\partial V_r}\right)_{T_r} = 0. \tag{6}$$

A plot of an inversion curve on a P-T plane in reduced temperature and pressure should yield a curve that is valid for all gases. This behaviour can only be justified by evoking the theorem of corresponding states: chemical compounds at equal reduced pressures and temperatures have equal reduced volumes. Strictly speaking, the theorem of corresponding states is only valid for the so-called simple fluids; those whose force field has a high degree of symmetry. Fortunately, most liquefied gases (Ar, CH_4, N_2, O_2, C_2H_4 etc.) fall into this category. Next, the derivatives $\left(\frac{\partial P_r}{\partial T_r}\right)_{V_r}$ and $\left(\frac{\partial P_r}{\partial V_r}\right)_{T_r}$ can be determined from an arbitrarily chosen equation of state. A judicious choice depends, to a large extent, on which class of fluids the equation of state was designed for. Van der Waals equation of state (vdW EoS), despite its severe limitations, offers a useful picture of the thermodynamic properties for simple fluids. And unlike modern cubic equations of state, it is far more superior (e.g. Redlich-Kwong-Soave (RKS) EoS [23], Peng-Robinson (PR) EoS [24] and RK-PR EoS [25]), vdW EoS

$$P = \frac{RT}{V-b} - \frac{a}{V^2} \tag{7}$$

obeys the theorem of corresponding states. Written in reduced form,

$$\left(P_r + \frac{3}{V_r^2}\right)(3V_r - 1) = 8T_r, \tag{8}$$

van der Waals equation applies in principle to any substance, but can only provide actual properties when critical properties are known.

Inserting the derivatives $\left(\frac{\partial P_r}{\partial T_r}\right)_{V_r}$ and $\left(\frac{\partial P_r}{\partial V_r}\right)_{T_r}$ of (8) in (6) yields,

$$-\frac{T_r}{(3V_r-1)^2} + \frac{3}{4}\frac{1}{V_r^2} = 0. \tag{9}$$

A rather involved algebraic manipulation to eliminate V_r between (6) and (7) results in the well-known van der Waals inversion curve,

$$T_r = 3\left[1 \pm \frac{\sqrt{9-P_r}}{6}\right]^2 \tag{10}$$

which is illustrated in Fig. 4.
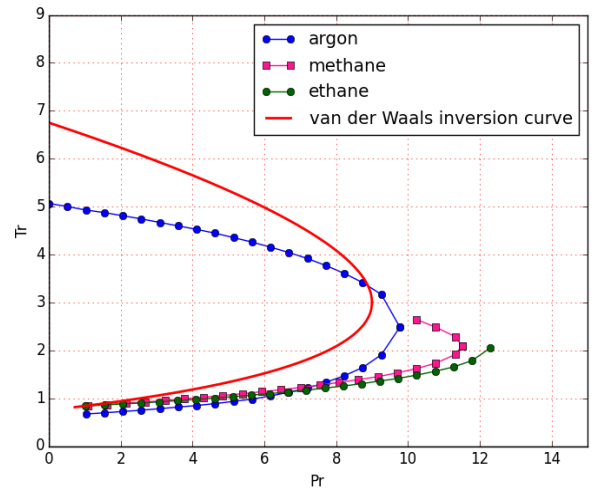
Figure 4. Van der Waals inversion curve and experimental data for three commercial gases (data collected from [26]) drawn by one the authors .

When $\left(\frac{\partial T}{\partial P}\right)_h = 0$ and $\left(\frac{\partial^2 T}{\partial P^2}\right)_h < 0$ are applied to vdW EoS, yields,

$$T_{inv} = \frac{2a}{Rb}\frac{(v-b)^2}{v^2} \cong \frac{2a}{Rb} \tag{11}$$

the maximum inversion temperature, T_{inv}, i. e. the highest temperature for which $\mu = \left(\frac{\partial T}{\partial P}\right)_h$ is positive so that a reduction in pressure results in a decrease in temperature. Table 2 shows maximum inversion temperature values, boiling points (for comparison) and critical points for common gases.

Table 2. Maximum inversion temperatures, boiling points and critical points for common gases (data collected from [27]).

cryogen	maximum inversion temperature, T_{inv} (K)	Critical temperature (K)	Normal boiling point (K)
He	51	5.2	4.2
H_2	205	33.2	20.4
Ne	250	44.4 K	27.07
N_2	621	126	77.4
O_2	893	154	90.2
Ar	794	150.7	87.3
CH_4	939	190.7	111.7

3. Results and Discussion

To achieve maximum liquefaction, h_i ought to be a minimum, i.e.:

$$\left(\frac{\partial h_i}{\partial P}\right)_{T=T_i} = 0 \quad \text{and} \quad \left(\frac{\partial^2 h_i}{\partial P^2}\right)_{T=T_i} > 0 \tag{12}$$

Or:

$$\left(\frac{\partial(-c_p\mu)}{\partial P^2}\right)_{T=T_i} > 0 \quad \text{since} \quad \left(\frac{\partial h_i}{\partial P}\right)_{T=T_i} = -c_p\mu$$

but $\mu = \frac{1}{c_P}\left[T\left(\frac{\partial v}{\partial T}\right)_P - v\right]$ or $-c_p\mu = \left[v - T\left(\frac{\partial v}{\partial T}\right)_P\right]$ (13)

thus:

$$\left(\frac{\partial(-c_p\mu)}{\partial P^2}\right)_{T=T_i} = \left\{\left(\frac{\partial v}{\partial P}\right)_T - \left(\frac{\partial T}{\partial P}\right)_v\left(\frac{\partial v}{\partial T}\right)_P - T\left(\frac{\partial^2 v}{\partial P \partial T}\right)_{T,P}\right\}_{T=T_i} \tag{14}$$

and by making use of the cyclic relation:

$$\left(\frac{\partial T}{\partial P}\right)_v\left(\frac{\partial P}{\partial v}\right)_T\left(\frac{\partial v}{\partial T}\right)_P = -1$$

Eq. (14) becomes:

$$\left(\frac{\partial(-c_p\mu)}{\partial P^2}\right)_{T=T_i} = \left\{2\left(\frac{\partial v}{\partial P}\right)_T - T\left(\frac{\partial^2 v}{\partial P \partial T}\right)_{T,P}\right\}_{T=T_i} \tag{15}$$

Given the pressure-explicit vdW EoS:

$$p = \frac{RT}{(v-b)} - \frac{a}{v^2} \tag{16}$$

one can easily determine $\left(\frac{\partial v}{\partial P}\right)_T$ and $T\left(\frac{\partial^2 v}{\partial T \partial P}\right)_{P,T}$. These are as follows:

$$\left(\frac{\partial v}{\partial P}\right)_T = \left[\frac{2a}{v^3} - \frac{RT}{(v-b)^2}\right]^{-1}$$

$$T\left(\frac{\partial^2 v}{\partial P \partial T}\right)_{T,P} = \frac{RT}{(v-b)^2}\left[\frac{2a}{v^3} - \frac{RT}{(v-b)^2}\right]^{-2}$$

And the expression for the second order derivative of the enthalpy with respect to pressure at constant temperature becomes,

$$\left(\frac{\partial^2 h_i}{\partial P^2}\right)_T = 2\left[\frac{2a}{v^3} - \frac{RT}{(v-b)^2}\right]^{-1} - \frac{RT}{(v-b)^2}\left[\frac{2a}{v^3} - \frac{RT}{(v-b)^2}\right]^{-2} \tag{17}$$

For $\left(\frac{\partial^2 h_i}{\partial P^2}\right)_T > 0$ (17) can be re-written as:

$$\frac{4a}{v^3} - \frac{3RT}{(v-b)^2} > 0 \tag{18}$$

And the solution of the inequality (18) becomes:

$$T_i < \frac{4a(v-b)^2}{3Rv^3}. \tag{19}$$

Written in reduced coordinates yields:

$$T_{ir} < \frac{3}{2}\frac{\left(V_r - \frac{1}{3}\right)^2}{V_r^3}. \tag{20}$$

Expressions for T_i obtained from RKS EoS [23] and PR EoS [24] are given in the Appendix.

4. Conclusions

Joule-Thomson liquefiers are a suitable means to produce the liquefaction of gases. They are technically much simpler than the multistage cascade liquefiers. And they have two important advantages. Firstly, the lower the temperature, the larger the drop in temperature for a given pressure drop. Secondly, the absence of moving parts requires no lubrication and this is crucial when working at low temperatures. Their efficiency, however, depends on several factors (performing work-consuming devices, effective heat exchangers, absence of heat leaks and the efficiency of the throttling process) to produce the maximum fraction liquefied.

By a simple 1st law analysis and elementary calculus prescriptions (maximum and minimum conditions imposed on functions of one variable) to a simple Linde-Hampson liquefying process, maximum fraction liquefied is obtained when h_i is a minimum. From a theoretical point of view, this is achieved when the pre-cooling temperature, T_i, and initial pressure, P_i, lie on the inversion curve and $T_{ir} < \frac{9}{4}\frac{\left(V_r - \frac{1}{3}\right)^2}{V_r^3}$. As for a more accurate equation of state than of van der Waals', such as RKS or PR EoS, expressions for the second order derivative of h_i (given in the Appendix), and therefore T_i, are algebraically too complicated to draw a conclusive physical picture.

Nomenclature

a	attraction parameter in the van der Waals equation of state [m^6 kPa/kg^2]
b	effective molecular volume in the van der Waals equation of state [m^3/kg]
c_p	specific heat capacity [kJ/kg K]
EoS	equation of state
FOM	figure of merit
h_i	enthalpy of the incoming gas at (T_i, P_i) [kJ/kg]
h_L	enthalpy of the liquid yield at (T_L, P_L) [kJ/kg]
h_f	enthalpy of the outgoing gas at (T_f, P_f) [kJ/kg]
PR	Peng-Robinson cubic equation of state
P	pressure [kPa]
R	universal gas constant [kJ/kg K]
RKS	Redlich-Kwong-Soave cubic equation of state
$RK\text{-}PR$	Combined Redlich-Kwong-Soave and Peng-Robinson equation of state
T	temperature [K]
vdW	van der Waals cubic equation of state
v molar	volume [m^3/kg]
y	fraction of liquefied gas [dimensionless]

Greek letters

μ	Joule-Thomson coefficient [K/Pa]
ω	acentric factor [dimensionless]

Subscripts

c	critical value
i	incoming
f	outgoing
L	liquid
r	reduced property

Appendix

For a matter of convenience, the cubic equations of state are written in the following form:

$$P = \frac{RT}{V-b} - \frac{\Gamma(T)}{\Psi(V)} \tag{A}$$

such that $\Gamma(T) \neq 0$ and $\Psi(V) \neq 0$

For the van der Waals EoS:

$$\Gamma(T) = a \quad \text{and} \quad \Psi(V) = V^2$$

For Redlich-Kwong-Soave (RKS) EoS:

$$\Gamma(T) = a\left(1 + m(1 - T_r^{0.5})\right)^2$$

where $m = 0.480 + 1.574\omega - 0.176\omega^2$

and ω is the acentric factor.

$$\Psi(V) = V(V - b)$$

And for Peng-Robinson (PR) EoS:

$$\Gamma(T) = a\left(1 + m(1 - T_r^{0.5})\right)^2$$

where $m = 0.37464 + 1.54226\omega - 0.26992\omega^2$

and ω is the acentric factor.

$$\Psi(V) = V^2 + 2bV - b^2$$

Rewriting (A) and making use of the implicit function theorem, yields:

$$f(P, T, V) = P - \frac{RT}{V-b} + \frac{\Gamma(T)}{\Psi(V)}$$

Then:

$$\frac{\partial V}{\partial P} = -\frac{\frac{\partial f}{\partial P}}{\frac{\partial f}{\partial V}} \quad \text{and} \quad \frac{\partial V}{\partial T} = -\frac{\frac{\partial f}{\partial T}}{\frac{\partial f}{\partial V}} \tag{B}$$

$$\frac{\partial f}{\partial V} = \frac{RT}{(V-b)^2} - \frac{\Gamma(T)}{\Psi(V)^2}\frac{d\Psi}{dV}$$

$$\frac{\partial f}{\partial P} = 1$$

$$\frac{\partial f}{\partial T} = \frac{RT}{V-b} - \frac{1}{\Psi(V)}\frac{d\Gamma(T)}{dT}$$

Inserting the derivatives above in B, one gets:

$$\frac{\partial V}{\partial P} = -\frac{1}{\left[\frac{RT}{(V-b)^2} - \frac{\Gamma(T)}{\Psi(V)^2}\frac{d\Psi}{dV}\right]}$$

$$\frac{\partial V}{\partial T} = \frac{\frac{R}{(V-b)} - \frac{1}{\Psi(V)}\frac{d\Gamma(T)}{dT}}{\left[\frac{RT}{(V-b)^2} - \frac{\Gamma(T)}{\Psi(V)^2}\frac{d\Psi}{dV}\right]}$$

and $\quad \dfrac{\partial^2 V}{\partial P \partial T} = 0 \quad$ since $\dfrac{\partial V}{\partial T}$ doesn't depend on P.

As a result:

$$\frac{\partial V}{\partial P} = -\frac{1}{\left[\frac{RT}{(V-b)^2} - \frac{\Gamma(T)}{\Psi(V)^2}\frac{d\Psi}{dV}\right]} > 0$$

$$\frac{RT}{(V-b)^2} - \frac{\Gamma(T)}{\Psi(V)^2}\frac{d\Psi}{dV} < 0 \qquad \text{or} \qquad \frac{RT}{(V-b)^2} < \frac{\Gamma(T)}{\Psi(V)^2}\frac{d\Psi}{dV}$$

Finally,

$$\frac{T}{\Gamma(T)} < \frac{1}{R}\left(\frac{V-b}{\Psi(V)}\right)^2\frac{d\Psi}{dV} \tag{C}$$

For vdW EoS, (C) becomes:

$$\frac{T}{a} < \frac{1}{R}\left(\frac{V-b}{V}\right)^2\frac{d\Psi}{dV} \qquad \text{or} \qquad \frac{T}{a} < \frac{1}{R}\left(\frac{V-b}{V}\right)^2 V^2$$

$$T < \frac{2a}{RV}\left(\frac{V-b}{V}\right)^2$$

For RKS EoS:

$$\frac{RT}{a\left(1 + m(1 - T_r^{0.5})\right)^2} < 2\left(\frac{V-b}{V(V-b)}\right)^2(2V - b) \qquad \text{or}$$

$$\frac{RT}{a\left(1 + m(1 - T_r^{0.5})\right)^2} < \frac{a}{RV^2}(2V - b).$$

And for PR EoS:

$$\frac{RT}{a\left(1 + m(1 - T_r^{0.5})\right)^2} < 2\left(\frac{V-b}{V^2 + 2bV - b^2}\right)^2(V + b)$$

$$\frac{RT}{a\left(1 + m(1 - T_r^{0.5})\right)^2} < 2\frac{a}{R}\left(\frac{V-b}{V^2 + 2bV - b^2}\right)^2(V + b).$$

References:

[1] W. Foerg, "History of cryogenics: the epoch of the pioneers from the beginning to the year 1911", *Int. J. of Refrigeration* 25: 283-292. https://doi.org/10.1016/S0140-7007(01)00020-2, 2002.

[2] J. P. Mosquera 2018 *"Applications of Cryogenics: Past, Present, Future – Physics World"*, Available : https://physicsworld.com/a/applications-of-cryogenics-past-present-future/2018, 2018.

[3] Joule–Thomson effect – Wikipedia.

https://pt.wikipedia.org/w/index.php?title=Efeito_Joule-Thomson&oldid=56114263, last update 29 August 2019.

[4] C. G. Haseldon, *Cryogenics Fundamentals*, Academic Press Inc. New York, 1971.

[5] M. Mukhopadhyay, *Fundamentals of Cryogenic Engineering*, PHI Learning, Eastern Economy Edition, Delhi (India), January 2021.

[6] T. M. Flynn, *Cryogenic Engineering,* Marcel Dekker, 2005.

[7] R. Barron , *Cryogenic Systems*, 2nd ed. Oxford Science Publications, Oxord University Press, New York, 1985.

[8] Kanoglu, M., Dincer, I., Rosen, M.A., "Performance analysis of gas liquefaction cycles", *Int. J. of Energy Research* 32(1): pp 35 – 43, January 2008

https//:doi.org:10.1002/er.1333

[9] B.-Z. Maytal, "Maximizing production rates of the Linde–Hampson machine", Cryogenics 46 : 49–54, 2006. https://doi:10.1016/j.cryogenics.2005.11.004

[10] C. Yilmaz, T. H. Cetin, B. Ozturkmen, M. Kanoglu "Thermodynamic Performance analysis of gas liquefaction cycles for cryogenic applications" *J. of Thermal Engineering*, (5, (1): pp. 62-75, January 2019. https://doi.org/10.18186/thermal.513038

[11] A. T. A. M. de Waele, "Basics of Joule–Thomson Liquefaction and JT Cooling", *J. of Low Temp Phys* 186:385–403, 2017. https://doi 10.1007/s10909-016-1733-3

[12] M. W. Zemansky, R. H. Dittman, *Heat and Thermodynamics: an Intermediate Textbook*, *7th ed.* New York, McGraw-Hill Companies Inc., pp. 282-284, 1997.

[13] G. D. Miller, "Joule-Thomson inversion curve, corresponding states, and simpler equations of state", *Ind. Eng. Chem. Fundamentals* 9: 585-589, 1970.

[14] R. D. Gunn, P. L. Chueh , J. M. Prausnitz, "Inversion temperatures and pressures for cryogenic gases and their mixtures", *Cryogenics* 6: 324-329, 1966.

[15] K. Juris, L. A. Wenzel, "A study of inversion curves", *AIChE Journal* 18: 684-68, 1972. https://doi.org/10.1002/aic.690180404

[16] W. G. Dilay, A. R. Heidemann, "Calculation of Joule-Thomson inversion curves from equations of state", *Industrial Eng. Chem. Fundamentals* 25: 158-164, 1986. https://doi.org/ 10.1021/i100021a024

[17] D. Geana , V. Feroiu, "Calculation of Joule-Thomson inversion curves from a general cubic equation of state",

Fluid Phase Equilibria 77: 121-132, 1992. https//:doi.org/10.1016/0378-3812 (92)85100-M.

[18] A. Maghari, S. Matin, "Prediction of Joule-Thomson inversion curves from van der Waals type equations of state", *J. of Chem. Eng. of Japan* 30: 520-525, 1997. https://doi.org/10.1252/jcej.30.520

[19] C. M. Colina, C. Olivera-Fuentes, "Prediction of the Joule-Thomson inversion curve of air from cubic equations of state". *Cryogenics* 38: 721-728, 1998. https//: doi.org/10.1016/S0011-2275(98)00036-8

[20] N. S. Matin, B. Haghighi, "Calculation of Joule-Thomson inversion curves from cubic equations of state". *Fluid Phase Equilibria* 175: 273-284, 2000. https//: doi.org/10.1016/S0378-3812(00)00443-X

[21] B. Haghighi, M. R. Laee , N. S. Matin,"A comparison among five equations of state in predicting the inversion curves of some fluids", *Cryogenics* 43: 393-398, 2003.

[22] B. Haghighi , M. R. Bozorgmehr, "Joule-Thomson inversion curves calculation by using equation of state", *Asian J. of Chemistry* 24: 533-537, 2002.

[23] G. S. Soave, " Equilibrium constants from a modified Redlich-Kwong equation of state", *Chemical Eng. Science* 27: 1197-1203, 1972.

[24] D. -Y Peng, D. B. Robinson, " A new two constant equation of state", *Ind. Eng. Chem. Fundamen.* vol 15, pp. 59-64, 1976.

[25] M. D. Cismondi, J. Mollerup, "Development and application of a three parameter RK-PR equation of state", *Fluid Phase Equilibria* 232: 74-89, 2005. https//: doi.org/10.1016/j.fluid.2005.03.020.

[26] P. E. Liley, R. C. Reid, E. Buck, *" Physical and Chemical Data in : Perry, R. H. and Green D., Perry's Chemical Engineers' Handbook", 7th Ed.* McGraw-Hill Companies Inc., Singapore, pp. 3-109, 3-110, 1984.

[27] D. Elwell and A. J. Pointon, *Classical Thermodynamics, 1st Ed.* Peguin Library of Physical Sciences, p.175, 1972.

Free Volume and Internal Pressure of Binary Liquid Mixtures from Ultrasonic Velocity at 303.15 K

Dhirendra Kumar Sharma[1*], Seema Agarwal[2]

[1*]Department of Chemistry Institute of Basic Science,
[2]Bundelkhand University, Jhansi (U.P), India
E-mail: [1*]dhirendra.dr@rediffmail.com

Abstract

Ultrasonic velocity (u), density (ρ), and viscosity (η) measurements have been taken in six binary liquid mixtures ethyl acetate + methanol, ethyl acetate + ethanol, ethyl acetate + propanol, ethyl acetate + butanol, ethyl acetate + hexanol and ethyl acetate + octanol at 303.15 K over the entire mole fraction range. The experimental data has been used to calculate the free volume, internal pressure and their excess values. Excess values of free volume (V_f^E) and internal pressure (p_i^E) were plotted against the mole fraction of ethyl acetate over the whole composition range at 303.15 K. They have been analyzed to discuss the nature and strength of intermolecular interactions in these mixtures.

Keywords: Ultrasonic velocity; binary liquid mixtures; internal pressure; free volume; intermolecular interactions.

1. Introduction

In recent years, ultrasonic investigation of binary liquid mixtures has revolutionized the pharmaceutical industries to great extent [1-6]. Ultrasonic technique has become a powerful tool for studying the molecular behavior of liquid mixtures [7-9]. This is because of its ability of characterizing physic-chemical behavior of liquid medium. Fundamental thermodynamic and thermo-physical properties are essential sources of information necessary for a better understanding of the non-ideal behavior of complex system. Excess thermodynamic functions have been used to explain the formation of complexes in liquid mixtures. These deviations have been interpreted as arising from the presence of strong or weak interactions. The free volume is an important fundamental factor to be considered in explaining variations in the physic-chemical properties many workers have studied this parameter for liquid and liquid mixtures. An-another thermodynamic property internal pressure was recognized many year ago by Hildebrand [10]. The main use of this property has for a long time been limited to descriptive or qualitative purpose. In recent year, it has been found to be an important tool in the study of molecular interactions in liquid and liquid mixtures. An internal pressure of liquid is highly useful in understanding molecular interactions, internal structure and the clustering phenomenon. Now days, many investigations have been carried out to evaluate it in pure and binary liquid mixtures.

The measurement of ultrasonic velocity has been adequately employed in understanding the molecular interactions in liquid mixtures. Ultrasonic velocity and viscosity measurements have been widely used in the field of molecular interactions and structural aspect evaluation studies.

Internal pressure and free volume has been a subject of active interest among several researchers during recent past [11]. Several attempts have been made by a number of investigators to calculate the internal pressure of liquids and liquid mixtures theoretically.

Fundamental thermodynamic and thermo physical properties are essential source of information necessary for a better understanding of the non-ideal behavior of complex systems because physical and chemical effects which are caused by molecular interactions, intermolecular forces etc. of unlike molecules [12] .

In order to examine molecular interactions, we report have the ultrasonic velocity (u), density (ρ), and viscosity (η) of binary liquid mixtures of ethyl acetate with alkanols over entire composition range at 303.15 K. The experimental value of u, ρ and η were used to calculate free volume (V_f), internal pressure (p_i) and their excess values. These parameters are quite sensitive towards the intermolecular interactions between the component molecules in the mixtures. The dependence of these parameters on composition of the mixtures reveals the nature and extent of interaction between component molecules.

2. Experimental
2.1 Material

The chemicals used in the present work were high purity laboratory reagent grade samples of ethyl acetate, methanol, ethanol, propanol, butanol, hexanol, octanol purchased from Merck Chem. Ltd India. All chemicals was stored over sodium hydroxide pellets for several days. All the chemicals were stored in dark bottles over freshly activated molecular sieve to minimize adsorption of moisture. The purity of the solvent was ascertained by comparing the measured density, dynamic viscosities and

sound velocity of the pure component at 303.15K with the available literature [13-22] as shown in Table 1.

2.2 Measurements

Six binary system viz. ethyl acetate + methanol, ethyl acetate + ethanol, ethyl acetate + propanol, ethyl acetate + butanol, ethyl acetate + hexanol and ethyl acetate + octanol were studied. Each sample mixture was prepared, on mass basis, by mixing the calculated volume of liquid components in specially designed glass stoppered bottles. All binary mixtures were prepared by weight covering the entire mole fraction range. The components of binary mixtures were injected by means of syringe in to the glass vials of sealed with rubber stopper in order to check evaporation losses during sample preparation. The mass measurements were carried out using an single pan analytical balance (Model K-15 Deluxe, K Roy Instruments Pvt. Ltd.) with an accuracy of $\pm 0.00001 \times 10^{-3}$ kg as described elsewhere [23]. The possible error in the mole fraction was estimated to be less than 1×10^{-4}. Five samples were prepared for one system, and their density and sound velocity were measured on the same day.

2.2.1 Density

Densities of pure liquids and their binary mixtures were determined by using a double-arm pycnometer [24] with a bulb of 25 cm^3 and a capillary of an internal diameter of about 1 mm is used to measure the densities (ρ) of pure liquids and binary mixtures. The pycnometer is calibrated by using conductivity water (having specific conductance less than 1×10^6 ohm^{-1}) with 0.9970 and 0.9940 gcm^{-3} as its densities at T = 303.15 K, respectively. The pycnometer filled with air bubbles free liquids is kept in a thermostate water bath (MSI Goyal Scientific, Meerut, India) controlled with a thermal equilibrium. The precision of the density measurements was estimated to be ± 0.0002 g cm^{-3}. The observed values of densities of pure ethyl acetate, methanol, ethanol, propanol, butanol, hexanol and octanol at 303.15K were 0.8820, 0.7840, 0.7720, 0.8070, 0.8040, 0.8128 and 0.8242 g.cm^{-3} which compare well with corresponding literature values of respectively.

2.2.2 Sound velocity

The ultrasonic velocities were measured using a multifrequency ultrasonic interferometer (Model F-80D, Mittal Enterprise, New Delhi, India) working at 3 M.Hz. The meter was calibrated with water and benzene at 303.15K. The measured values of ultrasonic velocities of pure ethyl acetate, methanol, ethanol, propanol, butanol, hexanol and octanol at 303.15K were 1125, 1084, 1141, 1182, 1196, 1298 and 1327 m.s^{-1} respectively, which compare well with the corresponding literature values.

2.2.3 Viscosity

The viscosity of pure liquids and their binary mixture were measured using suspended ubbelohde type viscometer [25-26] having a capacity of about 15 ml and the capillary having a length of about 90 mm and 0.5 mm internal diameter has been used to measure the flow time of pure liquids and liquid mixtures and it was calibrated with triply distilled water, methanol and benzene at 303.15 K. The details of the methods and techniques have been described by researchers [27-28]. The efflux time was measured with an electronic stop watch (Racer) with a time resolution (± 0.015), and an average of at least four flow time readings

was taken. Glass stopper was placed at the opening of the viscometer to prevent the loss due to evaporation during measurements. The two bulbs reservoir, one at the top and other at the bottom of the viscometer linked to each other by U type facilitate the free full of liquid at atmospheric pressure.

The measured values of viscosities of pure ethyl acetate, methanol, ethanol, propanol, butanol, hexanol and octanol at 303.15 K were 0.4402, 0.4949, 1.1399, 1.5477, 2.2045, 4.5642 and 7.8512 C.P. which compare well with the corresponding literature values.

Table 1. *Physical properties of pure components at 303.15K.*

Compon ent	Density (ρ) g.cm^{-3}		Ultrasonic Velocities (u) m.s^{-1}		Viscosity (η) CP	
	Observ ed	Literature	Obser ved	Literat ure	Observ ed	Literatur e
Ethyl acetate	0.8820	0.8885 [14]	1125	1115.0 [12]	0.4402	0.4000 [17]
Methanol	0.7840	0.7817 [14]	1084	1084.0 [21]	0.4949	0.5040 [15]
Ethanol	0.7720	0.7807 [13]	1141	1144.3 [15]	1.1399	1.3560 [13]
Propanol	0.8070	0.8003 [20]	1182	1182.6 [15]	1.5477	1.6626 [15]
Butanol	0.8040	0.8020 [15]	1196	1196.6 [15]	2.2045	2.2740 [16]
Hexanol	0.8128	0.8118 [15]	1298	1282.0 [22]	4.5642	4.5930 [18]
Octanol	0.8242	0.8187 [19]	1327	1330.8 [19]	7.8512	7.6630 [18]

3 Theoretical Aspects
3.1 Free Volume (V_f)

Liquid viscosity has been treated as free volume problem by a number of workers. Suryanarayana and Kuppusami derived a formula for the free volume based on one dimensional analysis of the situation. When a ultrasonic wave passes through a liquid medium.

$$V_f = (M U/ k \eta)^{3/2} \qquad (1)$$

Where, M is the molecular weight, u is the ultrasonic velocity, η is the viscosity, V_f , the free volume is in milliliters per mole and K is a constant, independent of temperature and it's value is 4.28×10^9 for all liquids.

3.2 Internal Pressure (p_i)

Suryanarayana and Kuppuswami [29-30] suggested a method for evaluation of internal pressure from the knowledge of ultrasonic velocity, u, density, ρ, and viscosity, η, the relation proposed is expressed as

$$p_i = bRT \left(\frac{k\eta}{u}\right)^{\frac{1}{2}} \frac{\rho^{2/3}}{M_{eff}^{7/6}} \qquad (2)$$

Where b is packing factor, which is assumed to be 2 for all liquid and solution. k is a constant, independent of temperature and its value is 4.28×10^9 for all liquids, R is universal gas constant and T is absolute temperature.

3.3 Excess Thermodynamic Parameters

The excess thermodynamic function (Y^E) provide a way to represent directly the deviation of a solution from ideal behavior. The difference between the thermodynamic function of mixing for a real system and the value corresponding to a perfect solution at the same temperature, pressure and composition is called the thermodynamic

excess function, denoted by Y^E. Excess values for all the parameters are computed using the general formula

$$Y^E = Y_{exp} - (X_1 Y_1 + X_2 Y_2) \qquad (3)$$

4. Result and Discussion

The experimental determinate values of density (ρ), viscosity (η) and sound velocity (u) of all the pure liquids at 303.15 K are presented in Table 1 and the same for the six binary systems are listed in Table 2. The excess value of viscosity (η^E), sound velocity (u^E), free volume (V_f^E) and internal pressure (p_i^E) at 303.15 K are reported in Table 3.

The result present in Table 2 show non-linear behavior of viscosity, sound velocity, free volume and internal pressure, which is further substantial by their excess values (Table 3). All the seven organic compounds namely ethyl acetate, methanol, ethanol, propanol, butanol, hexanol and octanol are a polar organic compounds having dipole moment 1.78 D, 1.70 D, 1.69 D, 1.68 D, 1.66 D, 1.60 D and 1.68 D respectively. Normally more the dipole moment, stronger is the intermolecular interaction, which result is decreasing of free space between molecules and increase in the ultrasonic velocity.

Table 2. Values of density, sound velocity, viscosity, free volume and internal pressure properties for binary liquids mixtures of ethyl acetate + methanol, ethyl acetate + ethanol, ethyl acetate + propanol, ethyl acetate + butanol, ethyl acetate + hexanol and ethyl acetate + octanol at 303.15 K.

Mole fraction of ethyl acetate (X_1)	Density (ρ) g.cm^{-3}	Sound velocity (u) m.s^{-1}	Viscosity (η) CP	Free volume (V_f) ml mol^{-1}	Internal pressure ($p_i \times 10^4$) atm
Ethyl Acetate + Methanol					
0.0000	0.7840	1084	0.4949	0.06639	1.85827
0.1039	0.7968	1099	0.4832	0.08953	1.39542
0.2248	0.8192	1103	0.4810	0.11699	1.07580
0.3129	0.8395	1105	0.4792	0.13807	0.91572
0.4370	0.8483	1110	0.4720	0.17316	0.73366
0.5474	0.8675	1114	0.4684	0.20581	0.62282
0.6409	0.8709	1117	0.4618	0.23810	0.53580
0.7128	0.8790	1118	0.4601	0.26139	0.49096
0.8164	0.8792	1122	0.4538	0.30139	0.43096
0.9104	0.8805	1123	0.4506	0.33654	0.38473
1.0000	0.8820	1125	0.4402	0.38161	0.34494
Ethyl Acetate + Ethanol					
0.0000	0.7720	1141	1.1399	0.03536	1.48567
0.1049	0.8025	1137	0.6563	0.09237	0.99503
0.2090	0.8157	1135	0.6096	0.11781	0.84487
0.3105	0.8278	1134	0.5420	0.15538	0.71041
0.4166	0.8392	1133	0.5298	0.17907	0.62822
0.5094	0.8496	1132	0.5059	0.20957	0.56071
0.6076	0.8604	1131	0.4743	0.25199	0.49618
0.7150	0.8639	1130	0.4667	0.28264	0.44587
0.8069	0.8776	1128	0.4472	0.32369	0.40652
0.9030	0.8827	1126	0.4461	0.34887	0.37581
1.0000	0.8820	1125	0.4402	0.38161	0.34494
Ethyl Acetate + Propanol					
0.0000	0.8070	1182	1.5477	0.03511	1.12536
0.1074	0.8133	1173	1.1104	0.06146	0.88659
0.2086	0.8262	1169	0.8458	0.09824	0.72795
0.3145	0.8321	1161	0.7144	0.13382	0.62680
0.4099	0.8428	1159	0.6106	0.17883	0.54900
0.4758	0.8509	1154	0.5718	0.20368	0.51357
0.5430	0.8609	1150	0.5071	0.25201	0.46810
0.6127	0.8647	1142	0.4850	0.27686	0.44151
0.7564	0.8685	1138	0.4593	0.32271	0.39664
0.9126	0.8788	1134	0.4510	0.35690	0.36363
1.0000	0.8820	1125	0.4402	0.38161	0.34494
Ethyl Acetate + Butanol					
0.0000	0.8040	1196	2.2045	0.02879	0.93886
0.1063	0.8056	1194	1.4102	0.05784	0.72809
0.2151	0.8168	1184	1.0541	0.09105	0.61710
0.3213	0.8269	1180	0.8149	0.13714	0.53084
0.4327	0.8322	1176	0.8129	0.14106	0.51618
0.5192	0.8420	1170	0.5978	0.22702	0.43625
0.6266	0.8424	1167	0.5290	0.27918	0.39871
0.7124	0.8581	1154	0.4890	0.31567	0.38101
0.8127	0.8666	1142	0.4611	0.34790	0.36421
0.9044	0.8742	1134	0.4533	0.36108	0.35557
1.0000	0.8820	1125	0.4402	0.38161	0.34494
Ethyl Acetate + Hexanol					
0.0000	0.8128	1298	4.5642	0.01768	0.76533
0.0996	0.8214	1292	2.8302	0.03523	0.62247
0.2225	0.8338	1287	2.0351	0.05597	0.54978
0.3149	0.8355	1275	1.5522	0.08122	0.49429
0.4151	0.8406	1257	1.2032	0.11401	0.45038
0.5186	0.8466	1247	0.9528	0.15624	0.41469
0.6083	0.8544	1240	0.7949	0.19927	0.39077
0.7096	0.8617	1222	0.6724	0.24487	0.37353
0.8066	0.8672	1210	0.5862	0.28991	0.36080
0.9041	0.8780	1192	0.5216	0.33007	0.34774
1.0000	0.8820	1125	0.4402	0.38161	0.34494
Ethyl Acetate + Octanol					
0.0000	0.8242	1327	7.8512	0.01165	0.66872
0.1056	0.8259	1312	4.7776	0.02292	0.55668
0.2095	0.8300	1294	3.2258	0.03838	0.49024
0.3174	0.8318	1275	2.2206	0.06206	0.43728
0.4286	0.8387	1239	1.5414	0.09634	0.37509
0.5083	0.8400	1225	1.2853	0.11928	0.38467
0.6196	0.8444	1214	0.9417	0.17562	0.35719
0.7090	0.8586	1192	0.8858	0.17723	0.37519
0.8064	0.8651	1164	0.6239	0.27175	0.34396
0.9044	0.8716	1148	0.5565	0.29587	0.35364
1.0000	0.8820	1125	0.4402	0.38161	0.34494

The measured values density (ρ), viscosity (η) and sound velocity (u) and the evaluated parameters are presented in Table 2. For the binary system ethyl acetate + methanol, ethyl acetate + ethanol, ethyl acetate + propanol, ethyl acetate + butanol, ethyl acetate + hexanol and ethyl acetate + octanol at 303.15 K. From Tables it can be noticed that, at the 303.15 K temp. The value of viscosity, sound velocity and internal pressure decease with increase in mole fraction of ethyl acetate (X_1) but the value of density (ρ) and free volume (V_f) increase with increase in mole fraction of ethyl acetate (X_1). It is evident that the pronounced increase or decrease in these parameters with composition of mixtures indicates the presence of interaction between the component molecules in the binary mixtures. It can also be observed that the ultrasonic velocity is decreasing with increase in mole fraction of ethyl acetate. This trend indicates specific interactions among the constituents of the mixtures. This behavior can be attributed to intermolecular interaction [31-32]. The chemical interaction may involve the association due to hydrogen bonding order to dipole-dipole interaction or may be due to the formation of charge-transfer complexes. All these process may lead to strong interaction forces [33]. The decrease in velocity in these liquid mixtures suggest that molecular interactions among the molecules of the components of liquid mixture.

An analysis of the viscosity values from the Table 2 it can be observed that the viscosity is in decrease trend with increase in mole fraction of ethyl acetate. Similar trend is also observed for the internal pressure values. This kind of non-linearity indicates the presence of molecular interactions.

It is observed that for the binary liquid mixtures, the density (ρ) and free volume (V_f) increase with increase in concentration of ethyl acetate. The increases the density (ρ) and free volume (V_f) in these liquid mixtures suggest that molecular interaction among the molecules of the components of liquid mixture.

4.1 Excess Acoustical and Thermodynamic Parameters

In order to understand the nature of molecular interactions between the components of the liquid mixtures, it is of interest to discuss the same in terms of excess parameters rather than actual values. Non-ideal liquid mixtures show considerable deviation from linearity in their concentrations and this can be interpreted as the presence of strong or weak interactions. The extent of deviation depends upon the nature of the constituents and composition of the mixtures. The thermodynamic excess properties are found to be more sensitive towards intermolecular interaction among the component molecules of liquid mixtures. The sign and extent of deviation of excess parameters depend on the strength of interaction between unlike molecules [34]. So various excess acoustic and thermodynamic parameters have been evaluated and corresponding graphs are also given.

Table 3. Excess values of sound velocity (u^E), viscosity (η^E), free volume (V_f^E) and internal pressure (P_i^E) properties for binary liquids mixtures of ethyl acetate + methanol, ethyl acetate + ethanol, ethyl acetate + propanol, ethyl acetate + butanol, ethyl acetate + hexanol and ethyl acetate + octanol at 303.15 K.

Mole fraction of ethyl acetate (X_1)	Excess sound velocity (u^E)	Excess Viscosity (η^E) CP	Excess Free volume (V_f^E) ml mol^{-1}	Excess internal pressure ($p_i^E \times 10^4$) atm
Ethyl Acetate + Methanol				
0.0000	0.00	0.0000	0.0000	0.0000
0.1039	+7.57	-0.0610	-0.0096	-0.3055
0.2248	+8.10	-0.0841	-0.0202	-0.4421
0.3129	+8.19	-0.1153	-0.0269	-0.4689
0.4370	+9.81	-0.2102	-0.0309	-0.4732
0.5474	+10.51	-0.2374	-0.0331	-0.4070
0.6409	+6.74	-0.1346	-0.0303	-0.2967
0.7128	+4.79	-0.1292	-0.0297	-0.2885
0.8164	+4.54	-0.0813	-0.0223	-0.1923
0.9104	+1.69	-0.0561	-0.0168	-0.0956
1.0000	0.00	0.0000	0.0000	0.0000
Ethyl Acetate + Ethanol				
0.0000	0.00	0.0000	0.0000	0.0000
0.1049	+0.83	-0.4101	-0.0206	-0.3708
0.2090	+1.32	-0.4321	-0.0257	-0.4023
0.3105	+2.01	-0.4805	-0.0312	-0.4209
0.4166	+2.30	-0.5123	-0.0389	-0.4438
0.5094	+2.64	-0.6432	-0.0412	-0.4821
0.6076	+1.84	-0.2704	-0.0495	-0.3438
0.7150	+1.76	-0.2475	-0.0325	-0.2963
0.8069	+1.73	-0.1280	-0.0246	-0.2240
0.9030	+0.76	-0.0615	-0.0211	-0.1585
1.0000	0.00	0.0000	0.0000	0.0000
Ethyl Acetate + Propanol				
0.0000	0.00	0.0000	0.0000	0.0000
0.1074	+1.04	-0.3182	-0.0108	-0.1542
0.2086	+1.37	-0.4707	-0.0191	-0.2345
0.3145	+1.87	-0.4848	-0.0216	-0.2530
0.4099	+1.90	-0.5026	-0.0369	-0.2564
0.4758	+2.86	-0.5618	-0.0486	-0.2640
0.5430	+3.05	-0.4390	-0.0512	-0.2334
0.6127	+1.88	-0.3840	-0.0416	-0.2056
0.7564	+1.50	-0.2506	-0.0315	-0.1384
0.9126	+0.96	-0.1659	-0.0186	-0.0495
1.0000	0.00	0.0000	0.0000	0.0000
Ethyl Acetate + Butanol				
0.0000	0.00	0.0000	0.0000	0.0000
0.1063	+3.29	-0.6066	-0.0084	-0.1476
0.2151	+5.57	-0.7707	-0.0134	-0.1939
0.3213	+6.83	-0.8224	-0.0150	-0.2171
0.4327	+10.74	-0.8880	-0.0404	-0.2656
0.5192	+10.88	-0.8905	-0.0450	-0.2942
0.6266	+15.51	-0.5698	-0.0512	-0.1679
0.7124	+8.60	-0.4585	-0.0355	-0.1347
0.8127	+3.72	-0.3094	-0.0131	-0.0919
0.9044	+2.24	-0.1552	-0.0108	-0.0460
1.0000	0.00	0.0000	0.0000	0.0000
Ethyl Acetate + Hexanol				
0.0000	0.000	0.0000	0.0000	0.0000
0.0996	+11.26	-1.3229	-0.0187	-0.1009
0.2225	+27.52	-1.6113	-0.0426	-0.1219
0.3149	+31.50	-1.7131	-0.0516	-0.1386
0.4151	+32.50	-1.8488	-0.0547	-0.1404
0.5186	+38.84	-1.9126	-0.0398	-0.1623
0.6083	+30.27	-1.4724	-0.0310	-0.1326
0.7096	+28.79	-1.2602	-0.0213	-0.1187
0.8066	+20.56	-0.9649	-0.0166	-0.0934
0.9041	+13.87	-0.6514	-0.0120	-0.0654
1.0000	0.000	0.0000	0.0000	0.0000
Ethyl Acetate + Octanol				
0.0000	0.00	0.0000	0.0000	0.0000
0.1056	+6.36	-2.2921	-0.0278	-0.0778
0.2095	+9.36	-3.0735	-0.0508	-0.1106
0.3174	+12.14	-3.2790	-0.0670	-0.1286
0.4286	+13.42	-3.4681	-0.0738	-0.1548
0.5083	+14.73	-4.2162	-0.0804	-0.1694
0.6196	+12.18	-2.7995	-0.0967	-0.1194
0.7090	+8.25	-2.3178	-0.0652	-0.1109
0.8064	+5.07	-1.7108	-0.0503	-0.0632
0.9044	+3.72	-1.1250	0.0315	-0.0222
1.0000	0.00	0.0000	0.0000	0.0000

The sign and magnitude of excess ultrasonic velocity (u^E) play an important role in describing molecular rearrangement as a result of the molecular interaction between the component molecules in the mixtures. The excess ultrasonic velocity (u^E) curves at 303.15 K varying with mole fraction of ethyl acetate are represented in Figure-1 for the six binary systems. The excess ultrasonic velocity values exhibiting positive in all six binary systems. Generally, the value of the excess function (u^E) depend upon several physical and chemical contributions [35-36]. The physical contribution depends mainly on two factors, namely:

1. The dispersion forces or weak dipole-dipole interaction that leads to positive values.

2. The geometrical effect allowing the fitting of molecules of two different sizes in to each other's structure resulting in negative values.

The chemical contributions include breaking up of the associates present in pure liquids, resulting in positive u^E. In the present mixture the graphical representation of excess sound velocity (u^E) are positive, presented in Figure 1. The positive values reveal that there are present weak interactions in the mixture.

The observed positive trends in excess sound velocity indicate that the effect due to the breaking up of self-associated structure of the components of the mixtures is dominant over the effect of hydrogen bonding and dipole-dipole interaction between unlike molecule. The excess sound velocity values in the sequence methanol < ethanol < propanol < butanol < hexanol < octanol which also reflects

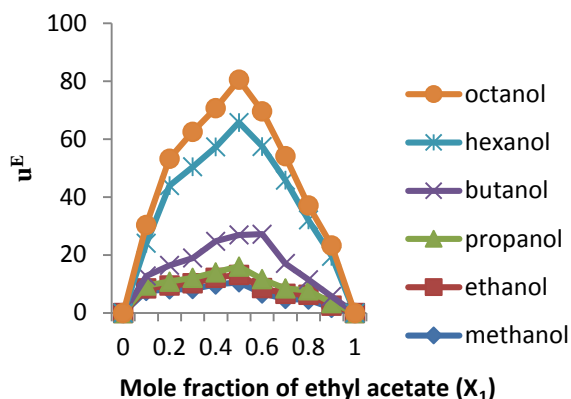the decreasing strength of interaction unlike molecule in the mixture.

Figure 1. Plots of excess sound velocity versus mole fraction of ethyl acetate (X_1) at 303.15 K for binary mixtures of ethyl acetate with methanol, ethanol, propanol, butanol, hexanol and octanol at 303.15 K.

The measurement of viscosity in binary liquid mixture gives some reliable information in the study of intermolecular interaction. The molecules of one or more components forming the temarise are either polar, associating or accordingly show non-ideal behavior's in mixtures. Negative values of η^E in most of the cases are the consequence of lower viscosity contributions of similar non-specific interaction and hydrogen bonding effect of molecular species in real mixtures rather than those in the corresponding ideal mixtures.

In the present study, it is observed that, for the six binary systems the η^E values gradually decrease up to the mole fraction around 0.5 and then begins to increase Figure 2 more over it is observed that the η^E values decrease as the concentration of X_1 increase. The negative values imply the presence of dispersion forces between the mixing components in the mixtures.

Figure 2. Plots of excess viscosity versus mole fraction of ethyl acetate (X_1) at 303.15 K for binary mixtures of ethyl acetate with methanol, ethanol, propanol, butanol, hexanol and octanol at 303.15 K.

The excess free volume (V_f^E) is another important parameter through which molecular interactions can be explained.

In the present investigation the negative excess free volume (V_f^E) for binary mixtures of ethyl acetate with alkanols may be attributed to hydrogen bond formation

through dipole-dipole interaction between alkanol and ethyl acetate molecule or to structural contributions arising from the geometrical fitting of one component (alkanol) into the other (ethyl acetate) due to difference in the free volume between components.
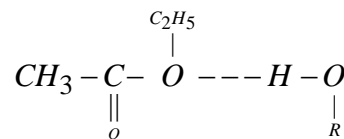
Figure 3. Hydrogen bonding between ethyl acetate and 1-alkanol molecule.

In order to substantiate the presence of interaction between the molecules, it is essential to study the excess parameter such as free volume. The deviation of physical property of the liquid mixtures from the ideal behavior is a measure of the interaction between the molecules which is attributed to either adhesive or cohesive forces [37]. In the present study, alkanols in a polar and has self - association character in other polar organic solvents.

Figure 4. Self association of 1-alkanol molecule.

The negative values of excess free volume (V_f^E) indicate the presence of strong molecular interaction [38-39]. We may conclude that alkanols, which is a self − associating polar organic liquid has a tendency to form complexes with ethyl acetate and the increase in its dilution causes disruption of aromatic C − H bond stretching as the self − association of alkanols is disrupted. It is also concluded that suryanarayana approach for estimating free volume of binary liquid mixtures, based on dimensional analysis using thermodynamic consideration is very well applicable in the present case.
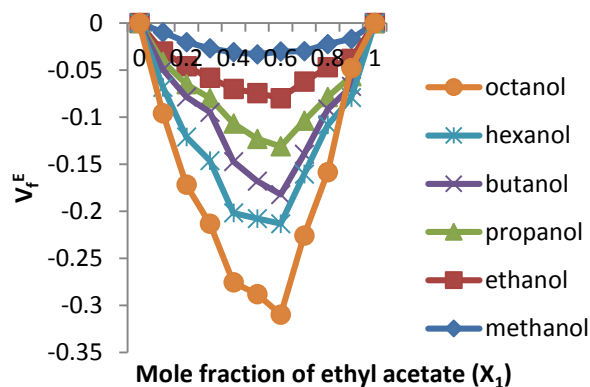
Figure 5. Plots of excess free volume versus mole fraction of ethyl acetate (X_1) at 303.15 K for binary mixtures of ethyl acetate with methanol, ethanol, propanol, butanol, hexanol and octanol at 303.15 K.

The excess internal pressure (p_i^E) is another important parameter through which molecular interactions can be explained. In the present investigation for the six binary systems it is observed that, as the mole fraction of ethyl acetate increase, the p_i^E values decreases. The values of p_i^E

are almost negative and gradually decrease and move towards the positive values by the increase of mole fraction of ethyl acetate. More over the p_i^E decrease with increase in X_1 . This situation is observed for all six binary system under study and can be viewed from plots Figure 6.
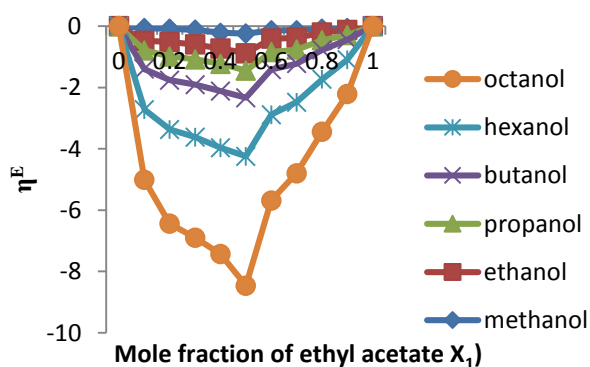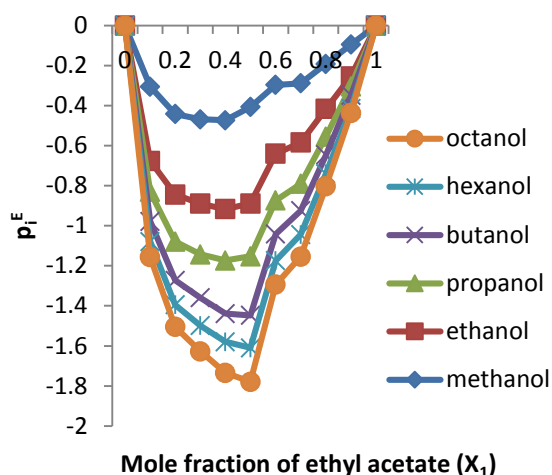

Figure 6. Plots of excess internal pressure versus mole fraction of ethyl acetate (X_1) at 303.15 K for binary mixtures of ethyl acetate with methanol, ethanol, propanol, butanol, hexanol and octanol at 303.15 K.

This suggests that dipole and dispersion force are operative in these systems, when the ethyl acetate concentration low. When the concentration of ethyl acetate leads to specific interactions, i.e. the interactions move from weak to strong which supports the above arguments is case of other parameters

5. Conclusions

From the observed thermodynamic studies of six binary liquid mixtures of six binary liquid mixtures ethyl acetate + methanol, ethyl acetate + ethanol, ethyl acetate + propanol, ethyl acetate + butanol, ethyl acetate + hexanol and ethyl acetate + octanol at 303.15 K are shown negative values of excess free volume and excess internal pressure may given information about the considerable interactions among the molecules of the between these binary mixtures, so we concludes that interactions are exist may be due to dipole-dipole interactions. It is also concluded that Suryanarayana [40] approach for estimating free volume and internal pressure of binary liquid mixtures, based on dimensional analysis using thermodynamic considerations is very well applicable in the present case.

Nomenclature

ρ Densities of liquid
u, Ultrasonic velocity
u^E, excess ultrasonic velocity
η, Viscosity
$η^E$, excess viscosity
V_f, Free Volume
V_f^E, Excess values of free volume
P_i, Internal pressure
P_i^E, Excess internal pressure
X_1, Mole fraction of ethyl acetae
Y^E, Thermodynamic excess function

References

[1] S. Agarwal, D. K. Sharma, "Ultrasonic, Volumetric and Isentropic Compressibility of Binary Mixtures of 1,4-Dioxane with Primary Alcohols at 303.15 K, " *Open Journal of Physical Chemistry, 11*, 168-181, 2021.

[2] GV Rama Rao, AV sarma, D. Ramachandran, C. Rambabu "Evaluation of excess free volume and inernal pressure of binary solution of o-chloro phenol at different temperatures" *Indian journal of Pure & Applied Physics, 43*, 602-609,2005.

[3] A. Ali, A. K. Nain, "Ultrasonic study of molecular interaction in binary liquid mixtures at 30°C," *Parmana J. Phys., 58*, 695-701, 2002.

[4] P. C. Sharma, "Ultrasonic interferometric study of the solutions of tetra alkyl ammonium iodides in dimethyl sulphoxide at 40, 50 and 60°C," *Ultrasonics, 29*, 344-347, 1991.

[5] F. Comeli, S. Ottani, R. Francesconi, C. Castellari, "Densities, Viscosities, and Refractive Indices of Binary Mixtures Containing *n*-Hexane + Components of Pine Resins and Essential Oils at 298.15 K," *J. Chem. Eng. Data, 47*, 93-97, 2002.

[6] C. Chauhan, S.K. Syal, M.S. Chauhan, " Viscosity and ultrasonic velocity studies of binary mixtures at different temperature 1:Acetonitrile-propylene carbonate" *Ind. J. Pure Appl. Phys., 32*, 186, 1994.

[7] A. Ali, A. K. Nain, "Study of intermolecular interaction in binary mixtures of Formamide with 2-propanol, 1,2-propanediol and 1,2,3-propanetriol through ultrasonic speed messurements" *Ind. J. Pure Appl. Phys., 39*, 421, 2001.

[8] S. Ottani, D. Vitalini, F. Comeli, C. Castellari, "Densities, Viscosities, Refractive Indices, and Excess Molar Enthalpies of Binary Mixtures Containing Poly (ethylene glycol) 200 and 400 + Dimethoxymethane and + 1,2-Dimethoxyethane at 298.15 K," *J. Chem. Eng. Data, 47*, 1226–1231, 2002 .

[9] R. Naejus, C. Damas, D. Lemordant, C. Coudert, P. Willmann, "Excess thermodynamic properties of the ethylene carbonate–trifluoroethyl methyl carbonate and propylene carbonate–trifluoroethyl methyl carbonate systems at *T* = (298.15 *or* 315.15) K," *J. Chem., Thermodyn., 34*, 795-806, 2002.

[10] J. H. Hildebrand and R. L.Scott, "*Solubility of Non-electrolytes*", (NewYork) 1965.

[11] P. Paul Divakar, K. Samatha, *Ind. Streams Research Journal, 1*, 9, 2011.

[12] S. Kaki, D. R. Chandran, "Studying various thermodynamic properties of binary mixture of ethyl acetate with ethanol at 303.15 and 313.15 K," *J. of Eng. and Applied Sciences 13*, 2693-2704, 2018.

[13] A. Rodriguez, J. Canosa, J. Tojo, "Physical Properties and Liquid-Liquid Equilibrium and Physical Properties of the Ternary Mixture (Dimethyl Carbonate +Methanol

+ Cyclohexane) at 298.15 K," *Journal of Chemical & Engineering Data, 46*, 846-850, 2001.

[14] P. S. Nikam, T. R. Mahale, M. Hasan, "Density and Viscosity of Binary Mixtures of Ethyl Acetate with Methanol, Ethanol, Propan-1-ol, Propan-2-ol, Butan-1-ol, 2-Methylpropan-1-ol, and 2-Methylpropan-2-ol at (298.15, 303.15, and 308.15) K," *J. Chem. Eng. Data, 41*, 1055-1058, 1996.

[15] M. N. Roy, A. Sinka, S. Biswajit, "Excess Molar Volumes, Viscosity Deviations and Isentropic Compressibility of Binary Mixtures Containing 1,3-Dioxolane and Mono alcohols at 303.15 K," *Journal of Solution Chemistry, 34*, 1311-1325, 2005 .

[16] B. U. Kadam, P. A. Hiray, B. A. Sawant, M. Hasan, "Densities, Viscosities, and Ultrasonic Velocity Studies of Binary Mixtures of Chloroform with Propan-1-oland Butan-1-ol at (303.15 and 313.15) K," *Journal of Chemical & Engineering Data, 51*, 60-63, 2006.

[17] P. S. Nikam, T. R. Mahale, M. Hasan, "Densities and Viscosities for Ethyl Acetate + Pentan-1-ol, + Hexan-1-ol, + 3,5,5-Trimethylhexan-1-ol, + Heptan-1-ol, + Octan-1-ol, and + Decan-1-ol at (298.15, 303.15, and 308.15) K," *J. Chem. Eng. Data, 43*, 436-440, 1998.

[18] A. J. Al-Kandary, A. S. Al-Jimaz, A.M. Abdul-Latif, "Densities, Viscosities, Speeds of Sound and Refractive Indices of Binary Mixtures of Tetrahydrofuran with 1-Hexanol, 1-Heptanol, 1-Octanol, 1-Nonanol and 1-Decanol at 298.15, 303.15, 308.15 and 313.15 K," *Physics and Chemistry of Liquid, 47*, 210-224, 2009 .

[19] G. P. Dubey, M. Sharma, "Excess Volumes, Densities, Speeds of Sound, and Viscosities for the Binary Systems of 1-Octanol with Hexadecane and Squalane at (298.15, 303.15 and 308.15) K," *International Journal of Thermophysics, 29*, 1361-1375, 2008.

[20] S. Elangovan, S. Mullainathan, "Ultrasonic Studies of Intermolecular Interaction in Binary Mixture of n-Methyl Formate with 1-Propanol at Various Temperatures,"*Indian Journal of Physics, 87*, 659-664, 2013.

[21] M. Yasmin, K. P. Singh, S. Parveen, M. Gupta, J. P. Shukla, "Thermoacoustical Excess Properties of BinaryLiquid Mixtures—A Comparative Experimental and Theoretical Study," *Acta Physica Polonica A, 115*, 890-900, 2009.

[22] A. Ali, S. Hyder, M. Tariq, "Measurements of the Properties of Binary Mixtures of Dimethylsulphoxide (DMSO) with 1-Alkanols (C$_4$, C$_6$, C$_7$) at 303.15," *Journal of Thermophysics, 26*, 1537-1548, 2005.

[23] R.R. Yadava, V.N. Singh, S.S. Yadava, "Excess Volume of Mixing for Binary Mixtures of Some Nitroalkanes and Symmetrical Aromatic Hydrocarbons," *J Chem. Eng. Data, 39*, 705-707, 1994 & "Shear viscosities of binary mixtures of polar solutes nitromethane, nitroethane, and 2-nitropropane with nonpolar aromatic solvents benzene, p-xylene, and mesitylene at 293.15 K," *J. Chem. Eng. Data, 33*, 402-404, 1988.

[24] B. Sathyanarayan, B. Ranjith Kumar, T. SavithaJyostna, N. Satyanarayan, "Densities and

[25] J. R. Suindells, T. B. Godfray, *J. Res. Natd. Bur.Stand. 48*, 1, 1952.

viscosities of binary liquid mixtures of N-methylacetamide with some chloroethanes and chloroethenes at T = 308.15 K," *J. Chem. Thermodyn., 39*, 16-21, 2007.

[26] P. S. Nikam, L. N. Shirsat, M. Hasan, "Density and Viscosity Studies of Binary Mixtures of Acetonitrile with Methanol, Ethanol, Propan-1-ol, Propan-2-ol, Butan-1-ol, 2-Methylpropan-1-ol, and 2-Methylpropan-2-ol at (298.15, 303.15, 308.15, and 313.15) K," *J. Chem. Eng. Data, 43*, 732-737, 1998.

[27] M. N. Roy, A. Jha, R. Dey, "Study of Ion−Solvent Interactions of Some Alkali Metal Chlorides in Tetrahydrofuran + Water Mixture at Different Temperatures," *J. Chem. Eng. Data, 46*, 1327–1329, 2001.

[28] M. N. Roy, A. Jha, A. Choudhury, "Densities, Viscosities and Adiabatic Compressibilities of Some Mineral Salts in Water at Different Temperatures," *J. Chem. Eng. Data, 49*, 291-296, 2004.

[29] J.Kuppusami and C.V. Suryanarayana, *Indian J Acoust Soc.India,*5,102-106,1977.

[30] C.V.Suryanarayana and J. Kuppusami, *Indian J Acoust Soc.India,*4,75,1976.

[31] J. A. Dean, Lange's Handbook of chemistry, 13th Ed. New York: McGraw Hill Int., 186, 1987.

[32] L. Palaniappan and K. Ramesh, "Thermoacoustical studies of some iso-alcohols in cyclohexane with toluene," *Indian J. Pure Appl. Phys., 40*, 828-830, 2002.

[33] R. Thiyagarajan, M. Suhaimi Jaafar and L. Palaniappan, *Journal of physical Science, 18*, 81-88, 2007.

[34] R. P. Singh, C.P. Sinha, J. C. Das and P. Ghosh, *Journal of Chem. Eng. Data, 35*, 93-97, 1990.

[35] T. Sumathi, S. Govindarajan, "Molecular interaction studies on some binary organic liquid mixtures at 303.15 K," *International Journal of Biology, Pharmacy and Allied Sciences (IJBPAS), 1*, 1153-1165, 2012.

[36] A. Ali, A. K. Nain, V. K. Sharma and S. Ahmed, "Ultrasonic studies in binary liquid mixtures," *Indian Journal of Physics B, 75*, 519-525, 2001.

[37] K. C Reddy, S. V. Subrahmanyan, J. Bhimsenachar, *J Phys Soc Japan, 19*, 59, 1964.

[38] P. S. Naidu, K. Ravindra Prasad, "Molecular interactions in binary liquid mixtures - An ultrasonic study," *Indian J Pure & Appl. Phys., 40*, 264-271, 2002.

[39] G. V. Rama Rao, A. Viswanatha Sama , D. Ramachandran & C. Rambabu, " Evaluation of excess free volumes and excess internal pressures of binary solutions of o-chlorophenol at different temperatures," *Indian Journal of Pure & Applied Physics, 43*, 602-608, 2005.

[40] C.V.Suryanarayana, "The liquid state-A new out look", Indian *J Acoust Soc.India,*5,11,1977.

Revisiting The Phase Diagram of Au – Cu Alloy at Nanoscales

F. Monji[1], M. A. Jabbareh[2]*

[1]Department of Mechanical Engineering, York University, Toronto, ON M3J 1P3, Canada.
[2]Department of Materials and Polymer Engineering, Faculty of Engineering, Hakim Sabzevari University, Sabzevar, Iran.
E-mail: [1]fmonji@yorku.ca, [2] m.jabbareh@hsu.ac.ir

Abstract

Au – Cu nanoparticles are widely used as catalysts in different chemical reactions. Since knowing the phase diagram of nano-alloys is crucial for effective design of nano-catalysts, there have been many efforts to predict the size effect on the phase diagram of the Au – Cu system. However, reported results are inconsistent and sometimes contradictory. In this work, a CALPHAD type thermodynamic model was applied to recalculate the phase diagram of Au – Cu binary alloy nanoparticles at different sizes. The results show that decreasing particle size decreases liquidus and solidus temperatures as well as the congruent melting point. It was also found that by reduction of the particle size, the composition of the congruent alloy shifts towards the Au – rich side of the phase diagram.

Keywords: Size effect; alloy nanoparticle; Au – Cu alloy; phase diagram; CALPHAD method.

1. Introduction

Gold - Copper (Au-Cu) alloy nanoparticles have attracted considerable interest in nanoscience and nanotechnology, especially as catalysis. They are widely used in the oxidation of carbon monoxide [1], reduction of carbon dioxide [2], selective oxidation of alcohols [3], and other chemical reactions [4,5]. It has been shown that the catalytic efficiency of nanoparticles directly depends on their melting temperatures [6]. Therefore, to achieve optimum performance, the knowledge of nanoscale phase diagram of desired system is essential for tuning the properties and optimal design of nano-catalysts. Since the calorimetric measurements are very difficult to apply to nanoparticles, theoretical methods are generally used for predicting phase diagrams at nanoscales [7,8].

Due to its importance, there have been several attempts to calculate the size dependent phase diagram of Au – Cu nano-alloy in recent years. Using their thermodynamic model, Vallee et al. [9] calculated the phase diagram of spherical Au – Cu nanoparticles with 106 atoms (~ 30 nm in diameter). They showed that compared to the bulk, at nanoscales solidus and liquidus temperatures drop to lower temperatures. According to their results, the congruent melting point had a shift to the Au – rich side of the Au – Cu phase diagram when the particle size dropped to the nanoscale. Guisbiers et al. [10] adopted a nano-thermodynamic model and calculated the phase diagram of different polyhedral Au – Cu nanoparticles at sizes of 4 and 10 nm. Regardless of the geometry of the nanoparticles, similar to Vallee et al., their results demonstrated a decrease in solidus and liquidus temperatures by decreasing particle size. However, in contrast to the results reported by Vallee et al., calculations by Guisbiers et al. showed a considerable shift in the congruent melting point towards Cu – rich side of the phase diagram. Based on the size dependent cohesive energy model, Cui et al. [11] developed a nano-thermodynamic model and investigated the effects of size,

shape, and segregation on the phase diagram of polyhedral and spherical Au-Cu nanoparticles at sizes of 4 and 10 nm. For spherical nanoparticles with a diameter of 4 nm, they reported a decrease of 400, 340, and 340 K in melting temperature of Au, Cu, and congruent melting point, respectively. Besides, their results showed that by decreasing particle size the congruent melting point linearly shifted to the Au – rich corner of the phase diagram which contradicts the results of Guisbiers et al. Using a nano-thermodynamic model, Chernyshev [12] calculated the phase diagram of ultrasmall (*d*=2 nm, 4 nm, and 8 nm) spherical nanoparticles of Au–Cu alloy. He reported approximately 470, 400, and 400 K decrease in melting temperatures of Au, Cu, and congruent alloy, respectively, for nanoparticles with diameter of *d*=4nm. Also, the calculated phase diagrams by Chernyshev [12] showed that the congruent melting point transfers to higher Au concentrations as the size of the particles decreases which is consistent with the results of Cui et al. [11]. However, the calculated melting temperatures of Au and Cu by Chernyshev [12] do not conform to the reported results by Cui et al. [11] Most recently, Muñoz and Rosales [13] studied the phase diagram of the Au-Cu nanoparticles with various polyhedral shapes by using a set of MD simulations. They found that there was a shift in the location of the congruent melting point towards high concentrations of Cu as the size of the system decreased, which conforms with the results reported by Guisbiers et al., nevertheless calculated melting temperatures of pure elements and congruent melting temperatures are different from those of calculated by Guisbiers et al. According to the literature, although many attempts have been made to calculate the size dependent phase diagram of the Au – Cu system, reported results are inconsistent and contradictory. Due to the lack of sufficient experimental data, the results of the calculations have not been compared with the experimental results in any of the previous studies. So, it is impossible to judge the validity of the presented results.

Recently, Chu et al. [14] Experimentally measured the melting temperature of Au – Cu alloy nanoparticles with a composition of 50% and a particle size of 10 nm. They also used the CALPHAD (CALculation of PHAse Diagrams) method to calculate the phase diagram of Au – Cu nanoparticles. Experimental results showed that the temperatures of solidus and liquidous for the studied nanoparticles are 1028.6 K and 1041.3 K, respectively. However, in this study, the effect of size on the chemical composition of the congruent alloy has not been discussed. Also, their calculations were limited to nanoparticles bigger than 10 nanometers in diameter.

CALPHAD (CALculation of PHAse Diagrams) method is a reliable and powerful technique for predicting phase diagram of bulk alloys which can be extended to nano-scale systems by adding the surface Gibbs free energy contributions to the total Gibbs energy of the system [8]. In conventional nano – CALPHAD models [8,14,15], the size dependency of the surface energies is neglected and replaced by the surface energies of the bulk materials. So, it is believed that conventional nano - CALPHAD models cannot be applied to nanoparticles generally smaller than 10 nm in diameter [16]. Recently Monji and Jabbareh [17], by considering the size dependent surface energies of the nanoparticles modified the conventional nano - CALPHAD models. This modified model can be applied to nanoparticles under critical size ($d < 10$ nm). The model has been used to calculate the phase diagram of Ag – Au [17] and Ag – Cu [17,18] nanoparticles with $d < 10$ nm and the achieved results have shown good agreements with the experiments.

This work aims to reassess the phase diagram of Au– Cu nanoparticles to answer the question of how the congruent melting temperature and the concentration of the congruent alloy in the Au – Cu system are affected by reducing the particle size. Whereas previous research works have given completely opposite answers to this question. To this end, the previously developed model by the authors [17] was applied to Au–Cu nanoparticles with different sizes from 4 nm to 40 nm in diameter. The effect of particle size on the phase diagram, congruent melting point, and congruent alloy composition are calculated theoretically and discussed in this work.

2. Model

Total Gibbs free energy of a nanoparticle system could be expressed as:

$$G^{nano}=G^{bulk}+G^{surf} \tag{1}$$

where G^{bulk} and G^{surf} are the Gibbs free energy of the bulk alloy and the surface contribution to the Gibbs free energy, respectively. The molar Gibbs free energy for two component alloys in their bulk state can be described as [8]:

$$G^{bulk}=X_A G_A^o+X_B G_B^o+RT(X_A \text{Ln} X_A+X_B \text{Ln} X_B)+ G^{ex, Bulk} \tag{2}$$

where R and T are the universal gas constant and absolute temperature, respectively. X_i ($i=$A or B) is the molar fraction and G_i^o is the standard Gibbs energy of component i. $G^{ex, Bulk}$ is the excess Gibbs energy of the bulk alloy. The excess Gibbs energy can be defined by the Redlich–Kister polynomials as [20]:

$$G^{ex, Bulk}=X_A X_B \sum L_v(X_A-X_B)^v \qquad (v=0, 1, 2,…) \tag{3}$$

where L_v is the interaction parameter and can be expressed as:

$$L_v=a_v+b_v T+c_v T\text{Ln}T+… \tag{4}$$

where a_v, b_v, and c_v are empirical constants.

The surface contribution to the Gibbs energy for an isotropic spherical nanoparticle is defined as [15]:

$$G^{surf}=2CV_{AB}\sigma_{AB}/r \tag{5}$$

where σ_{AB} is the surface energy of alloy nanoparticles, V_{AB} is the molar volume and r is the particle radius. The effects of shape, surface strain, and uncertainty of the surface energy measurements are also introduced as C which is known as the correction factor. The value of C for the liquid phases and spherical solid particles is considered to be unity [21].

Because the excess volume quantity is negligible in metallic binary alloys, the molar volume of the binary alloys, V_{AB} could be defined as:

$$V_{AB}=X_A V_A+X_B V_B \tag{6}$$

where V_i is the molar volume of the pure component i. The surface energy of liquid alloys could be calculated using Butler's equation [22]. In the case where the changes in shape and surface strain with the composition are negligible, Butler's model is still applicable for the calculation of the surface energy of solid alloys [8]. The Butler's equation for an A-B binary alloy is expressed as:

$$\sigma_{AB}=\sigma_A+\frac{RT}{A_A}\ln\left(\frac{X_A^{surf}}{X_A^{surf}}\right)+\frac{1}{A_A}[G_A^{ex, surf}(T, X_B^{surf})\text{-}G_A^{ex, bulk}(T, X_B^{bulk})]=\sigma_B+\frac{RT}{A_B}\ln\left(\frac{X_B^{surf}}{X_B^{Bulk}}\right)+\frac{1}{A_B}[G_B^{Ex, surf}(T, X_B^{surf})\text{-}G_B^{Ex, Bulk}(T, X_B^{bulk})] \tag{7}$$

where σ_i is the surface energy of the element i. A_i , is the molar surface area of element i when a close-packed monolayer is assumed. X_i^{surf} and X_i^{bulk} are concentrations of component i, respectively, in the surface and bulk phases. $G_i^{ex, surf}$ and $G_i^{ex, bulk}$ also indicate the partial excess Gibbs energy of component i in surface and the bulk phases.

The molar surface area of the component i could be calculated from Eq. (8) as follows:

$$A_i=1.091 \text{ N}_0^{1/3}(V_i)^{2/3} \tag{8}$$

where N_0 is Avogadro's number. $G_i^{ex, surf}$ could be expressed as [15]:

$$G_i^{ex, surf}(T, X_j^{surf})=\alpha \ G_i^{ex, Bulk}(T, X_j^{Bulk}) \tag{9}$$

where α resembles the ratio of the coordination number in the surface to that in the bulk. The values of α in the liquid and solid phases were estimated to be equal to 0.85 and 0.84, respectively [15].

It should be mentioned that in conventional nano – CALPHAD models, the surface energy of the pure components, σ_i, is replaced by the surface energy of the pure elements in the bulk state. In this model, however, we apply the size dependent surface energy adopted by Xiong et al. [23] to calculate the value of σ_i as follows:

$$\sigma_i = \sigma_i^{\infty}(1\text{-}1.45\ h_i/d) \tag{10}$$

where σ_i^{∞} is the temperature dependent surface energy of the element i at the bulk state, h_i is the atomic diameter of element i, and d is the particle diameter.

In the present study, the above model is used to calculate the phase diagram of spherical Au-Cu alloy nanoparticles and the outcomes are compared with available empirical and theoretical results. The information of thermodynamic and physical properties used in the present study are listed in Table 1. The values of the standard Gibbs energies, G_i^o, are taken from the SGTE database for pure elements [24]. To calculate phase diagrams, above equations were implemented in a computer program which is written using Wolfram Mathematica software.

Table 1. Thermodynamic and physical properties used in the calculation of Au–Cu nanoparticle phase diagram. L denotes liquid and S denotes solid phases.

Variables	Equations	Ref.
Surface energy (J/m²)	$^{L}\sigma_{Au}^{\infty}$=1.33-1.4×10⁻⁴T	[15]
	$^{S}\sigma_{Au}^{\infty}$=1.947-4.3×10⁻⁴T	[15]
	$^{L}\sigma_{Cu}^{\infty}$=1.624-2.26×10⁻⁴T	[25]
	$^{S}\sigma_{Cu}^{\infty}$=1.953-2.26×10⁻⁴T	[25]
Molar volume (m³/mol)	$^{L}V_{Au}$=1.02582×10⁻⁵+7.797×10⁻¹⁰T	[15]
	$^{S}V_{Au}$=1.07109×10⁻⁵	[15]
	$^{L}V_{Cu}$=6.95×10⁻⁶+8.08×10⁻¹⁰T	[25]
	$^{S}V_{Cu}$=7.09×10⁻⁶	[25]
Excess Gibbs energy (J/mol)	$^{L}G_{Au,Cu}^{Ex,Bulk}$=$X_{Au}X_{Cu}$[(-28230+3 T)]	[26]
	$\quad+X_{Au}X_{Cu}$[(3200 + 2 T)($X_{Au}-X_{Cu}$)]	
	$\quad+X_{Au}X_{Cu}$[(3900 − 5T)($X_{Au}-X_{Cu}$)²]	
	$^{S}G_{Au,Cu}^{Ex,Bulk}$=$X_{Au}X_{Cu}$[(-28000+7.8.8 T-10 $T\ln T$)]	[26]
	$\quad+X_{Au}X_{Cu}$[(6000)(X_{Au}-X_{Cu})]	
Atomic diameter (nm)	h_{Au}=0.27	[27]
	h_{Cu}=0.27	[27]

3. Results and discussion

Figure 1 shows the calculated surface energy of the liquid and solid Au − Cu nanoparticles with d=10 nm and d=4 nm as a function of Au composition. Calculated surface energy at the bulk state ($d=\infty$) is also plotted for comparison. As shown in figure 1 in all cases, surface energy decreases nonlinearly along with increasing Au concentration. According to Table 1, the gold surface energy is smaller than copper's for both liquid and solid states. So, it is reasonable that increasing Au content reduces the surface energy of the system. the non–linear dependency of surface energy to Au concentration also indicates that Au tends to segregate on the surface. These findings agree well with the results reported in Ref. [28]. The results also represent that decreasing the particle size decreases the surface energy of the nanoparticle which is in accordance with the previous reports on the surface energy of alloy nanoparticles [28,29]. The variation of surface energy between the bulk and the nanoparticles leads to the difference in calculated values of the surface contribution of the Gibbs free energy. However, in some previous thermodynamic models for calculation of Au − Cu nano–phase diagrams [10] the differences between the bulk and the nanoparticles surface energy were ignored.
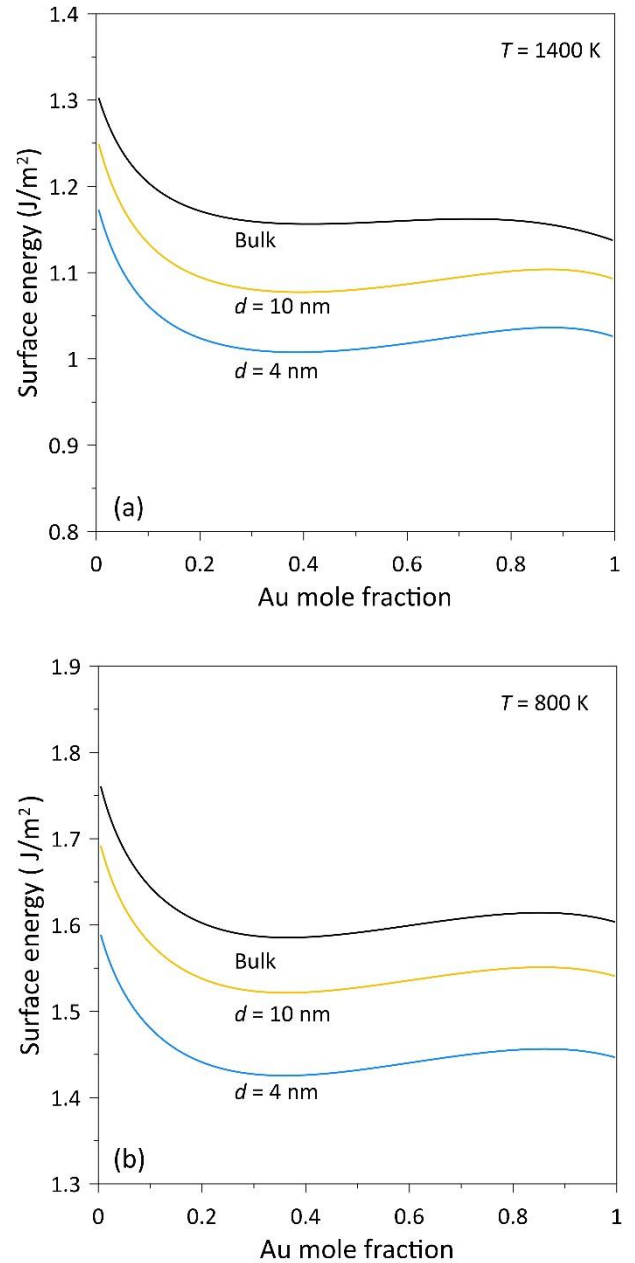
Figure 1. Calculated surface energy of Au − Cu nanoparticles with different diameters in comparison with the bulk surface energy. (a) Liquid phase at T=1400 K. (b) Solid phase at T=800 K.

Figure 2 shows the calculated surface contribution of the Gibbs free energy, G^{surf}, for the liquid and solid Au − Cu nanoparticles in different sizes. Calculations were performed with (solid lines) and without (dashed lines) considering size effect on the surface energy of the nanoparticles. It could be found from Figure 2 that decreasing particle size increases the surface contribution of the Gibbs free energy. This is consistent with experimental observations of melting temperature depression of alloy nanoparticles with size reduction [27, 28].

It is also revealed that by considering the size effect on the surface energy, calculated values of G^{surf} become smaller than those of calculated with the surface energy of the bulk state. Although this issue is not a considerable concern for large nanoparticles, the differences between calculated values of G^{surf}, with and without considering size effect on surface energy, become significant by decreasing the particle size. It should be noted that the decrease in melting temperature of nanoparticles is directly dependent to the

increase of the surface contribution of the Gibbs energy. Therefore, it can be concluded that ignoring the size effect on surface energy leads to smaller calculated melting temperatures. According to Figure 2, it is clear that the particle size decrement leads to noticeable difference in calculated melting temperatures (solidus and liquidus temperatures) between conventional and modified nano – CALPHAD models.
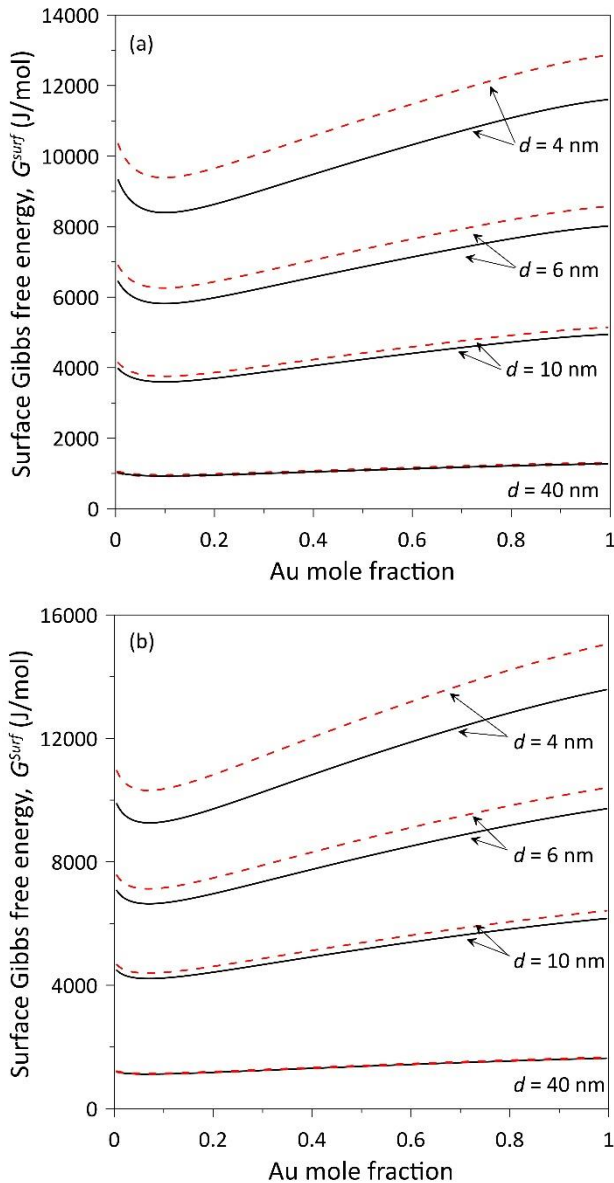
Figure 2. Calculated surface contribution of the Gibbs free energy for nanoparticles with d= 4, 6, 10 and 40 nm. Solid lines denote the calculations with considering size effect on the surface energy, and dashed lines indicates calculations with the surface energy of the bulk. (a) Liquid phase at T=1400 K. (b) Solid phase at T=800 K. (Figure is in color in the on-line version of the paper).

Calculated phase diagram of Au–Cu nanoparticles with d=20 nm, d=10 nm, and d=4 nm together with the bulk Au–Cu phase diagram are presented in Figure 3. The solidus temperatures calculated by Cui et al. [11] and Chernyshev [12] for some specific compositions are also given for comparison. In addition, experimental solidus temperature

[14] for Au-50%Cu nanoparticles with a diameter of 10 nm is also plotted on the figure 3.

The results show that decreasing the particle size leads to decrements in solidus and liquidus temperatures. This observation is consistent with the previously reported data where the size effect on nano-alloys phase diagram was studied [33]. However, the solidus temperatures calculated in this work are greater than those reported by Cui et al. [11] and Chernyshev [12]. This is reasonable because, as mentioned earlier in the introduction, the effect of size on surface energy is not considered in previous works, so these models are expected to predict smaller melting temperatures.

In addition, the calculated solidus temperature for nanoparticles with a diameter of 10 nm is greater than those achieved from experiments [14]. When comparing the experimental results with those achieved from computations, it should be noted that the experimental results are actually related to a set of nanoparticles with a size distribution of 7 to 14 nanometers [14], so, a difference in results between experimental data and those of modeling is expected. In addition, it should be brought to attention that the CALPHAD method is a semi-empirical technique, and the use of appropriate experimental data is essential to be able to optimize the model parameters and computational accuracy. The use of appropriate experimental data to determine the surface energy functions of solid and liquid phases as well as the molar volume functions is also a determining factor in accuracy of calculations. However, the experimental data of theses parameters are rarely available in case of nano-alloys.

According to the phase diagrams calculated for 20, 10, and 4 nm nanoparticles, as the particle size reduces the temperature drop becomes greater.
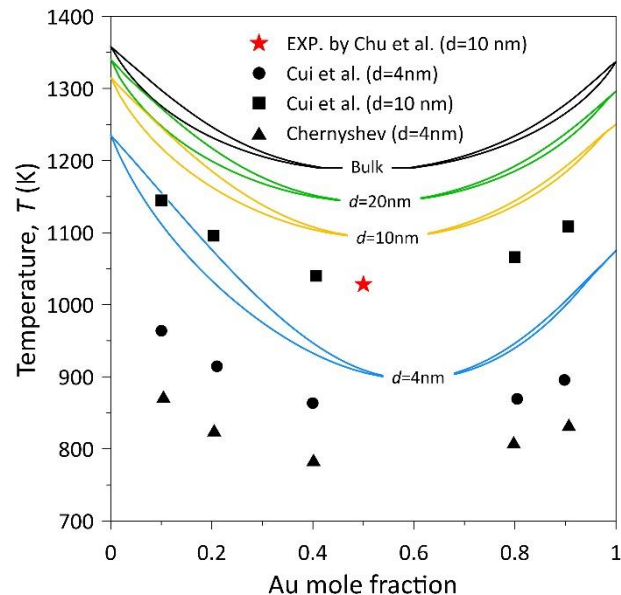
Figure 3. Calculated phase diagram of spherical Au – Cu nanoparticles with different particle sizes in comparison with the phase diagram of corresponding bulk alloy. Symbols denote calculated (Cui et al.[11] and Chernyshev [12]) or experimental (Chu et al.[14]) solidus temperatures from the literature). (Figure is in color in the on-line version of the paper).

The results also reveal that by decreasing the particle size the coexistence solid - liquid region at the Cu – rich side of

the phase diagram gets enlarged, while at the Au – rich side of the Cu-Au phase diagram the coexistence region contracts. This is due to the asymmetry of the surface contribution of the Gibbs free energy with changes in composition. As shown in Figure 2, at a certain particle size, increasing the Au concentration increases the surface Gibbs free energy. As a result, the relative position of the Gibbs free energies of the solid and liquid phases changes in comparison to the bulk. Therefore, changes in coexistence regions are expected. These findings are in contradiction with those reported in the literature. Cui et al. and Chernyshev predicted that decreasing the particle size slightly reduced the coexistence region size in the Cu – rich side of the phase diagram while considerable contraction of the coexistence region at the Au side were observed. Guisbiers et al. [10] reported that decreasing the particle diameter expanded the coexistence region at the Au – rich side of the phase diagram and contracted the coexistence region at the Cu – rich side which is completely in contrast to our findings.

It could be understood from figure 3 that the congruent melting point drops by decreasing the particle size and extends to the Au – rich side of the phase diagram. These findings are in agreement with the results reported by Cui et al. [11] and Chernyshev [12]. In contrast, Muñoz and Rosales [13] and Guisbiers et al. [10] predicted a shift in the congruent melting point towards high concentrations of Cu. Muñoz and Rosales and Guisbiers et al. also reported that for nanoparticles with $d = 4$ nm, the melting temperature of copper is lower than that of gold unlike the bulk state, which contradicts our findings and the results reported by Cui et al. and Chernyshev.

Unfortunately, there is not sufficient empirical data in the literature on the phase diagram of Au –Cu alloy nanoparticles. Hence, to investigate the validity of our results the calculated melting temperature of pure Au and Cu have been compared to the experimental [27,30,31] and MD simulation results [36] reported by others. Figure 4 (a) shows the calculated melting temperature of Au nanoparticles in this work in comparison with experimental data reported by Buffat and Borel [34]. Calculated melting temperatures by Vallee et al. [9], Cui et al. [11], and Chernyshev [12] are also plotted for comparison. As can be seen, calculated melting temperatures in this work are in good agreement with the experimental data. Especially in case of very small nanoparticles (e.g., d=4 nm) our results show better agreements with experiments than the outcomes of Vallee et al., Cui et al., and Chernyshev. In Figure 4 (b), the calculated melting temperature of Cu nanoparticles has been compared with experimental data reported by Huang et al. [31] and Cui et al. [35] and MD simulation results performed by Delogu [36]. It is readily apparent that calculated melting temperatures of Cu in this work show excellent agreement with experimental and MD simulation results. It is also clear that the predicted melting temperatures by Cui et al. and Chernyshev are very smaller than either the experimental or calculated temperatures in this work. It is also found from figures 3(a) and 3(b) that at any given particle diameter, the melting temperature of Cu nanoparticles is higher than that of their Au counterpart. Thus, in calculations of Muñoz and Rosales [13] and Guisbiers et al. [10] where the melting temperature of Cu nanoparticles were predicted to be lower than the melting temperature of their Au counterparts by size decrement, cannot be confirmed.
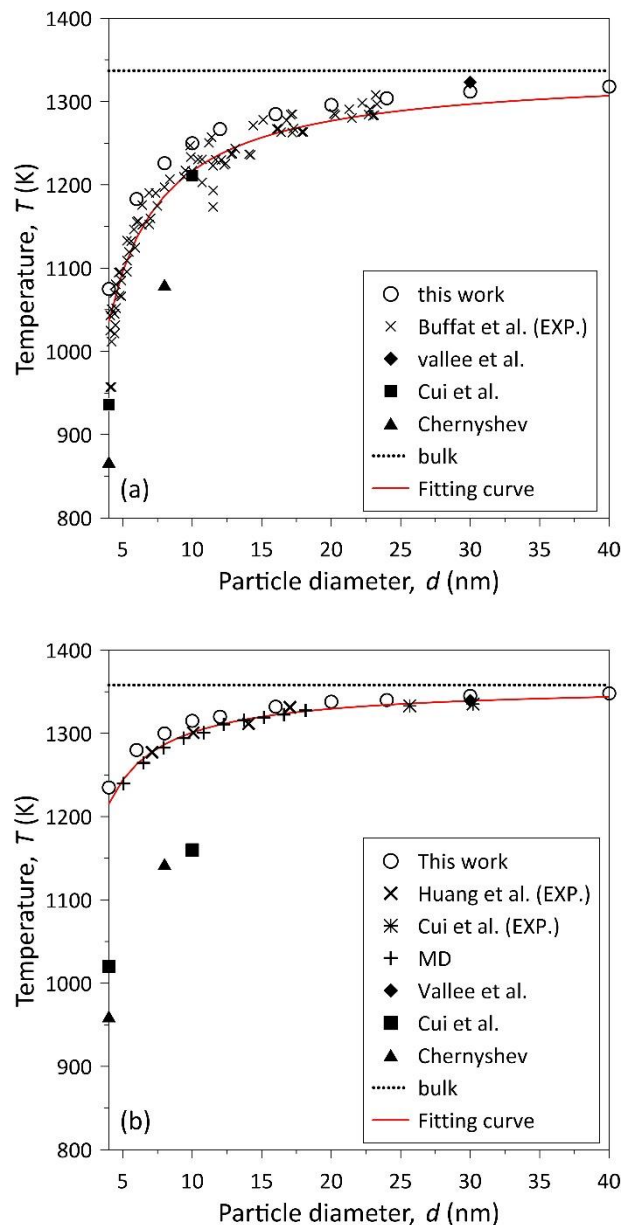
Figure 4. Calculated melting temperature of (a) Au and (b) Cu nanoparticles in this work together with calculated temperatures by Vallee et al. [9], Cui et al. [11], and Chernyshev [12] as well as some experimental data [27,30,31] and MD simulation results [36]. Solid lines indicate fitting curves for experimental data. (Figure is in color in the on-line version of the paper).

It is well known that the melting temperature of a nanoparticle can be derived by Eq.(11) [37]:

$$T_{m,NP} = T_{m,b}(1 - \beta/d) \tag{11}$$

where $T_{m,NP}$ and $T_{m,b}$ are the nanoparticle and bulk melting temperatures, respectively, d is the particle diameter and β is material constant. Eq. (11) can be applied to other transition temperatures as well [38]. We applied this model to predict the congruent melting temperature in Au – Cu system. To this end, Eq. (11) fitted to the experimental data on melting temperatures of Au and Cu (solid lines in Figures 3(a) and 3(b)) and the material constant, β, were derived as 0.9 nm and 0.42 nm for Au and Cu, respectively. Then, we estimated β for binary alloy system as $\beta_{Au-Cu} = X_{Au}\beta_{Au} + X_{Cu}\beta_{Cu}$ where X_i is the mole fraction of i component. Since at congruent melting temperature of the bulk alloy $X_{Au} \approx X_{Cu} \approx 0.5$, the value

of β_{Au-Cu} is calculated as 0.66 nm. According to the calculated phase diagram of the bulk alloy, the congruent melting temperature is 1190 K; Therefore, size dependent congruent melting temperature of Au–Cu alloy can be estimated from Eq. (12):

$$T_{cong,NP} = 1190(1 - 0.66/d) \tag{12}$$
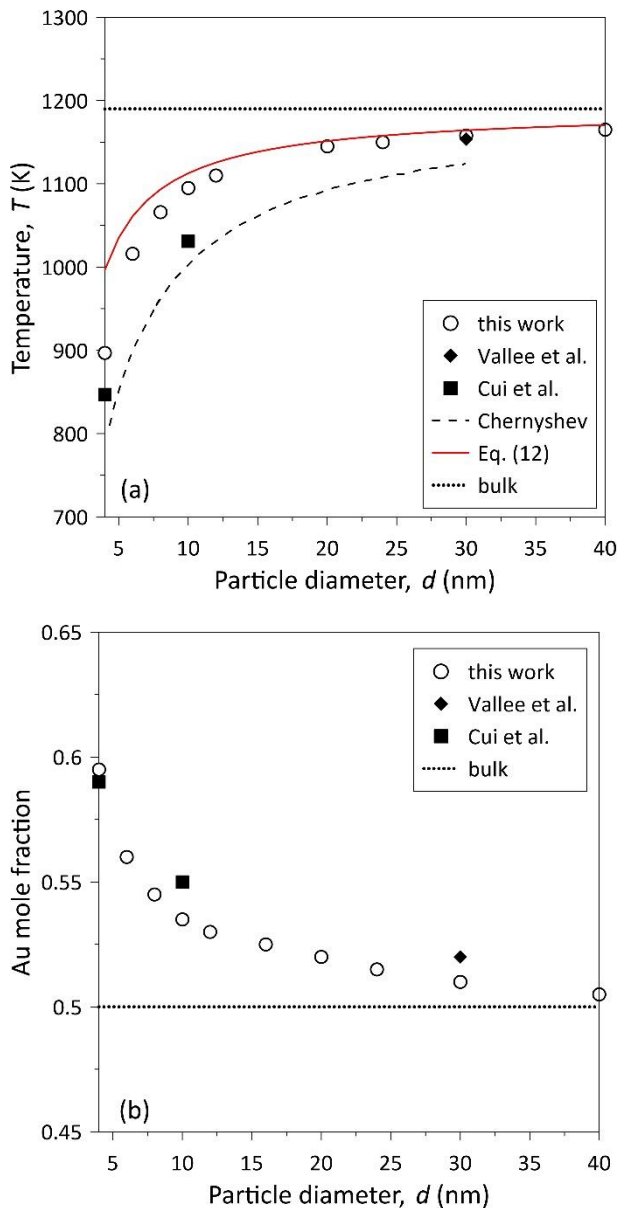
Figure 5. Calculated congruent melting point (a) and congruent alloy composition (b) as a function of particle diameter in comparison with previous calculations (Vallee et al. [9], Cui et al. [11], and Chernyshev [12]). (Figure is in color in the on-line version of the paper).

Figure 5(a) shows the congruent melting temperature of Au – Cu nanoparticles calculated from Eq (12) (solid line) together with calculated results of the thermodynamic model and those reported by Vallee et al., Cui et al. and Chernyshev. Depression of the congruent melting temperature by decreasing the particle size is evident. Also, calculated values of T_{cong} from Eq. (12) and the thermodynamic model in this work are in good agreement. It should be noted out that it is assumed that the composition of the congruent alloy is constant for all particle diameters in the development of Eq. (12). This assumption leads to a size

independent material constant, β. However, calculated results in this work (Figure. 4(b)) and those reported in the literature [10–13] show that the congruent alloy composition is size dependent. So, a discrepancy between the achieved results by the analytical model (Eq. (12)) and those calculated by using the CALPHAD approach is expected. It is also noteworthy that by increasing the particle size, this difference becomes negligible.

Variations of congruent alloy composition with respect to the particle diameter are shown in Figure 5(b). As can be seen, decreasing the particle size increases the Au content of the congruent alloy composition which is consistent with the results reported by Cui et al. and Chernyshev. However, in contrast to Cui et al., our results show non – linear dependency of congruent alloy composition to the particle size.

4. Conclusion

Size dependent phase diagram of Au – Cu nano-alloy was recalculated based on a CALPHAD type thermodynamic model. The results showed that decreasing the particle size leads to a drop in solidus, liquidus, and congruent melting temperatures. It was also found that by decreasing the particle size the coexistence solid – liquid phase region contracts at the Au – rich side of the phase diagram while it was expanded at the Cu – rich side of the phase diagram. The results cleared that by reducing the particle size the composition of congruent alloy extends to the Au – rich side of the phase diagram. In comparison with previous calculations, calculated results in this work showed better agreements with experiments. The results can be used as a guideline for the design of Au – Cu bimetallic nano-catalysts.

Nomenclature

A_i $(i = A, B)$	: molar surface area of pure elements (m²/mol)
a_v, b_v, c_v	: empirical constants (J/mol)
C	: correction factor
d	: particle diameter (m)
G^{nano}	: total Gibbs free energy at nanoscale (J/mol)
G^{bulk}	: Gibbs free energy of bulk state (J/mol)
G^{surf}	: surface contribution to the Gibbs free energy (J/mol)
G_i^0 $(i = A, B)$	: standard Gibbs energy of pure elements (J/mol)
$G^{ex,Bulk}$	: excess Gibbs energy of bulk state (J/mol)
$G_i^{ex,surf}$ $(i = A, B)$	: excess Gibbs energy of pure elements in surface (J/mol)
$G_i^{ex,bulk}$ $(i = A, B)$	: excess Gibbs energy of pure elements in bulk phase (J/mol)
h_i $(i = A, B)$	: atomic diameter (m)
L_v	: interaction parameter (J/mol)
N_0	: Avogadro's number
R	: universal gas constant (J/mol.K)
r	: particle radius (m)
T	: absolute temperature (K)
V_i $(i = A, B)$	: molar volume of pure elements (m³/mol)
V_{AB}	: molar volume of nanoparticles (m³/mol)
X_i $(i = A, B)$	: molar fraction of pure elements
X_i^{surf} $(i = A, B)$	: molar fraction of pure elements in surface

$X_i^{bulk}(i = A, B)$: molar fraction of pure elements in bulk phase

α : ratio of the coordination number in the surface to that in the bulk

σ_{AB} : surface energy of nanoparticles (J/m^2)

$\sigma_i (i = A, B)$: size dependent surface energy of pure elements (J/m^2)

σ_i^{∞} : surface energy of pure elements at the bulk state (J/m^2)

References

[1] X. Liu, A. Wang, T. Zhang, D. S. Su, and C. Y. Mou, "Au-Cu alloy nanoparticles supported on silica gel as catalyst for CO oxidation: Effects of Au/Cu ratios," *Catal. Today*, *160*, 103–108, 2011.

[2] M. K. Birhanu *et al.*, "Electrocatalytic reduction of carbon dioxide on gold–copper bimetallic nanoparticles: Effects of surface composition on selectivity," *Electrochim. Acta*, *356*, 136756, 2020.

[3] W. Li, A. Wang, X. Liu, and T. Zhang, "Silica-supported Au-Cu alloy nanoparticles as an efficient catalyst for selective oxidation of alcohols," *Appl. Catal. A Gen.*, *433–434*, 146–151, 2012.

[4] M. Hajfathalian *et al.*, "Photocatalytic Enhancements to the Reduction of 4-Nitrophenol by Resonantly Excited Triangular Gold-Copper Nanostructures," *J. Phys. Chem. C*, *119*, 17308–17315, 2015.

[5] R. Biswas, S. Singh, I. Ahmed, R. A. Patil, Y. R. Ma, and K. K. Haldar, "Rational Design of Bimetallic Au/Cu Nanostructure: An Efficient Catalyst for Methanol Oxidation," *ChemNanoMat*, *7*, 158–164, 2021.

[6] H. M. Lu and X. K. Meng, "Theoretical model to calculate catalytic activation energies of platinum nanoparticles of different sizes and shapes," *J. Phys. Chem. C*, *114*, 1534–1538, 2010.

[7] N. Zhao, Y. Q. He, and C. C. Yang, "A new approach to construct bulk and size-dependent continuous binary solution phase diagrams of alloys," *RSC Adv.*, *5*, 96323–96327, 2015.

[8] T. Tanaka and S. Hara, "Thermodynamic evaluation of binary phase diagrams of small particle systems," *zeitschrift fur Met.*, *92*, 467–472, 2001.

[9] R. Vallée, M. Wautelet, J. P. Dauchot, and M. Hecq, "Size and segregation effects on the phase diagrams of nanoparticles of binary systems," *Nanotechnology*, *12*, 68–74, 2001.

[10] G. Guisbiers, S. Mejia-Rosales, S. Khanal, F. Ruiz-Zepeda, R. L. Whetten, and M. José-Yacaman, "Gold-copper nano-alloy, " tumbaga ", in the era of nano: Phase diagram and segregation," *Nano Lett.*, *14*, 6718–6726, 2014.

[11] M. Cui, H. Lu, H. Jiang, Z. Cao, and X. Meng, "Phase Diagram of Continuous Binary Nanoalloys: Size, Shape, and Segregation Effects," *Sci. Rep.*, *7*, 1–10, 2017.

[12] A. P. Chernyshev, "The influence of the size effect on the transition of Au-Cu alloy nanoparticles to the dynamic amorphous state," *Mater. Today Proc.*, *25*, 370–372, 2020.

[13] H. R. Martínez-Muñoz and S. Mejía-Rosales, "The AuCu Phase Diagram at the Nano Scale: A Molecular Dynamics Approach," *J. Clust. Sci.*, *doi:* https://doi.org/10.1007/s10876-021-02015-6

[14] M. Z. Chu *et al.*, "Melting and phase diagram of Au-Cu alloy at nanoscale," *J. Alloys Compd.*, *891*, 162029, 2021.

[15] J. Park and J. Lee, "Phase diagram reassessment of Ag–Au system including size effect," *Calphad*, *32*, 135–141, Mar. 2008.

[16] G. Garzel, J. Janczak-rusch, and L. Zabdyr, "Reassessment of the Ag – Cu phase diagram for nanosystems including particle size and shape effect," *CALPHAD Comput. Coupling Phase Diagrams Thermochem.*, *36*, 52–56, 2012.

[17] F. Monji and M. A. Jabbareh, "Thermodynamic model for prediction of binary alloy nanoparticle phase diagram including size dependent surface tension effect," *Calphad Comput. Coupling Phase Diagrams Thermochem.*, *58*, 1–5, 2017.

[18] M. A. Jabbareh and F. Monji, "Thermodynamic modeling of Ag – Cu nanoalloy phase diagram," *Calphad*, *60*, 208–213, 2018.

[19] M. Z. Chu *et al.*, "Thermodynamic reassessment of the Ag–Cu phase diagram at nano-scale," *Calphad*, *72*, 102233, 2021.

[20] N. Sunders and A. P. Miodownik, *CALPHAD (Calculation of Phase Diagrams): A Comprehensive Guide*. Pergamon, 1998.

[21] W. H. Qi, M. P. Wang, and Q. H. Liu, "Shape factor of nonspherical nanoparticles," *J. Mater. Sci.*, *40*, 2737–2739, 2005.

[22] J. A. V Butler, "The thermodynamics of the surfaces of solutions," *Proc. R. Soc. A*, *135*, 348–375, 1932.

[23] S. Xiong, W. Qi, Y. Cheng, B. Huang, M. Wang, and Y. Li, "Modeling size effects on the surface free energy of metallic nanoparticles and nanocavities," *Phys. Chem. Chem. Phys.*, *13*, 10648–10651, 2011.

[24] A. Delsante, "SGTE data for pure elements" *Calphad*, *15*, 317–425, 1991.

[25] J. Sopousek *et al.*, "Cu – Ni nanoalloy phase diagram – Prediction and experiment," *CALPHAD Comput. Coupling Phase Diagrams Thermochem.*, *45*, 33–39, 2014.

[26] B. Sundman, S. G. Fries, and W. A. Oates, "A thermodynamic assessment of the Au-Cu system," *Calphad*, *22*, 335–354, 1988.

[27] K. K. Nanda, S. N. Sahu, and S. N. Behera, "Liquid-drop model for the size-dependent melting of low-dimensional systems," *Phys. Rev. A*, *66*, 013208, 2002.

[28] J. M. McDavid and S. C. Fain, "Segregation at CuAu alloy surfaces," *Surf. Sci.*, *52*, 161–173, 1975.

[29] F. M. Takrrori and A. H. Ayyad, "Surface energy of metal alloy nanoparticles," *Appl. Surf. Sci.*, *401*, 65–68, 2017.

[30] M. A. Jabbareh, "Size, shape and temperature dependent surface energy of binary alloy nanoparticles," *Appl. Surf. Sci.*, *426*, 1094–1099, 2017.

[31] C.-H. Huang, H. P. Wang, J.-E. Chang, and E. M. Eyring, "Synthesis of nanosize-controllable copper and its alloys in carbon shells," *Chem. Commun.*, *2*, 4663–4465, 2009.

[32] S. Delsante *et al.*, "Synthesis and thermodynamics of Ag–Cu nanoparticles," *Phys. Chem. Chem. Phys.*, *17*, 28387–28393, 2015.

[33] G. Guisbiers, "Advances in thermodynamic modelling of nanoparticles," *Adv. Phys. X*, *4*, 1668299, 2019.

[34] P. Buffat and J. P. Borel, "Size effect on the melting temperature of gold particles," *Phys. Rev. A*, *13*, 2287–2298, 1976.

[35] Z. Cui, B. Ji, Q. Fu, H. Duan, Y. Xue, and Z. Li, "Research on size dependent integral melting thermodynamic properties of Cu nanoparticles," *J. Chem. Thermodyn.*, *149*, 106148, 2020.

[36] F. Delogu, "Structural and energetic properties of unsupported Cu nanoparticles from room temperature to the melting point: Molecular dynamics simulations," *Phys. Rev. B - Condens. Matter Mater. Phys.*, *72*, 205418, 2005.

[37] G. Guisbiers, "Review on the analytical models describing melting at the nanoscale," *J. Nanosci. Lett.*, *2*, 8–18, 2012.

[38] S. S. Kim, "Thermodynamic modeling of the CeO 2 – CoO nano-phase diagram," *J. Alloys Compd.*, *588*, 697–704, 2014.

Study of Thermodynamic Properties of Monoclinic Sulfur (Sβ) Under High Pressure Using Three Different Equations of State for the Treatment Scabies in Dermatology

Abdullah M. Ali[1], Raed Hashim AL-Saqa[2*], Nashwa Salhuddin Sultan[3]

[1]Department of physics, University of Tikrit / Iraq
[2]Directorate General of Education/Nineveh / Iraq
[3]Almutamayizat High School, Directorate General of Education/ Iraq
E-mail: [*]raed1970ah@yahoo.com

Abstract

Thermodynamic properties of monoclinic β-sulfur S_β under high pressure up to 20 Gpa have been studied, where Orthorhombic α-sulfur S_α changes to S_β at 94.4℃. The high pressure technology used to tackle the crystallization volume of sulfur S_β without changes in the chemical properties. Sulfur S_β can be used after the effect of high pressure in the development of the medicine used to treat scabies. The present study is performed to calculate the effects of high pressure on some important physical properties of the material such as (bulk modulus (B), compression volume ratio (V_P/V_o), Grüneisen parameter (γ), Debye temperature (θ_D) and phonon frequency spectrum (pfs). Three different equations of state EOS's (Birch- Murnaghan EOS, Vinet EOS and modified Lennard-Jones EOS) were implemented to analyze pressure-volume relationship and then combining calculated data with various expressions of volume dependence of the other thermodynamic properties that are; Bulk modulus, Grüneisen parameter, Debye temperature and phonon frequency spectrum. The behavior of any of these concepts were described in different figures. It was found that, relative volume, and Grüneisen parameter were decreased with high pressure, while the other considered parameters; Bulk modulus, Debye temperature and phonon frequency spectrum were expected to increase as a high pressure is applied.

Keywords: *Bulk modulus; volume compression ratio; lattice parameter; phonon frequency spectrum; isothermal equations of state.*

1. Introduction

In the present work, the bulk modulus (B), compression volume (V_P/V_o), lattice constant (a) and phonon frequency spectrum (pfs) of a S_β compound under the influence of high pressure were calculated using the "Birch-Murnaghan and modified Lennard-Jones" EOS. The calculated results have been compared with experimental data, which confirms the validity of the present equations of state. The Grüneisen parameter variation assumption has improved the results of phonon frequency spectrum under compression.

In this study, sulfur will be used to compress to make it smaller than its present in nature, where [1] observed that the materials in small size "Nano scale" can have more useful applications than their bulk counterpart.

Sulfur can be crystallized in some different lattices, the well-known orthorhombic structure of S_α comprising of S_8 rings [2], it is stable under high pressure up to (20-30) Gpa and became gradually amorphous on further compression [3, 4,5]. Recrystallization starts around 37 Gpa and fully completes only at 75 Gpa [6]. The structure of three solid allotropes as:

1.1 Orthorhombic α-Sulfur S_α

S_α is the stable form of Cycloocta-S. [7] has reported very accurate structure parameters. [8] established "the stacking of molecules", (Fig. 1a) show the "crankshaft" structure of

this allotrope, is still erroneously assumed by many to contain coaxially stacked rings [7].

Lattice constants are "a = 10.4633 Å, b = 12.8786 Å, and c = 24.4784 Å, and the density is 2.069 g/cm³ "[9], where its unit cell volume 3299.5 Å³ [10].

1.2 Monoclinic β- Sulfur S_β

S_β forms at 94.4℃ from S_α [11], its structure determined by Trillat and Forestler [12], the unite cell contain six molecules S_8 i.e., 48 atoms, (Fig.1b), its lattice constant "a=10.778 Å, b=10.844 Å, and c=10.924 Å" [13], and its density is 1.94g/cm³ [14], about 12% smaller than S_α, and its unit cell volume 1276.41Å³ [15].

1.3 γ- Monoclinic Sulfur S_γ

The structure has been determined by [16], who confirmed the "sheared penny roll" staking, proposed by De Haan [17] (Fig. 1c). "The lattice constants are: a=8.44 Å, b=13.025Å, c=9.356Å" [16], four S_8 molecules occupy one unite cell and its density 2.19 g/cm³ (larger than S_α and S_β-sulfur) [16-17].

The purpose of studying (sulfur S_β under high pressure), is for treating humans from some skin diseases specially (Scabies), where we note that its drug contains sulfur 5% for child and 10% for young people [19-20].

*Corresponding Author

In some cases, the treatment is time-consuming about (5-10) weeks or more. The reason, that sulfur is used in the treatment S_α type, which it has larger size than S_β and therefore does not enter the pores of the skin [21]. using high-pressure technology by three different equations of state to obtain a crystalline volume up to 0.65 of its original size after applying high pressure (about 20Gpa) to reach the skin pores size and grooves size that made by the Scabies germ. By comparing the dimensions of the pores with the grooves made by microscopic skin scabies under the skin, we will be able to make sulfur molecules interfere with skin

pores and then into grooves created by bacteria and then kill them. In addition, the sulfur acts on the adhesion on the eggs completely so that it drowns grooves and thus kills the larvae that are born after (3-5) days.

The human body can be disinfected by treating sulfur S_β under high pressure mixed with petrolatum ointment or Vaseline to be highly viscous [20].
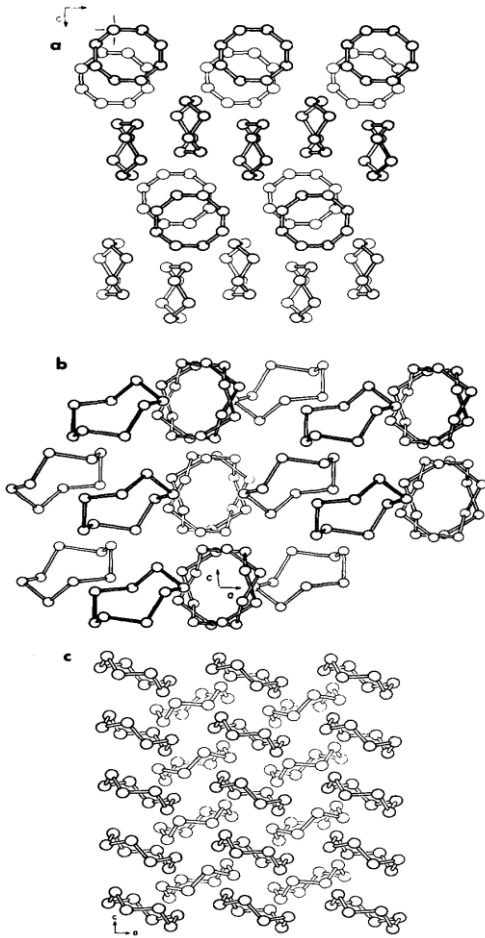
*Figure1. The structure of the solid Figure 1 allotropes of Cycloocta S :(a) orthorhombic Sα, (b) monoclinic Sβ, and (c) monoclinic Sγ. All views are perpendicular to the **c** axis [17].*

2. Materials and Method of Study

Equation of state as a mathematical tool is used find relationship between fundamental properties of solid phase such as pressure and volume, without requirement of experimental methodology. Several equations of state have been developed to describe the behavior of solid materials under high pressure [22].

2.1. Birch–Murnaghan EOS [23,24]

$$P_{B-M} = \frac{3B_0}{2}\left(\eta^{-7/3}-\eta^{-5/3}\right)\left(1+\frac{3}{4}\left(B'_O-4\right)\left(\eta^{-2/3}-1\right)\right) \tag{1}$$

Where, $\eta = \dfrac{V_P}{V_0}$

2.2. Vinet EOS [25]

$$P_{Vinet} = 3B_o\left[\left(\frac{V_P}{V_o}\right)^{-2/3}\left\{1-\left(\frac{V_P}{V_o}\right)^{1/3}\right\}\right]$$
$$\exp\left[\left(\frac{3}{2}\right)\left(B'_o-1\right)\left\{1-\left(\frac{V_P}{V_o}\right)^{1/3}\right\}\right] \tag{2}$$

2.3. Modified Lennard-Jones EOS [26]

$$P_{mL-J} = \frac{B_o}{n}\left(\frac{V_o}{V_P}\right)^n\left[\left(\frac{V_o}{V_P}\right)^n - 1\right] \tag{3}$$

Where B_O: Isothermal bulk modulus at atmospheric pressure
B'_o: First pressure Derivative of bulk modulus
V_o: Volume at ambient condition.
V_p: Volume under high pressure P

$$n = \frac{1}{3}B'_o \quad ; \quad B'_o = \frac{dB}{dp}$$

2.4. Bulk Modulus (*B*)

The Bulk modulus (*B*) relates the fraction change in volume to the change in the applied pressure as [27]:

$$B = -V\left(\frac{dP}{dV}\right)_T \tag{4}$$

On volume derivation of equations (1, 2, 3) and substituting in eq. (4) we can express the bulk modulus at pressure (p) as:

$$B_{B-M} = \frac{3B_o}{2}\left[\left(\frac{7}{3}\right)\eta^{-7/3} - \frac{5}{3}\eta^{-5/3} - \frac{9}{4}\left(B'_o-4\right)\eta^{-3} + \frac{7}{2}\left(B'_o-4\right)\eta^{-7/3} + \frac{5}{4}\left(B'_o-4\right)\eta^{-5/3}\right] \tag{5}$$

$$B_{Vinet} = \left[2B_o\left(\eta^{-2/3}-\eta^{-1/3}\right) + B_o\eta^{-1/3} + \frac{3}{2}B_o\left(B'_o-1\right)\left(\eta^{-1/3}-1\right)\right]$$
$$\exp\left[\left\{\frac{3}{2}\left(B'_o-1\right)\right\}\left(1-\eta^{1/3}\right)\right] \tag{6}$$

$$B_{mL-J} = B_o\left(\frac{V_o}{V}\right)^n\left[2\left(\frac{V_o}{V}\right)^n - 1\right] \tag{7}$$

2.5. First Grüneisen Parameter (γ)

The relation that describe (γ) is given as [28,29]:

$$\gamma_P = \gamma_0\left(\frac{V_P}{V_0}\right)^q \tag{8}$$

Where γ_o: First Grüneisen parameter at atmosphere pressure.
γ_P: First Grüneisen parameter under high pressure (P).

q: Second Grüneisen parameter.
q Has been considered as equal to unity or a constant value [25].

2.6. Debye Temperature (θ_D)

θ_D is a key parameter that determines the thermal transport dynamic properties. [30] Expressed Debye temperature under high pressure as:

$$\theta_{DP} = \theta_{Do} \left(\frac{V_o}{V_P}\right)^\gamma \qquad (9)$$

θ_{Do}: Debye temperature at atmospheric pressure

θ_{DP}: Debye temperature at pressure (P).

2.7. Phonon Frequency Spectrum (PFS)

$$\upsilon_P = \upsilon_o \left(\frac{V_P}{V_o}\right)^{-\gamma} \qquad (10)$$

The physical properties of solids can vary under high pressure, where the frequency of mode densities depend on specific volume eq. (10) [31]. The changes in the distribution function of the frequencies under high pressure expressed by eq. (11) [32].

$$g\left(\upsilon_P, V_P\right) = \left(\frac{V_P}{V_o}\right)^\gamma g\left[\upsilon_o, V_o\right] \qquad (11)$$

υ_o : Frequency at atmospheric pressure

υ_P : Frequency under high pressure (P)

3. Calculations and Results
3.1. Compression Volume V_P/V_0

Table (1) values of bulk modulus (B_o), its derivative (B_o') and first Grüneisen parameter γ for S_β compared with $S\alpha$ taken from its original references.

Sulfur-type	B_o Gpa	B_o'	Ref.	γ	Ref.
Sα	7.692	5.433	[32]	0.54	[33]
Sβ	7.046	5.597	[32]	0.54	[33]
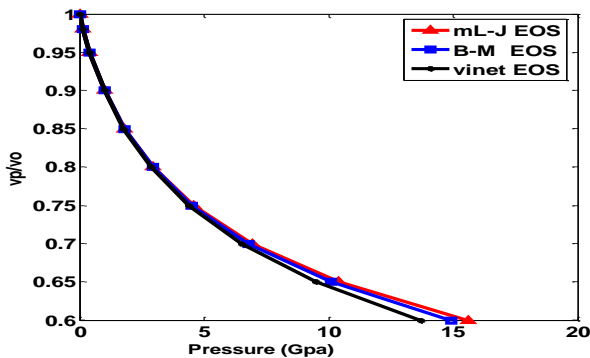
Figure 2. Variation of V_P/V_o for S_β at different values of pressure, using " mL- J, B-M & Vinet" EOSs.

By using data in Table (1) and using equations (1), (2) and (3) we get results for variations of V_P/V_0 with high pressure for S_β which are shown in fig.(1).

3.2. Bulk Modulus

By substituting values of B_o, B_o' for S_β from Table (1) and V_P/V_o rom Fig.(1) in equations (5),(6) and (7), we got the results of bulk modulus (B_{B-M}, B_{mL-J}, and B_{Vinet}) at different value of high pressure, and the results are shown in Fig. (3).
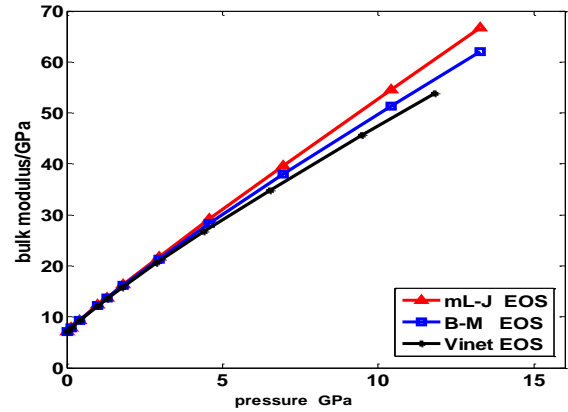
Figure 3. Variation of bulk modulus B_o for S_β at different values of pressure, using "mL- J, B-M & Vinet" EOSs.

3.3. First Grüneisen Parameter

First Grüneisen parameter γ belongs to the most important physical characteristics of crystal lattice dynamics [34]. Where γ is assumed to be volume dependent [35,36].

Fig.(4) show results for variation of (γ_P/γ_0) for sulfur S_β under high pressure using data of V_P/V_0 which is given from three equations (1), (2) and (3) at different value of pressure, and substituting it in eq.(8). Fig.4 shows a slightly reduction in Grüneisen parameter with increasing pressure from nearly 0.55 to just under 0.35.
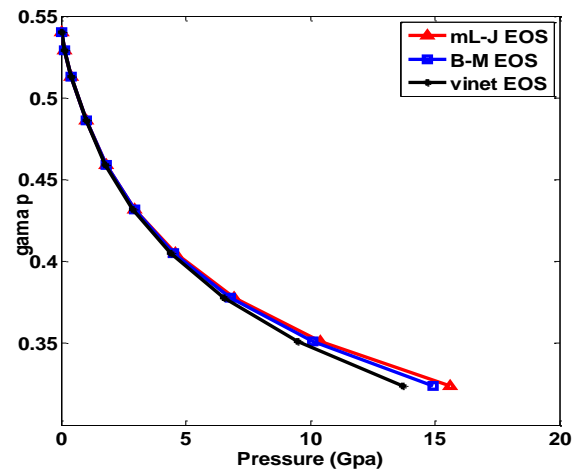
Figure 4. Variation of (γ_P/γ_0) mL- J, B-M & Vinet" EOSs.

3.4. Debye's Temperature

Figure (5) Shows results of variation of $(\theta_{D_P}/\theta_{D_0})$ with high pressure for S_β using equations (1), (2) and (3), when use V_P/V_0 values from Fig. (2) and substituting it in Eq. (9).
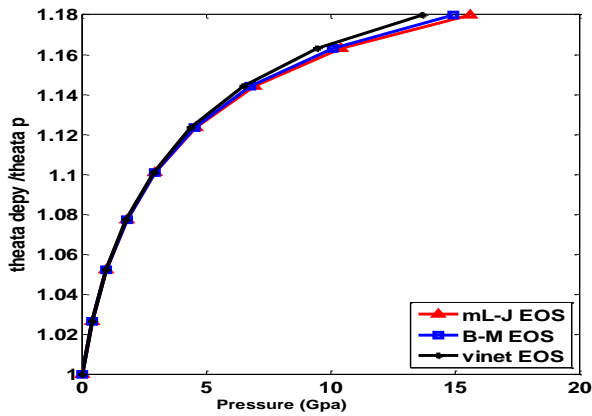
Figure 5. Variation of $\left(\theta_{D_P}/\theta_{D_0}\right)$ for S_β at different values of pressure, using" m.L-J, B-M & Vinet" EOSs.

3.5. Phonon Frequency Spectrum (pfs)

In the present work, the change in density of state (DOS) from (pfs) for sulfur is observed as expected by eq. (11). Fig. (6) show calculated pfs from literature [37]. by using values of V_P/V_0 under high pressure from Fig.(1) and compiling in eq.(10) and eq.(11) for the three equations (1), (2) and (3) which give the results of pressure effect on pfs and illustrated in Figs (7, 8 and 9).
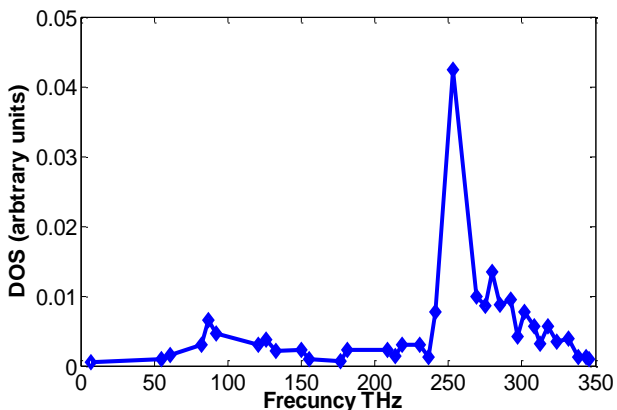
Figure 6. phonon frequency spectrum of S_β at ambient condition[36].
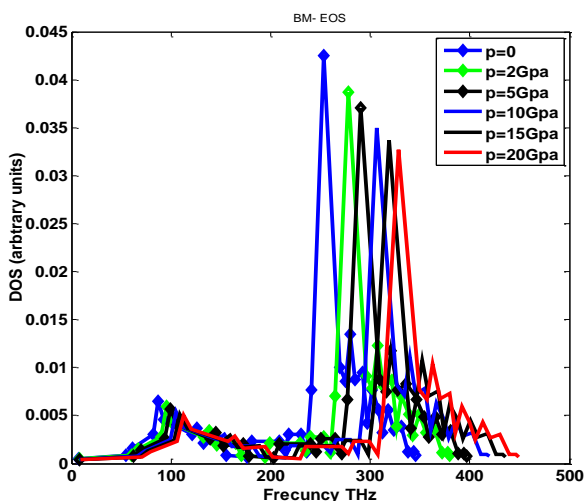
Figure 7. (pfs) for S_β at different value of high pressure using (B-M EOS).
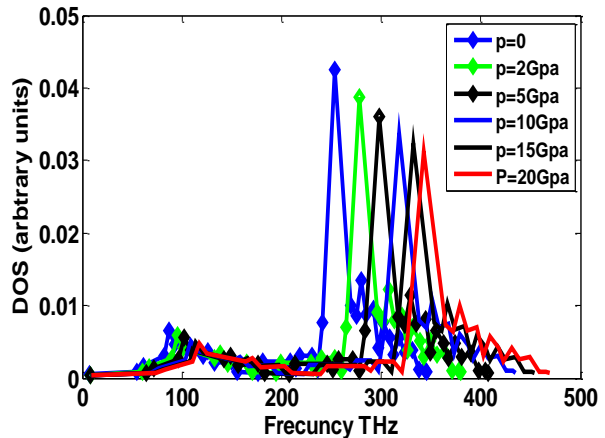
Figure 8. (pfs) for S_β at different value of high pressure using (mL-J EOS).
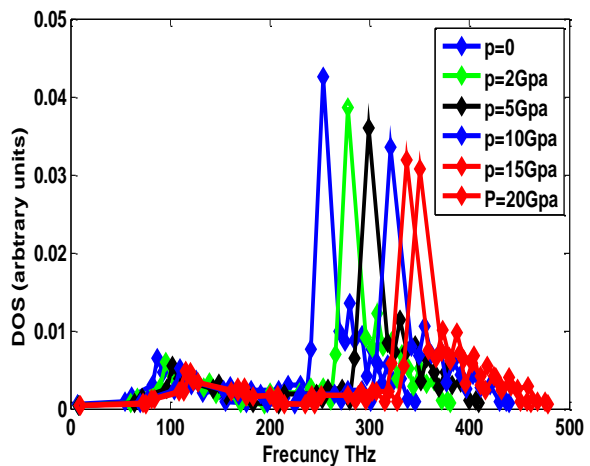
Figure 9. (pfs) for S_β at different value of high pressure using (Vinet EOS).

4. Results and Discussions

The aim of this study is to develop a medicine uses to treat the germ of scabies, of which its size is (0.25mm), and lives under the skin, we advise international pharmaceutical companies to use S_β treated under high pressure, less than "20Gpa" mixtures of Vaseline instead of S_α, by comparing volume under high pressure for S_β with germs size and grooves size that germs make, we found that S_β molecules are able to get into the grooves through skin pores (50μm) and thus killing larvae when the eggs are hatching, unlike S_α that remains on the surface of the skin and does not enter the grooves because of its large size compared to S_β. To establish this purpose, the present work reviewed some important physical properties of sulfur S_β have been studied under the effect of high pressure. Using three equations of state, its relative volume was observed under high pressure reaching 0.65 of its original size at pressures between (9 -11) GPa. Implementing the mathematical equations (1-11), the most important physical properties of sulfur were analyzed under high pressure up to 20 Gpa. The results were obtained and shown in Figures (1-8). The results in figs. 4-5 show an increasing trend for both bulk modulus and Debye temperature with increasing pressure. In fig. 5, it is noted that at lower pressure there is a more dramatic increase in Debye temperature, while as the pressure is increased more and more, the Debye temperature curve shifts up slowly, this can be attributed as a result of electrical repulsive force between adjacent atoms and molecules. On the other hand, the

Grüneisen parameter and phonon density of state decreased with the application of high pressure. Regarding to the volume of S_β particles, high pressure up to 16Gpa results in a dramatic change. Therefore, the present characteristics under strong compression results in only slight changes in other properties, with no change in chemical properties. All the studied properties gave excellent results for two equations (B-M EOS and mL-J EOS) more than (Vinet EOS), but when we study the (pfs), equations (Vinet EOS and mL-J EOS) give better results than (B-M EOS).

5. Conclusion

High pressure effects on some vital thermo-elastic properties of sulfur S_β material are analyzed such as relative volume, Grüneisen parameter, bulk modulus and phonon frequency spectrum. We have used some EOSs to derive formula for bulk modulus dependence on high pressure as given in Eqs. 5-7. Results in figs. 6-8 illustrate shifts in the energy of the modes (states) that high pressure causes exciting many new modes of vibration.

Nomenclature

V_P/V_0	Volume compression ratio
V_0	Volume at ambient condition
V_P	Volume under high pressure
EOS	Equation of state
P_{B-M} EOS	Birch–Murnaghan equation of state
P_{mL-J} EOS	Modified Lennard-Jones equation of state
γ_o	First Grüneisen parameter
γ_P	Grüneisen parameter under pressure
B_o	Bulk modulus
υ_o	Frequency under ambient condition
υ_P	Frequency under high pressure
θ_{Do}	Debye temperature at atmospheric pressure
θ_{DP}	Debye temperature under high pressure

References

[1] S. K. Jalal, A. M. Al-Sheikh, R.H. Al-Saqa,"High Pressure Effects on the Phonon Frequency Spectrum of the Silicon Nanoparticale", *Iran J. Sci. Technol. Trans Sci*. 45, 391-396.2021 https://doi.org/10.1007/s40995-020-01041-9

[2] S. Rettig, J. Trotter," Refinement of the structure of orthorhombic sulfur, α-S8", Acta Crystallographica Section C: *Crystal Structure Communications*" vol. 43, (12), 2260-2262,1987.

[3] Y. Akahama, M. Kobayashi, H. Kawamura, "Pressure-unduced structural phase transition in sulfur at 83 GPa.", *Phys. Rev*. B. vol. 48, (10), 6862-6864. 1993.

[4] P. N. Gavryushkin, K. D.Litasov, S. S. Dobrosmislov, and Z. I. Popov," High-pressure phases of sulfur: Topological analysis and crystal structure prediction, *Phys. Status Solidi B*". 1600857.2017.

[5] A. V. Tobolsky and J. W. MacKnight, "Polymeric Sulfur and Related Polymers", *Interscience, New York*, N.Y., 1968.

[6] H. Luo, , R. G.Greene, A. L.Ruoff ,1993 "Beta-Po phase of sulfur at 162 GPa: X-Ray diffraction study to 212 GPa." *Physical Review Letters*, vol. 71, (18), 2943-2946.1993.

[7] S. C. Abraham, "The crystal and molecular structure of orthorhombic sulfur," *Acta Crystallogr*. 8, 661.1955.

[8] A. Caron and J. Donohue, (1965), *Acta Crystallogr*. 18, 562.1995.

[9] P. Coppens, Y. W. Yang, R. H. Blessing, Cooper W. F., Larsen, F. K.: J. Amer, *Chem. Soc., Vol*. 99, p760. 1977.

[10] R. W. Wyckoff, Crystal Structures, John Wiley & Sons, New York.1963.

[11] M. Thackray, *J. Chem. Eng. Data*, vol. 15, 495. 1970.

[12] J. J. Trillat , J. Forestier, C. R., Acad. Sci., Paris, 192,(1931). 559. 1970.

[13] L. Gmelin's, "Handbuch der Anorganischen Chemie", Part 9A, 8th ed, Verlag Chemie. Weinheim. 1953.

[14] D. E., Sands, *J. Am.*, *Chem*. Soc. 87, 1395,1965.

[15] L. M. Goldsmithand, and C. E. Strouse, "Molecular dynamics in the solid state. The order-disorder transition of monoclinic sulfur", *J. Am. Chem*. Sot., 99, 7580-7589,1977.

[16] Y. Watanabe, Acta Crystallogr., Sect. B,30. 1396,1974.

[17] Y. M. de Haan, Physica, 24, 855,1958

[18] E. Meyer. E d.,"Elemental Sulfur, Chemistry and Physics", *Inter- science,* New York, N.Y,1965.

[19] N. Ishii, "Guideline for the diagnosis and treatment of scabies in Japan" , (second edition*). Journal of Dermatology* 35, 378–393,2008.

[20] k. Sharquie, J. Al-Rawi, A. Noaimi and H.Al-Hassany, "Treatment of scabies using 8% and 10% topical sulfur ointment in defferent regimens of application", *J Drugs Dermotol.,* 11, Mar, (13):375-64,2012.

[21] H. Luo, A. L. , "Ruoff, X-ray-diffraction study of sulfur to 32 GPa: Amorphization at 25GPa", *Phys. Rev*. B, 48, (1), 569.1993.

[22] R. H. AL-Saqa, S. J. AL-Taie,"Theoretical Study of Mechanical, Elastic and Phonon Frequency Spectrum Properties for GaAs at High Pressure" , *Journal of Siberian Federal University. Mathematics & Physics*, 12, (3), 371–378,2019.

[23] F. Birch," Finite elastic strain of cubic crystal", *Phys. Rev*. Vol. 71, 809- 824,1947.

[24] A. M. Al sheikh, S. K. Jalal, S. A. Mawlood, "Theoretical High Pressure Study of Phonon Density of State and Debye Temperature of Solid C60: Grüneisen Approximation Approach", *International journal of*

thermodynamics, vol. 25, No. 1, 2022. https://doi.org/10.5541/ijot.900071.

[25] P. Vinet, J. Ferrante, J. Rose, and J. Smith, " Compressibility of solids*", J. .Geophys. Res.*, vol. 92, 9319–9325,1987a.

[26] S. Jiuxun, "A modified Lennard-Jones type equation of state for solids strictly satisfying the spinodal condition", *J. Phys.: Condens. Matter*, vol. 17, L103–L111,2005.

[27] R. Boehler, "Melting temperature, diabetes and Gruneisen parameter lithium, sodium and potassium versus pressure", *Phys. Rev*. B., 127, No. 11, pp. 6754-6762,1993.

[28] A. M. Al-sheikh, S. K. Jalal, R. H. Al-saqa, "Equation of State and Thermo Dynamic Behaviour of C60 under High Pressure", *Universal Journal of Mechanical Engineering* 8, (1), 59-65,2020. DOI: 10.13189/ujme.2020.080108

[29] A. M. Al-Sheikh, S. J. Al-Faris, S. K. Jalal, " Grüneisen Parameter Variation Consideration in Theoretical High Pressure Studies *for* C60", *Iran J. Sci. Technol. Trans Sci*. A, 46, 2022. https://doi.org/10.1007/s40995-021-01253-7.

[30] R.S. Preston, S.S. Hanna, J. Helerle(1962), Mössbaur effect in metallic Iron. *Phys. Rev*., 128, (5), 2207-2218.

[31] J. Dlouha., " The influence of pressure on the Mössbauer effect", *Czech. J. Phys*., B, vol. 14, 571-579,1964.

[32] P.W. Guan a, S.-Li Shang, G. Lindwall , T. Anderson b, Z.-Kui Liu,"First-principles calculations and thermodynamic modeling of the S-Se system and implications for chalcogenide alloys"*, Journal of Alloys and Compounds*, vol. 694, 510-521,2017.

[33] G. A. Saunders, Y. K. Yoğurtçu , J. E., "Macdonald and Godfrey Stuart Pawley, The elastic behavior of orthorhombic sulfur under pressure", *The Royal Socilty Open Scince Journal*, ,vol. 407. Issue 1883,1986.

[34] Q. Lio, L. R. Chen., "Pressure dependence of the Grüneisen parameter and thermal expansion c oefficient of solids" , *Indian Journal of pure &applied physics*,vol. 55, 368-371,2017.

[35] S. Kareem Jalal, A. M. AL-Sheikh, "Theoretical High Pressure Study for Thermoelastic Properties of NaCl-B1", *Rafidain Journal of Science*, Volume 25, Issue 6, Pages 80-89,2014. Doi 10.33899/rjs.2014.131357.

[36] S. J. AL-Faris , R. H. Al-Saqa, H. M. Mohammed and S. K. Jalal, "High pressure effects on the structural properties of GaN compound using equations of state ", *International journal of thermodynamics*, vol. 25, No. 1,2022. https://doi.org/10.5541/ijot.960849.

[37] M. Güler, E. Güler, "Theoretical Analysis of Elastic, Mechanical and Phonon Properties of Wurtzite Zinc Sulfide under Pressure", *Crystals*, 7, 161,2017.

Study on Interaction Capabilities of Ternary Liquid Mixtures by Thermodynamic Parameters at 308.15 K

K. UmaSivakami[1], S. Vaideeswaran[2], A. RoseVenis[3*], K. Shenbagam[4]

[1, 4] Department of Chemistry, Cauvery College for Women, Affiliated to Bharathidasan University, Tiruchirappalli, Tamilnadu
[2] Department of Science and Humanities, Amrita College of Engineering and Technology, Nagercoil, Tamilnadu
[3] Department of Chemistry, St. Josephs College, Affiliated to Bharathidasan University, Tiruchirappalli, Tamilnadu
E-mail: [1]Email-k.umasivakami.chem@cauverycollege.ac.in, [3*]rosevenis_ch1@mail.sjctni.edu

Abstract

Thermodynamic properties provide a deep and significant insight of the various interactions taking place multi component liquid mixtures especially in the field of petrochemical and reservoir engineering. The density, viscosity and ultrasonic velocity were measured experimentally for diethylmalonate (DEM) +1,4-dioxane with nitrobenzene (TM-1) and diethylmalonate (DEM) +1,4-dioxane + toluene (TM-2) at the temperature of 308.15K and atmospheric pressure over the entire range of mole fraction. The excess thermodynamic properties such as excess volume (V^E), excess adiabatic compressibility (ΔK_s), excess viscosity ($\Delta\eta$), excess free volume (ΔV_F), excess free length (ΔL_F), excess isothermal compressibility ($\Delta\beta_T$), were calculated from measured values and applied to Redlich - Kister polynomial equation to determine the appropriate coefficients. The excess or deviation properties were found to be either negative or positive depending on the molecular interactions and the nature of liquid mixtures. The deviations of the ternary mixtures from its ideal behaviour were determined in order to investigate the molecular interaction between the components of ternary liquid mixtures.

Keywords: Mole fractions; ternary liquid mixtures; structural activities; Redlich - Kister polynomial equation; molecular interactions.

1. Introduction

Many fields such as pharmaceuticals, petroleum and chemical engineering require information regarding thermodynamic properties of the liquid mixtures. The study of transport fluid phenomena entails the data regarding density and viscosity of the system [1] Other than density and viscosity the ultrasonic study provides huge data about the molecular interactions [2] and the structural activities of the molecules in the mixture. The variation in thermodynamic and transport properties of liquid mixtures from its pure constituents is a energetic tool to study the nature of molecular interactions (either intermolecular or intramolecular) between mixing liquids. The study of physical properties like density, viscosity, excess molar volume, volume fraction and adiabatic compressibility aid in understanding the nature and strength of intra and intermolecular interactions occurring in multi component liquid systems[3]. Also the thermodynamic and transport properties of liquid systems are vital for engineering process design and operation. There are several predictive equations for estimating thermodynamic properties. The thermodynamic properties of organic liquids help in separation of organic liquid mixtures through fractional distillation which can be helpful to reduce pollution of environment. In the present work, a binary mixture of diethylmalonate (DEM) + 1,4- dioxane or p-dioxane has been used to prepare ternary solutions by adding nitrobenzene and toluene separately [4-8]. The thermodynamic and transport properties of prepared ternary solutions have been studied at 308.15 K and 318.15K over a wide range of compositions. The investigated properties such as excess volume, viscosity, adiabatic compressibility, free length, free volume and isentropic compressibility can be used to parameterize the energy transfer process and interactions between the ternary mixtures. Therefore the detailed study of the thermodynamic and transport properties of the ternary mixtures of diethylmalonate (1) + 1,4-dioxane (2) with nitrobenzene (3) and toluene (3) at 308.15 hence form the main scope of the present work.

2. Materials and Methods

Diethylmalonate and 1,4 dioxane (Merck, Mumbai, India), nitrobenzene and toluene (Loba, Mumbai, India), all Analar grades with 99% pure. All the chemicals used were directly purchased from the producers and purified by double distillation method. Hence the techniques to ascertain purity are not attempted but the measured densities, viscosities, and ultrasonic velocities were confirmed by comparing with earlier literature reports in Table1. Ternary liquid mixtures were prepared by weight by volume in airtight stoppered bottles using an analytical balance with an accuracy of $\pm\pm0.1$ mg. Densities of pure liquids and their mixtures were measured using relative density method. Relative density bottle of 10ml capacity

was cleaned successively with chromic acid, distilled water and acetone and then dried and used for density measurements [10]. An electronic balance was used to measure the density [11]. The accuracy of the measurement of density in relative density method depends on the accuracy of mass. Density values are accurate to ±0.0002 gcm^{-3}. Viscosities were measured using an Ostwald. viscometer. Viscometer was thoroughly cleaned with chromic acid. An electronic digital stopwatch with readability of ±0.01 s was used to measure the flow time of liquid between the marks. The ultrasonic velocity values were measured using an ultrasonic interferometer (Pico, Chennai, India) with a frequency of 2MHz was calibrated using water and nitrobenzene. The overall accuracy in the measurement is ±0.2%. All the measurements were made using a digital thermostat which displays accuracy ±0.01 K. The details of the methods and techniques of the measurements have been described earlier [12, 13]. The following are the equations used in calculating thermodynamic parameters nitrobenzene (3) and toluene (3) at 308.15 hence form the main scope of the present work. The excess volume values for the ternary mixtures were calculated using the relation.

$$V^E = \left(\frac{X_1M_1+X_2M_2+X_3M_3}{\rho_{mix}}\right) - \left(\frac{X_1M_1}{\rho_1}\right) - \left(\frac{X_2M_2}{\rho_2}\right) - \left(\frac{X_3M_3}{\rho_3}\right) \quad (1)$$

where X_1, X_2 & X_3, M_1, M_2 & M_3 and ρ_1, ρ_2 & ρ_3 are the mole fractions, molar mass, densities of pure components 1, 2, 3 respectively.

Adiabatic compressibility (K_s) has been calculated from Laplace's equation [14]

$$K_s = \frac{1}{\rho U^2} \quad (2)$$

Where ρ and U are the density and ultrasonic velocity of liquid mixtures. From the above equation excess adiabatic compressibility (ΔK_S) has been calculated by

$$K_s = K_s - \phi_1 K_{s1} - \phi_2 K_{s2} - \phi_3 K_{s3} \quad (3)$$

K_{s1}, K_{s2}, K_{s3} are adiabatic compressibility of pure liquids and ϕ_1, ϕ_2, ϕ_3 are the volume fractions of pure liquids calculated by the relation

$$\phi_1 = \frac{\left(\frac{X_1M_1}{\rho_1}\right)}{\left(\frac{X_1M_1}{\rho_1} + \frac{X_2M_2}{\rho_2} + \frac{X_3M_3}{\rho_3}\right)} \quad (4)$$

Viscosity has been calculated using the relation

$$\eta = \left(At - \frac{B}{t}\right)\rho \quad (5)$$

A and B are the constant characteristics of viscometer calculated using the standard liquids water and nitrobenzene, t is the flow time, ρ is the density.

Excess viscosity values are calculated using the following relation

$$\Delta\eta = \eta - (X_1\eta_1 + X_2\eta_2 + X_3\eta_3) \quad (6)$$

Where η_1 and η_2 are the viscosity values of pure components 1 and 2 respectively.

Free length is calculated using the relation,

$$L_f = \frac{K}{up^{1/2}} \quad (7)$$

K is Jacobson's [15] constant, which is temperature dependent constant but independent of the nature of the liquid.

Isothermal compressibility is calculated using the relation.

$$\beta_T = \frac{1.71 \times 10^{-3}}{\left(\frac{T^4}{9u^2\rho^{\frac{4}{3}}}\right)} \quad (8)$$

A relation to calculate free volume is [16]

$$V_f = \left(\frac{M_{eff}u}{K\eta}\right)^{\frac{3}{2}} \quad (9)$$

K is a temperature independent constant which is equal to 4.28×10^9 for all the liquids; M_{eff} is effective molecular weight of the mixture calculated using the relation.

$$M_{eff} = X_1M_1 + X_2M_2 + X_3M_3 \quad (10)$$

Where X_1, X_2, X_3 and M_1, M_2, M_3 are the mole fractions and molar mass of pure components 1, 2, 3 respectively.

Excess values of other parameters are calculated using the relation

$$A^E = A_{exp} - A_{id}$$
$$A_{id} = \Sigma X_i A_i \quad (11)$$

Where X_i and A_i are mole fraction and parameters of the ith component.

All the calculated excess parameters are fitted to Redlich–Kister [17] type polynomial equation by the method of least squares to derive the adjustable parameters a, b, c.

For binary

$$A^E = [X_1X_2(a + b(X_1 - X_2) + c(X_1 - X_2))] \quad (12)$$

For ternary

$$A^E = [X_1X_2X_3(a + bX_1(X_2 - X_3) + cX_1^2(X_2 - X_3)^2)] \quad (13)$$

Using the theoretical values for all excess parameters were calculated and the standard deviation values were calculated using the relation

$$\sigma = \left[\frac{(A_{exp} - A_{cal})^2}{(n-m)}\right]^{\frac{1}{2}} \quad (14)$$

n is the number of measurements and m is the number of adjustable parameters.1,4-dioxane could be classified as a non- polar solvent, but the distribution of electric charge gives a large quadruple moment to 1,4-dioxane[18]. The presence of substituent in the aromatic hydrocarbon should

modulate its electron-acceptor ability [19]. In diethylmalonate there are two types of molecular surface, the non-polar ethyl group and the polar carboxyl residues –COO-[20]. Nitrobenzene is an aromatic hydrocarbon containing NO2 as a functional group. The electron withdrawing -NO2 group draws π- electrons from the aromatic electron cloud of benzene generating a δ+ charge in it. Hence the mode of self-interaction in nitrobenzene is the potential anionic - π stacking interaction possible through the nucleophilic oxygen atom of the –NO2 group with the generated δ+ charge of the aromatic π electron cloud of benzene moiety [21]. Toluene, a methyl carrying benzene ring in which the methyl releases electron to the benzene moiety.

3. Results and Discussion

The ternary liquid solutions have been prepared by mixing diethylmalonate (1) +1,4-dioxane (2) with nitrobenzene (3) and toluene (3) varying their mole fractions. Experimental densities, viscosity, ultrasonic velocities of pure components of the liquid mixture were compared with literature values and are reported in Table 1. Also their excess thermodynamic parameters have been calculated and tabulated at a temperature of 308.15K to understand the interactions possible between them.

Calculated thermodynamic parameters and excess acoustical parameters for the ternary liquid mixtures of diethylmalonate(1) + 1, 4-dioxane(2) with nitrobenzene(3) and toluene(3) are represented in table 2 and table 3 respectively.

The greater interaction in the ternary system results in volume contraction in the system containing nitrobenzene as one of the component are indicated by the negative V^E values for the entire mole fractions at 308.15K. When comparing the corresponding binaries the V^E the interaction between the p-dioxane and nitrobenzene is lower than DEM and nitrobenzene. The values of ΔKs are directly proportional to different size and shape of the components and inversely proportional to velocity. Also ΔKs vary due to change in free volume. The ΔK_s values are negative for the considered mole fractions at 308.15. The negative values of ΔK_s clearly indicate the presence of molecular interactions and which make the flexible and more compressible. The deviation in viscosity values are low positive for maximum mole fractions at 308.15K may designate that the interaction between the component molecules are higher. The ΔL_F values are also negative may indicate the existence of interactions between the component molecules. The viscosity of a mixture depends on the molecular interaction between the components of the liquid mixtures. Components showing strong interactions are indicated by the positive deviations of viscosity. The viscosity deviation values indicate the existence of interaction between the component molecules values of the considered ternary mixture is greater and the prediction is supported by V^E and ΔKs values. The deviation in isothermal compressibility and thermal expansion coefficient are negative. The negative values may clearly indicate the greater interstitial accommodation of the molecules to each other. The deviation of the free volume for the considered ternary mixture shows negative deviations for the entire mole fractions also supports the above predictions. The greater interactions between the mixing components in the ternary systems results in

negative deviation values and the positive values may indicate the existence of weak interactions.

The calculated thermodynamic properties for the considered binary liquid mixtures of diethylmalonate + p-dioxane + toluene are tabulated in Table 3 for 308.15K. The V^E values for the ternary mixtures of diethylmalonate + p-dioxane + toluene shows positive values at 308.15K. The positive values are due to the presence of weak Vander Waals force existing between the molecules of ternary system. The weak Vander Waals force between the molecules of ternary system may make the system very slightly compressible and somewhat flexible which is indicated by low positive and low negative values of ΔKs. The compactness of the system is clearly designated by free length, ΔL_F values are positive. The viscosity deviations values shown by maximum number of mole fractions are negative at 308.15 K, due to the presence of weak forces existing between the component molecules. The deviation in isothermal compressibility $\Delta\beta_T$ is low negative values may be due to the better interstitial accommodation of the molecules where the prediction supports the viscosity deviation values.
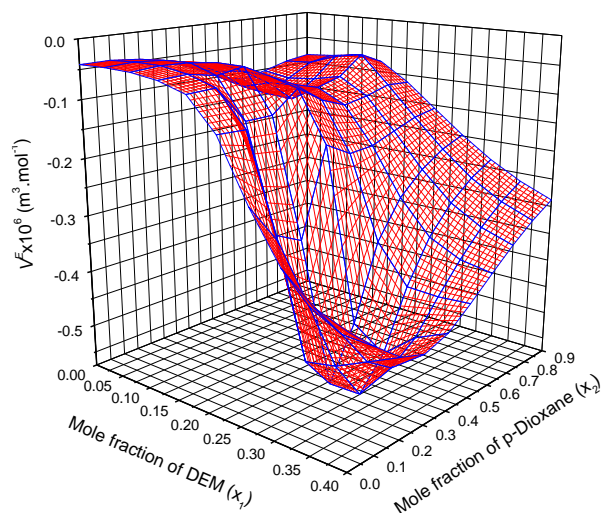
Figure 1. V^E versus mole fractions plots for TM1.
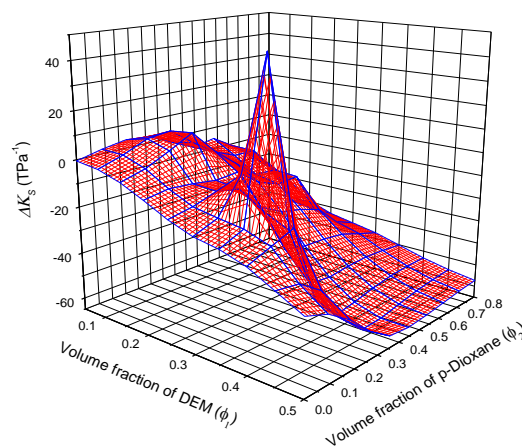
Figure 2. ΔK_s versus volume fraction plots for TM 1.

The ΔV_F value is negative is due to the presence of weak force of attraction between the molecules of the

system. The calculated excess thermodynamic parameters were fitted to Redlich – Kister polynomial equation to determine the adjustable coefficients and tabulated in Table 4 and Table 5 for DEM (1) + p-dioxane (2) and nitrobenzene(3) and toluene(3) respectively.
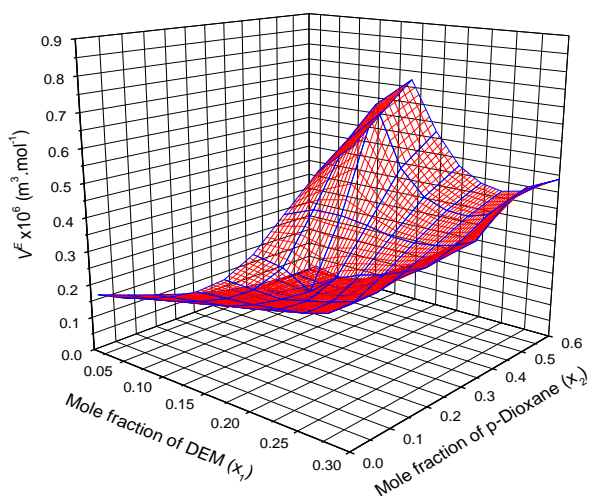
Figure 3. V^E versus mole fractions plots for TM 2.

Figure 1 and 3 represents 3D schematic diagrams of excess volume (V^E) of nitrobenzene and toluene versus mole fractions plots for DEM (X_1).
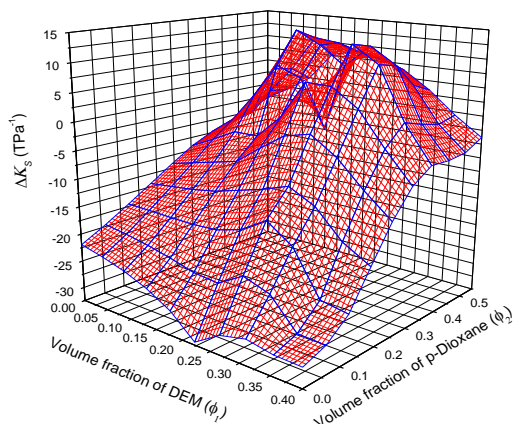
Figure 4. ΔK_s versus volume fraction plots for TM 2.

p-dioxane (X_2) respectively. Figure 2 and 4 represents 3D schematic diagrams of adiabatic compressibility (ΔK_s) of nitrobenzene and toluene versus volume fractions plots for DEM (φ_1) + p-dioxane (φ_2) at 308.15K and 318.15K respectively.

4. Conclusion

The densities, ultrasonic velocities, viscosities have been measured for the two ternary mixtures of diethylmalonate +1,4-dioxane + nitrobenzene and morpholine+1,4-dioxane + toluene and other excess thermodynamic properties such as excess volume, adiabatic compressibility, deviation in viscosity, free length, isothermal compressibility, free volume for have been calculated at atmospheric pressures and at the temperature of 308.15 K. The relevant values for pure components of the mixtures are also provided for reference. The corresponding thermodynamic excess parameters were calculated with the formulas reported earlier and fitted to a Redlich – Kister type polynomial equation to determine the adjustable coefficients. The behaviour of the liquid mixtures and the deviation from the ideal behaviour has been discussed based on experimental and calculated values. The V^E values suggest that existence of inter-molecular interactions between the component molecules in the liquid mixtures of diethylmalonate + p-dioxane wit nitrobenzene is higher than with toluene. The intermolecular interactions may make diethylmalonate + 1,4-dioxane + nitrobenzene mixture slightly flexible and little compressible indicated by its ΔKs values. On contrast the ΔKs values of diethylmalonate +1,4-dioxane + toluene mixture suggests the possibility for the occurrence of stiffness and less compressible nature. Both the ternary mixtures exhibit intermolecular interactions between like molecules. All the other calculated thermodynamic parameters supports the above predictions. The self-interaction may prevalent in ternary mixture containing nitrobenzene, and it may become less significant for the ternary mixture associated with toluene. According to the measured and calculated properties it can be assumed that strong molecular interactions is possible in diethylmalonate + 1,4-dioxane + nitrobenzene than diethylmalonate + 1,4-dioxane + toluene.

Nomenclature:

V^E	Excess volume
K_s	Adiabatic compressibility
K	Jacobson's constant
X_i	Mole fraction of the ith component.
A_i	Parameters of the ith component. (Redlich–Kister equation Coefficients)
ρ_{mix}	Density of liquid mixture
n	Number of measurements
m	Number of adjustable parameters
t	Flow time

Appendix

Table 1. Densities (ρ), viscosities (η) and ultrasonic velocities (U) of pure diethylmalonate, 1,4- dioxane nitrobenzene and toluene at 308.15K.

Compounds	T/K	$\rho \times 10^{-3} / kgm^{-3}$		η / cP		U / ms^{-1}	
		Exp	Lit	Exp	Lit	Exp	Lit
Diethylmalonate[4]	308.15	1.032	1.0387	1.2754	1.2672	1258	-
Nitrobenzene[22]	308.15	1.1877	1.1911	1.5678	1.5543	1375	1379
1,4-dioxane[23,24]	308.15	1.0167	1.0166	1.025	1.0280	1300	1300.3
Toluene[25,26]	308.15	0.8378	0.8566*	0.5099	0.5270*	1250	-

* refers to values at 303.15 K

Table 2. Values of thermodynamic properties of TM 1 ternary liquid mixture at 308.15K.

X_1	X_2	$\rho \times 10^{-3}/ kgm^{-3}$	$V^E \times 10^6/ m^3mol^{-1}$	U/ ms^{-1}	ϕ_1	ϕ_2	$\Delta K_s/ TPa^{-1}$
0.0315	0.4800	1.1081	-0.0992	1340	0.0500	0.4285	-8.9827
0.0445	0.5263	1.0981	-0.1252	1330	0.0709	0.4704	-5.8929
0.0363	0.5451	1.0966	-0.1358	1324	0.0582	0.4911	-0.7401
0.1030	0.5693	1.0798	-0.0977	1330	0.1602	0.4975	-14.3211
0.0752	0.6958	1.0630	-0.1097	1318	0.1213	0.6306	-8.4314
0.0840	0.6218	1.0749	-0.1582	1338	0.1332	0.5537	-21.8074
0.1522	0.3626	1.1039	-0.0570	1318	0.2232	0.2988	0.9901
0.0953	0.2946	1.1248	-0.0456	1312	0.1421	0.2468	15.5596
0.0961	0.7914	1.0418	-0.0679	1352	0.1560	0.7215	-42.1416
0.1106	0.8013	1.0374	-0.0441	1346	0.1784	0.7261	-39.2197
0.1319	0.7323	1.0467	-0.0841	1318	0.2079	0.6484	-16.2031
0.1357	0.2957	1.1171	-0.0474	1350	0.1984	0.2430	-17.5995
0.1406	0.7591	1.0403	-0.0579	1350	0.2216	0.6723	-43.5497
0.1569	0.4111	1.0960	-0.0979	1335	0.2314	0.3406	-15.9636
0.1636	0.7655	1.0360	-0.0976	1336	0.2551	0.6707	-35.4932
0.1858	0.4119	1.0907	-0.0862	1346	0.2703	0.3366	-26.4027
0.2103	0.0964	1.1325	-0.0446	1354	0.2880	0.0742	-18.4343
0.2107	0.3960	1.0884	-0.0336	1356	0.3022	0.3191	-35.9233
0.2587	0.1774	1.1157	-0.3547	1336	0.3509	0.1352	-15.4330
0.2424	0.3816	1.0891	-0.4081	1358	0.3417	0.3022	-41.7232
0.2564	0.2254	1.1123	-0.6643	1370	0.3507	0.1732	56.4284
0.2930	0.3729	1.0842	-0.6119	1380	0.4030	0.2883	-62.2624
0.3083	0.3930	1.0779	-0.5193	1372	0.4224	0.3026	-59.2086
0.3520	0.4392	1.0636	-0.4382	1367	0.4763	0.3339	-60.7545

Table 2. Continued…………..

X_1	X_2	η cP	$\Delta\eta$ cP	ΔL_F x10^{-10}/ M	$\Delta\beta_T$ x10^{-12}/ kg^{-1}K^{-1}m^{2}s	ΔV_F x 10^{-10}/ m^{3}mol^{-1}
0.0315	0.4800	1.3146	0.0129	-2.0967	-2.2907	-1.3218
0.0445	0.5263	1.2035	-0.0706	-1.8973	-1.7605	-1.3348
0.0363	0.5451	1.2763	0.0109	-1.8137	-1.2117	-1.3298
0.1030	0.5693	1.2323	-0.0071	-1.7379	-2.5441	-1.3819
0.0752	0.6958	1.1891	0.0128	-1.4130	-1.8271	-1.3693
0.0840	0.6218	1.2558	0.0412	-1.7578	-3.6844	-1.3711
0.1522	0.3626	1.1847	-0.1574	-1.8971	7.2852	-1.4055
0.0953	0.2946	1.1814	-0.2085	-2.0194	1.8534	-1.3579
0.0961	0.7914	1.3058	0.1854	-1.5556	-6.2589	-1.3915
0.1106	0.8013	1.3096	0.1973	-1.4520	-5.7575	-1.4031
0.1319	0.7323	1.1233	-0.0222	-1.2637	-2.4619	-1.4147
0.1357	0.2957	1.3852	0.0037	-2.3542	-2.4340	-1.3885
0.1406	0.7591	1.2714	0.1421	-1.5409	-6.2577	-1.4230
0.1569	0.4111	1.3247	0.0099	-1.9926	-2.2572	-1.4123
0.1636	0.7655	1.1823	0.0609	-1.3551	-4.9915	-1.4409
0.1858	0.4119	1.3135	0.0046	-2.0671	-3.6750	-1.4342
0.2103	0.0964	1.4397	-0.0355	-2.5995	-1.3892	-1.4318
0.2107	0.3960	1.3885	0.0758	-2.1596	-4.7531	-1.4521
0.2587	0.1774	1.4753	0.0533	-2.2663	-1.2557	-1.4739
0.2424	0.3816	1.4421	0.1276	-2.1968	-5.4598	-1.4751
0.2564	0.2254	1.5175	0.1211	-2.5612	-5.3632	-1.4754
0.2930	0.3729	1.4552	0.1459	-2.3869	-8.2573	-1.5128
0.3083	0.3930	1.4325	0.1369	-2.2518	-7.7740	-1.5258
0.3520	0.4392	1.4088	0.1467	-2.0731	-8.1429	-1.5620

Table 3. Values of thermodynamic properties of TM 1 ternary liquid mixture at 308.15K.

X_1	X_2	ρx10^{-3}/ kgm^{-3}	V^Ex 10^6/ m^{3}mol^{-1}	U/ ms^{-1}	ϕ_1	ϕ_2	ΔK_s/ TPa^{-1}
0.0287	0.5220	0.9283	0.0201	1270	0.0447	0.4566	-5.5670
0.0454	0.5708	0.9416	0.0193	1256	0.0710	0.5013	12.8820
0.0470	0.5743	0.9428	-0.0021	1276	0.0734	0.5044	-8.1611
0.0695	0.5936	0.9523	-0.0057	1262	0.1080	0.5186	8.0889
0.0686	0.5487	0.9439	-0.0025	1258	0.1056	0.4745	9.6732
0.0807	0.5283	0.9433	0.0153	1254	0.1230	0.4523	13.4806
0.0994	0.4731	0.9383	0.0278	1250	0.1484	0.3967	15.5374
0.1003	0.4281	0.9308	0.0360	1256	0.1481	0.3552	6.9368
0.1041	0.3855	0.9245	0.0493	1266	0.1521	0.3164	-6.4699
0.1449	0.3621	0.9309	0.0584	1254	0.2070	0.2907	6.8564
0.1377	0.3160	0.9215	0.0687	1260	0.1953	0.2520	-2.1055
0.1591	0.2911	0.9226	0.0985	1264	0.2227	0.2288	-6.8384

0.1578	0.4517	0.9487	0.0899	1270	0.2287	0.3678	-5.5527
0.1638	0.3533	0.9338	0.0898	1252	0.2318	0.2809	9.1343
0.1755	0.0090	0.8827	0.3321	1280	0.2302	0.0066	-33.0351
0.1853	0.4734	0.9582	0.1828	1250	0.2668	0.3829	17.4318
0.2119	0.4914	0.9674	0.1993	1255	0.3029	0.3946	14.4956
0.2188	0.1316	0.9112	0.2800	1264	0.2894	0.0978	11.7303
0.2371	0.5305	0.9793	0.2731	1270	0.3382	0.4253	2.8790
0.2411	0.5656	0.9856	0.3535	1276	0.3460	0.4561	-0.2428
0.2689	0.5736	0.9922	0.4703	1284	0.3823	0.4582	-5.9190
0.2831	0.1938	0.9323	0.6596	1280	0.3700	0.1424	22.4068
0.2931	0.1471	0.9259	0.8883	1284	0.3782	0.1066	26.5679
0.2618	0.1318	0.9173	0.7924	1282	0.3407	0.0964	26.5710

Table 3. Continued……………..

X_1	X_2	$\eta/$ cP	$\Delta\eta/$ cP	$\Delta L_F \times 10^{-10}/$ M	$\Delta\beta_T \times 10^{-12}/$ $kg^{-1}K^{-1}m^2s$	$\Delta V_F \times 10^{-10}/$ m^3mol^{-1}
0.0287	0.5220	0.7662	-0.1148	-9.7436	-1.2275	-6.2006
0.0454	0.5708	0.7053	-0.1978	-9.4891	-1.2034	-5.0628
0.0470	0.5743	0.8021	-0.1028	-9.4965	-1.2016	-6.1760
0.0695	0.5936	0.8244	-0.0980	-9.3309	-1.1861	-6.2579
0.0686	0.5487	0.8067	-0.1033	-9.4946	-1.2029	-6.3753
0.0807	0.5283	0.7539	-0.1574	-9.5237	-1.2059	-5.8387
0.0994	0.4731	0.6614	-0.2454	-9.6588	-1.2193	-4.6816
0.1003	0.4281	0.6827	-0.2126	-9.8301	-1.2355	-5.294
0.1041	0.3855	0.7085	-0.1776	-9.9871	-1.2498	-5.9004
0.1449	0.3621	0.7318	-0.1705	-9.9198	-1.2433	-6.2602
0.1377	0.3160	0.6993	-0.1868	-10.1231	-1.2629	-6.0419
0.1591	0.2911	0.7138	-0.1774	-10.1473	-1.2641	-6.2959
0.1578	0.4517	0.7236	-0.2095	-9.5640	-1.2056	-5.4184
0.1638	0.3533	0.7313	-0.1790	-9.8853	-1.2395	-6.2243
0.1755	0.0090	1.1564	0.3312	-11.1510	-1.3619	-11.9368
0.1853	0.4734	0.6273	-0.3267	-9.3638	-1.1874	-3.4775
0.2119	0.4914	0.6607	-0.3127	-9.2124	-1.1709	-3.8691
0.2188	0.1316	1.0626	0.1810	-10.5343	-1.3007	-10.5621
0.2371	0.5305	1.0760	0.0782	-8.9989	-1.1472	-8.0226
0.2411	0.5656	1.0751	0.0659	-8.8619	-1.1328	-7.7616
0.2689	0.5736	1.0879	0.0612	-8.7448	-1.1195	-7.6788
0.2831	0.1938	1.1050	0.1715	-10.1013	-1.2540	-10.1811
0.2931	0.1471	1.1508	0.2243	-10.2449	-1.2675	-1.0698
0.2618	0.1318	1.1430	0.2377	-10.4063	-1.2847	-1.0844

Table 4. Values of a, b, c and corresponding standard deviation for TM 1 ternary liquid mixture at 308.15K.

Parameters	A	b	c	σ
V^E x10^6/m^{3}mol^{-1}	-921.044	-11310.3	-11987.2	0.3299
ΔK_s /TPa^{-1}	47.2244	62.3324	2520.54	0.0454
$\Delta \eta$ /cP	1.1080	36.3825	359.618	0.0008
ΔL_F x 10^{-10} /m	-74.064	57.21	-303.41	1.2792
$\Delta \beta_T$ x 10^{-11} /kg^{-1}K^{-1}m^{2}s	-13.500	15.548	-1108.6	0.0005
ΔV_F x 10^{-07} /m^{3}mol^{-1}	-50.295	-117.34	-2.7000	0.0250

Table 5. Values of a, b, c and corresponding standard deviation for the ternary liquid mixtures of TM 2 at 308.15K.

Parameters	A	b	c	σ
V^Ex10^6/m^{3}mol^{-1}	2.1405	-31.2506	1828.93	0.0010
ΔK_s /TPa^{-1}	290.497	1735.11	-54175	0.7515
$\Delta \eta$ /cP	-9.0419	-10.7226	1324.86	0.0025
ΔL_F x 10^{-10} /m	4176	6139.6	27713	2.6680
$\Delta \beta_T$ x 10^{-08} /kg^{-1}K^{-1}m^{2}s	526.14	690.71	3616.5	1.8650
ΔV_F x 10^{-10} /m^{3}mol^{-1}	231.91	638.35	126.07	2.1610

References:

[1] A. Sharma, M. Rani, S. Maken, "Thermodynamics of haloarenes with n-hexane at 298.15-318.15 K, density, ultrasonic speed and viscosity," *J. Mol. Liq.*, 321, 114366, 2021.

[2] P. Prabhu, A. R. Venis,. "Molecular interaction of hexylene glycol with toluene, aniline, chlorobenzene, nitrobenzene, benzalehyde, and N.N-dimethyl aniline at 308.15 and 318.15K," *Phys. Chem. Liq.*, 58, 529, 2020.

[3] S. M. Pereira, M. A. Rivas, J. N. Real, "Densities speed of sound, and refractive indices of the mixture nanone + triethylglycol + dimethyl ether 288.15K, 293.15K, 298.15K and 308.15K," *J. Chem. Eng. Data.*, 47, 919, 2002.

[4] S. Baluja, N. Pandaya, N. Kachhadia, "Thermodynamic and acoustical studies of binary mixtures of diethylmalonate at 308.15K," *Phys. Chem. Liq.*, 43, 309, 2005.

[5] W. Acree. *Thermodynamic properties of nonelectrolyte solutions, 2nd Ed.* Academic Press. 2012.

[6] A. K. Nain, P. Chandra, J. D. Pandey, "Densities, refractive indices and excess properties of binary mixtures of 1,4-dioxane with benzene, toluene, o-xylene, m-xylene, p-xylene, and mesitylene at 288.15-308.15K," *J. Chem. Eng. Data.*, 53, 2654, 2008.

[7] R. Besbes, N. Ouerfelli, H. Latrous, "Density, dynamic viscosity and derived properties of binary mixtures of 1,4-dioxane with water at T=298.15K," *J. Mol. Liq.*, 145, 1, 2009.

[8] S. Kumar, V. K. Sharma, I. Moon, "Speed of sound and excess isentropic compressibility of 1,4-dioxane +1-butanol or 2-butanol binary mixtures at 308.15K and atmospheric pressure," *Ind. Eng. Chem. Res.*, 49, 8365, 2010.

[9] G.P. Dubey, P. Kaur, "Thermodynamic and spectral studies of molecular interactions of 1-butoxy-2-propanaol with 1-alcohols," *J. Chem. Eng. Data.*, 60, 2232, 2015.

[10] S. Gahlyan, N. Verma, S. Verma, "Volumetric, enthalpic and VLE studies of binary mixtures of isomers of butyl chloride with cyclohexane at 298.15 K", *J. Mol. Liq.*, 298, 111946, 2020.

[11] J. Litkenhous, W. Spanyer, "The physical properties of the ternary system acetone-n-butyl alcohol-water," *J. Phys. Chem.* 36, 842, 2002.

[12] A. R. Venis, X. R. Rajkumar, "Molecular Interactions in Ternary Liquid Mixture of Morpholine, Cyclohexanone and 1-Hexanol at 308.15 K and 318.15 K," Orient. J. Chem. 27,105, 2011.

[13] A. I. Vogel, B. S. Furniss, *Vogel's Textbook of practical organic chemistry, 5th Ed.* London- Longman, 1989.

[14] M. Hasan, A. P. Hiray, U. B. Kadam, D. F. Shirude, K. J. Kurhe, A. B. Sawant, "Densities, sound speed, and IR studies of methanol+1-acetoxybutane and methanol + 1,1-dimethylethylester at 298.15-303.15K," *J. Chem. Eng. Data*, 55, 535, 2010.

[15] J. S. Rowlinson, F. Swinton, *Liquids and liquid mixtures: Butterworths monographs in chemistry.*, 3rd Ed. Butterworth-Heinemann, 2013.

[16] V. H. Alvarez, S. Mattedi, M. Martin-Pastor, M. Aznar, M. Iglesias, "Thermo physical properties of binary mixtures of ionic liquids2-hydroxy ethyl ammonium acetate + (water + ethanol + methanol)," *J. Chem. Thermodyn.* 43, 997, 2011.

[17] Madhuresh Makavana, Sangita Sharma, "Ultrasonic, optical and IR studies of binary mixtures of morpholine with some aromatic hydrocarbons

at T = (303.15, 308.15 and 313.15) K," *J. Mol. Liq.*, 222, 535, 2016.

[18] A R. Venis, X R. Rajkumar, 'Molecular interactions in binary liquid mixtures cyclohexanone with morpholine, bromobezene and anisole at 308.15 and 318.15K," *Asian J. Chem.*, 26, 471, 2014.

[19] M. Das, M. N. Roy, "Studies on thermodynamic and transport properties of binary mixtures of acetonitrile with some cyclic ethers at different temperatures by volumetric viscometric and interferometry techniques," *J. Chem. Eng. Data.*, 51, 2225, 2006.

[20] P. S. Nikam, S. J. Kharat, "Density and viscosity studies of binary mixtures of N,N-dimethyl fomamide with toluene and ethyl benzoate at 298.15 - 313.15K," *J. Chem. Eng. Data.*, 50, 455, 2005.

[21] J. Marrero, R. Gani, "Group contribution based estimation of pure component properties," *Fluid Phase Equilib.*, 183, 183, 2001.

[22] Y. Marcus, "*Preferential solvation in mixed solvents, in Fluct. Theory Solut. Appl. Chem. Eng. Bio phys.*, *2nd Ed.* Taylor & Francis Group Boca Raton, 2013.

[23] S. Sharma, M. Makavana. "Density and viscometry study of binary liquid mixtures of morpholine with some aromatic hydrocarbons at temperatures at 303.15 to 313.15K," *Fluid Phase Equilib.*, 375, 219, 2014.

[24] D. Vijayalakshmi , M. Gowrisankar, K. Sivakumar and P. venkateswarlu, "Densities, Ultrasonic Sound Speed And Viscosity Data of Binary Liquid Mixture of Ethyl benzoate," *Int. J. Phy and Res.,* 4, 21, 2014.

[25] B. Giner, I. Gascón, H. Artigas, "Phase equilibrium of binary mixtures of cyclic ethers + chlorobutane isomers experimental measurements of SAFT-VR modelling," *J. Phys. Chem. B.*, 111, 9588, 2007.

[26] Contreras S M. "Densities and viscosities ofbinary mixtures of 1,4-dioxane with 1-propanol and 2-propanol at 25 to 40^0 C," *J. Chem. Eng. Data.*, 46, 1149,2001.

[27] K. Umasivakami, V. Sundararajan , A. Rosevenis. "Density, viscosity, ultrasonic velocity and excess thermodynamic parameters of ternary liquid mixtures of morpholine + 1,4-dioxane+ toluene and nitrobenzene at 308.15K," *J. Serb. Chem. Soc.*, 83, 1131, 2018.

A Residual Thermodynamic Analysis of Turbulence – Part 1: Theory

M. Gustavsson[*]

Hot Disk AB, c/o Chalmers Science Park, Sven Hultins Gata 9, SE-41288 Gothenburg, Sweden
E-mail: Mattias.Gustavsson@hotdiskinstruments.com

Abstract

A new theoretical groundwork for the analysis of wall-bounded turbulent flows is offered, the application of which is presented in a parallel paper. First, it is proposed that the turbulence phenomenon is connected to the onset of an irreversible process – specifically the action of a slip flow – by which a new fundamental model can be derived. Fluid cells with specific dimensions – of length connected with the local slip length and thickness connected with the distance between two parallel slipping flows – can be hypothetically constructed, in which a specific kinetic energy dissipation can be considered to occur. Second, via a maximum entropy production process a self-organized grouping of cells occurs – which results in the distinct zones viscous sublayer, buffer layer, and the log-law region to be built up. It appears that the underlying web structure may take the form of either representing a perfect web structure without any visible swirls, or a partially defect web structure where unbalanced forces may result in the generation of apparent swirls – which in turn might grow into larger turbulent eddies. Third, on the transition from laminar to turbulent flows, a nominal connection between the onset of a turbulent wall boundary layer (in a pipe flow), the Reynolds number as well as the wall surface roughness can be derived.

Keywords: Discrete slip flow; maximum entropy production; turbulent eddy; fracture structure.

1. Introduction

The topic of turbulence covers a broad range of experiments and attempts to analyse the phenomenon [1], [2], [3], [4], [5], [6]. The vastness of applications and results does not allow for any comprehensive summary in this paper.

However, most scientists within the field of turbulence would agree on the following points:

- Analysis of turbulent flows in simple geometries (pipes, plates etc.) is possible with empirical formulas. This is the default engineering approach [1].
- Wind tunnel experiments and scaling of results are a useful complement to empirical or numerical analysis in *e.g.* the aerospace and automobile industries. Corresponding experiments and scaling of results regarding marine- or submarine vessels is also possible in *e.g.* water channel experiments [2].
- Most attempts to model turbulence in a CFD (Computational Fluid Dynamics) flow solver employs the Navier-Stokes relations directly [7], or a modified- or altered version of these relations [3].
- The theory of a turbulent cascade process [8] is presumed, in which larger eddies are broken up downstream into smaller ones. The idea is to connect eddies to the concept of "turbulent kinetic energy", where the largest eddies are considered to have the highest amount of turbulent kinetic energy. After a cascade breakdown of eddies, eventually to the smallest scales (the Kolmogorov scales [9]), any further breakdown is the conversion into viscous dissipation.
- Perhaps the most ambitious computational-intense approach is the DNS (Direct Numerical Simulation) approach [7], [10], computing the time-dependent solutions of the flow utilizing the unaltered Navier-Stokes relations. Unfortunately, when modelling a situation where turbulence has triggered and is growing downstream (*e.g.* in a turbulent wall boundary layer), the corresponding DNS simulations hitherto arrive at opposite results, *i.e.* showing a receding turbulence downstream [11].
- In the LES (Large Eddy Simulation) approach [12], a low-pass filtering of the Navier-Stokes relations removes the information from the small eddies. The impact of the small eddies on the solution is instead modelled, while the large-scale eddies are analysed with the unaltered Navier-Stokes relations. It is argued that this approach removes the need to resolve small flow- and time scales.
- The k-ε turbulence model [13] simulates the mean-flow behaviour. It incorporates expressions for the turbulent kinetic energy k, as well as expressions for the "rate of dissipation of turbulent kinetic energy" ε. The concept of "eddy viscosity" is introduced – representing a "property of the flow".
- Despite various approaches results in various degrees of success, it is generally acknowledged that from hitherto acquired knowledge, one is not yet able to predict turbulent fluid motion in detail.
- There is no clear definition of turbulence. Reference is often made to *a list of characteristics of fluid flow behaviour*, *cf. e.g.* [3], which all need to be met to characterise the flow as "turbulent".
- It is fair to state that our understanding of turbulence is rather limited.

Would a fundamentally different approach have potential merit? Arguably yes, if one would consider the following:

- It is here believed that the use of Newton's viscosity law $\tau_{ij} = \mu\left(\frac{\partial u_i}{\partial y_j} + \frac{\partial u_j}{\partial y_i}\right)$ (for an incompressible and Newtonian fluid) [2], [14] as a fundamental model for turbulent flows can be contested.[1] Clearly, a replacement fundamental model would approach the analysis of turbulence in a different way.

- The non-linear *slip flow* process occurs at far-from-equilibrium conditions [15] and has a corresponding residual thermodynamic process formulation [16]. Often ordered structures (often referred to as "dissipative structures") may be created in connection with the initiation of such a residual process [15].

- A simple *fracture* model based on multiple, but vertically separated slip flows, can fully resolve the time-averaged velocity profile of the so-called *viscous sublayer*, the *buffer layer*, the *log-law region,* and *outer region* of a turbulent wall boundary layer [1], [2]. The total kinetic energy dissipation can be integrated and compared with corresponding experiments with a certain degree of agreement, *cf.* Table 1 and computations in [17] for pipe flows.

- The concept of *perfect* slips fracture structure, and *defect* slips fracture structure can be introduced, where the defect slips fracture structure is associated with a reduced kinetic energy dissipation. For a perfect slips fracture structure, which appears to represent the situation within the viscous sublayer, all flow downstream occurs parallel to the wall, with no experimental evidence of swirls initiating within this zone. In addition, the viscous sublayer can also be considered to represent a *saturated* kinetic energy dissipation zone. Considering the buffer layer and log-law region, swirls may initiate (which downstream may form turbulent eddies, *cf.* discussion below and in [17]). But these may form only at relatively few spot-wise positions within the flow, *i.e.,* the connection between visible turbulence would relate to the presence of defects in the fracture structure.
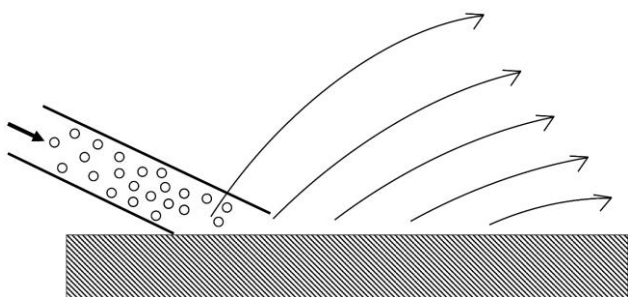

Figure 1. Impinging jet of round particles (erosives), impacting a ductile target surface, at an "initial state" of stationary conditions. Finnie and Kabil [18] characterised the reflected stream as "laminar".

In this paper, and in the associated paper [17], the discussion is focused on analysing the above-proposed model and evaluating it against experiments carried out on pipe channel flows.

Table 1. Comparison of traditional- versus proposed residual thermodynamic process approach.

Traditional approach on pipe cross-section:	Proposed approach on pipe cross-section:
$\bar{\mathbf{U}}_{model}$ does not agree with $\bar{\mathbf{U}}_{experiment}$ when solving the unaltered Navier-Stokes relations (in DNS simulations).	$\bar{\mathbf{U}}_{model}$ agrees with $\bar{\mathbf{U}}_{experiment}$, *cf.* [17].
$\mathbf{U}'_{model}$ in various degrees of agreement with $\mathbf{U}'_{experiment}$ (depending on alterations and artificial settings for closure when studying Reynolds decomposed Navier-Stokes relations).	$\mathbf{U}'_{model}$ considered to be of secondary importance.
Fundamental model: $\tau_{ij} = \mu\left(\frac{\partial u_i}{\partial y_j} + \frac{\partial u_j}{\partial y_i}\right)$ All irreversible thermodynamic processes occur close to equilibrium conditions, soft gradients.	Fundamental model: $\dfrac{d(ke)_{res}}{dt} = C_A \dfrac{\rho L}{\delta} U_{slip}$ valid at far-from-equilibrium conditions.
No specific triggering mechanism is presented in the turbulence sciences literature, to the author's knowledge.	Mechanism accounting for turbulence is believed to occur at far-from-equilibrium conditions and may trigger/onset at certain conditions.
1st law balance: No agreement yet claimed in the literature between model and experiments.	1st law balance: Agreement inferred.
2nd law balance: Not applicable (*cf.* incompressible flow assumption)	2nd law balance: Not applicable (*cf.* incompressible flow assumption)
Provides physical insight into origination of different zones in a turbulent wall boundary layer (viscous sublayer, buffer layer, and the log-law region): no.	Provides physical insight into origination of different zones in a turbulent wall boundary layer (viscous sublayer, buffer layer, and the log-law region): yes.
Connection surface roughness with analytical approach: not understood (the CFD modeller is referred to black-box model options).	Connection surface roughness with analytical approach: yes, experimental flow behaviour indicates effects to be accounted for when mapping the velocity profile.
The sciences of fluid dynamics have derived a closed set of equations, referred to as the non-altered set of Navier-Stokes relations for laminar flow. From a set of initial and boundary conditions, the Eulerian fluid flow field can be computed. Variants of this set of relations have been developed for analysis of turbulent flows. After a Reynolds decomposition, a set of relations can be derived without knowledge of all terms – the so-called "closure problem" of turbulence. These unknown terms need to be estimated (in a semi-empirical manner) to solve the set of equations.	To develop a closed set of relations solving the time-averaged Eulerian turbulent fluid flow field (including $\bar{\mathbf{U}}_{model}$), this remains to be developed (it is not the focus of the present work).

2. Theory
2.1 Preamble

Experimental observations made by [18] on a steady-state impinging dense particle-flow jet stream, resulting in erosion of a ductile material, is discussed. For round particles (so-called "erosives" within the field of Wear), impacting a continuum processes are the only possibility to consider for turbulent flows. The author of the present work believes that this argument is circular.

---

[1] In Capter 1.5 of [3] it is stated that "The Kolmogorov length and time scales are the smallest scales occurring in turbulent motion." – followed by a scientific argument concluding that

ductile target surface at relatively low impact angles, the initial behaviour when attacking a fresh target surface – not considering the first within 100 milliseconds or so when a "protective zone" [19] has not yet developed – behaves differently than later behaviour: At first, the net erosion rate is lower (which cannot be associated with any initial deviating surface material composition or oxide layer) than the net erosion rate observed later. Also, during this "initial state" the reflected flow is characterised as "laminar" [18]. As Finnie and Kabil were interested in the erosion behaviour of the target surface, they did not photograph or further characterise the reflection flow stream. However, Gustavsson [19] performed numerical simulations of an impinging 2D laminar particle-jet stream (at various flow conditions, width of jet, and impact angle against the target surface), cf. Figs 6-7 in [19]. These transient simulations were performed using a two-phase Eulerian-Eulerian flow solver [20], [21], [22]. For the impinging jet simulations, it was necessary to perform the simulations for a certain period (around a one-second simulation time), modelling the initial impact, followed by a build-up of a "protective layer" in the vicinity of the target surface, until eventually a steady-state flow condition was obtained, with results principally similar to the laminar flow situation depicted in Fig. 1, cf. [19].

Returning to the Finnie and Kabil experiments, after a "long-term" exposure of this steady-state impinging particle-flow jet stream of round erosives at relatively low impact angle, a regular pattern – a so-called "erosion ripple" pattern – would form in the target material. In addition, when ripples formed, it appeared that the net erosion rate was higher. For this later state, which we can refer to as the "state of erosion rippling", the observed reflected flow was characterised as "turbulent" [18], cf. Fig. 2.

The latter erosion ripple pattern formed on the target surface could be presumed to remain overly flat across the target surface, with the ripple wavelength representing typically a half- to full diameter of the erosives [18].

If one would consider modelling the turbulent flow of Fig. 2 in a two-phase Eulerian-Eulerian CFD flow solver involving only continuum models, an immediate complicating issue is that the erosion ripple wavelength is smaller than any envisioned continuum-length scale.
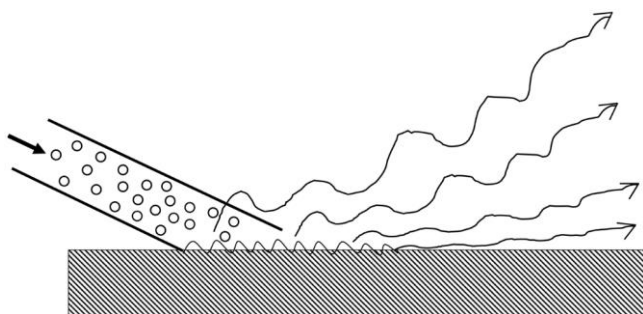

Figure 2. Impinging jet of round particles (erosives), impacting a ductile target surface, at a later state here referred to as a "state of erosion rippling". Finnie and Kabil [18] characterised the reflected stream as "turbulent".

Later, the tools of the residual thermodynamics framework [16] were employed to analyse the same case; First, the irreversible non-linear process of "ductile erosion" (the traditional description in the field of Wear) – or more precisely the irreversible process identified as "ductile wear" [23], [24] – was derived. Secondly, it was in [16] argued that

the self-organisation of round erosives along the target surface through a "slip-roll" mechanism would result in ductile erosion, incorporating a geometrically fixed ripple wavelength pattern. The analysis of this case in [16] predicted ripple wavelengths close to- or in agreement with those observed in experiments.

The nominal slip-roll process resulting in erosion rippling was shown as possible to enhance by means of strengthened "dual-coupling" oscillation, cf. [16], i.e., via further self-organisation of the effective thermodynamic forces and fluctuating thermodynamic flows. This enhancement – which is associated with an increase in the total residual entropy generation rate – results in increased net erosion rates.

Still, the net erosion rate is limited. Hence, for the net entropy generation around the entire impact zone of interest, it is fair to say that some kind of maximization of the net entropy generation (MEP = Maximum Entropy Production) appears to occur over time [25].

During this entire experiment, from onset of rippling through maximization, the nominal inflow jet stream is stationary and does not change with time.

Apparently, this self-organising behaviour occurs outside the target surface, hence this phenomenon occurs within the two-phase flow field (near the target surface). Consequently, this finding indicates that irreversible residual thermodynamic processes (cf. [16]) occur within the particle-gas or particle-vacuum flow field (i.e. outside the target surface) during the erosion rippling process.

In this paper, the observation by Finnie and Kabil [18] on characterising the reflected stream as turbulent is of interest to study further: When a turbulent reflective stream is at hand, this represents an outflow behaviour, which originates from an upstream condition in the flow field where one or several near-surface irreversible residual thermodynamic processes are acting, cf. Fig. 2. This, in contrast to the reflected stream being laminar when the outflow originates from an upstream condition in the flow field where only non-residual irreversible thermodynamic processes (cf. [16]) can be regarded as acting, cf. Fig. 1.

In other words, it appears not possible to model or simulate the "turbulent" flow situation in Fig. 2 utilizing only continuum models.

2.2 Appearance of Turbulence

Consider the physics in the immediate surroundings of the triggered slip-roll residual process resulting in erosion rippling in Fig. 2. According to [15] and [16], a continual supply of mechanical energy, or mass, or both combined, is required, in order to self-sustain the residual irreversible thermodynamic process (within the zone where $d_i S_{res} > 0$) above the onset condition. This supply comes from the immediate surroundings.

Next, consider a principal sketch of the immediate surroundings of the target surface subject to erosion rippling process, cf. Fig. 3.

The zone in which the discrete residual-process interaction accounting for ductile wear combined with erosion rippling is a certain zone stretching a certain distance from the wall itself, i.e., the zone where $d_i S_{res} > 0$, cf. Fig. 3. This zone might have a different size in case erosion ripples have just begun to form, or when the erosion ripples reach their geometrical maximum amplitude (in other words, when overall net entropy generation has reached a maximum rate). Perhaps, the slip-rolling mechanism may not only

occur in the first 1-2 particle layers along the wall, but it may also influence the particle's organization – say 4-5 particle layers (or more) – outside the solid wall, *cf.* Figs 3-4.

If we choose to select the geometrical zone in which the slip-rolling mechanism creates a highly self-organized slip-rolling and entropy-generating zone, we can identify an exterior zone in which one is below the onset threshold for this residual process to enable – *i.e.,* within a non-residual thermodynamic condition $d_iS_{res} = 0$, *cf.* Figs 3-4.
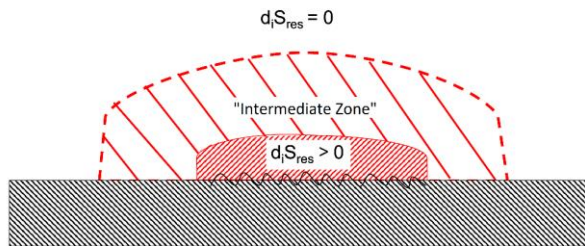

Figure 3. Principle separation of three different geometrical zones around the erosion ripples formed on the target surface. A zone with residual irreversible thermodynamic process, above onset threshold condition ($d_iS_{res} > 0$), with significant residual entropy generation (for a mechanical system), is present. This is the slip-roll process, possibly with some dual-coupling action. An exterior zone with sub-threshold conditions ($d_iS_{res} = 0$) can be identified, where no residual processes occur. Between these two zones, an "intermediate zone" can be imagined, which represents a geometrical zone in which both sub-threshold- or above-threshold conditions may exist for potential residual processes.
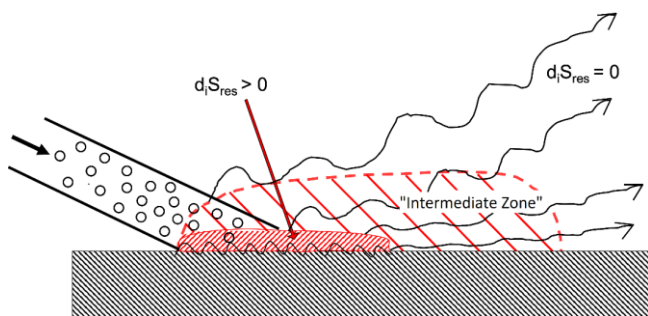

Figure 4. Author's estimation of zone sizes and locations (not to scale) for the three different geometrical zones – with fundamentally different physical behaviour in each of the respective zones – for the flow situation depicted in Fig. 2.

Between these two zones, we have an intermediate zone, *cf.* Figs 3-4. In this intermediate zone, which necessarily exists between the two extremes, one could reason that it would – for instance – represent a process condition A in Fig. 2 in [16]. In many instances in time and for most regions within this zone, one would be at sub-threshold conditions $d_iS_{res} = 0$, while for some instances in time and at certain regions within this zone, one would be at above threshold conditions $d_iS_{res} > 0$. Any fluctuations in thermodynamic forces may result in sudden entropy generation.

Such a process condition A is typically – according to [16] (with reference to experimental observations by Prigogine) – associated with high variations in concentrations, fluctuations etc., which might account for the

downstream apparent "turbulent" behaviour of the reflected stream flow. Gustavsson states that (*cf.* below Table I in [16]): "However, fluctuations in the effective thermodynamic forces will render residual entropy generation for position A, where *dissipative structures appear as more chaotic and strong fluctuations in concentration can be induced, …*".

2.3 The Support Zone, and Connection with an Eddy, in The Erosion Ripple Jet Stream Flow

One may speculate on how the irreversible residual thermodynamic processes in the vicinity of the target surface (above the erosion ripple zone) interact with its nearest surroundings, and the behaviour of a possible locally-onset residual process at a position further downstream. In particular, **the model envisions the _downstream leakage_ of the residual-thermodynamic process zone, i.e., downstream extending of the zone $d_iS_{res} > 0$, followed by breakage of the downstream-extended-zone $d_iS_{res} > 0$ from the fixed erosion ripple region, and continued lifetime of this residual process zone $d_iS_{res} > 0$ as it moves _downstream_.**

The downstream leaked – or broken-off – *R.Th.d.P.* (Residual-Thermodynamic Process) *zones* could be imagined as a thin, nonetheless extended in the downstream direction and yet with a significant width. Necessarily, the immediate surroundings will support this self-sustaining R.Th.d.P. zone with kinetic energy and possible mass flow from both sides, maintaining the onset condition of the downstream moving R.Th.d.P. zone.

The following experimental evidence supports this proposition:

1. The turbulent appearance of the reflected flow in Fig. 2 suggests that any given fixed geometrical position downstream of the onset residual-process zone $d_iS_{res} > 0$ might consist of either a sub-threshold condition $d_iS_{res} = 0$ or an above-threshold condition $d_iS_{res} > 0$ at different times.

2. A downstream moving broken-off R.Th.d.P. zone is necessarily surrounded by a much-larger *support zone*. In the following discussion, the R.Th.d.P. zone and associated support zone is referred to as a *turbulent eddy*, *cf.* Fig. 5. The concept of a turbulent eddy observed in experiments originally represent the size of coherent (or identifiable) structures observed in the flow. It is stated that eddies represent "packets" of fluid of different sizes (ranging from macroscopic to microscopic scales).

3. The maximisation of the net entropy generation in the entire impact zone appears to occur over time, after the residual thermodynamic process has been triggered to onset (for a stationary impinging particle jet flow). In order to maximize the net entropy generation, a downstream leakage of the onset process zone $d_iS_{res} > 0$ will occur.

4. As the natural behaviour tends towards maximising the net total entropy generation, after the onset of an erosion rippling process, it seems that one viable way to further increase the net total entropy generation, would be to self-organise additional life-support for these separated R.Th.d.P. zones as they move downstream. This maximization of entropy generation will possibly extend the length and/or width of the separated R.Th.d.P. zones, as well as extend the lifetime of the R.Th.d.P. zones as they move further downstream. This, in turn, would stretch the length of the "intermediate zone" yet further downstream, *cf.* Fig. 4.
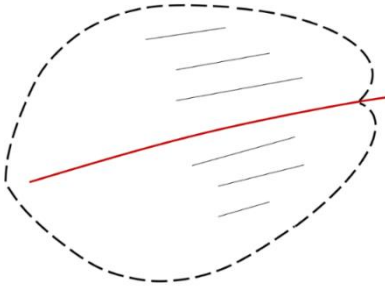
Figure 5. Consider an instantaneous condition: A geometrical zone supporting the above-threshold conditions to maintain onset of a separated discrete slip layer. In this paper, this supporting zone is referred to as a turbulent eddy.

Figure 5 depicts the possibility of an onset residual process (in red colour) that extends outside the specifically depicted turbulent eddy, into a connected turbulent eddy neighbour. At some point in time, these two co-joined turbulent eddies may break off from one another and reduce or increase in respective size.

The active R.Th.d.P. zone will reduce in size and the presence of R.Th.d.P. zones will cease to exist just prior to exiting the intermediate zone, *cf.* Fig. 4.

2.4 First Law Balance Relation Applied to a Single-Phase Turbulent Pipe Flow

We need an expression, allowing us to compute the Darcy friction factor from the total kinetic energy dissipation in a single-phase (nominally Newtonian fluid) pipe flow, valid for both viscous laminar and turbulent flows.

This can be obtained from the 1st law of thermodynamics, together with some common assumptions made in fluid dynamics of incompressible flows:

Consider a fully developed horizontal pipe flow (*i.e.,* no change in potential energy between inlet and outlet). Assume the fluid inside is incompressible, $v = 1/\rho =$ constant. Consider next an open system encompassing inlet to outlet, incorporating the fluid medium in the pipe. Assume in turn adiabatic conditions, $\dot{Q} = 0$, and no shaft work, $\dot{W}_{\text{shaft}} = 0$. Furthermore, assume steady state flow rate, $\dot{m} =$ constant.

We then obtain from the 1st law for open systems the following (valid for both viscous laminar- and turbulent flows):

$$\Delta \dot{E}_{\text{system}} = \underbrace{\dot{Q}}_{=0} - \underbrace{\dot{W}_{\text{shaft}}}_{=0} + (\dot{m}h)_{\text{in}} - (\dot{m}h)_{\text{out}} = 0 \qquad (1)$$

where $h = u + Pv$ is the enthalpy.

The total kinetic energy dissipation is manifested as an increase in internal energy of the fluid at the outlet, minus inlet, multiplied by the mass flow rate. From Eq. (1) we get the following (valid for both viscous laminar- and turbulent flows):

$$\frac{\text{d(KE)}}{\text{d}t} = \dot{m}(u_{\text{out}} - u_{\text{in}}) = -\dot{m}v\Delta P = -\frac{\dot{m}\Delta P}{\rho} \qquad (2)$$

Where we note that pressure change is negative (in the downstream direction) following thermodynamic sign conventions, and that the internal energy of the fluid leaving the pipe is higher than that of fluid entering the pipe, possible to record as an increase in temperature according to $\text{d}u =$

$c_v \text{d}T$, *cf.* "incompressible flow" assumption in Section 2.10. Below, the fluid dynamic term pressure drop is discussed, a positive quantity, *i.e.,* pressure drop $= -\Delta P$.

In the following, it is important to keep track of whether assumptions and formulas relate to either viscous laminar flows, or turbulent flows.

Before connecting a new turbulence model to a pressure drop, it is a good first step to demonstrate that the outlined 1st law balance relations also apply for a viscous laminar flow. It is well-known from the fluid dynamics literature that there is an analytical connection between the Darcy friction factor (connected with pressure drop) and the Reynolds number for a fully developed laminar pipe flow of a Newtonian fluid.

Let us do the exercise of: Viscous laminar flow assumption → determine the kinetic energy dissipation locally (at radial positions in the pipe) from the linear fundamental model correlating shear stress, viscosity, and velocity gradients → integrating into total kinetic energy dissipation (which equals viscous dissipation) → via 1st law compute the pressure drop → allowing for estimation of the friction factor.

For a fully developed viscous laminar flow, with the above assumptions, we can from the Navier-Stokes expressions derive the pipe-downstream-direction velocity profile as:

$$U_1 = U_1(r) = U_{\text{max}} \left(1 - \frac{r^2}{R^2}\right) \qquad (3)$$

where R represents the radius of the pipe interior, and radius r stretches from the inner centreline $r = 0$ to $r = R$.

Also, the average-, or mean, flow speed for this viscous laminar case can be expressed as:

$$U_{\text{mean}} = U_{\text{max}}/2 \qquad (4)$$

From the fundamental model for viscous laminar flows, we have the connection $\tau = -\mu \frac{\partial U}{\partial r}$, where μ represents the dynamic viscosity of the Newtonian fluid.

According to fluid dynamic textbooks, the viscous laminar case gives us that the total kinetic energy dissipation in the pipe equals the integration of the viscous dissipation:

$$\frac{\text{d(KE)}}{\text{d}t} = \iiint \mu \left(\frac{\partial U_1}{\partial r}\right)^2 r \, \text{d}r \, \text{d}\theta \, \text{d}z \qquad (5)$$

After a straightforward integration (using Eq. (3)) in the radial direction, and for all angles 0 to 2π, we obtain for the viscous laminar flow case:

$$\frac{\text{d(KE)}}{\text{d}t} = 2\pi\mu \int U_{\text{max}}^2 \text{d}z \qquad (6)$$

Using Eq. (4), and integrating over the entire pipe length section Z, we then obtain for the viscous laminar flow case:

$$\frac{\text{d(KE)}}{\text{d}t} = 8\pi\mu \cdot U_{\text{mean}}^2 \cdot Z \qquad (7)$$

From Eq. (2), and the relation (valid for both viscous laminar- and turbulent flows):

$$\dot{m} = \rho\pi R^2 U_{\text{mean}} \qquad (8)$$

we can directly compute the pressure drop for the viscous laminar flow case as:

$$\text{Pressure drop} = -\Delta P = \frac{8\mu \cdot U_{\text{mean}} \cdot Z}{R^2} \qquad (9)$$

From Darcy's formula on pressure drop, the friction factor f is introduced (valid for both viscous laminar- and turbulent flows):

$$\text{Pressure drop} = f \cdot \frac{\rho Z \cdot U_{\text{mean}}^2}{2D} \qquad (10)$$

Hence, inserting the pressure drop obtained for viscous laminar flows, Eq. (9), into Eq. (10), we can compute the dimensionless friction factor as:

$$f = \frac{64 \cdot \mu}{\rho \cdot U_{\text{mean}} \cdot D} = [\nu = \mu/\rho] = \frac{64 \cdot \nu}{U_{\text{mean}} \cdot D} = \left[\text{Re} = \frac{U_{\text{mean}} \cdot D}{\nu}\right] = \frac{64}{\text{Re}} \qquad (11)$$

where ν represents the kinematic viscosity of the Newtonian fluid, and Re represents the dimensionless Reynolds number for pipe flows.

The friction factor, with above derivation, hence agrees with the friction factor as stated for viscous laminar flows in the fluid dynamics literature, *i.e.* $f = 64/\text{Re}$.

However, the traditional fluid dynamics derivation arriving at the same result was determined – instead of computing the total kinetic energy dissipation within the entire volume of the pipe – by computing the shear stress acting on solid walls. To illustrate:

From the surface wall shear stress acting on the cylindrical element surface, the parallel force defined by the wall shear stress (units N/m^2) multiplied by the area circumference multiplied by length of the cylinder $F = \tau_{\text{wall}} \cdot 2\pi R \cdot Z$, gives a pressure drop, which can be computed as $-\Delta P = F/A$, where $A = \pi R^2$. This gives (valid for both viscous laminar- and turbulent flows):

$$-\Delta P = 2\tau_{\text{wall}} Z/R \qquad (12)$$

As the wall shear stress can be computed from $\tau_{\text{wall}} = \tau(r = R)$, we utilize the relationship for laminar flows $\tau = -\mu \frac{\partial U}{\partial r}$ and compute the derivative using Eq. (3), which gives us: $\tau_{\text{wall}} = 2\mu U_{\text{max}}/R$. Inserting this wall shear stress into Eq. (12) gives: $-\Delta P = 4\mu Z U_{\text{max}}/R^2$ for the viscous laminar flow case. Comparing this latter expression for laminar flows with the Darcy formula (Eq. (10)), we obtain the same result $f = 64/\text{Re}$ for the viscous laminar case. However, it is stressed that it is derived from Newton's laws of mechanics (not the 1$^{\text{st}}$ law of thermodynamics combined with a total integration of the total kinetic energy dissipation).

Hence, to compute the Darcy friction factor for turbulent flows Eq. (2) and Eq. (10) are used to compute the friction factor according to:

$$f = \frac{\left(\frac{d(\text{KE})}{dt}\right)}{\dot{m}} \cdot \left(\frac{D}{Z}\right) \cdot \frac{1}{\frac{1}{2}(U_{\text{mean}})^2} \qquad (13)$$

Note: Eq. (13) is valid for both viscous laminar flows as well as turbulent flows.

Our computational analysis work, in the following, will be to test our model, compute the net kinetic energy dissipation by integration, and compute the Darcy friction factor from Eq. (13). Hence, the proposed model can be compared to corresponding turbulent experiments – tabulated for turbulent pipe flows for different flow rates, surface roughnesses, pipe diameters, and fluid flow properties.

2.5 Single-Phase Turbulent Flows – Proposed Fracture Model and Fundamental Model

Unless otherwise stated, an Eulerian framework is adopted in the following.

The proposed web of fractures – assuming the MEP fracture model is active – is depicted in Fig. 6.
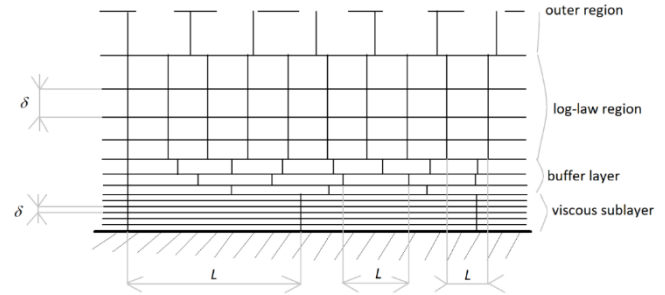
Figure 6. MEP fracture zone. In this 2D cross-section of the flow, assume Cartesian axis nr. 1 along the wall plane (in direction of the flow), and Cartesian axis nr. 2 perpendicular to the wall plane.

Assume that no velocity gradients exist between the fractures. The velocity of a flow parallel to a solid surface, $U_1(y_2)$, at a given y_2-position, is hence possible to determine by summation of the slip flow velocities from the solid surface to the y_2-position, where the corresponding resolution parameter δ (*cf.* Fig. 6) is summarized from the solid surface to the y_2-position. Thus, the experimentally recorded time-averaged velocities, and the stepwise discrete velocity variations, will closely match for a fine-enough resolution δ.

Considering the MEP process, the net kinetic energy dissipation is the highest possible if all kinetic energy dissipation occurs in the horizontal slips fracture zones, without presence of defects (and no swirls).

In this perfect fracture structure, without swirls, accounting for mass conservation or momentum conservation is not necessary. Blocks of fluid do flow downstream, at constant velocity.

In this fracture model, a first assumption is that the slip length L (considered a positive quantity in this work) correlates approximately linearly to the slip velocity U_{slip} (also considered a positive quantity in this paper):

$$L = C_B U_{\text{slip}} \qquad (14)$$

Note: parameter L is finite, since an infinitely large L suggests an infinitely large U_{slip}, which is not possible.

Consider the conditions at a steady-state flow of parallel-positioned flakes, of thickness δ, of length L, and width K.

Consider a friction force acting on a slipping single flake, F_1, and assume a set of equidistant, and equally sized flakes of parallel flow, moving with the same relative slip flow U_{slip}. The friction force of a single flake can be replaced by a shear stress acting on the flake is $\tau = F_1/A = F_1/(K \cdot L)$, which gives a kinetic energy dissipation rate per unit volume $d(\text{ke})_{\text{res}}/dt = \tau \cdot U_{\text{slip}}/\delta$ locally within the flow when ensemble averaging, due to this residual process.

A second assumption is that $\tau \propto U_{\text{slip}}$. From this, one may postulate: $\tau = C_A \cdot \rho \cdot C_B \cdot U_{\text{slip}}$, which gives:

$$\frac{\mathrm{d(ke)}_{\text{res}}}{\mathrm{d}t} = C_A \frac{\rho L}{\delta} U_{\text{slip}} \qquad (15)$$

which represents a new fundamental model.

From a thermodynamic point of view, the entropy generation for this residual process can be expressed as: $\mathrm{d}_i S_{\text{res,gen}}/\mathrm{d}t = (G_{\text{proc}} - G_{\text{no proc}}) \cdot \mathrm{d}X/\mathrm{d}t$, *cf.* [16].

The work loss rate per unit volume resulting from this residual process can in turn be expressed as $|\delta w_{\text{res}}/\mathrm{d}t| = T \cdot \mathrm{d}_i s_{\text{res,gen}}/\mathrm{d}t$, where for this case $\mathrm{d}_i s_{\text{res,gen}}/\mathrm{d}t = (\mathrm{d}_i S_{\text{res,gen}}/\mathrm{d}t)/(K \cdot L \cdot \delta)$. This work loss rate also equals the kinetic energy dissipation rate, *i.e.* $\mathrm{d(ke)}_{\text{res}}/\mathrm{d}t = |\delta w_{\text{res}}/\mathrm{d}t|$.

From this, the corresponding effective thermodynamic force for this fracture model can be expressed (in units J/(m³K)) as:

$$G_{\text{proc}} - G_{\text{no proc}} = C_A C_B \cdot \rho \cdot \frac{L}{\delta} \cdot \frac{U_{\text{slip}}}{T} \qquad (16)$$

and where the corresponding thermodynamic flow (in units m³/s) is $\mathrm{d}X/\mathrm{d}t = U_{\text{slip}} \cdot K \cdot \delta$.

A principally varying kinetic energy dissipation rate per unit volume (multiplied by $2\pi r\Delta r$) in an inner turbulent wall boundary layer is illustrated in Fig. 7.

Notwithstanding statements made in Section 2.3 and Fig. 5, the fracture model considers only the flake on one side of the slip process to act as support zone (or eddy). This perspective is adopted to simplify the computations, and to establish a well-defined L and δ, as well as K if the computations are to be made in 3D.

From a numerical point of view, a fine-enough resolution in δ will reduce errors occurring from this simplification.

2.6 Variation in L and δ, and The Presence of Defects

The presence of some non-symmetrical slip flows and/or some defects, will not automatically trigger or initiate a swirl. If the defects are large, or non-symmetry is considerable, then sometimes unbalanced forces may occur which results in the creation of a swirl.

Parameters L and δ can resolve and characterize an eddy: For instance, L and δ are invariant concepts connected with the instantaneous velocity vector, where a ***macroscopic eddy*** should be considered as a summation of flakes in the web fracture structure both lengthwise and crosswise, having a coherent motion. The parameters L and δ of a flake within a macroscopic eddy can be used to compute (or estimate) the local kinetic energy dissipation from Eq. (15).

Also, according to this proposed theory, the smallest-scale eddy, or the ***microscopic eddy***, would then be represented by the flakes defined by the parameters L and δ.

The MEP process acts to repair defects – maintaining the underlying fracture structure.

The ensuing web fracture structure is assumed to appear as follows:

1. The viscous sublayer has a constant $L = L_{\text{max}}$ and a constant $\delta = \delta = \delta_{\text{min}}$. The viscous sublayer can be considered to represent a saturated MEP fracture zone. Indeed, the constant L and constant δ across the viscous sublayer, indicates a constant kinetic energy dissipation across this viscous sublayer. Hence, it is assumed to represent a maximum state. Interestingly, when the

surface roughness is increased, this maximum state zone is expanded in the y_2^+ direction (see below). Again, this experimental behaviour suggests that the viscous sublayer is a saturated MEP zone.

2. The buffer layer is simply an MEP fracture zone, linking the transition from the viscous sublayer zone to the log-law region. Turbulence scientists, albeit not discussing in terms of MEP behaviour, and not connecting their discussion to the present proposal, do indeed discuss the turbulent buffer layer as some kind of "transition" zone (of unclear definition) between the viscous sublayer and the log-law region. In the buffer layer, δ increases with increasing y_2. Simultaneously, the L parameter decreases with increasing y_2. The buffer layer is a zone which has a lot of "turbulence production", that is, the initiation of turbulent swirls, according to experiments. Indeed, if spreading out defects in this zone, and comparing with spreading out defects in the neighbouring viscous sub-layer zone, or in the log-law region, the non-symmetry will be highest in the buffer layer zone.

3. The log-law region has a fixed L (significantly smaller than in the viscous sublayer) throughout this region. However, δ increases with y_2. An important finding is that it can be mathematically shown that the log-law region, assuming the MEP fracture model, if applied all the way towards to the solid wall $y_2 = 0$, would correspond to integrating a kinetic energy dissipation expression corresponding to $1/y_2$ multiplied by a proportionality constant, which in turn if integrated all the way towards $y_2 = 0$ would tend to infinity. Since this is impossible, there is a position at a certain distance from the wall when the log-law region ceases to exist – which happens to be the position where the buffer layer ends, and the log-law region begins.
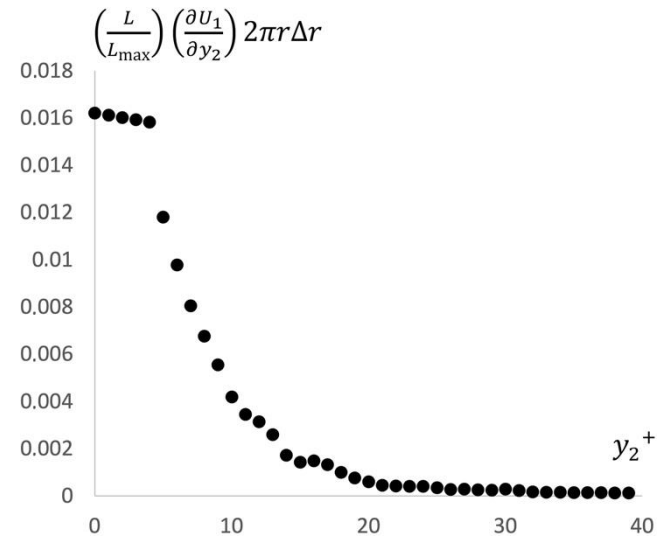
Figure 7. Variation of $\left(\frac{L}{L_{\max}}\right)\left(\frac{\partial U_1}{\partial y_2}\right) 2\pi r\Delta r$ vs. y_2^+ for the first case listed in Table 1 in [17] – cf. Eq. (18) – where the resolution Δr is 1 wall unit. Note the saturated (constant) kinetic energy dissipation in the viscous sublayer.

In the outer layer, the web fracture structure breaks up almost immediately, and the presence of large swirly behaviour is present. The outer layer makes up approximately 80% of the entire thickness of the turbulent wall boundary layer, while the inner layers (viscous, buffer, and log-law) make up maybe around 20% of the total boundary layer thickness.

2.7 Accounting for The Surface Roughness

To evaluate the proposed model, the following two main considerations need to be addressed:

1. What can be said on the turbulent flow velocity profile variation with surface roughness? Traditional turbulence literature does not consider anything of importance to happen within the viscous sublayer zone. However, the implications in this paper (*e.g.* Fig. 7) as well as computations in [17], are that a considerable – if not the major – part of the net kinetic energy dissipation occurs within the viscous sublayer zone.

In experiments, the wall surface roughness does seem to have an impact. It increases the intercept value C of the log-law relation with increasing roughness. Also, some different sources suggest an y_2^+ thickness somewhere between 5 to 8 for the viscous sublayer. It is here proposed that an improved dimensionless correlation can be outlined between the non-dimensional flow U_1^{++} and the non-dimensional position y_2^{++} in accordance with Fig. 8, for the smoothest as well as for the roughest wall surface roughness. Any intermediate surface roughness can use Fig. 8 to compute interpolated variations of U_1^{++} *vs.* y_2^{++}.

Note that the proposed variations in U_1^{++} *vs.* y_2^{++} in Fig. 8 are by no means necessarily accurate, as there is little experimental data available today to back up the proposed variations. The maximum C^{++} in Fig. 8 could possibly be even higher, as well as the upper limit $y_2^{++} = 8$ thickness of the viscous sublayer thickness. Hopefully, future experimental studies can be made addressing this problem.
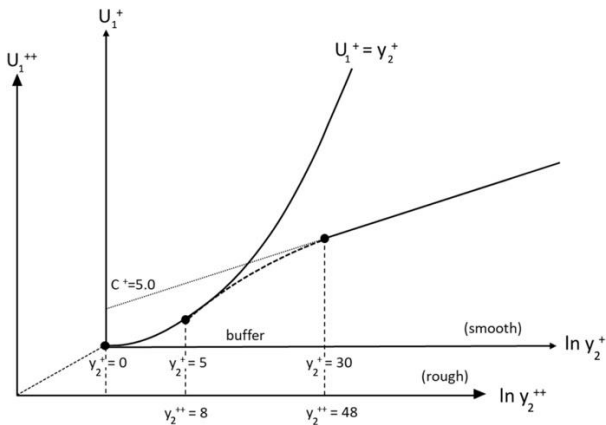
Figure 8. The non-dimensional velocity U_1^{++} varies with y_2^{++}. In this figure is depicted the smoothest condition in accordance with $U_1^{++} = U_1^+$ and $y_2^{++} = y_2^+$ as depicted, or the viscous sublayer varies between $y_2^{++} = 0$ and $y_2^{++} = 5$, the buffer layer between $y_2^{++} = 5$ and $y_2^{++} = 30$. The log-law region is assumed valid for $y_2^{++} = 30$ to $y_2^{++} = 300$. The intercept in the log-law will then be around $C^{++} = 5.0$. For the roughest case, it is assumed that the viscous sublayer varies between $y_2^{++} = 0$ and $y_2^{++} = 8$, the buffer layer between $y_2^{++} = 8$ and $y_2^{++} = 48$, and the log-law region between $y_2^{++} = 48$ and $y_2^{++} = 300$. The intercept in the log-law will then be around $C^{++} = 7.0$. Any surface roughness between these two extreme states, the U_1^{++} variation with y_2^{++}, as well as C^{++}, is obtained from a linear interpolation between these two extreme states.

2. What can be said on the fracture model variations of L and δ *vs.* y_2 – for different wall surface roughnesses?

Well, this question can be simplified in two steps:

First, it may be noted that if $U_{\text{mean}}(y_2^+)$ and L are known, and the connection between U_{slip} and L is defined, *cf.* Eq.

(14), then δ can be calculated. Hence, the following discussion need to only concern the variation of L *vs.* y_2 – for different wall surface roughnesses.

Second, since L_{max} may vary with surface roughness and the relevant flow conditions, it appears beneficial to work with a normalised $L = L(y_2)$:

$$L(y_2) = L_{max} \times \left(\frac{L}{L_{max}}\right)(y_2) \qquad (17)$$

The implication that δ varies depending on the selection of L, suggests that the variation of L throughout a turbulent boundary layer can be modelled according to Fig. 9 for the smoothest- and roughest wall, respectively, where $L = L_{\text{max}}$ at the solid wall.
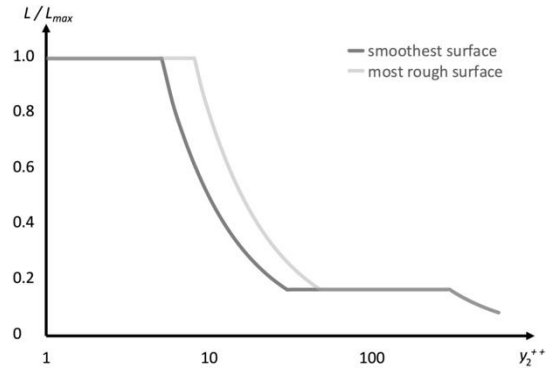
Figure 9. It is assumed that $L = L_{\text{max}}$ throughout the viscous sublayer, and $L = L_{\text{max}}/6$ throughout the log-law region. For the smoothest surface, y_2^{++} will range between 0 and 5 in the viscous sublayer, and between 30 and 300 in the log-law region. For the roughest surface, y_2^{++} will range between 0 and 8 in the viscous sublayer, and between 48 and 300 in the log-law region. In the buffer layer, it can be assumed that $L = 5L_{\text{max}}/y_2^{++}$ for the smoothest surface, and $L = 8L_{\text{max}}/y_2^{++}$ for the roughest surface. In the outer zone, in turn, it can be assumed that $L = 300L_{\text{max}}/6y_2^{++}$.

2.8 Computations of Total Kinetic Energy Dissipation in Turbulent Pipe Flows

For a 1-meter pipe length ($Z = 1$ m), we connect directly the total kinetic energy dissipation to the volume integral of the local kinetic dissipation rate per unit volume, caused by the residual processes, according to:

$$\frac{\text{d(KE)}}{\text{d}t} = Z \int \frac{\text{d(ke)}_{\text{res}}}{\text{d}t} 2\pi r \text{d}r = 1 \cdot \int C_A \frac{\rho L}{\delta} U_{\text{slip}} 2\pi r \text{d}r \approx$$
$$\int C_A \rho L \left(\frac{\partial U_1}{\partial y_2}\right) 2\pi r \text{d}r = \rho C_A L_{\text{max}} \int \left(\frac{L}{L_{\text{max}}}\right)\left(\frac{\partial U_1}{\partial y_2}\right) 2\pi r \text{d}r \quad (18)$$

where we immediately realize that $\left(\frac{\partial U_1}{\partial y_2}\right)(y_2)$ and $L(y_2)$ are known functions, *cf.* Figs 8-9.

When deriving Eq. (18), we utilize the approximation $\frac{U_{\text{slip}}}{\delta} \approx \frac{\partial U_1}{\partial y_2}$. This approximation is rather accurate, because where flow gradients are high, the fracture model requires a fine resolution of δ.

Furthermore, it is possible to replace L in Eq. (18) with the normalized L in Eq. (17), which allows the grouping of the terms L_{max}, together with C_A and ρ, outside the integral.

From the above assumption, we can proceed computing the total kinetic energy dissipation, without information on the resolution, or C_B.

As regards the variation of kinetic energy dissipation per unit volume, in the different zones, or the net kinetic energy

dissipation associated with the fracture flakes, the following findings are important to note:

First finding: In the log-law region, we obtain:

$$\frac{L}{c_B \delta} = \frac{U_{\text{slip}}}{\delta} \approx \frac{\partial U_1}{\partial y_2} = \frac{1}{\kappa} \cdot \frac{U^*}{y_2} \tag{19}$$

where the only varying parameter on the left-hand side of Eq. (19) is δ, and the only parameter varying on the right-hand side is y_2 (the distance from the wall). Hence, if we would apply Eq. (19) in Eq. (18), and integrate all the way to the wall, the total kinetic energy dissipation would become infinite – which is not possible.

Second finding: It appears that for zones where $L =$ constant, the net kinetic energy dissipation in the fracture flakes is equally large. That is, **in the viscous sublayer zone and log-law region, the net kinetic energy dissipation in the flakes is equal to the net kinetic energy dissipation of their neighbouring flakes in the y_2-direction**. In particular for the log-law region – where the kinetic energy dissipation rate per unit volume does decrease with increasing distance from the wall – the increasing flake size in the y_2-direction compensates for the decreasing kinetic energy dissipation rate per unit volume. This, in a way amounting to the product of flake volume and dissipation rate per unit volume, *i.e.* net kinetic energy dissipation rate, turns out equal in the y_2-direction.

2.9 Triggering of Turbulence

The fluid dynamics literature discusses the transition from viscous laminar flow to turbulent flow, *cf. e.g.* [2]. Influencing parameters are typically the Reynolds number, as well as the wall surface roughness (for boundary layer flow).

Other types of disturbances may also influence the onset of turbulence, such as a trip wire[2] positioned near the wall surface (positioned at or near the leading edge), or a sound wave. Normally, for a specific wall surface roughness, the transition to onset a turbulent wall boundary layer occurs at a specific Reynolds number. In case any artificially introduced disturbance such as a trip wire or an external sound wave is applied, the transition will occur at lower Reynolds numbers.

Observations have been made on turbulent spots [2] occurring near the solid wall just prior to the onset of the turbulent wall boundary layer. Some references argue that the concentration of these turbulent spots grow, and that when the concentration is large enough (effectively along the circumference of the inner pipe wall at a specific downstream position), the turbulent wall boundary layer triggers.

To analyse such transition theoretically, the principles of "linear stability analysis" – *cf.* [2] p. 673 – can be applied, where small disturbances are tested in linearized governing equations and boundary conditions. For a student of fluid dynamics, sometimes the concepts of discrete slip flow examples are encountered. For instance, for the "ideal slip flow" scenario (without any viscous processes occurring), it can be shown that disturbances of any wavelength (*cf.* [2] p. 679) may – under certain conditions – be amplified downstream. [This observation was utilized in the analysis of the erosion ripple process, where a connection between

the erosion ripple wavelength and the slip-roll mechanism was proposed in [16].]

Equation (15) indicates that most of the net kinetic energy dissipation occurs within the viscous sublayer. This implies that a trip wire, sound wave or wall surface roughness directly influencing the viscous sublayer may have a significant influence on the onset of the turbulence process.

As is the case for the turbulence phenomenon, including the transition, the literature admits that the processes of transition from a laminar boundary-layer flow into a turbulent boundary layer flow is not fully understood.

However, to study the transition with the propositions made in this work – instead of analysing amplification of disturbances in linearized sets of equations – what if the transition would instead connect with a ***real*** process transition? Consider the transition of one active physical process (*e.g.* an irreversible process which is governed by the fundamental law for Newtonian fluids) resulting in laminar flow behaviour, to flip into another active physical process (*e.g.* an irreversible process which is governed by the here-proposed new fundamental model) which results in turbulence.

What would be suitable requirements for this process transition to occur?

Consider the following:

1. Apparently, it is required to occur at a specific geometrical position. (According to the residual thermodynamics dynamics framework, the geometry where transition/flipping may occur is typically rather limited, *i.e.,* the entire flow region will not instantaneously flip from a laminar flow process into a turbulent flow process.)

2. Probably the same (essentially) local kinetic energy dissipation for both processes would exist at this specific geometrical position. (Kinetic energy dissipation are key to the laminar flow relations, expressed as a viscous dissipation, while the kinetic energy dissipation is directly expressed in the here-proposed fundamental model for the slip-flow process, Eq. (15).)

3. The same essential flow conditions should also occur at this specific geometrical position, *i.e.,* the same flow gradients should pertain.

4. The process transition must occur in the vicinity of a solid wall, partly because when the velocity gradually increases, the viscous dissipation of the laminar flow increases until transition occurs, but also partly because the kinetic energy dissipation is the highest near the solid wall for the laminar flow, *i.e.*, the viscous laminar flow gradients are the highest in the vicinity of the solid wall.

From these conditions it is proposed that a turbulence transition analysis may be performed as follows:

First, the viscous laminar kinetic energy dissipation at the transition position can be expressed as:

$$\frac{d(ke)}{dt} = \frac{d(ke)_{\text{viscous}}}{dt} = \mu \left(\frac{\partial U_1}{\partial y_2} \right)^2 \tag{20}$$

At the same transition position, the proposed new fundamental relation gives the kinetic energy dissipation as:

$$\frac{d(ke)_{\text{res}}}{dt} = C_A \frac{\rho L}{\delta} U_{\text{slip}} \approx C_A \rho L_{\text{max}} \frac{\partial U_1}{\partial y_2} \tag{21}$$

---

[2] The use of trip wires is sometimes valuable in experimental scaling work.

Equating these two expressions yields the following equation:

$$\mu \left(\frac{\partial U_1}{\partial y_2}\right)^2 - C_A \rho L_{\max} \left(\frac{\partial U_1}{\partial y_2}\right) = 0 \qquad (22)$$

which gives the trivial solution $\frac{\partial U_1}{\partial y_2} = 0$, or $\frac{\partial U_1}{\partial y_2} = \frac{C_A \rho L_{\max}}{\mu}$.

For a pipe laminar flow, the velocity gradient $\frac{\partial U_1}{\partial y_2} = -\frac{\partial U_1}{\partial r}$ at the wall can be determined from Eq. (3). This gives the following nominal expression for the transition:

$$\frac{8U_{\text{mean}}^2}{C_A L_{\max}} = \frac{\rho U_{\text{mean}} D}{\mu} = \text{Re} \qquad (23a)$$

For a pipe turbulent flow, the velocity gradient $\frac{\partial U_1}{\partial y_2}$ at the wall has an alternative formulation (in the viscous sublayer zone), *cf.* [17], which is: $\frac{\partial U_1}{\partial y_2} = \frac{(U^*)^2}{\nu}$. This gives, applying Eq. (10) and Eq. (12) the following alternative nominal formulation:

$$\frac{8 C_A L_{\max}}{U_{\text{mean}}^2} = f \qquad (23b)$$

Hence, Eq. (23a) presents a direct connection between the proposed new model and the Reynolds number at the turbulence onset transition point. Alternatively, Eq. (23b) presents a direct connection between $C_A L_{\max}$ and the Darcy friction factor f at the transition point.

Regarding these two expressions, Eqs (23a)-(23b), please note that the surface roughness and flow conditions influence the parameter $C_A L_{\max}$.

In [17], for a series of pipe cases, the proposed theory will be used to compute $C_A L_{\max}$.

2.10 Comments on The Incompressible Flow Assumption, and Prospects on a 2nd-law Balance

While the tools of residual thermodynamics and the 2nd law were pivotal in deriving a proposed new slip-flow process model and in identifying the proposed MEP processes, what else can be said on the application of the 2nd law on the present analysis?

Connecting with the developments of fluid dynamics, the assumption that the flow is incompressible (*i.e.*, the flow has constant density, viscosity, specific heat capacity and thermal conductivity) is made to simplify the derivations, and effectively separates the mechanical and thermal aspects of the flow (see [2], page 157).

According to [2], page 237, "The layman is usually surprised to learn that the pattern of the flow of air can be similar to that of water. From a thermodynamic standpoint, gases and liquids have quite different characteristics. As we know, liquids are often modelled as incompressible fluids. However, "incompressible fluid" is a thermodynamical term, whereas "incompressible flow" is a fluid-mechanical term. We can have an incompressible flow of a compressible fluid." Panton states that the main criterion for incompressible flow is that the Mach number be low ($M \rightarrow 0$). In addition, other criteria need to be fulfilled, *cf.* [2]. (Relating to this, all computations in [17] are performed for $M < 1/3$.)

While a general CFD flow solver analysis is based on the governing equations of fluid dynamics, continuity equation (conservation of mass), momentum equation (Newtons second law) and energy equation (conservation of energy), it was early in the present derivation stated that computations accounting for conservation of mass or momentum were not required for the analysis the time-averaged steady state turbulent flows in horizontal pipes. The focus was on the 1st law balance, and is the balance analysed in [17] for determination of model constants and evaluation of this approach.

How about a 2nd-law balance consideration?

The incompressible flow assumption appears to remove the need to consider a 2nd-law balance analysis in a regular CFD flow solver. It appears also to be the case here. In simple terms, the incompressible flow assumption makes a 2nd law net balance not meaningful to apply due to a lack of experimental data – a lack of data which anyway is not particularly important:

Consider, for instance, the following derived 2nd-law balance, reformulated as an expression of net entropy generation of water for a steady-state flow through a pipe:

$$\frac{d_i S_{\text{gen}}}{dt} = \sum \dot{m}(s_{\text{out}} - s_{\text{in}}) = \dot{m}c \cdot \ln\left(\frac{T_{\text{out}}}{T_{\text{in}}}\right), \qquad (24)$$

where $c = c_v = c_p$.

The derivation assumes an adiabatic process, but generally, no experimental efforts have been made by fluid dynamists to arrange for an adiabatic process in the reference experiments. In addition, there appears to be no experimental data available on temperature increase of the water for reference pipe flows, to the author's knowledge (unless heat transfer is being analysed – a totally different field of science). This above expression assumes good mixing (which is the case for turbulent flows), *i.e.,* the same temperature across a pipe section inlet and outlet. It is immediately clear that it is not meaningful to apply a 2nd-law balance of the pipe flow, as there is no recorded experimental temperature data available to connect with.

A corresponding 2nd-law net balance for dry air (assumed to be an ideal gas) gives the following expression for the entropy generation of a steady-state flow through a pipe:

$$\frac{d_i S_{\text{gen}}}{dt} = \sum \dot{m}(s_{\text{out}} - s_{\text{in}}) = \dot{m}\left[\int_{T_{\text{in}}}^{T_{\text{out}}} c_p \frac{dT}{T} - \text{R}_{\text{specific}} \cdot \ln\left(\frac{P_{\text{out}}}{P_{\text{in}}}\right)\right].$$

$$(25)$$

Again, although experimental data is available on the pressure drop from reference experiments, there is no experimental data available on the temperature increase. Hence, again, it appears not meaningful to try to apply a 2nd-law balance analysis.

3. Discussion and Conclusions

The framework in [16], together with basic ideas of the Coulomb friction law, is utilized to derive a non-linear mechanism, associating slip flow with a kinetic energy dissipation rate. This serves as a new fundamental model, in a setting where the entire flow field is represented by a web of fractures. In accordance with [16], as this mechanism can be categorized as a residual irreversible thermodynamic process, the model coefficients in this new fundamental model do not represent any true material properties of the fluid.

It appears that the different zones (viscous sublayer, buffer layer and log-law regions) originating in the inner turbulent wall boundary layer does so, based on the action of

an overall MEP process occurring. Also, it appears that a downstream leakage[3] of slips appears to occur which appear to slightly increase the net kinetic energy dissipation rate downstream – implicating an overall slowly-evolving transient behaviour of turbulence, *cf.* [17].

The results indicate the highest net kinetic energy dissipation rates occurs in the viscous sublayer[4], followed by the buffer layer. The net kinetic energy dissipation appears to be somewhat limited in the log-law region, but still large enough to maintain an ongoing MEP process.

In addition, the present investigation proposes two alternative equations, where each of them indicates the transition condition from viscous laminar flows to the onset (or offset) of the slip flow fundamental model.

The large-scale eddies and swirls are solely distractors from the main processes occurring, having – as shown in [17] – little influence on the net kinetic energy dissipation rates.

On the matter of cascade theory, is there any equivalent such theory possible to apply for the present proposed theory? Perhaps not: While certainly kinetic energy can be estimated for a large-scale eddy, the matter of kinetic energy dissipation is more complex: While a small flake in the viscous sublayer, which is not associated with any turbulent behaviour or turbulent eddy, can have a much higher kinetic energy dissipation rate per unit volume as compared to a comparatively much larger flake (with large δ) within a large-scale turbulent eddy, it appears questionable to discuss kinetic energy dissipation of visible fluid structures, when these have a small contribution to the overall kinetic energy dissipation.

Finally, with the here-proposed onset of a slip-flow- and MEP process, the concept of turbulence can be physically and strictly well-defined.

Nomenclature

A	area (m^2)
c	speed of sound in fluid (m s^{-1})
C^+, C^{++}	log-law intercept on U^+- or U^{++}-axis, respectively (-)
C_A	model constant (m s^{-2})
C_B	model constant (s)
c_p	specific heat at constant pressure (J kg^{-1} K^{-1})
c_v	specific heat at constant volume (J kg^{-1} K^{-1})
D	diameter of pipe interior (m)
K	flake width (in y_3-direction in Fig. 6) (m)
$\dfrac{d(KE)}{dt}$	total kinetic energy dissipation rate (W)
$\dfrac{d(ke)_{viscous}}{dt}$	viscous dissipation rate per unit volume (W m^{-3})
$\dfrac{d(ke)}{dt}$	kinetic energy dissipation rate per unit volume (W m^{-3})
E	energy (J)
F	force (N)
f	Darcy friction factor (-)
G	thermodynamic force (intensive unit)
h	specific enthalpy (J kg^{-1})
L	slip length of flake (in y_1-direction in Fig. 6) (m)
M	Mach number, *e.g.* $M = U_{mean}/c$ (-)
m	mass (kg)
$\dot{m}$	mass flow rate (kg s^{-1})
P	static pressure (N m^{-2})
Q	heat (J)
$R_{specific}$	specific gas constant (J kg^{-1} K^{-1})
R	radius of pipe interior (m)
r	radial distance from centerline (m)
Re	Reynolds number (-)
S	entropy (J K^{-1})
s	specific entropy (J kg^{-1} K^{-1})
T	absolute temperature (K)
t	time (s)
U	Velocity (m s^{-1})
$\mathbf{U}$	velocity vector (m s^{-1})
U_i	Cartesian component i of velocity vector (m s^{-1})
U^*	Friction velocity, *cf.* [17] (m s^{-1})
U_{max}	Maximum velocity (m s^{-1})
U_{mean}	Mean (average) velocity (m s^{-1})
U_{slip}	slip velocity (m s^{-1})
u	specific internal energy (J kg^{-1})
V	volume of flake fracture (m^3)
$v = \rho^{-1}$	specific volume (m^3 kg^{-1})
W	work (J)
$\lvert \delta w_{res}/dt \rvert$	work loss rate due to residual process (W m^{-3})
X	thermodynamic flow (extensive unit)
y_1, y_2, y_3	Cartesian co-ordinates (m)
Z	pipe axis length of section (m)
z	length position in pipe axis direction (m)

Greek letters

θ	angle (between 0 and 2π) (-)

---

[3] *The net effect of the active MEP process is to slightly increase the net kinetic energy dissipation downstream.* The means at disposal for this is a complex re-arrangement of flakes (with respect to L and δ), mending "defect" slip layers, and likely extending slip lengths, possibly in combination with break-ups of slip layers, or by changing the number of slip layers. Hence the wording "leakage of slips".

[4] As the proposed theory suggests a stronger concentration of kinetic energy dissipation is shifted towards the wall – compared to the assumptions of traditional turbulence theory

– it would be prudent to consider whether a high kinetic energy dissipation within the viscous sublayer, would result in increased local temperatures and adjusted local fluid properties? If so, what would be the effects? A ballpark estimation by the author for different fluids at $M < 1/3$ indicates that the primary behaviour would not be effected in a way which would directly overturn the proposed new theory, however there might be secondary phenomena that may result from the locally high kinetic energy dissipation.

δ	gap width between slip layers, also referred to as thickness of flake fracture, or resolution parameter (m)
κ	von Kármán constant, *cf.* [17] (-)
μ	dynamic viscosity of Newtonian fluid ($\text{kg m}^{-1}\text{ s}^{-1}$)
ν	kinematic viscosity of the Newtonian fluid ($\text{m}^2\text{ s}^{-1}$)
ρ	density (kg m^{-3})
τ	shear stress (N m^{-2})
$\bar{\bar{\tau}}$	Cartesian shear stress tensor (N m^{-2})
τ_{ij}	components i, j of tensor $\bar{\bar{\tau}}$ (N m^{-2})

Subscripts

gen	generation
max	maximum
min	minimum
no proc	excluding specific sub-process of interest
proc	including specific sub-process of interest
res	for residual process
wall	wall position

Special notations

$\Delta(\cdot)$	difference
$\text{d}(\cdot)$	differential [*e.g.* $\text{d}_i S_{res}$ represents the differential entropy change due to residual process (J K^{-1})]
$\delta(\cdot)$	inexact differential
$\overline{(\cdot)}$	time average, used in Reynolds decomposition $\mathbf{U} = \bar{\mathbf{U}} + \mathbf{U}'$
$(\cdot)'$	fluctuating component, used in Reynolds decomposition $\mathbf{U} = \bar{\mathbf{U}} + \mathbf{U}'$
$\dot{(\cdot)}$	rate (s^{-1})
$\frac{\text{d}}{\text{d}t}, \frac{\delta}{\text{d}t}$	time derivative (s^{-1})
$(\cdot)^+$	dimensionless scaling (traditional).
$(\cdot)^{++}$	dimensionless scaling – depending on the wall surface roughness.

References:

[1] F.M. White, *Fluid Mechanics*, 2nd Ed., McGraw-Hill Book Company, 1986.

[2] R.L. Panton, *Incompressible Flow*, John Wiley & Sons, New York, USA, 1984.

[3] H. Tennekes, J.L. Lumley, *A First Course in Turbulence*, MIT Press, 1972.

[4] P.A. Davidson, *Turbulence: An Introduction for Scientists and Engineers*, Oxford University Press, 2004.

[5] K. Sreenivasan, P.A. Davidson, Y. Kaneda, K. Moffatt, *A Voyage Through Turbulence,* Cambridge University Press, 2011.

[6] B. Herrmann, P. Oswald, R. Semaan and S. L. Bunton, "Modeling synchronization in forced turbulent oscillator flows", *Commun Phys 3:195*, 2020. DOI: 10.1038/s42005-020-00466-3.

[7] P. Moin, K. Mahesh, "DIRECT NUMERICAL SIMULATION: A Tool in Turbulence Research", *Annual Review of Fluid Mechanics 30*, 539-578, 1998.

[8] L.F. Richardson, *Weather Prediction by Numerical Process*, Cambridge University Press, 1922.

[9] A.N. Kolmogorov, "The Local Structure of Turbulence in Incompressible Viscous Fluid for Very Large Reynolds Numbers", *Proceedings of the USSR Academy of Sciences (in Russian), 30*, 299-303, 1941. Translated into English by L. Levin: A.N. Kolmogorov, "The Local Structure of Turbulence in Incompressible Viscous Fluid for Very Large Reynolds Numbers", *Proceedings of the Royal Society A, 434*, 9–13, 1991.

[10] C. Liu, P. Lu, L. Chen, Y. Yan, "New Theories on Boundary Layer Transition and Turbulence Formation", *Modelling and Simulation in Engineering*, Article ID 619419, 2012.

[11] R. Bose, P.A. Durbin, "Transition to Turbulence by Interaction of Free-Stream and Discrete Mode Perturbations", *Physics of Fluids 28*:114105, 2016.

[12] F. Ducros, P. Comte, M. Lesieur, "Large-Eddy Simulation of Transition to Turbulence in A Boundary Layer Developing Spatially Over a Flat Plate", *Journal of Fluid Mechanics, 326*, 1–36, 1996.

[13] B.E. Launder, D.B. Spalding, "The Numerical Computation of Turbulent Flows", *Computer Methods in Applied Mechanics and Engineering 3*, 269–289, 1974.

[14] Y. Demirel, *Nonequilibrium Thermodynamics: Transport and Rate Processes in Physical, Chemical and Biological Systems,* 3rd Ed., Elsevier, 2014.

[15] D. Kondepudi, I. Prigogine, *Modern Thermodynamics: From Heat Engines to Dissipative Structures*, Wiley, 1998.

[16] M. Gustavsson, ''Residual Thermodynamics: A Framework for Analysis of Non-Linear Irreversible Processes'', *Int. J. Thermodynamics*, *15*, 69–82, 2012.

[17] M. Gustavsson, "A Residual Thermodynamic Analysis of Turbulence – Part 2: Pipe Flow Computations and Further Development of Theory", *submitted for publication.*

[18] I. Finnie, Y.H. Kabil, "On The Formation of Surface Ripples During Erosion", *Wear 8*, 60-69, 1965.

[19] M. Gustavsson, "Fluid Dynamic Mechanisms of Particle Flow Causing Ductile and Brittle Erosion", *Wear 252*, 845-858, 2002.

[20] H. Enwald, E. Peirano, GEMINI: A Cartesian Multiblock Finite Difference Code for Simulation of Gas-Particle Flows, Publikation Nr 97/4, Department of Thermo and Fluid Dynamics, Chalmers University of Technology, Sweden, 1997.

[21] M. Gustavsson, A.E. Almstedt, "Numerical Simulation of Fluid Dynamics in Fluidized Beds with Horizontal Heat Exchanger Tubes", *Chemical Engineering Science 55*, 857–866, 2000.

[22] M. Gustavsson, A.E. Almstedt, "Two-Fluid Modelling of Cooling-Tube Erosion in A Fluidized Bed", *Chemical Engineering Science 55*, 867–879, 2000.

[23] M. Gustavsson, "A Residual Thermodynamic Analysis of Inert Wear and Attrition, Part 1: Theory",

International Journal of Thermodynamics 18, 26-37, 2015.

[24]   M. Gustavsson, "A Residual Thermodynamic Analysis of Inert Wear and Attrition, Part 2: Applications", *International Journal of Thermodynamics 18*, 39-52, 2015.

[25]   A. Kleidon, Y. Malhi, P.M. Cox, "Maximum Entropy Production in Environmental and Ecological Systems", *Phil. Trans. R. Soc. B* 365, 1297-1302, 2010.

A Residual Thermodynamic Analysis of Turbulence – Part 2: Pipe Flow Computations and Further Development of Theory

M. Gustavsson[*]

Hot Disk AB, c/o Chalmers Science Park, Sven Hultins Gata 9, SE-41288 Gothenburg, Sweden
E-mail: Mattias.Gustavsson@hotdiskinstruments.com

Abstract

Single-phase turbulent pipe flows are analysed utilizing a new theory presented in a parallel paper. Arguably this new theory implies improvements in matching modelling results with experimental observations: To illustrate, unique for these computations is that a 1st law balance agreement between simulations and corresponding experiments is achieved, while resolving the time-averaged fluid flow velocity (including the various inner turbulent zones) and accounting for the wall surface roughness. Testing this new approach, the computations of 20 cases of turbulent pipe flow arrives at a remarkably high amount of kinetic energy dissipation occurring at near-wall positions, where some 54-83% of the net kinetic energy dissipation occurs within the viscous sublayer-, and 17-39% within the buffer layer. Although turbulence incorporates time-varying phenomena, *e.g.* swirls, large eddies, and breakup of the latter, it is argued that simulating these would have practically no effect on the net kinetic energy dissipation – and the associated wall shear stress – for the present pipe flow cases. Another illustration of the improvements relate to transition computations: While a proposed nominal transition model arrives at fair values of transition Reynolds numbers, some improvements on this transition analysis can be made, *e.g.* allowing for the modelling of the turbulence onset/offset hysteresis behaviour. For scientists who wish to model time-varying phenomena, *e.g.* for the study of mixing, boundary layer thickness, or wall-pressure fluctuations, there should be possibilities to implement this new theory in computational flow solvers.

Keywords: Kinetic energy dissipation; onset and offset; wall surface roughness; defect web.

1. Introduction

The knowledge of turbulence, as well as the transition into turbulence – in the relevant scientific literature – is stated to not be completely understood [1], [2], [3], [4].

The use of Navier-Stokes relations for the solving of viscous laminar flows works excellently, when applied to Newtonian fluids [5]. The default assumption within the sciences of turbulent flows is that the same set of relations valid for laminar flows is also valid for turbulent flows [1], [2].

In a parallel paper, a different perspective and approach to the problem of turbulent flows is presented: In short, the *slip flow process* is considered as a possible mechanism active in turbulent flows *at discrete locations*. By assuming a local generation of kinetic energy dissipation where slips occur, a candidate alternative fundamental model can be derived for turbulent flows [6].

A Maximum Entropy Production (MEP) process is assumed active, which generates- as well as influences the entire behaviour of a web of slips in a slowly evolving transient manner. For instance, the MEP process may result in a downstream "leakage" of slips [6].

Within a nominally "perfect" web fracture structure, "defect" zones can be assumed. These defect zones may downstream be "mended" from leaked slips (from an upstream position) – a process which may influence the overall apparent turbulent behaviour [6].

By assuming a connection between slip length L and slip flow velocity U_{slip}, as well as a spread-out of slips controlled by the slip resolution δ, it is possible to build a web of slips, in a way which approximately reproduces the experimentally known flow velocity profile of a pipe flow cross-section.

The specific selection of slip length and slip resolution is in these introductory computations not critical (perhaps these can be estimated at a later stage): This partly because a selection of a numerical value representing L automatically requires a specific numerical value representing δ for the correct time-averaged flow velocity profile to be met. Also, in case L is reduced by a factor of 50%, then δ is also reduced with a factor of 50%. The net effect is that since U_{slip} is reduced by 50% but occurs at two separated parallel positions instead of a single position, the net fluid flow representation will be approximately the same. However, the apparent kinetic energy dissipation rate per unit volume, assuming C_A would be independent of L, will reduce by 50%. But the latter is not the case: if the slip length L is reduced by 50%, then C_A is doubled, in order for the kinetic energy dissipation per unit volume in the split L and split δ situation to be the same as in the original L and original δ flake.

Hence, when discussing the fracture model, it is important to hold this in terms of a fully resolved turbulent boundary layer (in terms of L and δ), *i.e.* the viscous sub-layer, buffer layer, log-law region, and outer region, as well as the flow outside the turbulent wall boundary layer, must all be fully resolved zones in order to allow for a correct

computation. Furthermore, the model coefficients C_A derived for a specific L_{max} should be represented in the form of the product $C_A L_{max}$, where L_{max} is the assumed slip flow length within the viscous sublayer region, and C_A is the model coefficient for this selection of L_{max}. In sum, regardless of the resolution of L and δ, the product $C_A L_{max}$ will be numerically the same.

In order to obtain a correct time-averaged flow velocity profile, to be applied within the fracture structure, the traditional definition of a turbulent wall boundary layer is assumed, *cf.* Section 2. Also a preliminary accounting of the influence of wall surface roughness on the time-averaged flow profile is included in the analysis, *cf.* [6].

Section 2 presents a summary background on the scaling parameters used in the scientific field of single-phase turbulence to describe the turbulent wall boundary layer.

Also, an engineering example computation on turbulent air flow in a pipe section is presented, illustrating how different parameters can be computed, using a traditional engineering approach.

The same pipe geometry employed in this example is used also in Section 3, when testing the proposed model at different mean flow velocities and wall surface roughnesses. Beyond a discussion on initial results, the discussion also focuses on incorporating process thresholds and what type of errors and deviations can be expected from model-fitting a perfect web fracture structure to the experimental behaviour, when a model representation of a corresponding defect web fracture structure is not at hand.

Finally, the implications and consequences of a defect fracture structure is investigated in Section 4, where it is suggested that swirls may sometimes develop, followed by expansion, contraction or splitting.

2. Turbulent Boundary Layer
2.1 Traditional Definition
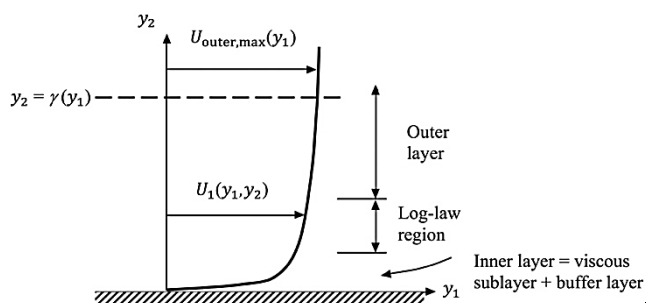The extant literature assumes the following:

Figure 1. Typical time-averaged velocity distribution in a turbulent flow near a wall, according to [5]. (Not according to scale.) [Note: separate sources may have different definitions of the inner layer and outer layer, where sometimes the log-law region is included in both of these, and where the specific log-law region serves as an "overlap region".]

Assume τ_{wall} represents the wall shear stress, $U_{outer,max}$ the velocity at the edge of the outer layer, and $\gamma_{outer,max}$ represents and boundary layer thickness (defined by the y_2 position at the edge of the outer layer).

According to [5], it can be assumed that for the inner layer, the velocity U_1 is independent of the shear layer thickness (Prandtl proposition in 1930), *i.e.* $U_1 = b(\mu, \tau_{wall}, \rho, y_2)$, where μ is the dynamic viscosity and ρ is the density of the fluid. By dimensional analysis, this can be

rephrased into the equivalent expression $U_1^+ = B(y_2^+)$, which is referred to as the "law of the wall", where $U_1^+ = U_1/U^*$ and $U^* = (\tau_{wall}/\rho)^{1/2}$. Also, $y_2^+ = y_2 U^*/\nu$, where ν is the kinematic viscosity. The measure U^* is referred to as the "friction velocity" (as it is computed in the same units as velocity), although it does not represent any real flow velocity.

According to [5], it can be assumed that the velocity U_1 in the outer layer is independent of molecular viscosity but that its deviation from $U_{outer,max}$ depends on the turbulent flow layer thickness $\gamma_{outer,max}$ (Kármán 1933), *i.e.* $U_{outer,max} - U_1 = o(\gamma_{outer,max}, \tau_{wall}, \rho, y_2)$ in the outer layer. By dimensional analysis, this can be rephrased into the equivalent expression $(U_{outer,max} - U_1)/U^* = O(y_2/\gamma_{outer,max})$ in the outer layer, which is referred to as the "velocity-defect law" for the outer layer, where U^* represents the same friction velocity as for the inner layer.

According to [5], both the law of the wall, as well as the velocity-defect law, are found to be accurate for a wide variety of experimental situations in turbulent duct and turbulent boundary layer flows.

Furthermore, according to [5] these laws must overlap smoothly in the intermediary zone, which can only be the case if the velocity in the intermediary zone varies according to $U_1^+ = C^+ + \frac{1}{\kappa}\ln y_2^+$ (demonstrated by Millikan in 1937), hence reference of this zone as the low-law region. Here, the dimensionless constants $\kappa \approx 0.41$ and $C^+ \approx 5.0$.
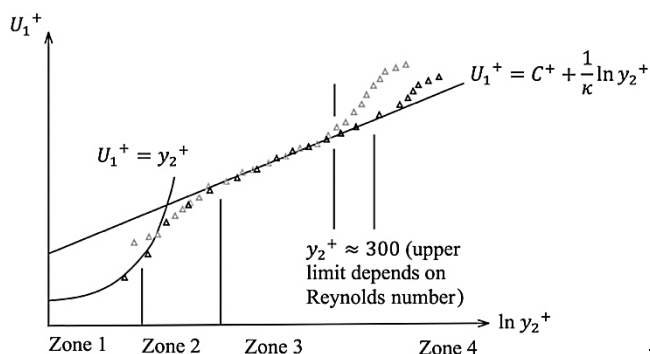
Figure 2. Time-averaged flow velocity in downstream wall direction, vs. distance from wall, across a turbulent wall boundary layer. White states that "Believe it or not, this figure, which is nothing more than a shrewd correlation of velocity profiles, is the basis for all existing "theory" of turbulent-shear flows." [5]

The following 4 zones are present inside the turbulent wall boundary layer:

Zone 1: The "viscous sublayer" – from the wall to approximately $y_2^+ \approx 8$.

Zone 2: The "buffer layer" – from approximately $y_2^+ \approx 8$ to $y_2^+ \approx 30$.

Zone 3: The "log-law region" – from approximately $y_2^+ \approx 30$ to $y_2^+ \approx 300 - 1000$.

Zone 4: The outer region – typically represents 80% of total thickness of turbulent wall layer.

An exterior zone, identified as the flow outside the turbulent wall boundary layer, can be attributed to as a fifth zone:

Zone 5: outside the outer layer, *i.e.* outside the turbulent wall boundary layer.

Table 1: Computations. The net integrated kinetic energy dissipation across a 1 m pipe, across the radius, using Eq. (18) in [6], for below flow cases, arrives at a number multiplied by $C_A L_{max}$. This number is compared to the corresponding experiments computed using Eq. (13) in [6]. The $C_A L_{max}$ coefficient is determined resulting in the net kinetic energy dissipation of the computations matching the corresponding experiments. Time-averaged mass flow rates in full agreement. Time-averaged velocity profile is in full agreement.

Re	f	τ_{wall} (N m^{-2})	ε/D	U_{mean} (m s^{-1})	$C_A L_{max}$ (m^2 s^{-2})	% of $\frac{d(KE)}{dt}$ in v. subl.	% of $\frac{d(KE)}{dt}$ in buffer r.	% of $\frac{d(KE)}{dt}$ in log-law
5000	0.03739	0.001638	0	0.5393	0.002103	60.0	36.1	3.9
5000	0.03745	0.001641	0.00005	0.5393	0.002105	60.0	36.1	3.9
5000	0.03795	0.001663	0.0005	0.5393	0.002114	59.8	36.2	3.9
5000	0.04261	0.001867	0.005	0.5393	0.002178	58.2	37.9	3.9
5000	0.07595	0.003327	0.05	0.5393	0.002695	82.8	17.2	0.0
10000	0.03088	0.005415	0	1.079	0.007380	58.2	35.9	5.9
10000	0.03096	0.005429	0.00005	1.079	0.007386	58.2	35.9	5.9
10000	0.03164	0.005549	0.0005	1.079	0.007445	58.0	36.0	6.0
10000	0.03763	0.006599	0.005	1.079	0.008109	58.0	38.8	3.2
10000	0.07380	0.01294	0.05	1.079	0.01052	82.6	17.4	0.0
100000	0.01799	0.3155	0	10.79	0.5251	54.6	34.5	8.5
100000	0.01826	0.3202	0.00005	10.79	0.5290	54.6	34.5	8.5
100000	0.02033	0.3565	0.0005	10.79	0.5587	54.7	34.8	8.4
100000	0.03131	0.5491	0.005	10.79	0.7179	56.6	38.6	4.8
100000	0.07178	1.259	0.05	10.79	1.028	82.4	17.6	0.0
1000000	0.01165	20.43	0	107.9	41.39	53.6	33.9	8.7
1000000	0.01265	22.18	0.00005	107.9	43.14	53.6	34.0	8.7
1000000	0.01721	30.18	0.0005	107.9	50.66	54.0	34.4	8.7
1000000	0.03047	53.43	0.005	107.9	71.14	56.9	38.9	4.2
1000000	0.07157	125.5	0.05	107.9	102.5	82.4	17.6	0.0

2.2 Example (Traditional Engineering Approach)

The discussion centres around Example 6.3 in [5]: Air at 20 °C flows through a 14-cm-diameter tube under "fully developed" conditions. The centreline time-averaged velocity is $U_{max} = 5$ m/s. The following computation demonstrates how Fig. 2 can be used to compute (a) the friction velocity U^*, (b) the wall shear stress τ_{wall}, and (c) the average velocity U_{mean}.

In order to compute (a), White [5] argues that the log-law relation can be assumed accurate to the centre of the tube, *i.e.* at the centre: $U_1 = U_{max}$, $y_2 = R$ and the log-law relation can be expressed as: $\frac{U_{max}}{U^*} = 5.0 + \frac{1}{0.41} \ln \frac{RU^*}{\nu}$. Since $U_{max} = 5$ m/s and $R = 0.07$ m, the friction velocity U^* is the only unknown parameter. The solution can be estimated – by trial and error – $U^* = 0.228$ m/s, according to [5], where the kinematic viscosity of air is $\nu = 1.51 \times 10^{-5}$ m^2/s from literature tables.

In order to compute (b), assuming a normal atmospheric pressure of 1 atm, gives $\rho = 1.205$ kg/m^3. Since $U^* = (\tau_{wall}/\rho)^{1/2} = 0.228$ m/s, the wall shear stress can be directly computed as $\tau_{wall} = 0.062$ Pa.

In order to compute (c), the average velocity U_{mean} can be found by integration of the log-law relation: $U_{mean} = \frac{1}{\pi R^2} \int_0^R U_1 2\pi r \, dr$, *cf.* [5]. Introducing $U_1 = U^* \left[C^+ + \frac{1}{\kappa} \ln \left(\frac{y_2 U^*}{\nu} \right) \right]$, and substituting y_2 with $R - r$, the integration can be performed. The computed result is: $U_{mean} = 0.835 U_{max} = 4.17$ m/s.

Finally, it is good to verify that the flow is really turbulent, which can be done by checking the Reynolds number Re $= U_{mean} D/\nu = 38700$. Here it is greater than 4000[1], and hence the flow is clearly turbulent [5].

Note that several results can be obtained from the velocity correlation, without need of solving any basic relations.

Finally, it is interesting to compare the shear stress of the wall in case a hypothetical laminar flow of air at would be present in the same tube, with the same average flow speed of air $U_{mean} = 4.17$ m/s: From the text following Eq. (12) in [6] the shear stress at the wall for laminar flows was computed as $\tau_{wall,laminar} = 2\mu U_{max}/R = [cf.$ Eq. (4) in [6]] $= 4\mu U_{mean}/R = 0.0043$ Pa, *i.e.* approximately 7% of the wall shear stress for the laminar flow situation as compared to the turbulent flow situation.

---

[1] The ranges of Reynolds numbers where the flow is considered to be laminar, "transitional", or turbulent depend on to what degree the flow is disturbed: In fact, vibrations of the pipe, surface roughness of inner walls (entrance region) may trigger turbulent flows to occur at lower Reynolds numbers. Furthermore, artificial disturbances, such as adding a so-called "trip wire" (which is common in turbulent laboratory experimental setups) or subjecting the pipe to a sound-shock wave, may trigger turbulent flow behavior at even lower Reynolds numbers. However, for many engineering applications the flow in a pipe can be assumed to be laminar if the relevant Reynolds number is less than approximately 2100, and turbulent if the Reynolds number is greater than approximately 4000. Between these numbers, the flow may switch between laminar and turbulent in an apparently random manner, which in the field of fluid dynamics is referred to as a transitional flow condition.
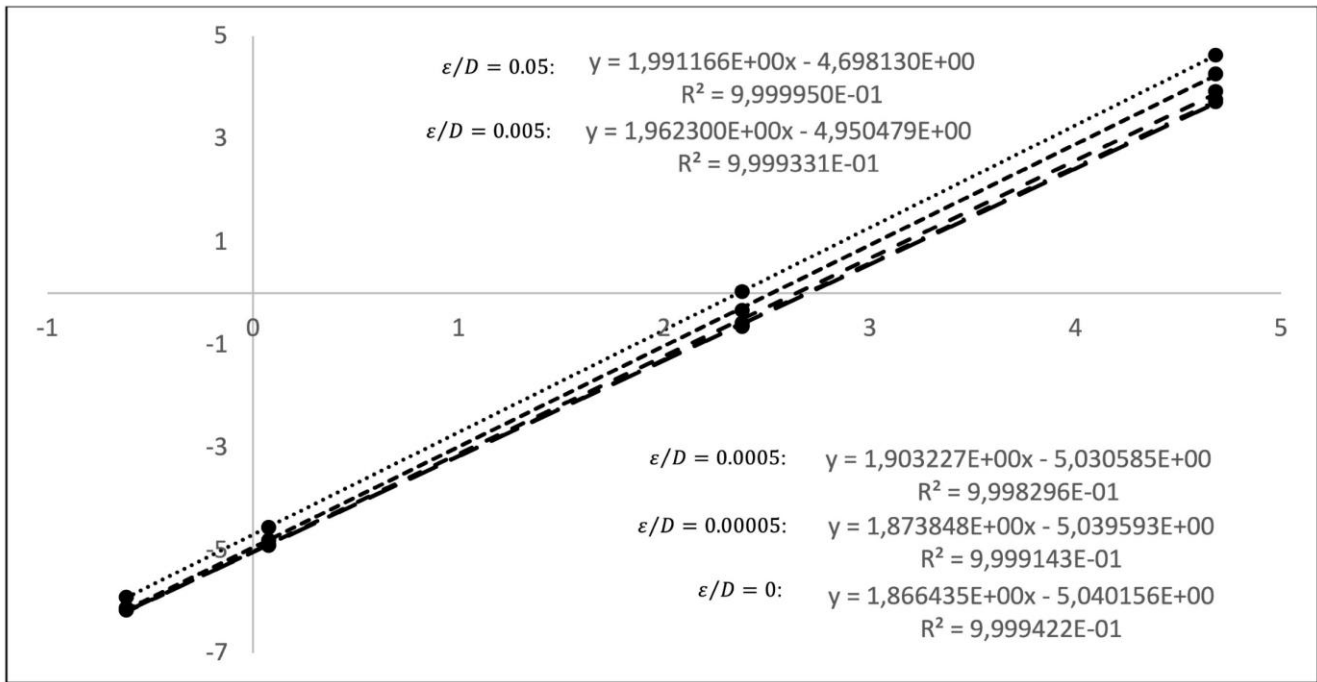
Figure 3: The x-axis is here represented by $\ln(U_{\text{mean}})$, *and the y-axis is represented by* $\ln(C_A L_{\text{max}})$.

3. Applying the Proposed Model
3.1 Computations – 20 Cases

Computations are made for the same geometry, fluid and temperature as described in Section 2.2, however at different velocities U_{mean} and different relative surface roughness ε/D, listed in Table 1 for 20 cases, together with the corresponding results. These 20 cases were selected to cover a wide range of pipe flows at subcritical velocities ($M < 1/3$). All computations assume a 1-metre-long pipe section, and where the resulting $C_A L_{\text{max}}$ value represents the value which gives 1st law agreement between experiment and the corresponding perfect fracture model computation. The Darcy friction factor f is computed from the Colebrook equation (providing 1-2% accuracy in determining f for the entire Moody diagram). The non-dimensional velocity variations U_1^{++} *vs.* y_2^{++} following the Section 2.7 and Fig. 8 in [6] are assumed, where C^{++} varies between 5.0 and 7.0 depending on surface roughness. Also, L/L_{max} following Fig. 9 in [6] is assumed, *i.e.* the variation in L/L_{max} *vs.* y_2^{++} depends on the surface roughness.

3.2 Graphical Presentation of Results

A number of statements, as well as interpretations, can now be made, looking at these results and comparing them with a Moody diagram.

First: Since the trends are rather clear in terms of mean velocity as well as relative surface roughness, interpolation can be used to estimate the $C_A L_{\text{max}}$ value, *cf.* Fig. 3. Using the proposed fracture model, and integrating radially as well as axially, the local kinetic energy dissipation (per unit volume), will result in a net kinetic energy dissipation rate approximately equal to the estimations obtained with the Colebrook equation and Eq. (13) in [6].

Second: The correlations presented in Fig. 3 appear to reflect a connection between $C_A L_{\text{max}}$ and approximately – but not exactly – the square of the mean velocity:

For relative roughness $\varepsilon/D = 0.05$:

$$C_A L_{\text{max}} = e^{-4.698130}(U_{\text{mean}})^{1.991166} \qquad (1)$$

(for $5000 < \text{Re} < 1000000$)

For relative roughness $\varepsilon/D = 0.00$:

$$C_A L_{\text{max}} = e^{-5.040156}(U_{\text{mean}})^{1.866435} \qquad (2)$$

(for $5000 < \text{Re} < 1000000$)

Third: The correlation presented in Fig. 4 indicate that while $C_A L_{\text{max}}$ shows a strong variation depending on Reynolds number, it appears that $C_A L_{\text{max}}$ varies moderately when changing the surface roughness (at a fixed Reynolds number). For instance, at Re = 5000, the difference between $C_A L_{\text{max}}$ at relative roughness $\varepsilon/D = 0.05$ and $C_A L_{\text{max}}$ at relative roughness $\varepsilon/D = 0.00$ is only a factor 1.28, and at Re = 1000000, the difference between $C_A L_{\text{max}}$ at relative roughness $\varepsilon/D = 0.05$ and $C_A L_{\text{max}}$ at relative roughness $\varepsilon/D = 0.00$ is only a factor 2.48. This relatively small variation is interesting at low Reynolds numbers, in the context of $C_A L_{\text{max}}$ as a proposed critical parameter for the transition at certain Re numbers, both in the nominal model (*cf.* Section 2.9 in [6]) and for the more advanced model (*cf.* Section 3.3). A limited variation in $C_A L_{\text{max}}$, at low Reynolds numbers, suggests a similar range in Re numbers, where transition from laminar flow to an onset of the turbulence process can occur, regardless of surface roughness.

3.3 Onset and offset of turbulence

Consider the Re numbers at which turbulence is onset, *i.e.* the mean flow velocity, if starting from a flow rate at laminar flow conditions, which is steadily increased – until turbulence onset is triggered. The typical onset condition for turbulence in pipe flows, is stated to occur at Re numbers around 2300.
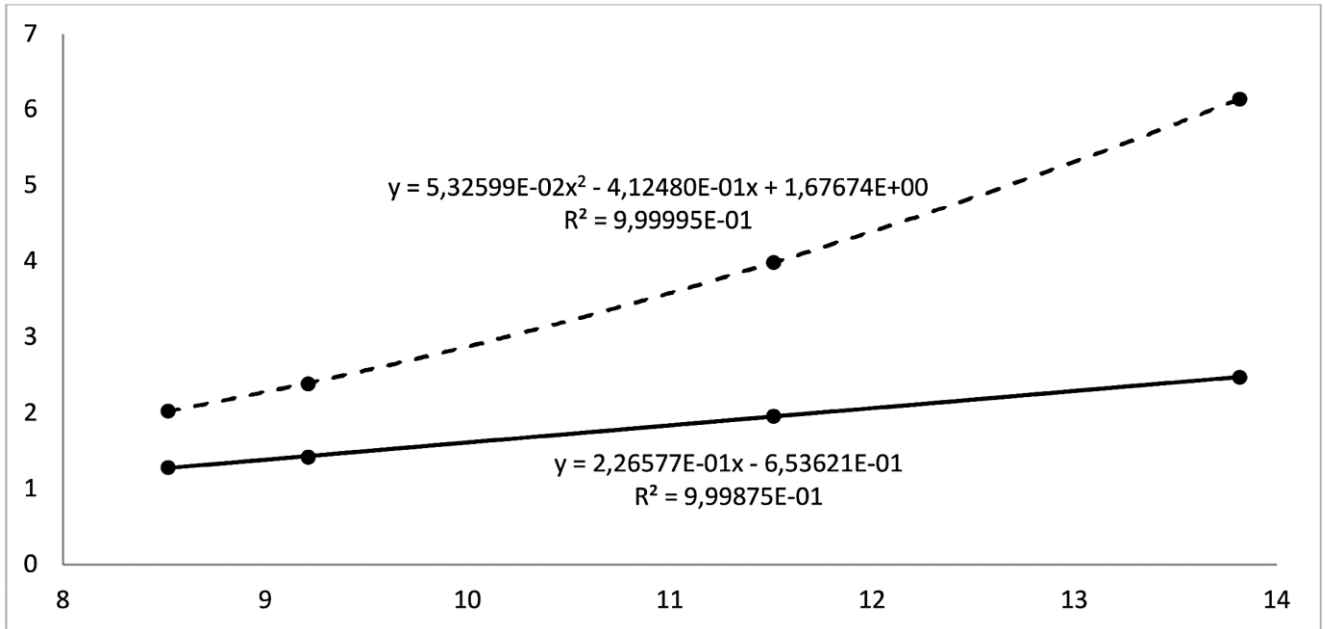
Figure 4: The x-axis represents $\ln(\text{Re})$. *The full line represents the ratio* $\{C_A L_{\max}(\varepsilon/D = 0.05)\}/\{C_A L_{\max}(\varepsilon/D = 0)\}$ – *which appears to vary linearly with* $\ln(\text{Re})$, *for the present computations. The hashed curve represents the ratio* $\left\{\frac{d(KE)}{dt}(\varepsilon/D = 0.05)\right\}/\left\{\frac{d(KE)}{dt}(\varepsilon/D = 0)\right\}$ – *which varies against* $\ln(\text{Re})$ *following a polynomial expression.*

It turns out that the Re number at which turbulence off-sets (or disappears) will be different, if running this experiment in the opposite direction, *i.e.* starting from a turbulent flow condition, and steadily decreasing the flow rate until a transition occurs (to laminar flows).

The estimation in Eq. (23a) in [6] predicts a transition Re number around 870 for $\varepsilon/D = 0$ in the case depicted in Fig. 3 (or by using Eq. (2)) – where we note that we have assumed the same relation for extrapolation outside the valid range $5000 < \text{Re} < 1000000$.

The alternative estimation in Eq. (23b) in [6] predicts a transition Re number around 975 for $\varepsilon/D = 0$ in the case depicted in Fig. 3 (or by using Eq. (2)). Also in this case, the variation of f *vs.* Re number, and variation of $C_A L_{\max}$ required extrapolations outside the valid range.

Hence, both these nominal estimations project the onset of turbulence to occur around 2.5 times lower than the experimentally obtained Re number for turbulence onset. Possibly, utilizing these two relations would however – possibly – be a good indicator for the offset Re number of turbulence.

In order to approach this apparent deviation in turbulence onset, we turn to experimental observations:

The literature provides an excellent range of descriptions on the various forms of instabilities and flow behaviours prior to the onset of the turbulence, *cf. e.g.* [1].

One of the final forms of structures that appears just prior to the onset of a turbulent wall boundary layer, a structure that the relevant literature has focused on significantly *cf. e.g.* [1], [7], [8], [9], [10], [11], is the so-called turbulent spot. Arguably, the flow appears to be laminar on one side of the spot, while turbulent on the other side. Considerable experimental work on studying turbulent spots has been made, and the reason for stating the arrowhead forward side as representing a turbulent flow is that the identical mean flow velocity variations *vs.* distance from the wall is observed inside the turbulent side of the turbulent spot, as compared to the regular variations found in a fully-developed turbulent wall boundary layer.

True, the turbulent spots behave in a strange way, as they first occur as spots – which grow in-plane in both y_1- and y_3-directions (for a flow in the y_1 direction, and where y_2 axis represents the normal direction from the wall plane spanned by the y_1-axis and y_3-axis unit vectors, *cf.* Fig. 1) when following their formation. Due to activities occurring inside a spot, the spot will span about the **total thickness** of a turbulent wall boundary layer (*i.e.* the thickness of inner + outer layers). In a pipe flow, the front arrow-head forward side of the turbulent spot will move at about 2/3 speed of U_{mean}, while the rear laminar side of the turbulent spot will move around 1/3 the speed of U_{mean}.

There are experimental observations made on the presence of "hairpin-" or "horse-shoe" vortexes on the turbulent side, near the wall, which **perhaps form an experimental indicator** of the influence the discrete web-slip structures with separated δ.

Although the real flow in a turbulent spot involves flows in all three dimensions y_1-, y_2- and y_3 (a necessity according to the equation of continuity), and while the nominal transition model **only** accounts for irreversible thermodynamic processes occurring in the y_1-direction, one might contemplate the possibilities of irreversibilities in primarily the y_2-direction (as well as some effects in the y_3-direction flow). However, the author of the present work does not believe this to be the case.

Also, looking at the theory, there appears to be no clear candidate regarding the residual thermodynamic *no process* behaviour that would provide the possible threshold behaviour – *cf.*, *e.g.* similar reasoning on the difficulties on finding a threshold behaviour for Coulomb friction (*cf.* [12]).

However, one observation that is made experimentally, considering particle trajectories when inserting small particles into and around a turbulent spot, is that the turbulent spot appears to exhibit some "suction" process of fluid flow on the laminar side.

Considering the assumed conditions 1-4 in Section 2.9 in [6], and the presence of turbulent spots – which scientists

have focused on regarding the onset of turbulence, the conditions 1-4 may need to be slightly reconsidered:

Condition 1: Assuming the transition occurs in a turbulent spot, this is strictly speaking a rather spread-out zone. Hence, in order to improve the nominal model for turbulence onset, one may need to consider conditions for the laminar *vs.* turbulent **transformation to occur at slightly different positions**.

Condition 2: Assuming equal kinetic energy dissipation conditions is probably reasonable. However, the turbulent spot itself alters the flow velocity and thus the local kinetic energy dissipation, which is relevant for this transition formula to work well. Hence, the overall U_{mean} velocity gradient cannot be used to directly compute the wall viscous dissipation – assuming no velocity interruption on the laminar flow side. Hence, it is assumed that **the laminar flow velocity gradient for the kinetic energy dissipation needs to be adjusted**.

Condition 3: Not applicable, if reconsidering the positions of transformation to occur (Condition 1).

Condition 4: Still valid. The process transition is still believed to occur in the vicinity of a solid wall.

Considering the particle trajectories in the experimental observations in Fig. 7 on p. 134 in [9], and also the experimental observations to the effect that the same turbulent flow wall behaviour is observed on the turbulent side of the turbulent spot, the computations can be adjusted according to the following: the viscous laminar kinetic energy dissipation on the laminar side can assume a – say – **50% higher laminar flow velocity gradient** (as compared to the nominal velocity gradient value), while the kinetic energy dissipation – and local flow gradient - for the turbulent side is extracted without any alternations as compared to the nominal computations in [6].

This gives for the viscous laminar side:

$$\frac{d(ke)_{viscous}}{dt} = \mu \left(\frac{1.5 \partial U_1}{\partial y_2}\right)^2 \tag{3}$$

where $\partial U_1/\partial y_2$ is computed for the laminar flow not assuming the presence of a turbulent spot.

On the turbulent side, the kinetic energy dissipation is:

$$\frac{d(ke)_{res}}{dt} = C_A \frac{\rho L}{\delta} U_{slip} \approx C_A \rho L_{max} \frac{\partial U_1}{\partial y_2} \tag{4}$$

cf. Eq. (21) in [6].

Hence, equating Eq. (3) with Eq. (4) at the onset transition point, gives:

$$2.25\mu \left(\frac{\partial U_1}{\partial y_2}\right)^2 - C_A \rho L_{max} \left(\frac{\partial U_1}{\partial y_2}\right) = 0 \tag{5}$$

Which gives a revised formula for the onset transition point according to:

$$\frac{18 U_{mean}^2}{C_A L_{max}} = \frac{\rho U_{mean} D}{\mu} = \text{Re} \tag{6}$$

For a perfectly smooth pipe wall surface with $\varepsilon/D = 0.00$, we can insert Eq. (2) in Eq. (6), which gives onset at Re=2310 for the case depicted in Fig. 3.

Note: To be clear, the author did not select "50% higher laminar flow velocity" from any data source, other than identifying a likely larger inflow velocity gradient on the laminar side of the turbulent spot compared to the situation

if the turbulent spot would not be present. The specific selection of 50% higher inflow velocity was intentionally selected in order to arrive at a matching turbulent onset Re number, as found in experiments. In any case, Eq. (6) is a **proposed improved model for the onset of turbulence**, where the influence from wall surface roughness can be accounted for.

Experimentally, if a tracing fluid is injected into a core of a pipe, one may find that the turbulence onset is associated with an apparent "burst", "flash" or "puff" which might trigger near (but just below) the transition Reynolds number. An interpretation of this suggests the quick and immediate development of a local fracture structure around and near the wall transition point. If there for some reason would not be enough kinetic energy available to maintain this onset structure the burst will quickly die out, and the flow will return to the viscous laminar flow situation.

Interestingly, the presence of "bursts" appears also to exist after turbulence boundary layer onset, *cf. e.g.* [13], which might suggest the sudden and local development of ordered web fractures within a geometric region of large defects (after turbulence onset). An interesting finding by [13] was that the intermittency of these boundary-layer bursts appears to connect with "outer" variables – which if one would allow oneself to speculate might further suggest a direct connection with the consumption of kinetic energy from the overall surroundings.

Regarding the matter of **turbulence offset**, note that there is no corresponding Re number, lower than the nominally proposed transition Re number in Eqs (23a-3) in [6], since there is no experimental evidence on the formation of turbulent spots when reducing the average velocity of a turbulent flow.

Consider the situation when the flow is reduced, and the available kinetic energy to be dissipated is reduced below a critical point: In such case, the web-fracture flow will release from the wall surface, flow downstream, and eventually die out (similarly as described in Section 2 in [6]). The flow that replaces the web structure at the original position is a viscous laminar flow.

3.4 Defect *vs.* Perfect Web-Fracture Structure

First, consider a model-fitting of a perfect web fracture structure to an experiment, which gives a net kinetic energy dissipation. This is followed by estimating the volume of defect zones, while assuming these defect zones to be suddenly present in this model-fitted perfect web structure. For this artificially-assumed defect web fracture structure, the net kinetic energy dissipation is estimated. What is the difference in net kinetic energy dissipation between these two cases?

Second, consider a model-fitting of a defect web fracture structure to an experiment – assuming a certain distribution of defect zones. How much would the model-fitted parameter $C_A L_{max}$ for the defect web fracture structure differ from the model-fitted parameter $C_A L_{max}$ if assuming a perfect web structure?

Start with estimating the first difference of interest:

Consider the locations of the defects: None would occur in the viscous sublayer region, as this is concluded experimentally: recall that "nothing happens in the viscous sublayer region" according to scientists.

Most would occur in the buffer layer, due to the presence of non-symmetry in both L and δ, followed by the log-law region (only non-symmetric in terms of δ).

The presence of a local defect means that the defect zone does not represent a zero kinetic energy dissipation, but perhaps a reduction of X% (per unit volume) compared to the corresponding perfect web fracture structure.

The volume occupied by a defect zone is difficult to estimate (due to a lack of experimental data), and it is noteworthy that not all defect zones would necessarily result in the generation of swirls or offset eddies. However, defect zones always reduce the kinetic energy dissipation rate (per unit volume).

The downstream effects of a generated swirl are a complicating factor, as discussed in Section 4: The generated swirl may offset downstream behaviour which may appear to displace locally the δ and L. However, as argued in Section 4, it would seem unrealistic that the large visible offsets in L and δ – which give large downstream fluctuations – result in very different net kinetic energy dissipations in the large-scale offset defect structures, as compared to the nominal non-offset perfect web fracture structures. The defect web fracture structure condition should be considered a thermodynamically rather stable condition, as the generation of a local defect does not trigger multiple downstream defects. The latter would locally trigger separate eddies, literally resulting in an uncontrolled explosion of events (a true thermodynamic instability condition). No: from a single defect zone, a long eddy may be generated, and it is assumed that the point of origination can be identified – also when the defect zone is flowing downstream.) Hence, it is assumed that the most important view (for net kinetic energy dissipation computations) is to solely focus on the nominal defect zones as locally-distributes zones or clouds within the turbulent flow.

Example 1: Re = 5000, and $\varepsilon/D = 0$ for flow condition described in Table 1.

Assume that 15% of the buffer region contains defect zones, and 15% of the log-law region. (Of the 15% of the buffer region perhaps only 3% generates swirls, and of the 15% in the log-law region, perhaps only 2% generates swirls.) Assuming furthermore that the defect zones reduce the kinetic energy dissipation by 50% (a crude guess with no experimental support), the net effect on the total net kinetic energy dissipation can be estimated as:

Viscous sublayer: 60.0% of nominal net kinetic energy dissipation = no effect

Buffer layer: 36.1% of nominal net kinetic energy dissipation → reduction to: 85%*100% + 15%*50%=92.5% of nominal → reduction to 36.1%*0.925 = 33.4%

Log-law region: 3.9% of nominal net kinetic energy dissipation → reduction to: 85%*100% + 15%*50%=92.5% of nominal → reduction to 3.9%*0.925=3.6%

Hence: A reduction in net kinetic energy dissipation = approximately equal to difference in net kinetic energy dissipation between defect web fracture and perfect web fracture: from 100% to 60.0%+33.4%+3.6%=97.0%, *i.e.* a **difference of around 3%.**

Example 2: Re = 1000000, and $\varepsilon/D = 0.05$ for flow condition described in Table 1:

Assume that 15% of the buffer layer contains defect zones (of the 15% of the buffer layers perhaps only 3% generate swirls, and of the 15% in the log-law region, perhaps only 2% generate swirls.) The log-law region does not seem to pertain for this flow case, as there are no time-average flow gradients in the core zone from the centreline position in the pipe, all the way to the buffer region. Assuming that the defect zones reduce the kinetic energy

dissipation by 50% (a crude guess with no experimental support), the net effect on the total net kinetic energy dissipation can be estimated as:

Viscous sublayer: 82.4% of nominal net kinetic energy dissipation = no effect

Buffer layer: 17.6% of nominal net kinetic energy dissipation → reduction to: 85%*100% + 15%*50%=92.5% of nominal → reduction to 17.6%*0.925 = 16.3%.

Hence: A reduction in net kinetic energy dissipation = approximately equal to difference in net kinetic energy dissipation between defect web fracture and perfect web fracture: from 100% to 82.4%+16.3%=98.7%, *i.e.* a **difference of around 1%.**

Regarding the second difference of interest, a model fitting of a hypothetically defect fracture structure to turbulence pipe experiments would arrive at precisely the same wall shear stresses as fitted for the perfect web fracture structure (*i.e.* the same 1st law balance agreement between experiment and corresponding defect fracture computation can be obtained); yet the difference in the resulting $C_A L_{\max}$ for these two cases – perfect web *vs.* defect web – is likely rather small (likely within the 1-3% range).

3.5 Defect Web-Fracture Structure on General Trends

Consider the computed trends in Fig. 3. Is there anything suggesting that these trends may connect, somehow, with any defect web fracture structure?

A partial answer may be obtained by reformulating this question: Explain the variations of $C_A L_{\max}$ proportional to $U_{\text{mean}}^{1.87}$ to $U_{\text{mean}}^{1.99}$, and also explain what would it take utilize the proposed model to reach a theoretical variation of $C_A L_{\max}$ proportional to U_{mean}^2 ?

Considering the proposed fundamental model, it appears that for high Re numbers, and also for high ε/D numbers, the variation of $C_A L_{\max}$ approaches being proportional to U_{mean}^2, however, it does not fully reach this variation.

Considering the fundamental model:

$$\frac{d(\text{ke})_{\text{res}}}{dt} = C_A \frac{\rho L}{\delta} U_{\text{slip}} \tag{7}$$

and hypothetically assume that <u>only</u> the viscous sublayer dissipates kinetic energy. As the viscous sublayer zone is very close to the wall (and relatively thin in terms of the entire pipe diameter, although rather thick in terms of y_2^{++} number), this would resemble a situation similar to that of a solid plug which moves at velocity U_{mean} and with a $C_A L_{\max}$ that correlates with U_{mean}^2.

Hence, it appears that it is not the defect fracture structure that hinders $C_A L_{\max}$ from being proportional to U_{mean}^2. Instead, it seems that the distribution of kinetic energy dissipation across the pipe has variations mostly due to variations in velocity at different pipe radii – preventing all kinetic energy dissipation from occurring near the solid wall.

In sum, it appears that defects in the fracture structure would not have any major influence on the trends in Fig. 3.

3.6 Scaling Laws in Context of Proposed Model

It is not immediately obvious whether dimensional analysis applies to situations involving discrete relations. Apparently, some kind of linear relationship may be required with intersection at 0 in order to allow for a dimensional analysis. On this matter, note that the approximations of assumed connection between slip velocity and slip length, *cf.*

Eq. (14) in [6], as well as the assumption $\tau \propto U_{\text{slip}}$ in [6], both represent linear relationships with intersection at 0.

Even though possible offsets from linearity, as well as offsets from intersections at 0, may occur for defect web fractures, it is reasonable to assume that such offsets would not occur for the saturated flakes in the viscous sublayer.

In most of computations in Table 1, the kinetic energy dissipation in the outer layer is 0, or comparatively negligible. For a couple of computations, the kinetic energy dissipation in the outer layer accounts to a maximum around 4% of the total kinetic energy dissipation.

In the derivation of the "velocity-defect law" for the outer layer by dimensional analysis, described in Section 2.1, it is assumed that the mean velocity U_1 is independent of molecular viscosity. This statement is arguably similar to assuming that no viscous dissipation is occurring in the outer layer, or more generally, that no kinetic energy dissipation is occurring in the outer layer. This is in line with present theory and present computations. Hence, the traditional scaling correlations proposed in Section 2.1 for the outer region should arguably also apply for present computations.

On the matter of inner-layer velocity, if molecular viscosity does not play a role in the velocity variation in the viscous sublayer – according to the proposed new theory – arguably one should be able to make similar assumptions regarding the scaling of the viscous sublayer as for the outer region:

$$U_1 = o_{\text{vs}}\big(\gamma_{\text{viscous sublayer, max}}, \tau_{\text{wall}}, \rho, y_2\big) \qquad (8)$$

allows for the derivation of the expression $U_1{}^+ = C_{\text{vs}} y_2{}^+$, where we have utilized the observation from the viscous sublayer that $L = L_{\text{max}}$ and $\delta = \delta_{\text{min}}$ are equal for neighbouring flakes in the y_2-direction.

For the buffer layer, a corresponding scaling as for the outer region is called for:

$$U_1 = o_{\text{bl}}\big(\gamma_{\text{buffer layer, max}}, \tau_{\text{wall}}, \rho, y_2\big). \qquad (9)$$

This gives:

$$U_1{}^+ = O_{\text{bl}}\left(y_2{}^+ / y_2{}^+{}_{\text{buffer layer, max}}\right) = O_{\text{bl,2}}(y_2{}^+) = B(y_2{}^+), \qquad (10)$$

i.e. an identical "law of the wall" is obtained for the buffer layer, but derived from a different perspective, and utilizing different original assumptions.

In sum, the same scaling parameters as the original ones employed in the traditional theories dating back to the 1930's can be employed with present theories.

The traditional theory assumption $C_{\text{vs}} = 1$ for the viscous sublayer come from the traditional fundamental model assumption between shear stress and strain rate, *cf.* Section 5, and is hence not connected with any scaling law.

The present theory opens up the possibility that $C_{\text{vs}} \neq 1$. In fact, one would expect a different value from 1, in the context of present theory. (Possibly, if δ resolution can be observed in the viscous sublayer, the velocity profile may appear to be similar to a "stair-case" variation with y_2.)

Note: The computations in Table 1 all assume $C_{\text{vs}} = 1$ in the viscous sublayer for the computation of the velocity variation with y_2. There is at present no suggestion of a better value to use. Even with a different coefficient value, equally-good and equally-stable general correlations as obtained in computations in Section 3.1 can be assumed.

4. Generation of Swirls with Proposed Model

The numerical simulation of swirls and eddies has proven difficult when employing traditional turbulence theory. It appears difficult to find any significantly increased kinetic energy dissipation in these simulation results. The inability to find the levels of kinetic energy dissipation (or viscous dissipation) anywhere close to the levels observed in experiments is a major problem.

The new theory here proposed completely alters the need for studying the generation of swirls and eddies: For the purpose of finding out where the overall kinetic energy dissipation occurs in a turbulent wall boundary layer, the results with the present theory have provided clear answers – swirls and eddies appear to have negligible to no impact on the overall kinetic energy dissipation.

However, there may be a remaining interest in numerically simulating swirls and eddies – for instance for the study of pressure fluctuations at walls as caused by turbulence.

The following aspects may influence the generation of swirls for the new proposed model:

- Local and instantaneous conditions such as: (a) large imbalances of forces that may occur at defect zones.
- Wide, transverse span-wise processes across a wall influencing the MEP processes, or as a result of the MEP processes, such as: (b) local deficiency in kinetic energy at hand for dissipation, during redistribution, resulting in defect zones appearing. (c) following the principles of far-from-equilibrium ("order by fluctuations" principle), the downstream movement of defect zones (these can be visualized as *clouds*) may occur in a cyclical manner, *i.e.* clouds of defects generated upstream in a repeat manner (at a certain frequency), which moves downstream. In this way, long-downstream-, or large transverse span-wise coherent structures may be generated.
- History or memory effects: (d) Connecting with (c) is the proposed new theory's downstream movement of slips (the R.Th.D.p. zones) – and possibly additional leakage phenomena. A connection can be made to an earlier "history theory" described in [14]. This history theory assumes that:

"the turbulence which produces the shear at any point has its origin at the surface upstream from its present location".

Ross and Robertson's history theory was arguably designed to be applied for airfoils and diffusers where the following general assumption does not hold [14]:

"For the case of flow with zero or small pressure gradients, the flow conditions and the wall shear stress do not vary significantly in the direction of flow, and one can correlate the entire boundary layer distribution with local conditions."

In agreement with this latter statement, all computations in this paper assumed local conditions at a pipe intersection. However, the author of this paper yet believes such history and memory effects are possible to observe experimentally. Partly, the downstream movement of the slips (or R.Th.D.p. zones) will generate

apparent eddies which appear to be stretched in the direction of the fluid flow, which in turn connects with experiments on the anisotropy level of turbulence: Experiments indicate a much larger degree of observed turbulence anisotropy, as compared to the corresponding simulations, which tend to display more isotropic turbulence when modelling according to the traditional approach. Furthermore, the accumulated effect of downstream leakage will for very long (smoothly polished) narrow pipes eventually lead to turbulence to apparently disappear, *i.e.* overall turbulence behaves in a slowly evolving transient manner in agreement with experimental observations [17], [18], [19].

In this context, it is interesting to re-cite Ross and Robertson's [14] recounting of the space-history theory proposed by Schultz-Grunow [15] based on the original experiments by Jacobs [16]:

"Jacobs measured the change in the velocity profile along a smooth surface preceded by a rough surface. An analysis of these profiles yielded the shear stress distribution at several stations. As shown in Fig. 1 (in [14]), Jacobs found that the shear stress gradient in the outer portion of the boundary layer retained the value which it had had over the rough surface for a considerable distance along the smooth surface, while the wall shear fell almost immediately to its smoothest-surface value. Jacobs also studied the flow from a smooth to a rough surface, and he again found that the upstream shear stress gradient persisted for a considerable distance, the rough-surface shear gradually being diffused across the boundary layer as the flow proceeded downstream. As noted by Schultz-Grunow, these experiments clearly establish the importance of the history of the flow."

Connected with the generation of swirls is the phenomenon of eddy growth, which here is assumed to connect with these points. In particular, the author believes that the history- or memory effects may contribute considerably to the growth of eddies.

5. Discussion

The traditional theory has issues to resolve which are partly summarized in Table 1 in [6]. In the review paper by George [4], these issues are further discussed.

George states that (A) "Over the past decade **almost every aspect of our traditional beliefs about wall-bounded flows has been challenged**." Furthermore, George states that "No matter whether we pay our allegiance to the traditional ideas or the new ones, **the continuing difficulties** with computations of complex wall-bounded flows (or even simple flows with pressure gradients) **suggest strongly that we have missed something important**." [4]

Considering the gradual improvements in experiments, and supporting CFD computations, George furthermore states that (B): "So confident was the turbulence community in its beliefs that **virtually no one even bothered to measure the skin friction**, and it was simply inferred from fitting the log profile to a few points near the wall, usually for values of y+ between 30 and 100. In fact the 'log'-based ideas were so well-accepted that it seemed to bother only a few that **real shear stress measurements** (both momentum integral and direct) **differed consistently and repeatably from these inferred results**." [4]

On the matter of options to take to resolve the issues, George states that (C): "**Instead of causing a re-examination of the theory**, it became common wisdom that there was something wrong with these techniques. The careful drag and mean velocity measurements laboriously performed in the 30's and 40's were discarded as being in error." [4]

In contrast, *the present work focuses on re-examining the theory utilizing a fundamentally different discrete process*, which allows for the time-averaged velocity profile to be accurately reproduced, and in addition allows for the 1st law balance of the simulations to match the corresponding 1st law balance of the experiments – for several different pipe flows.

It should be noted that many experimental tools are designed assuming the Navier-Stokes relations for laminar flows to be valid. Caution on which reference experiments to select in the present case is warranted.

The very "careful … mean velocity measurements laboriously performed in the 1930's and 1940's", are the basis of the computations in this paper, as this reference data represents experimental data obtained using experimental tools **not requiring the validity of the viscous laminar flow correlation between shear stress and strain rate**.

Although some experiments appear questionable, the author recommends not discarding any experiments outright. If experiments can be reinterpreted, assuming a new theory as basis, they may provide valuable additional insight.

One major problem within this field, however, is that while the literature provides a large amount of descriptive information on experimental observations in different zones, little or no information is provided to the reader on the importance of these different observations.

Connecting to this topic, George states that "the most attention-getting aspect of this debate has been about the validity of the log law or the power law alternative. Even those who still hold the classical views have been left in the uncomfortable position that **their 'universal' constants appear to be time-dependent, and vary from one experiment to the next**. But the new ideas have not been without their problems either. Some seem to work and be definitive, but other consequences of the same assumptions are less successful. To the casually interested on-looker and devoted researcher alike, the entire field appears to be in chaos." [4]

According to the new theory here proposed, the instability in the recorded log-law data and model constants, when looking more closely, are that *these experimental recordings all appear to be performed in large geometrical regions where the net kinetic energy dissipation is rather small* – perhaps 5% of net kinetic energy dissipation occurs in the log-law region according to present new model, a log-law region which practically spans most of the cross-section of a pipe. **Arguably, these instabilities connect directly with the very low kinetic energy dissipation rates per unit volume and are arguably to be considered as *secondary* phenomena.** Secondary phenomena are always much less stable to record in experiments, as compared to *primary* phenomena. It comes at no surprise to the author of the present work, that results obtained in measurements in the log-law region are rather unstable and vary from measurement to measurement.

This vexing problem with instabilities not only relates to experimental situations, but also to the here-proposed new theory. For instance:

- It is clearly more difficult to analyse accurately what occurs in zones of low rates of kinetic energy dissipation: For instance, the length L within the log-law region assumed to be around 1/6 of L_{max} in the viscous sub-layer region, appears speculative (see assumption in [6]).
- The assumption on the amount and range of the defect regions within the buffer zone and log-law region in Examples 1-2 in Section 3.4 appears speculative.
- The suggestions in Section 4 on how swirls may trigger, grow, and move into other zones and downstream behaviour, also appears to have small influence on the net kinetic energy dissipation rate and hence is admittedly speculative.

Despite these speculations and observed instabilities, secondary issues are here believed not to have very much influence on the stable results obtained in Table 1, and Figs. 3-4.

One aspect of the physics of the proposed new model, which is challenging to treat in a thermodynamic analysis, is the leakage of growing slips (and associated eddies) downstream.

In addition, the MEP process could mend defect zones utilizing the upstream-leaked slips (and associated eddies) – while the net kinetic energy dissipation across the cross-section of the pipe will slowly increase downstream.

These phenomena may suggest an overall slowly evolving transient behaviour of turbulence.

The experiments by [18] presents a situation of onset turbulence, which in long (smoothly polished) narrow pipes far downstream (from upstream-leaked slips) may reach a state in which the apparent turbulent behaviour ceases to exist – and instead form an apparent laminar flow situation.

In the context of present theory, perhaps one possible explanation of this transition from turbulence to a laminar flow situation indicates the accumulated effects of downstream mending – albeit the experiments performed by [18] showing a slowly evolving transient behavior would in turn indicate a rather small rate of mending to occur. Also, possibly, the mending might only occur in regions with relatively high kinetic energy dissipation rates.

It is of key interest to search for traces within experimental flow which may connect with the new proposed theory.

Regarding an MEP process, the author of the present work envisions a rather limited number of web fractures in the y_1-, y_2- and y_3-directions. Experimentally, there may be traces of behaviour in the rim of the turbulent side of a turbulent spot, where the presence of hair-pin vortexes might suggest a layered structure in the following downstream flow, possibly indicating a δ resolution within the viscous sublayer zone.

Also, consider the streamwise long streaks which "refer to narrow strips of low-momentum coherent motions extending lengthwise in the streamwise direction" [20] that exist within the viscous sublayer zone, an example of which is depicted in Fig. 23-8 (p. 717) in [1]. The spanwise (y_3-direction) gap between these are around 100-140 wall units. Could the presence of these streaks and the gap between them indicate an estimation of the length K of the flakes?

(Perhaps the flakes are not perfectly in alignment with each other in the y_3-direction, while the possible differences in local y_2-direction flow – conceivably due to leakage or other fluctuation – could result in some vortex generation resulting in these streaks.) This is admittedly speculation. However, experimentally it appears that the same gap exists between these streaks all the way up the through the buffer- and log-law regions according to [20].

Also of speculative interest is the experimental observation of these streamwise streaks with equal gap width. They appear to have a length which is much longer in the viscous sublayer as compared to the corresponding length in the log-law region [20]. Again, this triggers additional speculation as to whether there may be a connection between the lengths of these long streaks and the parameter L, which varies similarly from the viscous sublayer region up through the buffer- and log-law region.

For future work, it would be of interest to estimate a minimum δ within the viscous sublayer. What key parameters would control this thickness, and what is the kinetic energy dissipation "saturation" level? Is there a connection to kinetic theory of gases and mean-free paths?

Finally, to comment on the arguably most important zone, namely the viscous sub-layer, the author has utilized the best-available knowledge on the velocity profile across this layer, which in turn is based on the original scaling laws and experimental results dating back to the 1930's. A peculiarity that needs addressing is one of possible inconsistency:

The law of the wall for the viscous sublayer region states a relationship $U_1{}^+ = y_2{}^+$ to be approximately valid. What this relationship really presents is a reformulation of the correlation between shear stress and strain rate: $U_1/U^* = y_2 U^*/\nu$, or $U_1 = y_2(U^*)^2/\nu$, or $U_1 = y_2\tau/\mu$, which gives upon differentiation with y_2: $\mu(\partial U_1/\partial y_2) = \tau$, which in turn is the well-known fundamental model valid for viscous laminar flows.

According to Section 3.6, a different slope might be present – however with an approximately constant velocity gradient throughout this viscous sublayer region.

However, arguably **the rather fair results on the turbulence onset and present at-face agreement would suggest that the velocity slope in the viscous sublayer is not too different from the original assumptions made in the 1930s.**[2] Also, it is difficult to challenge the carefully performed mean-flow velocity experiments, although the literature has presented the viscous sublayer thickness in rather approximative numbers: Indeed, if the velocity recorded accurately in the interface between viscous sublayer and buffer layer, and the distance to the wall is accurately recorded, then a result close to $U_1{}^+ = y_2{}^+$ throughout the viscous sublayer region would be difficult to contest.

It is interesting to observe scientists recently placing more attention on experimentally recording the velocity profile across the viscous sublayer zone, *cf. e.g.* [21].

The renewed recent experimental focus on the viscous sublayer is very welcome, in the context of present work, where this zone is arguably the most important zone as

---

[2] Several physical reasons may contribute to the apparent finding $C_{vs} \approx 1$. For instance: (a) Between the flakes in the non-slip interfaces, one may assume fluid to exist, possibly with a no-slip line-wise contact with a solid wall. (b) The

proposed residual slip-flow processes do not significantly change the local density of the fluid.

regards to net kinetic energy dissipation and contribution to the skin friction.

6 Conclusions

On the matter of turbulence onset and offset, it was demonstrated here how the nominal model in [6] can be adjusted to obtain more realistic transition Re numbers for pipe flow while accounting for the surface roughness. As the nominal model of [6] indicated a transition point at Re numbers around 870-975, it was demonstrated that an approximately 50% higher flow gradient assumed on the laminar flow side – as a result of a suction process in a turbulent spot – appears to improve the estimated onset transition Re number (to around Re=2300).

In sum, the present results combine the remarkably high kinetic energy dissipation rate occurring in the viscous sublayer, with onsets predicted (based on the conditions inside the viscous sublayer) at Re numbers in fair agreement with experiments using a nominal transition model, and at Re numbers in close agreement with experiments using a slightly adjusted transition model. The remarkably high kinetic energy dissipation concentrated near- and in the vicinity of the wall implies that little or almost no effects on the net kinetic energy dissipation as a result of the large-scale turbulent eddy motion can be found – and hence the need to adopt computationally-intense flow solvers can be questioned.

On the matter of adopting the present new theory in CFD flow solvers, the findings made here amount to good news for the modeller concerned with turbulent skin friction computations, on the prospect of working generally with a perfect web fracture structure. The modeller no longer has to worry too much about the differences between the defect web and the perfect web, or the transient simulation of eddies.

However, for the study of mixing, boundary-layer thickness, or wall-pressure fluctuations, it can be noted that the discrete framework of residual thermodynamics [12] allows for the utilizing of "apparent material properties", *i.e.* a corresponding continuum model formulation derived from a discrete process formulation, which implies possibilities to adapt the present theory to a CFD flow solver.

Nomenclature

b, B	functions used in dimensionless scaling
c	speed of sound in fluid (m s^{-1})
C^+, C^{++}	log-law intercept on U^+- or U^{++}-axis, respectively (-)
C_A	model constant (m s^{-2})
C_{vs}	model constant (-)
D	diameter of pipe interior (m)
K	width of flake (in y_3-direction) (m)
$\frac{d(KE)}{dt}$	total kinetic energy dissipation rate (W)
$\frac{d(ke)_{res}}{dt}$	kinetic energy dissipation rate per unit volume, due to residual process (W m^{-3})
$\frac{d(ke)_{viscous}}{dt}$	viscous dissipation rate for viscous laminar flows of Newtonian fluids, per unit volume (W m^{-3})
$\frac{d(ke)}{dt}$	kinetic energy dissipation rate per unit volume (W m^{-3})
f	Darcy friction factor (-)
L	slip length of flake fracture (m)
M	Mach number, where $M = U_{mean}/c$ in pipe flow computations (-)
o, O	functions used in dimensionless scaling
R	radius of pipe interior (m)
r	radial distance from centerline (m)
Re	Reynolds number (-)
U	Velocity (m s^{-1})
U_i	Cartesian component i of velocity vector (m s^{-1})
U_{max}	Maximum velocity (m s^{-1})
U_{mean}	Mean (average) velocity (m s^{-1})
U_{slip}	slip velocity (m s^{-1})
U^*	Friction velocity (m s^{-1})
y_1, y_2, y_3	Cartesian co-ordinates (m)

Greek letters

γ	boundary layer thickness (m)
δ	gap width between slip layers, also referred to as thickness of flake fracture, or resolution parameter (m)
ε	surface roughness (m)
κ	von Kármán constant (−)
μ	dynamic viscosity of Newtonian fluid (kg m^{-1} s^{-1})
ν	kinematic viscosity of the Newtonian fluid (m^2 s^{-1})
ρ	density (kg m^{-3})
τ	shear stress (N m^{-2})

Subscripts

bl	for buffer layer
max	maximum
min	minimum
outer,max	referring to position at edge of outer layer
res	for residual process
vs	for viscous sublayer
wall	wall position

Special notations

$\frac{d}{dt}$	time derivative (s^{-1})
$(\cdot)^+$	dimensionless scaling for fixed log-law intercept C^+, with fixed range in y_2^+ for viscous sublayer, buffer layer and log-law regions (*cf.* Fig. 2) (traditional scaling).
$(\cdot)^{++}$	dimensionless scaling for a variable log-law intercept, with variable range in y_2^+ for viscous sublayer, buffer layer and log-law regions (*cf.* Fig. 8 in [6]) – depending on the wall surface roughness.

References:

[1] R.L. Panton, *Incompressible Flow*, John Wiley & Sons, New York, USA, 1984.

[2] H. Tennekes, J.L. Lumley, *A First Course in Turbulence*, MIT Press, 1972.

[3] C. Liu, P. Lu, L. Chen, Y. Yan, "New Theories on Boundary Layer Transition and Turbulence Formation", *Modelling and Simulation in Engineering*, Article ID 619419, 2012.

[4] W.K. George, "Recent Advancements Toward the Understanding of Turbulent Boundary Layers", *American Institute of Aeronautics and Astronautics* Paper AIAA-2005-4669.

[5] F.M. White, *Fluid Mechanics*, 2nd Ed., McGraw-Hill Book Company, 1986.

[6] M. Gustavsson, "A Residual Thermodynamic Analysis of Turbulence – Part 1: Theory", *submitted for publication*.

[7] H.W. Emmons, "The laminar-turbulent transition in a boundary layer – Part I", *J. Aero. Sci.* 18, 490–498, 1951.

[8] H.W. Emmons, A.E. Bryson, "The laminar-turbulent transition in a boundary layer (Part II)", *Proc. 1st US Natl. Cong. Appl. Mech.*, 859–868, 1952.

[9] S.H. Davis, J.L. Lumley (eds.), *Frontiers in Fluid Mechanics: A Collection of Research Papers Written in Commemoration of the 65th Birthday of Stanley Corrsin,* Springer Verlag, 1985.

[10] P. Jonáš, "On the Turbulent Spot and Calmed Region", Engineering Mechanics 2007, National Conference with International Participation, Svratka, Czech Republic, May 14-17, 2007.

[11] K. Sreenivasan, P.A. Davidson, Y. Kaneda, K. Moffatt, *A Voyage Through Turbulence*, Cambridge University Press, 2011.

[12] M. Gustavsson, ''Residual Thermodynamics: A Framework for Analysis of Non-Linear Irreversible Processes'', *Int. J. Thermodynamics*, *15*, 69–82, 2012.

[13] K. Narahari Rao, R. Narasimha, M.A. Badri Narayanan, "The 'Bursting' Phenomenon in A Turbulent Boundary Layer", *J. Fluid Mech. 48,* 339-352, 1971.

[14] D. Ross, J.M. Robertson, "Shear Stress in a Turbulent Bounday Layer", *J. Appl. Phys.* 21, 557-561, 1950.

[15] F. Schultz-Grunow, "Über das Nachwirken der Turbulenz bei Örtlich und Zeitlich Verzögerter Grenzschichtströmung", *Proc. 5th Int. Cong. Appl. Mech.,* Cambridge, Massachusetts, 428-435, 1938.

[16] W. Jacobs, *Zeit. f. angew. Math. u. Mech.* 19, 1939. Translated in NACA Tech. Memo 951 (1940).

[17] D. Lathrop, "Turbulence Lost in Transience", *Nature* 443**,** 36–37, 2006.

[18] B. Hof, J. Westerweel, T.M. Schneider, B. Eckhardt, "Finite Lifetime of Turbulence in Shear Flows", *Nature* 443, 59–62, 2006.

[19] D. Vergano, "Turbulence theory gets a bit choppy", *USA Today*, September 10, 2006.

[20] W. Wang, C. Pan, J. Wang, "Wall-Normal Variation of Spanwise Streak Spacing in Turbulent Boundary Layer With Low-to-Moderate Reynolds Number", *Entropy* 21, p. 24-, 2019

[21] J. K. Abrantes, "Holographic Particle Image Velocimetry for Wall Turbulence Measurements", Ph.D. thesis, Ecole Centrale de Lille, 2012.

Computer Subroutines for Rapid Calculation of the Liquid Entropies of Ammonia/NaSCN and Ammonia/LiNO₃ Solutions

Julbin Paul NJOCK[1,3*], Simon KOUMI NGOH[2], Max NDAME NGANGUE[2], Olivier Thierry SOSSO MAYI[3], Robert NZENGWA[1]

[1]Laboratory of Energy, Materials, Modelling and Methods, Higher National Polytechnic School of Douala, University of Douala, P.O. BOX 2701, Douala, Cameroon
[2]Laboratory of Technology and Applied Sciences, University Institute of Technology of Douala, University of Douala, P.O. BOX 8698, Douala, Cameroon
[3]Laboratory of Thermal and Environment, Advanced Teacher's Training College for Technical Education of Douala, University of Douala, P.O. BOX 1872, Douala, Cameroon
E-mail: *julbinpaulnjock2@gmail.com

Abstract

This paper proposes an alternative to the calculation of the liquid entropy of ammonia/NaSCN and ammonia LiNO₃ solutions in the form of correlation equations with higher computation speed. These correlation equations were obtained by using both the least squares method for the modelling of the reference liquid entropy and a classical matrix computer solving for modeling the liquid entropy. Goodness-of-fit parameters such as sum of squares of estimation errors (*SSE*), Pearson's factor (*R-squared*), root mean square error (*RMSE*) and relative error (ε) were computed and the different results were compared with those of the digitized data. The suggested correlations showed good accuracy in estimating the liquid entropy of ammonia/NaSCN and ammonia/LiNO₃ solutions, with an average *SSE* of $1.23.10^{-4}$, *R-squared* of 0.99, *RMSE* of $2.90.10^{-3}$ and ε of 0.59 % for ammonia/LiNO₃, and *SSE* of $1.57.10^{-4}$, *R-squared* of 0.99, *RMSE* of $3.2.10^{-3}$ and ε of 0.83 % for ammonia/NaSCN. These correlations are for the temperature range from 0 to 100 °C, and are decision support tools for combined systems for waste heat recovering at very low temperature and in which the couples ammonia/NaSCN and ammonia/LiNO₃ must be used.

Keywords: Entropy; binary solutions; correlation equations; computer subroutines; thermodynamic.

1. Introduction

The thermodynamic analysis of absorption systems using the Second Law of Thermodynamic can be directly carried out by the Carnot's theory. But when the energy improvement of components within the thermodynamic system is required, it is essential to calculate the entropy values. According to Farshi *et al*. [1], it is increasingly accepted that exergy analysis provides more meaningful information when assessing the performance of energy conversion systems and for this purpose, the entropy of solutions are needed as well. This task can be easy for the case of a simple pure solution but complicated for mixing solutions [2].

A widely used methodology in the entropy calculation of binary solutions as working fluids such as ammonia/NaSCN and ammonia/LiNO₃ solutions is based on the theories presented by Gupta *et al*. [3] and Koehler *et al*. [4]. In these theories, the reference entropy is calculated from Gibbs' free energy which the calculation needs some knowledge of the chemical potentials of the refrigerant and salt in the liquid solution. In the specific case of the salt chemical potential, the evaluation of the activity coefficient from a discretized integral relation [5] or based on the Meissner's method [6] is essential. With these procedures, many researches have theoretically obtained the entropies of ammonia/NaSCN and ammonia/LiNO₃ solutions [7, 8, 1], and more recently Saheli and Yari [9] used it in the exergoeconomic assessment of two novel absorption-ejection heat pump. Nevertheless, Aphornratana and Eames [6] as well as Farshi *et al*. [2] have indicated that such procedures for calculating the entropies of ammonia/LiNO₃ and ammonia/NaSCN solutions remain long and complicated. The field of using is thus restricted to specialists in chemical engineering and limited to some in energy engineering whose studies can be based on exergy analyses of systems using such mixtures.

In recent years, numerous research initiatives related to the dynamic simulation of organic Rankine cycles (ORC) combined with absorption cycles (Pourfarzad et al. [10]) for the conversion of energy at low temperatures (T < 230 °C [11]) have been carried out. More of these studies are those which use the water/LiBr couple as working fluid (CaO et al. [12], Morais et al. [13], Jafary et al. [14], Goigo and Hazarika [15], Cimşit [16]), and whose entropy models are easily implemented in simulation software as Engineering Equation Solver (EES). The use of ammonia/LiNO3 and ammonia/NaSCN in absorption machine systems appears as an alternative to resolve the efficiency and working fluid purification problems when using water/LiBr and ammonia/water solutions as working fluids. However,

simulations of low temperature energy systems with ammonia/NaSCN or ammonia/LiNO$_3$ require entropy data when applying the Second Law. Such simulations require many thermodynamic property evaluations and therefore use very large amounts of computer process time if they use the methods proposed by Gupta *et al*. [3] or Koehler *et al*. [4]. Their implementation into computer simulation programs with low capabilities is, therefore, not always practical [17]. For this reason, simple correlations like those proposed by Gu and Gan [18] as well as Infante [19] using less process time would be helpful.

Farshi *et al*. [2], in order to overcome the weakness of Zhu's methodology in entropy calculation, provided a First and Second Law analysis of ammonia/salt absorption refrigeration systems. Over the entropy values of ammonia/NaSCN and ammonia/LiNO$_3$ generated using the method of Gupta *et al*. [3], a model in the form of a rational equation has been shown for these working fluids respectively. These equations presented a maximum error of 2 % and remain the only correlation equations indicated at the present time for the entropy calculation of ammonia/NaSCN and ammonia/LiNO$_3$ solutions. However, they have been defined for different temperature and ammonia concentration ranges; which does not already allow a comparative study of an absorption system because, as specified by Farshi *et al*. [2], the accuracy of the results will be lower and often unacceptable when the concentration values in ammonia and temperature will be taken outside the ranges for which these models were established. Apart these summary limitations, Cai *et al*. [5] also highlighted certain limitations of Farshi's [2] method in ammonia/salt solution entropy calculation. One of the limitations noted is the lack of enough accuracy in the exergy analysis of the absorption refrigeration cycle due to the neglect of the solution concentration variation from initial concentration to equilibrium concentration at corresponding surrounding temperature and pressure. Another noted limitation of Farshi's [2] method was related to the process adopted for obtaining the salt activity coefficient by integrating the Gibbs-Duhem equation from the solution concentration in liquid-solid equilibrium state to solution concentration in initial state at 0 °C. According to Cai *et al*. [5], such process did not firstly take into account the liquid-solid equilibrium state conditions for which ammonia/NaSCN and ammonia/LiNO$_3$ solutions can exhibit liquid ammonia mixtures with ammine sodium thiocyanate and liquid ammonia with ammine lithium nitrate, respectively, having different properties, and secondarily the maximum allowable generating temperature of the weak solution at the outlet of the generator according to the minimum mass concentration limit of ammonia linked to both the risk of crystallization and high viscosity of the solution.

Cai *et al*. [5] overcame weakness of Farshi's [2] method in entropy calculation by proposing an exergy analysis of a novel air-cooled non-adiabatic absorption refrigeration cycle with ammonia/NaSCN and ammonia/LiNO$_3$ refrigerant solution. The solution concentration variation from initial concentration to equilibrium concentration at corresponding surrounding temperature and pressure has been taken into account; the Debye-Hückel limiting law [20] has been utilized to obtain the salt activity coefficient in the solution at a very low salt concentration and the mass concentration has been taken at $X_{NH_3} = 0.36$ for both ammonia/NaSCN and ammonia/LiNO$_3$ solution in order to

specify the maximum allowable value of generating temperature to avoid crystallization as well as high viscosity of the solution. The entropy calculation results have been shown in the form of graphical curves. Although these graphical curves can be exploited, the entropy calculation in a computational process always remains long and complicated.

The aim of this paper is to propose an alternative solution for the liquid entropy calculation of ammonia/NaSCN and ammonia/LiNO$_3$ solutions from the simple correlations adapted to computer subroutines and giving both a fewer stages and greater computation speed. Cai's [5] graphical curves will be digitized and a database will be built. The least squares adjustment method will be applied.

2. Modelling
2.1. Mathematical Formulation

Neglecting the pressure effects and choosing the temperature of 0 °C ($T_0 = 273.15$ K) as the reference state for saturated liquid ammonia and pure solid NaSCN or LiNO$_3$, the liquid entropy $s(X_{NH_3}, T)$ at any temperature can be written as [5]:

$$s(X_{NH_3}, T) - s(X_{NH_3}, 0°C) = \int_{T_0}^{T} C_P(X_{salt}, T) \frac{dT}{T} \quad (1)$$

Where $s(X_{NH_3}, 0\,°C)$ is the reference liquid entropy, and $C_p(X_{salt}, T)$ its heat capacity as a function of the salt concentration and temperature.

In Eq. (1), the integral calculation of the second member becomes easy when the correlation of $C_p(X_{salt}, T)$ is known. But the real difficulty lies in the calculation of the reference liquid entropy $s(X_{NH_3}, 0\,°C)$. As mentioned in the introduction, the current scientific approach is based on Koehler's [4] or Gupta's [3] method which remain however long and complex, which does not make it easy to use.

In the present study, the integral form of the right-hand side of Eq. (1) was transformed into an integral form defining the heat capacity according to the ammonia concentration and temperature. To make this, a function $\aleph(X_{NH_3}, T)$ was defined to take into account the errors related to the choice of $C_p(X_{NH_3}, T)$ model and the transformation of $C_p(X_{salt}, T)$ into $C_p(X_{NH_3}, T)$. Hence, Eq. (1) is rewritten as:

$$s(X_{NH_3}, T) = s(X_{NH_3}, 0°C) + \int_{T_0}^{T} [C_P(X_{NH_3}, T) + \aleph(X_{NH_3}, T)] \frac{dT}{T} \quad (2)$$

The different correlations of the heat capacities of ammonia/NaSCN and ammonia/LiNO$_3$ solutions established by Infante [19] result from the experimental data obtained by Roberson *et al*. [21] for ammonia/LiNO$_3$ solution, and Blytas and Daniels [22] and Sargent and Beckman [23] for ammonia/NaSCN solution. In this present work, the correlation equation used for the heat capacity was defined as a function of ammonia concentration of the solution as [18, 19]:

$$C_p\left(X_{NH_3},T\right)= A_0 + A_1\left(T-T_0\right)+ A_2\left(T-T_0\right)^2 \quad (3)$$

Where,

$$A_0 = 2.4081 - 2.2814X_{NH_3} + 7.9291X_{NH_3}^2 - 3.5137X_{NH_3}^3 \quad (4)$$

$$A_1 = 10^{-1}\left(0.251 - 0.8X_{NH_3}^2 + 0.612X_{NH_3}^3\right) \quad (5)$$

$$A_2 = 10^{-3}\left(-0.1 - 0.3X_{NH_3}^2 - 0.1X_{NH_3}^3\right) \quad (6)$$

The coefficients of the equations for calculation of the constants A_0, A_1, and A_2 (Eq. 4, 5 and 6) have taken in the Refs. 18-19.

The function $\aleph\left(X_{NH_3},T\right)$ was defined under the non-nodal interpolation principle which consists to search the form of this function such as described in Eq. (7).

$$\aleph\left(X_{NH_3},T\right)= \sum_{i=0}^{n} K_i\left(T-T_0\right)^i \quad (7)$$

Where n, is the maximum number of parameters K_i, and defined according to the accuracy of the liquid entropy model sought.

The parameters K_i were defined as a function of the mass concentration of ammonia in the solution. The upper degree of the largest monomial was assumed to be 3, which corresponds to four parameters defined as follows:

$$\begin{cases} K_0 = \sum_{j=0}^{3} a_j X_{NH_3}^j \\ K_1 = \sum_{j=0}^{3} b_j X_{NH_3}^j \\ K_2 = \sum_{j=0}^{3} c_j X_{NH_3}^j \\ K_3 = \sum_{j=0}^{3} d_j X_{NH_3}^j \end{cases} \quad (8)$$

Where a_j, b_j, c_j and d_j, are the coefficients to determine. By integrating the form of the functions $C_p\left(X_{NH_3},T\right)$ and $\aleph\left(X_{NH_3},T\right)$, the liquid entropy described by Eq. (2) can therefore be written as

$$s\left(X_{NH_3},T\right)- s\left(X_{NH_3},0°C\right) = \pi_0 \ln\left(\frac{T}{T_0}\right)+ \sum_{i=1}^{n} \pi_i\left(T^i - T_0^i\right) \quad (9)$$

Where,

$$\begin{cases} \pi_0 = \sum_{j=0}^{3} \eta_j X_{NH_3}^j \\ \pi_1 = \sum_{j=0}^{3} \tau_j X_{NH_3}^j \\ . \\ . \\ . \\ \pi_n = \sum_{j=0}^{3} \chi_j X_{NH_3}^j \end{cases} \quad (10)$$

The ultimate goal is therefore to determine with good precision the various coefficients $\eta_j, \tau_j, ..., \chi_j$ in the Eq. (10). Subsequently, the liquid entropy at any temperature is obtained by associating the reference liquid entropy with the two right-hand members of Eq. (9).

2.2. Methodology
2.2.1. Curves digitizing
Cai's [5] graphical curves were digitized using the Getdata Graph Digitizer 2.26 software. This software allows you to digitize the original graphics, plots and maps, scanned in graphic formats of type TIFF or JPEG. It allows easy reorganization of points on a graph and export of data to Excel spreadsheet. Database obtained and exported to the Excel file were exported into Matlab 2015a. These database are reported in Table 1 and Table 2 for ammonia/NaSCN and ammonia/LiNO$_3$ respectively)

2.2.2. Modeling of reference liquid entropy
The least square method is a procedure which requires calculation and linear algebra to determine what the best fit line is to the data. The reference liquid entropy model can be reduced to a static model with a separable structure between spaces of descriptive quantities. In its linearized form, it is written as:

$$\hat{s}\left(X_{NH_3}(k),0°C\right)= k^T\left(X_{NH_3}(k)\right)\theta \quad (11)$$

The parameter θ is the vector of unknown parameters, k is the digitizing sequence and h^T is a vector function of the input quantity $X_{NH_3}(k)$.

Considering the sample of digitized values $\{X_{NH_3}(k), s\left(X_{NH_3}(k), 0°C\right)\}$ of the process described by Eq. (11) as being acquired, it is calculated at each sequence k the absolute error $\varepsilon(k,\theta)$ between the digitized and model values given by:

$$\varepsilon(k,\theta)= s\left(X_{NH_3}(k),0°C\right)- \left[h_1\left(X_{NH_3}(k)\right)\ h_2\left(X_{NH_3}(k)\right)\ ... \right.$$
$$\left. ...\ h_N\left(X_{NH_3}(k)\right)\right]\begin{bmatrix} \theta_1 \\ \theta_2 \\ \theta_3 \end{bmatrix} \quad (12)$$

Table 1. Digitized data of the ammonia concentration and specific entropy obtained in this work for ammonia/NaSCN pair at the different temperatures from 0 to 100 °C.

X_{NH_3}	T_0	T_{10}	T_{20}	T_{30}	T_{40}	T_{50}	T_{60}	T_{70}	T_{80}	T_{90}	T_{100}
0.3500	-0.792474	-0.706251	-0.626187	-0.539964	-0.459900	-0.373677	-0.293613	-0.219707	-0.143964	-0.073390	-0.010309
0.3994	-0.730886	-0.644663	-0.564599	-0.484535	-0.404471	-0.330565	-0.256660	-0.176596	-0.109849	-0.043110	0.025144
0.4501	-0.675457	-0.594109	-0.509685	-0.426788	-0.342883	-0.262819	-0.195072	-0.121167	-0.053420	0.017065	0.090439
0.4995	-0.620028	-0.527647	-0.445265	-0.359042	-0.268978	-0.195072	-0.115008	-0.041103	0.028644	0.101708	0.180614
0.5502	-0.564599	-0.472217	-0.376752	-0.282895	-0.188913	-0.105849	-0.023806	0.057438	0.131343	0.211408	0.297631
0.5996	-0.521488	-0.414471	-0.309977	-0.201231	-0.108849	-0.013567	0.072914	0.155979	0.248360	0.334583	0.420806
0.6490	-0.466059	-0.349042	-0.238503	-0.124247	-0.021426	0.082073	0.180614	0.279154	0.371536	0.463918	0.562458
0.6997	-0.416788	-0.287295	-0.163401	-0.041103	0.072914	0.180614	0.291472	0.402330	0.507029	0.605570	0.710269
0.7491	-0.361359	-0.219707	-0.084214	0.044821	0.168296	0.291472	0.408489	0.525506	0.642523	0.747222	0.864239
0.7998	-0.299771	-0.145802	-0.001181	0.134423	0.266837	0.396171	0.525506	0.648681	0.771857	0.895033	1.024370
0.8492	-0.232025	-0.066738	0.082733	0.223725	0.365377	0.500871	0.636364	0.771857	0.901192	1.036680	1.172180
0.8999	-0.158119	0.012165	0.168137	0.316107	0.457759	0.599411	0.741063	0.882715	1.024370	1.172180	1.313830
0.9506	-0.084214	0.090489	0.251836	0.402330	0.549982	0.685634	0.833445	0.981256	1.129070	1.283040	1.443160
1.0000	-0.004150	0.168296	0.334583	0.482394	0.630205	0.778016	0.919668	1.067480	1.227610	1.387740	1.560180

Table 2. Digitized data of the ammonia concentration and specific entropy obtained in this work for ammonia/LiNO$_3$ pair at the different temperatures from 0 to 100 °C.

X_{NH_3}	T_0	T_{10}	T_{20}	T_{30}	T_{40}	T_{50}	T_{60}	T_{70}	T_{80}	T_{90}	T_{100}
0,3500	-0,741166	-0,666387	-0,591608	-0,510597	-0,429586	-0,348576	-0,267565	-0,186555	-0,107976	-0,033610	0,037782
0,3998	-0,753629	-0,672618	-0,585376	-0,498134	-0,410892	-0,323650	-0,236407	-0,149165	-0,061815	0,018856	0,100098
0,4496	-0,747397	-0,660155	-0,567081	-0,471321	-0,379734	-0,280028	-0,192786	-0,099313	-0,009570	0,078517	0,165241
0,4994	-0,747397	-0,641460	-0,535523	-0,435818	-0,336113	-0,236407	-0,136702	-0,041228	0,052703	0,149951	0,243425
0,5505	-0,710008	-0,604071	-0,498134	-0,385965	-0,273797	-0,167860	-0,063192	0,037782	0,137488	0,237193	0,343130
0,5990	-0,653923	-0,535523	-0,423355	-0,304955	-0,192786	-0,080618	0,027435	0,134088	0,243425	0,346556	0,461530
0,6501	-0,587376	-0,460744	-0,338113	-0,217713	-0,097313	0,021191	0,137488	0,249656	0,360806	0,480225	0,598625
0,6999	-0,516829	-0,385965	-0,255102	-0,124239	0,002085	0,125025	0,249656	0,368056	0,486456	0,611088	0,735720
0,7510	-0,435818	-0,298723	-0,161628	-0,027194	0,106330	0,237193	0,361825	0,486456	0,617320	0,748183	0,879046
0,8008	-0,354807	-0,211481	-0,068155	0,073217	0,212267	0,349362	0,480225	0,611088	0,748183	0,885278	1,022370
0,8493	-0,267565	-0,118007	0,031551	0,174877	0,318204	0,455298	0,598625	0,735720	0,879046	1,022370	1,171930
0,9004	-0,180323	-0,016786	0,139256	0,290981	0,438937	0,579930	0,723257	0,872815	1,016140	1,171930	1,333950
0,9502	-0,093081	0,075172	0,237961	0,394568	0,542541	0,692099	0,841657	0,997446	1,153240	1,315260	1,483510
1,0000	-0,005839	0,174877	0,343130	0,498920	0,660941	0,822962	0,978752	1,134540	1,296560	1,471050	1,651760

For $k = 1,2,\cdots,N$ an error vector is obtained having N components $\varepsilon(1,\theta), \varepsilon(2,\theta), \cdots, \varepsilon(N,\theta)$ whose mean square $J(k,\theta)$ is equal to:

$$J(N,\theta) = \frac{1}{N}\sum_{k=1}^{N}\|\varepsilon(k,\theta)\|^2$$
$$= \frac{1}{N}\sum_{k=1}^{N}\left[s\left(X_{NH_3}(k),0°C\right) - \hat{s}\left(X_{NH_3}(k),0°C\right)\right]^2$$

(13)

The principle of the least square's method consists in solving the problem of static optimization without constraint, the functional criterion of which is given by the Eq. (14).

$$\overset{Min}{\theta}\left(J(N,\theta) = \frac{1}{N}\sum_{k=1}^{N}\|\varepsilon(k,\theta)\|^2\right)$$

(14)

The best estimated parameter $\theta^*(N)$ in the sense of the least squares is then defined by:

$$\theta^*(N) = \left[\sum_{k=1}^{N}h\left(X_{NH_3}(k)\right)h^T\left(X_{NH_3}(k)\right)\right]^{-1} \times \left[\sum_{k=1}^{N}h\left(X_{NH_3}(k)\right)s\left(X_{NH_3}(k)\right)\right]$$

(15)

Table 3. Selected data of the ammonia concentration and specific entropy after calculation for modeling of the liquid entropy difference for ammonia/NaSCN.

X_{NH_3}	T_0	T_{10}	T_{20}	T_{30}	T_{40}	T_{50}	T_{60}	T_{70}	T_{80}	T_{90}	T_{100}
0.3500	0	0.086223	0.166287	0.252510	0.332574	0.418797	0.498861	0.572767	0.648510	0.719084	0.782165
0.3994	0	0.086223	0.166287	0.246351	0.326415	0.400321	0.474226	0.554290	0.621037	0.687776	0.756030
0.4501	0	0.081348	0.165772	0.248669	0.332574	0.412638	0.480385	0.554290	0.622037	0.692522	0.765896
0.4995	0	0.092381	0.174763	0.260986	0.351050	0.424956	0.505020	0.578926	0.648672	0.721736	0.800642
0.5502	0	0.092382	0.187847	0.281704	0.375686	0.458750	0.540793	0.622037	0.695942	0.776007	0.862230
0.5996	0	0.107017	0.211511	0.320257	0.412639	0.507921	0.594402	0.677467	0.769848	0.856071	0.942294
0.6490	0	0.117017	0.227557	0.341813	0.444633	0.548132	0.646673	0.745213	0.837595	0.929977	1.028517
0.6997	0	0.129493	0.253387	0.375686	0.489702	0.597402	0.708260	0.819118	0.923817	1.022358	1.127057
0.7491	0	0.141652	0.277145	0.406180	0.529655	0.652831	0.769848	0.886865	1.003882	1.108581	1.225598
0.7998	0	0.153969	0.298590	0.434194	0.566608	0.695942	0.825277	0.948452	1.071628	1.194804	1.324141
0.8492	0	0.165287	0.314758	0.455750	0.597402	0.732896	0.868389	1.003882	1.133217	1.268705	1.404205
0.8999	0	0.170284	0.326256	0.474226	0.615878	0.757530	0.899182	1.040834	1.182489	1.330299	1.471949
0.9506	0	0.174703	0.336050	0.486544	0.634196	0.769848	0.917659	1.065470	1.213284	1.367254	1.527374
1.0000	0	0.172446	0.338733	0.486544	0.634355	0.782166	0.923818	1.071630	1.231760	1.391890	1.564330

From the database imported into Matlab 2015a, a script was first generated and next the reference liquid entropy model as a function of the mass concentration of ammonia was obtained using a subroutine of least square method. The polynomial correlation function was chosen with regard to the shape of the point cloud of the reference liquid entropy and the degree of polynomial was fixed with respect to the good fit parameters obtained after several iterations as the sum of squared estimate errors (*SSE*), Pearson's factor (*R-squared*), root mean square error (*RMSE*) and the relative error (ε). These parameters show how close each model is to the fitted values.

2.2.3. Modelling of the liquid entropy $s(X_{NH_3}, T)$

A calculation of the liquid entropy difference was performed for each temperature relative to the reference temperature at 0 °C as shown in the attached Excel file (see third and fourth tabs for ammonia/NaSCN and ammonia/LiNO₃ respectively).

The model of Eq. (8) indicates four unknown variables depending on the concentration of X_{NH_3} which justify the choice of four curves to generalize the fit (shaded X_{NH_3} values in Tables 3 and 4, respectively).

Table 4. Selected data of the ammonia concentration and specific entropy after calculation for modeling of the liquid entropy difference for ammonia/LiNO₃.

X_{NH_3}	T_0	T_{10}	T_{20}	T_{30}	T_{40}	T_{50}	T_{60}	T_{70}	T_{80}	T_{90}	T_{100}
0,3500	0	0,074779	0,149558	0,230569	0,311580	0,392590	0,473601	0,554611	0,633190	0,707556	0,778948
0,3998	0	0,081011	0,168253	0,255495	0,342737	0,429979	0,517222	0,604464	0,691814	0,772485	0,853727
0,4496	0	0,087242	0,180316	0,276076	0,367663	0,467369	0,554611	0,648085	0,737827	0,825914	0,912638
0,4994	0	0,105937	0,211874	0,311579	0,411284	0,510990	0,610695	0,706169	0,800100	0,897348	0,990822
0,5505	0	0,105937	0,211874	0,324043	0,436211	0,542148	0,646816	0,747790	0,847496	0,947201	1,053138
0,5990	0	0,118400	0,230568	0,348968	0,461137	0,573305	0,681358	0,788011	0,897348	1,000479	1,115453
0,6501	0	0,126632	0,249263	0,369663	0,490064	0,608567	0,724864	0,837032	0,948182	1,067601	1,186001
0,6999	0	0,130864	0,261727	0,392590	0,518914	0,641854	0,766485	0,884885	1,003285	1,127917	1,252549
0,7510	0	0,137095	0,274190	0,408625	0,542148	0,673011	0,797643	0,922274	1,053138	1,184001	1,314864
0,8008	0	0,143326	0,286652	0,428024	0,567074	0,704169	0,835032	0,965895	1,102990	1,240085	1,377177
0,8493	0	0,149558	0,299116	0,442442	0,585769	0,722863	0,866190	1,003285	1,146611	1,289935	1,439495
0,9004	0	0,163537	0,319579	0,471304	0,619260	0,760253	0,903580	1,053138	1,196463	1,352253	1,514273
0,9502	0	0,168253	0,331042	0,487648	0,635622	0,785180	0,934738	1,090527	1,246321	1,408341	1,576591
1,0000	0	0,180716	0,348969	0,504759	0,666780	0,828801	0,984591	1,140379	1,302399	1,476889	1,657599

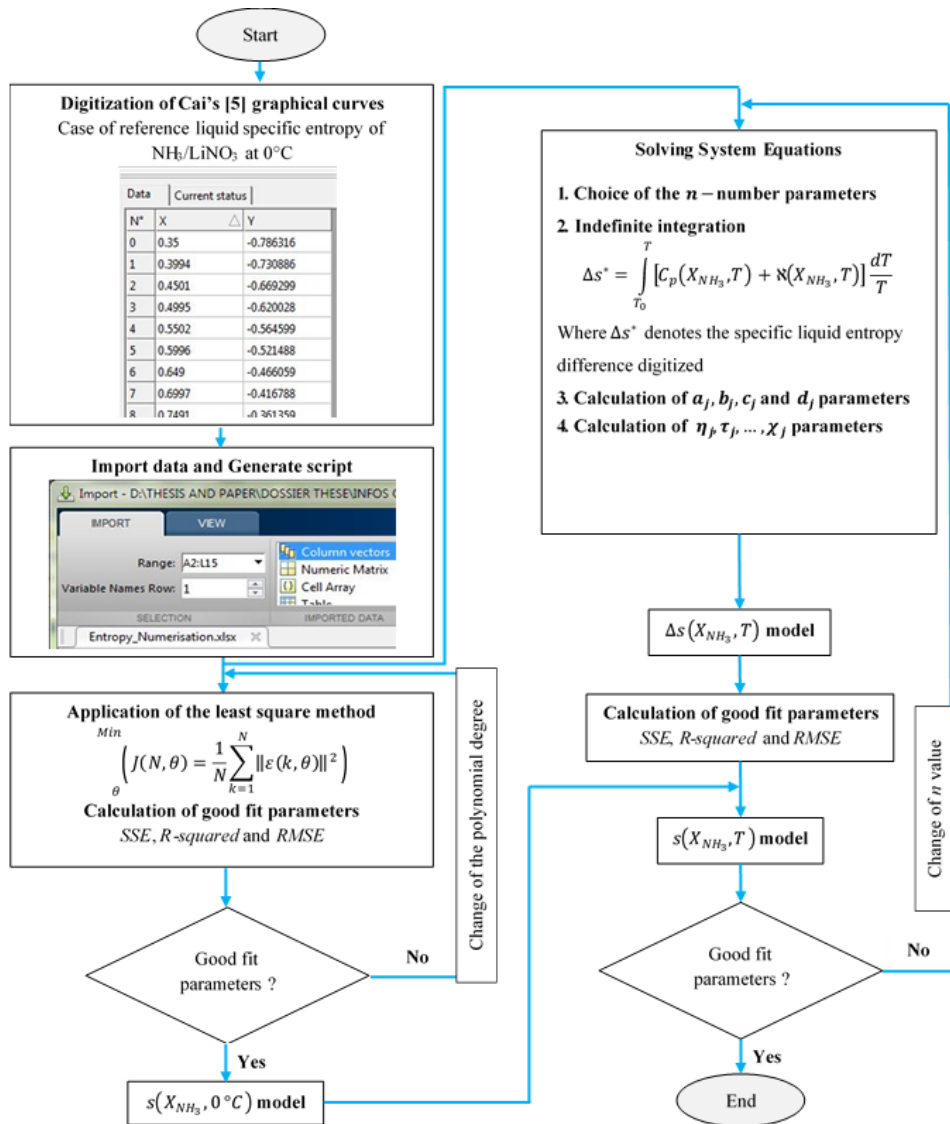**Figure 1.** *Flow chart of the methodology used in calculation of specific liquid entropies of NH₃/NaSCN and NH₃/LiNO₃ solutions at any temperature.*

Subsequently, each Cai's [5] selected curve was considered to be a one-dimensional cubic element defined in 2D in a (X_{NH_3}, s) plane (four nodes in temperature) whose fitting node coordinates for each binary pairs are shaded in Tables 3 and 4, respectively. Thus, for any (X_{NH_3}, T) pair, the explicit approach leading to the formulation of the liquid entropy difference of each binary pair is such that:

- Choice of the parameter n from the Eq. (7);
- Indefinite integration of equation Eq. (2);
- Calculation of the coefficients a_j, b_j, c_j and d_j from the Eq. (8);
- Calculation of the coefficients $\eta_j, \tau_j, \ldots, \chi_j$ from the Eq. (10);
- Calculation of the liquid entropy $s(X_{NH_3}, T)$ from the Eq. (9);
- Check of the goodness-of-fit parameters and proceeding to the following iteration $(n + 1)$ if necessary.

A computer subroutine of resolution was developed in Matlab 2015a for the rapid calculation of the parameters sought. Fig. 1 is a simplified illustration of the methodology used in the modeling of the liquid entropies of ammonia/NaSCN and ammonia/LiNO₃ solutions.

3. Results and Discussions
3.1. Reference Liquid Entropy Model

Fig. 2 shows the comparison between the reference liquid entropy curves of ammonia/NaSCN from this study with that corresponding to the digitized data from Cai *et al*. [5], for different values of the number of parameters Np into the model. As shown in Fig. 2.a, some points of the liquid entropy curve obtained in the present study remain slightly shifted from the digitized ones, despite the quality of the fitting parameters obtained.

This shift is observed when the number of parameters Np = 3 for ammonia mass concentrations between 0.35 and 0.6, and between 0.75 and 0.9. Figure 2.b shows that by increasing the number of parameters Np in the reference liquid entropy model, the fitting parameters are improved and the points of the entropy curve obtained in the present study are considerably closer to the digitized ones. However, the final choice of the number of parameters Np was conditioned by the accuracy of the final ammonia/NaSCN liquid entropy model. The best model obtained for the reference liquid entropy for ammonia/NaSCN solution is an eighth-degree polynomial function written as:

$$s\left(X_{NH_3}, 0°C\right) = \sum_{k=0}^{N} \beta_k X_{NH_3}^k \qquad (16)$$

Where β_k denotes the different coefficients found of reference liquid entropy model of ammonia/NaSCN and reported in Fig. 2.b and Table 5. A value of *SSE* of $3.28 \cdot 10^{-5}$, *R-squared* of 0.99, and *RMSE* of $1.53 \cdot 10^{-3}$ were observed for Np = 9. The maximum relative error ε of 1.65 % was observed for the mass concentration of $X_{NH_3} = 1.00$.
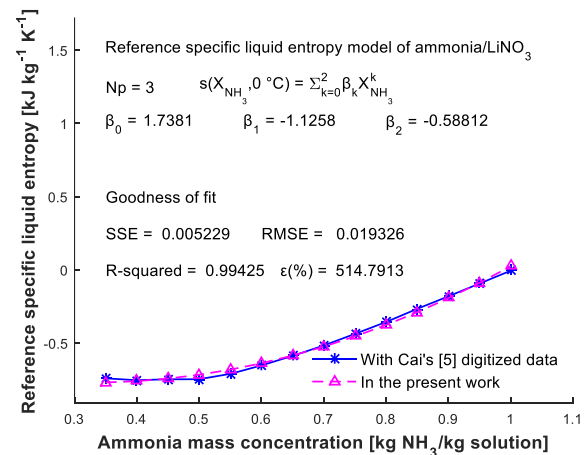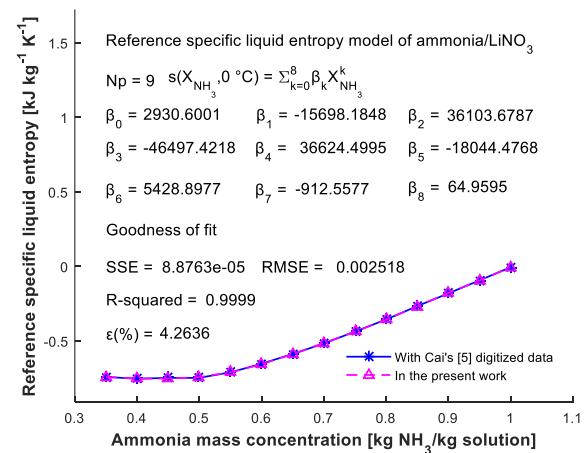
considerably closer to the digitized curve. As in the case of ammonia/NaSCN, the final choice of the number of parameters Np was conditioned by the accuracy of the final ammonia/LiNO₃ liquid entropy model. Therefore, the best model obtained for the reference liquid entropy for the ammonia/LiNO₃ solution is also an eighth-degree polynomial function as defined in equation (16).

Table 5. Coefficients of the Eq. (eq.16).

	Ammonia/NaSCN	Ammonia/LiNO₃
k	β_k	β_k
0	199.8016	2930.6001
1	−891.7618	−15698.1848
2	1633.4152	36103.6787
3	−1565.39	−46497.4218
4	814.8179	36624.4995
5	−199.1124	−18044.4768
6	−0.72722	5428.8977
7	11.6898	−912.5577
8	−2.7373	64.9595
Goodness-of-fit parameters		
SSE	3.28×10^{-5}	8.88×10^{-5}
RMSE	1.53×10^{-3}	2.52×10^{-3}
R-squared	0.99	0.99
Maximum relative error	1.65	4.26

Figure 2. Comparison of the reference specific liquid entropy of ammonia/NaSCN solution in the present work with that of the digitized data of Cai's [5] at 0 °C, for the optimal parameters Np in the model (a): Np = 3 and (b): Np = 9.

Fig. 3 shows the comparison between the reference liquid entropy curves of ammonia/LiNO₃ from this study with that corresponding to the digitized data from Cai [5], for different values of the number of parameters Np into the model. As shown in Figure 3.a, some points of the liquid entropy curve obtained in the present study for ammonia/LiNO₃ are slightly shifted with respect to the points of the digitized curve. This shift is also observed when Np = 3 for the whole range of ammonia mass concentrations except for the concentrations of 0.40, 0.65 and 0.95. Figure 3.b shows that by increasing the number of parameters Np in the reference liquid entropy model, the fitting parameters also are improved and the entropy curve of ammonia/LiNO₃ obtained in the present study are

Figure.3. Comparison of the reference specific liquid entropy of ammonia/LiNO₃ solution in the present work with that of the digitized data of Cai's [5] at 0 °C, for the optimal parameters Np in the model (a): Np = 3 and (b): Np = 9.

The β_k coefficients for the liquid entropy reference of ammonia/LiNO$_3$ are also reported in Fig. 3.b and Table 5. A value of *SSE* of $8.88.10^{-5}$, *R-squared* of 0.99 and *RMSE* of $2.52.10^{-3}$ were observed for Np = 9. The maximum relative error ε of 4.65 % was observed for the mass concentration of $X_{NH_3} = 1.00$.

The reference liquid entropy models obtained is valid for the mass concentration range of ammonia of $0.35 \leq X_{NH_3} \leq 1$. These models can be applied to interpolate the intermediate values of reference liquid entropy in the considered range of mass concentration of ammonia.

For example, at 0 °C, the reference liquid entropy of mass concentration of ammonia at 0.56 is $-0.5572 \, kJ.kg^{-1}.K^{-1}$ for ammonia/NaSCN, whereas it is $-0.7009 \, kJ.kg^{-1}.K^{-1}$ for ammonia/LiNO$_3$.

3.2. Liquid Entropy Model

The best fitting parameters for the liquid entropy are obtained for $n = 3$. Their maximum values are observed at the temperature T = 90 °C respectively, where for the ammonia/NaSCN solution, a *SSE* of $0.32.10^{-3}$, *R-squared* of 0.99 and *RMSE* of $4.7.10^{-3}$ were observed, whereas for the ammonia/LiNO$_3$ solution a *SSE* of $0.22.10^{-3}$, *R-squared* of 0.99 and *RMSE* of $2.6.10^{-3}$ were observed. The maximum relative errors are respectively observed at concentration $X_{NH_3} = 0.39$ such as for the ammonia/NaSCN solution it is 1.84 %, while for the ammonia/LiNO$_3$ solution it is 1.45 %.

The value $n = 3$ corresponds to 4 parameters $(\eta, \lambda, \tau, \chi)$ which are listed in the Table 6 for both binary fluids studied. From these coefficients, the parameters $\pi_i; i \in \{0, ..., 3\}$ in the liquid entropy can be calculated.

Finally, the liquid entropy model at any temperature was obtained by combining the reference liquid entropy with the liquid entropy difference models.

Table 6: Coefficients obtained in the present work for the calculation of specific liquid entropy parameters in Eq. (10)

	Ammonia/NaSCN			
j	η_j	λ_j	τ_j	χ_j
0	4.1608×10^3	-39.4125	0.0621	-4.3257×10^{-5}
1	-2.0869×10^4	197.5409	-0.3108	2.1642×10^{-4}
2	3.1729×10^4	-300.2053	0.4723	-3.2889×10^{-4}
3	-1.5032×10^4	142.3542	-0.2242	1.5634×10^{-4}
	Ammonia/LiNO$_3$			
j	η_j	λ_j	τ_j	χ_j
0	564.2332	-5.5382	0.0090	-6.4399×10^{-6}
1	-1.8383×10^3	18.1902	-0.0297	2.1346×10^{-5}
2	533.5661	-6.2264	0.0115	-9.1956×10^{-6}
3	828.4942	-7.1147	0.0101	-6.2051×10^{-6}

The average goodness-of-fit obtained are like, an *SSE* of $1.23.10^{-4}$, *R-squared* of 0.99, *RMSE* of $2.90.10^{-3}$ and ε of 0.59 % for ammonia/LiNO$_3$, and *SSE* of $1.57.10^{-4}$, *R-*

squared of 0.99, *RMSE* of $3.2.10^{-3}$ and ε of 0.83 % for ammonia/NaSCN.

Fig. 4 and 5 show the comparison of the entropy curves of ammonia/NaSCN and ammonia/LiNO$_3$ solutions obtained in the present work with those of the digitized data of Cai's [5], respectively. For the optimal parameters Np = 9 and n = 3, a good corroboration between the curves of this study and those obtained from the digitized Cai's [5] data is observed. This is justified with the goodness-of-fit parameters listed in Table 7 and 8, respectively for ammonia/NaSCN and ammonia/LiNO3, and related to each curve for a given temperature. These parameters show indeed that the obtained entropy models allow computing with a good approximation the values of the liquid entropies of the ammonia/NaSCN and ammonia/LiNO$_3$ solutions, respectively.
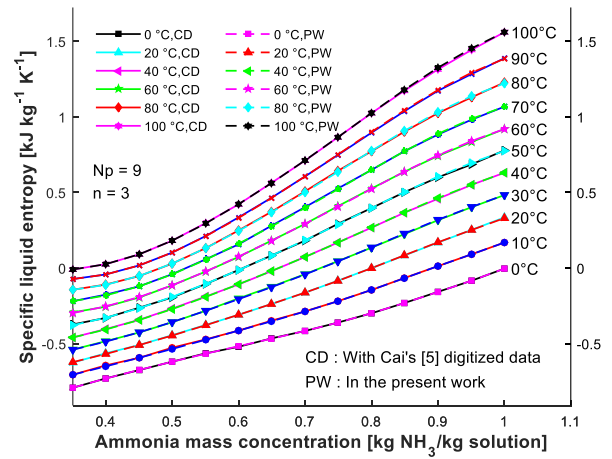

Figure. 4. Comparison of entropy curves of ammonia / NaSCN solution obtained in the present work with those of the digitized data of Cai's [5].
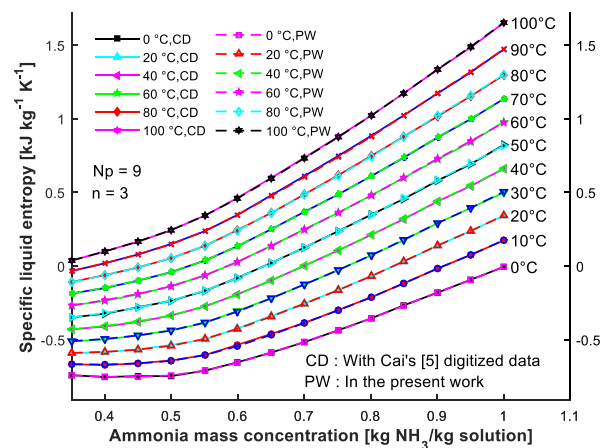

Figure 5. Comparison of entropy curves of ammonia/LiNO$_3$ solution obtained in the present work with those of the digitized data of Cai's [5].

In summary, the implementation of the algorithm realized of each model proposed uses 03 steps with 18 lines of code, in particular: (i) the declaration of the coefficients or constants of the different models, (ii) the declaration of the variables of temperature and ammonia concentration, and (iii) the development of the iterative loop for the calculation of specific entropy. The classical approach used in the literature [4, 5], would require more than 03 steps and

more than 18 lines of code for the calculation of specific entropy. This supplementary steps and lines of code would lead to more computation time compared to the approach proposed which in addition of its simplicity will allow relative gains of time.

Table 7. Goodness-of-fit parameters of the specific liquid entropy of ammonia/NaSCN.

Temperature (°C)	Ammonia/NaSCN			
	$SSE \times 10^{-3}$	$R-squared$	$RMSE \times 10^{-2}$	$\varepsilon(\%)$
0	0.03	0.99	0.15	0.36
10	0.14	0.99	0.31	0.59
20	0.07	0.99	0.22	0.86
30	0.08	0.99	0.24	1.32
40	0.06	0.99	0.21	0.88
50	0.21	0.99	0.39	1.01
60	0.12	0.99	0.30	0.95
70	0.19	0.99	0.37	1.37
80	0.32	0.99	0.47	0.88
90	0.21	0.99	0.39	0.45
100	0.29	0.99	0.45	0.44
Average	0.16	0.99	0.32	0.83

Table 8. Goodness-of-fit parameters of the specific liquid entropy of ammonia/LiNO$_3$ solutions in the present work.

Temperature (°C)	Ammonia/LiNO$_3$			
	$SSE \times 10^{-3}$	$R-squared$	$RMSE \times 10^{-2}$	$\varepsilon(\%)$
0	0.09	0.99	0.25	0.80
10	0.15	0.99	0.33	0.47
20	0.11	0.99	0.28	0.50
30	0.09	0.99	0.26	0.62
40	0.07	0.99	0.22	0.49
50	0.17	0.99	0.35	0.77
60	0.15	0.99	0.33	0.68
70	0.04	0.99	0.17	0.47
80	0.16	0.99	0.33	0.68
90	0.22	0.99	0.40	0.64
100	0.10	0.99	0.26	0.44
Average	0.12	0.99	0.29	0.59

4. Conclusion

A widely used methodology for calculating the liquid entropy of binary solutions as working fluids, such as ammonia/NaSCN and ammonia/LiNO$_3$ solutions, is based on the theories presented by Gupta and Koehler. These procedures for calculating the entropies of ammonia/LiNO$_3$ and ammonia/NaSCN solutions remain long and complicated, as some researchers have indicated. For this reason, simple correlations using less processing time would be helpful. In this paper, an alternative in the form of correlated equations with greater computation speed was proposed. The least square method was used to model the reference liquid entropy and a subroutine was used to calculate the entropy difference. The fitting parameters were calculated. The results obtained were compared with those of Cai. The correlations suggested for an optimal number of parameters Np equal to 9, showed good accuracy in estimating the entropy of ammonia/NaSCN and ammonia/LiNO$_3$ solutions with, in general, an average *SSE* of $1.23.10^{-4}$, an *R-squared* of 0.99, an *RMSE* of $2.90.10^{-3}$ and a relative error ε of 0.59 % for ammonia/LiNO$_3$, and a *SSE* of $1.57.10^{-4}$, an *R-squared* of 0.99, an *RMSE* of $3.2.10^{-3}$ and an ε of 0.83 % for ammonia/NaSCN.

The suggested correlations may be suitable for many practical situations in the simulation of thermodynamic systems using ammonia/NaSCN and ammonia/LiNO$_3$ binary solutions. Moreover, these correlations appear to be simple mathematical tools for engineers and researchers.

An additional advantage of this work is its approach that can be well applied to real background data without going through digitized data. In summary, the proposed models use 03 steps with 18 lines of code which in addition of its simplicity will allow relative gains of time compared to the classical approaches used in the literature.

Nomenclature

Ancronyms

CD	Cai's digitized data
JPEG	Joint photographic experts group
NH$_3$	Ammonia refrigerant
NaSCN	Sodium thiocyanate
LiBr	Lithium bromide
LiNO$_3$	Lithium nitrate
PW	In the present work
RMSE	Root mean square error
R − squared	Coefficient of determination or Pearson's factor
SSE	Sum of squares of estimation errors
TIFF	Tagged image file format

Symbols

A_0, A_1 and A_2	Coefficients in the calculation of the heat capacity model
a, b, c and *d*	Coefficients used to calculate the parameters of the function ψ
C_p	heat capacity ($kJ.kg^{-1}.K^{-1}$)
h	Vector function of the input quantity
J	Mean square
k	Digitization sequence
Min	Minimal function
s	Liquid entropy ($kJ.kg^{-1}.K^{-1}$)
T	Temperature (°C or K) or Transpose of *h*-vector
X	Mass concentration of ammonia (kg ammonia/kg solution)

Greek Symbols

Δ	For the liquid entropy difference
β	Coefficients in the calculation of the reference entropy model
ε	Relative error (%)
θ	Vector of unknown parameters
π	Coefficients in the calculation of the liquid entropy model
τ, η and χ	Coefficients in the calculation of the parameters π_i

Subscripts

i, j	Iteration values
N	End iteration value

N_p	Number of parameters in the reference liquid entropy model
n	Number of parameters in the function א
salt	Salt

References:

[1] L. G. Farshi, C. A. I. Ferreira, S. M. S. Mahmoudi and M. A. Rosen, "Using new properties data for enthalpy and entropy calculation of ammonia/salt solutions," in *4th IIR Conference on Thermophysical Properties and Transfer Processes of Refrigerants*, Delft, 2013.

[2] L. G. Farshi, C. A. I. Ferreira and S. M. S. Mahmoudi, "First and second law analysis of ammonia/salt absorption refrigeration systems," *International Journal of Refrigeration,* vol. 40, pp. 111-121, 2014, https://doi.org/10.1016/j.ijrefrig.2013.11.006.

[3] C. P. Gupta, C. P. Sharma and R. K. Mehrotra, "Thermodynamic properties of solutions of sodium thiocyanate in liquid ammonia and their vapors," in *Xiv International Congress of IIR*, Moscou, pp. 170-178, 1995.

[4] W. Koehler, W. Ibele, J. Soltes and E. Winter, "Entropy calculations for lithium bromide aqueous solutions and approximation equation," *ASHRAE Trans,* vol. 93, pp. 2379-88, 1987.

[5] D. Cai, G. He, Q. Tian and W. Tang, "Exergy analysis of a novel air-cooled non-adiabatic absorption refrigeration cycle with NH_3–$NaSCN$ and NH_3–$LiNO_3$ refrigerant solutions," *Energy Conversion and Management,* vol. 88, pp. 66-78, 2014, https://doi.org/10.1016/j.enconman.2014.08.025.

[6] S. Aphornratana and I. W. Eames, "Thermodynamic analysis of absorption refrigeration cycles using the second law of thermodynamics method," *International Journal of Refrigeration,* vol. 18, no. 4, pp. 244-252, 1995, https://doi.org/10.1016/0140-7007(95)00007-X.

[7] L. Zhu and J. Gu, "Second law-based thermodynamic analysis of ammonia/sodium thiocyanate absorption system," *Renewable Energy,* vol. 35, no. 9, pp. 1940-1946, 2010, https://doi.org/10.1016/j.renene.2010.01.022.

[8] A. Myat, K. Thu, Y.-D. Kim, A. Chakraborty, W. G. Chun and K. C. Ng, "A second law analysis and entropy generation minimization of an absorption chiller," *Applied Thermal Engineering,* vol. 31, no. 14-15, pp. 2405-2413, 2011, https://doi.org/10.1016/j.applthermaleng.2011.04.004.

[9] S. Saheli and M. Yari, "Exergoeconomic assessment of two novel absorption-ejection heat pumps for the purposes of supermarkets simultaneous heating and refrigeration using $NaSCN/NH_3$, $LiNO_3/NH_3$ and H_2O/NH_3 as working pairs," *International Journal of Refrigeration,* vol. 101, pp. 178-195, 2019, https://doi.org/10.1016/j.ijrefrig.2019.03.029.

[10] H. Pourfarzad, M. Saremia and M. R. Ganjali, "A novel tri-generation energy system integrating solar energy and industrial waste heat," *Journal of Thermal Engineering,* vol. 7, no. 5, pp. 1067-1076, 2021, https://doi.org/10.18186/thermal.977910.

[11] B. F. Tchanche, G. Lambrinos, A. Frangoudakis and G. Papadakis, "Low-grade heat conversion into power using organic Rankine cycles-A review of various applications.," *Renewable and Sustainable Energy Reviews,* vol. 15, pp. 3963-3979, 2011, https://doi.org/10.1016/j.rser.2011.07.024.

[12] L. Cao, J. Wang, Y. Yang, Y. Wang, H. Li, J. Lou and Q. Rao, "Dynamic analysis and operation simulation for a combined cooling heating and power system driven by geothermal energy," *Energy Conversion and Management,* vol. 228, p. 113656, 2021.

[13] P. H. d. S. Morais, A. Lodi, C. A. Aoki and M. Modesto, "Energy, exergetic and economic analyses of a combined solar biomass-ORC cooling cogeneration systems for a Brazilian small plant," *Renewable Energy,* vol. 157, pp. 1131-1147, 2020, https://doi.org/10.1016/j.renene.2020.04.147.

[14] S. Jafary, S. Khalilarya, A. Shawabkeh, M. Waehayee and M. Hashemian, "A complete energetic and exergetic analysis of a solar powered trigeneration system with two novel orgaic Rankine cycle (ORC) configurations," *Journal of Cleaner Production,* 2020, https://doi.org/10.1016/j.jclepro.2020.124552.

[15] T. K. Gogoi and P. Hazarika, "Comparative assessment of four novel solar based triple effect absorption refrigeration systems integrated with organic Rankine and Kalina cycles," *Energy Conversion and Management,* vol. 226, p. 113561, 2020, https://doi.org/10.1016/j.enconman.2020.113561.

[16] C. CİMŞİT, "Organik Rankine Çevrim (ORC) İle Çalışan Tek Kademeli Absorbsiyonlu-Buhar Sıkıştırmalı Kaskad Soğutma Çevriminin Analizi," *Firat Üniversitesi Mühendislik Bilimleri Dergisi,* vol. 31, no. 1, pp. 29-37, 2019 <https://dergipark.org.tr/en/pub/fumbd/issue/43638/534749.

[17] A. C. Cleland, "Computer subroutines for rapid evaluation of refrigerant thermodynamic properties," *International Journal of Refrigeration,* vol. 9, no. 6, pp. 346-351, 1986, https://doi.org/10.1016/0140-7007(86)90006-X.

[18] J. Gu and Z. Gan, Entransy in Phase-Change Systems, SpringerBriefs in Applied Sciences and Technology, 2014, doi:10.1007/978-3-319-07428-3.

[19] C. A. Infante Ferreira, "Thermodynamic and physical property data equations for ammonia-lithium nitrate and ammonia-sodium thiocyanate solutions," *Solar Energy,* vol. 32, no. 2, pp. 231-236, 1984, https://doi.org/10.1016/S0038-092X(84)80040-7.

[20] J. J. F. Zemaitis, D. M. Clark, M. Rafal and N. C. Scrivner, Handbook of aqueous electrolyte thermodynamics: theory & application, New York: John Wiley & Sons, 2010, https://doi:10.1002/9780470938416.

[21] J. P. Roberson, C. Y. Lee, R. G. Squires and L. F. Albright, "Vapor pressure of ammonia and monomethylamine in solutions for absorption refrigeration systems," *ASHRAE Trans.,* vol. 72, no. 1, pp. 198-208, 1966.

[22] G. C. Blytas and F. Daniels, "Concentrated Solutions of NaSCN in Liquid Ammonia. Solubility, Density, Vapor Pressure, Viscosity, Thermal Conductance, Heat of Solution and Heat Capacity," *Journal of the American Chemical Society,* vol. 84, no. 7, pp. 1075-1083, 1962, https://doi.org/10.1021/ja00866a001.

[23] S. L. Sargent and W. A. Beckman, "Theoretical performance of an ammonia-sodium thiocyanate intermittent absorption refrigeration cycle," *Solar Energy,* vol. 12, no. 2, pp. 137-146, 1968, https://doi.org/10.1016/0038-092X(68)90001-7.

Two-Dimensional Generalized Magneto-Thermo-Viscoelasticity Problem for a Spherical Cavity with One Relaxation Time Using Fractional Derivative

Satish G. Khavale[1] and Kishor R. Gaikwad *[2]

[1,2]P.G. Department of Mathematics, N.E.S. Science College, Nanded-431602, (M.S.), India.
E-mail: [1]khavalesatish8@gmail.com, [2]drkr.gaikwad@yahoo.in

Abstract:

The present paper is aimed to studying the two-dimensional generalised magneto-thermo-viscoelasticity problem for a spherical cavity with one relaxation time using fractional derivative. The formulation is applied to generalised thermoelasticity based on the theory of generalised thermoelastic diffusion with one relaxation time. The spherical cavity of the solid surface is assumed to be traction free and subjected to both heating and an external magnetic field. The Laplace transform technique is used to obtain the general solution. The inverse Laplace transform is carried out using a numerical inversion method based. The temperature, displacement, and stresses are obtained and represented graphically with the help of Mathcad software.

Keywords: Fractional order; magneto-thermo-viscoelasticity; spherical cavity; electromagnetic field.

1. Introduction

The classical theory of thermoelasticity has been generalised and modified into various thermoelastic models that run under the label of hyperbolic thermoelasticity. The notation hyperbolic reflects the fact that thermal waves are modelled, avoiding the physical paradox of the infinite propagation speed of the classical model. At present, there are several theories of hyperbolic thermoelasticity.

Biot [1] introduced the theory of coupled thermoelasticity, which predicts infinite speeds of wave propagation, which is physically unacceptable. Lord and Shulman [2] introduced the generalized dynamical theory of thermoelasticity with one relaxation time, for the isotropic body. Caputo [3] proposed viscoelastic energy dissipation mechanism based on a memory mechanism with two degrees of freedom for the problem. Ezzat [4] discussed the generalised magneto-thermoelastic waves by thermal shock in half-space. Ezzat [5] used the fractional order derivative to investigate magneto-thermoelasticity with thermoelectric properties. Roychoudhuri et al. [6, 7] investigated magneto-thermoelastic interactions in a viscoelastic cylinder of temperature rate dependent material subjected to periodic loading, as well as the effect of rotation and relaxation times in generalised thermoviscoelasticity. Sherief et al. [8] proposed the new theory of coupled thermoelasticity and generalised thermoelasticity with one relaxation time using the method of fractional calculus. Povstenko [9] solved some thermoelastic problems based on the heat conduction equation in one dimensional and two dimensional domains with a time fractional derivative and associated thermal stresses. Deswal and Kalkal [10] introduced the effects of viscosity and diffusion on thermoelastic interactions in thermally, isotropic and electrically conducting half-space solids whose surfaces are subjected to thermal and mechanical loads.

Zenkour et al. [11] studied the generalised thermodiffusion of an unbounded body for a spherical cavity subjected to periodic loading. Gaikwad et. al. [12] studied the quasi-static thermoelastic mathematical model for an infinitely long circular cylinder by using the integral transform technique. Gaikwad [13] analysed the thermoelastic deformation of a thin hollow circular disk due to a partially distributed heat supply. Gaikwad et. al. [14] studied the non-homogeneous heat conduction problem and its thermal deflection due to internal heat generation in a thin hollow circular disk. Gaikwad [15] analysed the thermoelastic deformation of a thin hollow circular disk due to partially distributed heat supply. H. Sherief and A. M. Abd El-Latief [16] discussed the application of fractional order theory of thermoelasticity problem for a half-space. Raslan [17] solved one dimensional problem of fractional order theory of thermoelasticity of an infinitely long cylindrical cavity using integral transform technique. Kalkal and Deswal [18] investigated the effects of fractional order parameter, viscosity, magnetic field, and diffusion on thermoelastic interaction in an infinite body with a mechanical load on its surface. Hussain [19] solved the fractional order thermoelastic problem for an infinitely long solid circular cylinder. Raslan [20] introduced the fractional-order theory of thermoelasticity to the two-dimensional problem of a thick plate whose lower and upper surfaces are traction-free and subjected to the given axi-symmetric temperature distribution. Gaikwad [21] proposed the two-dimensional study-state temperature distribution of a thin circular plate due to uniform internal energy generation.

Tripathi et al. [22] analyzed the fractional order thermoelastic problem for a thick circular plate with finite wave speeds. Gaikwad [23] discussed the axi-symmetric thermoelastic stress analysis of a thin circular plate due to heat generation. Gaikwad [24] studied the time-fractional

heat conduction problem in a thin hollow circular disk and its thermal deflection. Khavale et al. [25] introduced the generalized theory of magneto-thermo-viscoelastic spherical cavity problem under fractional order derivative using the state space approach. Gaikwad et al.[26] analyzed the transient thermoelastic temperature distribution of a thin circular plate and its thermal deflection under uniform heat generation. Gaikwad et al.[27] proposed the fractional order thermoelastic problem for finite piezoelectric rod subjected to different types of thermal loading using direct approach. Gaikwad et al.[28] solved the fractional order transient thermoelastic problem using the integral transform technique and discussed stress analysis of a the thin circular sector disk.

In the present work, a new model of time-fractional derivative of order α has been considered in the context of a two-dimensional generalised magneto-thermoviscoelasticity problem for a spherical cavity with one relaxation time. The spherical cavity of the solid surface is assumed to be traction free and subjected to both heating and an external magnetic field. Laplace transform have been employed for the general solution of the problem. The results obtained theoretically have been computed numerically and are depicted graphically. It is believed that this particular problem has not been considered by anyone. This is a new and novel contribution to the field of thermoelasticity. Applications of this study are more useful in the fields of seismology, geomechanics, earthquakes engineering and soil dynamics etc,.

2. Basic Equations and Formulation

The constitutive equations and field equations for an isotropic, homogeneous elastic solid in the absence of body forces under the fractional order theory of generalized thermo-viscoelasticity with temperature-dependent modulus of elasticity can be written in the following form.
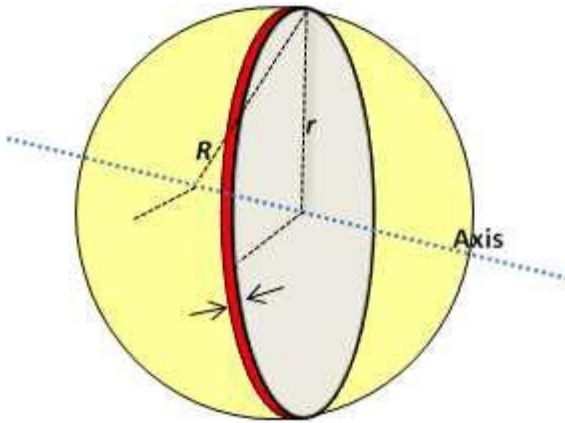
Figure 1. Geometrical representation of the problem.

(i) Maxwell governing equations:

$$curl\ \boldsymbol{h} = \boldsymbol{J} \tag{1}$$

$$curl\ \boldsymbol{E} = -\mu_0 \frac{\partial \boldsymbol{h}}{\partial t} \tag{2}$$

$$\boldsymbol{E} = -\mu_0 \frac{\partial \boldsymbol{u}}{\partial t} \times \boldsymbol{H}_0 \tag{3}$$

$$div\ \boldsymbol{h} = 0 \tag{4}$$

$$div\ \boldsymbol{E} = 0 \tag{5}$$

where F_i is the components of Lorentz force, whose expression is

$$F_i = \mu_0 (\boldsymbol{J} \times \boldsymbol{H})_i \tag{6}$$

(ii) Equation of motion:

$$\rho \frac{\partial^2 u_i}{\partial t^2} = F_i + \mu \left(1 + \alpha_2 \frac{\partial}{\partial t}\right) u_{i,jj}$$
$$+ \left(\lambda \left(1 + \alpha_1 \frac{\partial}{\partial t}\right) + \mu \left(1 + \alpha_2 \frac{\partial}{\partial t}\right)\right) u_{j,ij}$$
$$- (3\lambda + 2\mu)\beta(\alpha_t \theta_{,i} - \alpha_c C_{,i}) \tag{7}$$

where α_1 and α_2 are the thermoviscoelastic relaxation times and $\beta = \left(1 + \frac{3\lambda\alpha_1 + 2\mu\alpha_2}{3\lambda + 2\mu} \frac{\partial}{\partial t}\right)$.

(iii) Heat conduction equation:

$$k'^{\theta}_{,ii} = \left(\frac{\partial}{\partial t} + t_0 \frac{\partial^{\alpha+1}}{\partial t^{\alpha+1}}\right)(\rho C_E \theta + (3\lambda + 2\mu)\alpha_t \beta T_0 e + a T_0 C) \tag{8}$$

The Caputo type fractional derivative given by [30]

$$D^\alpha f(t) = \begin{cases} \dfrac{1}{\sqrt{n-\alpha}} \displaystyle\int_0^t \dfrac{f^n(\tau)}{(t-\tau)^{\alpha+1-n}} d\tau, & n-1 < \alpha < n; \\ \dfrac{df(t)}{dt}, & n = 1 \end{cases} \tag{9}$$

For finding the Laplace transform, the Caputo derivative requires information of the initial values of the function $f(t)$ and its integer derivative of the order $k = 1, 2, ..., n - 1$

$$L\{D^\alpha f(t); s\} = s^\alpha F(s) - \sum_{k=0}^{n-1} s^{\alpha-k-1} f^{(k)}(0), \qquad n-1 < \alpha < n \tag{10}$$

(iv) Mass diffusion equation:

$$D(3\lambda + 2\mu)\alpha_c \beta e_{,ii} + Da\nabla^2 \theta_{,ii} + \left(\frac{\partial}{\partial t} + t_1 \frac{\partial^2}{\partial t^2}\right)C - Db\nabla^2 C_{,ii} = 0 \tag{11}$$

where D is diffusion coefficient, a is a coefficient describing the measure of thermoelastic diffusion effects and b is a coefficient describing the measure of diffusive effects.

(v) Constitutive equations:

$$\sigma_{ij} = 2\mu \left(1 + \alpha_2 \frac{\partial}{\partial t}\right) e_{ij} + \delta_{ij} \left(\lambda \left(1 + \alpha_1 \frac{\partial}{\partial t}\right) e_{kk} + (3\lambda + 2\mu)\beta(\alpha_t \theta - \alpha_c C)\right) \tag{12}$$

(vi) Chemical potential equation:

$$P = -(3\lambda + 2\mu)\alpha_c \beta e_{kk} + bC - a\theta \tag{13}$$

where P is the chemical potential per unit mass.

Consider the spherical polar coordinates (r, Θ, ϕ) are taken for any representative point of the body at at time t and the origin of the coordinate system is at the center of the spherical cavity of radius *R*. Considering radial variations of the medium, the only non-zero displacement component is $u = u(r, t)$, so that, the component of strain tensor are

$$e_{rr} = \frac{\partial u}{\partial r}, \ e_{\theta\theta} = \frac{u}{r} = e_{\phi\phi}, \ e_{r\phi} = e_{r\theta} = e_{\theta\phi} = 0 \tag{14}$$

$$e = div\ \mathrm{u} = e_{rr} + e_{\phi\phi} + e_{\theta\theta} = \frac{\partial u}{\partial r} + \frac{2u}{r} = \frac{1}{r^2}\frac{\partial(r^2 u)}{\partial r} \tag{15}$$

From equation (12), we obtained the stress tensor components as

$$\sigma_{rr} = 2\mu\left(1 + \alpha_2\frac{\partial}{\partial t}\right)\frac{\partial u}{\partial r} + \lambda\left(1 + \alpha_1\frac{\partial}{\partial t}\right)e - (3\lambda + 2\mu)\beta(\alpha_t\theta - \alpha_c C) \tag{16}$$

$$\sigma_{\theta\theta} = 2\mu\left(1 + \alpha_2\frac{\partial}{\partial t}\right)\frac{u}{r} + \lambda\left(1 + \alpha_1\frac{\partial}{\partial t}\right)e - (3\lambda + 2\mu)\beta(\alpha_t\theta - \alpha_c C) \tag{17}$$

and from equation (11), the chemical potential is
$$P = -(3\lambda + 2\mu)\alpha_c\beta e + bC - a\theta \tag{18}$$
Due to the application of the initial magnetic field $\mathbf{H_0}$, there results an induced magnetic field $\mathbf{h} = (0,0,h)$ which be small, so that, their products with u_i and their derivatives can be neglected for linearization and an induced electric field E. Applying an initial magnetic field vector $\mathbf{H_0} = (0,0,H_0)$ then equations (1),(2) and (3) yield.

$$J = \left(o, -\frac{\partial h}{\partial u}, 0\right) \tag{19}$$

$$\square = -\boldsymbol{H_0}\left(\frac{\partial u}{\partial r} + \frac{2u}{r}\right) \tag{20}$$

$$\boldsymbol{E} = \left(o, \mu_0 H_0\frac{\partial u}{\partial t}, 0\right) \tag{21}$$

The components of Lorentz force can be obtained from equation (19-21) in the form

$$F_r = \mu_0(\boldsymbol{J} \times \boldsymbol{H})_r = \mu_0 H_0^2\frac{\partial}{\partial r}\left(\frac{\partial u}{\partial r} + \frac{2u}{r}\right) \tag{22}$$

The equation of motion, equation (7) can be written as:

$$\sigma_{rr,r} + \frac{\sigma_{rr} - \sigma_{\theta\theta}}{r} + F_r = \rho\frac{\partial^2 u}{\partial t^2} \tag{23}$$

Using equations (16),(17) and (23), we get

$$\rho\frac{\partial^2 u}{\partial t^2} = \left[\lambda\left(1 + \alpha_1\frac{\partial}{\partial t}\right) + 2\mu\left(1 + \alpha_2\frac{\partial}{\partial t}\right) + \mu_0 H_0\right]\frac{\partial e}{\partial r} - (3\lambda + 2\mu)\beta\left(\alpha_t\frac{\partial\theta}{\partial r} - \alpha_c\frac{\partial C}{\partial r}\right) \tag{24}$$

Applying the operator $(\partial/\partial r + 2/r)$ to both sides of equation (24), one obtains

$$\rho\frac{\partial^2 u}{\partial t^2} = \left[\lambda\left(1 + \alpha_1\frac{\partial}{\partial t}\right) + 2\mu\left(1 + \alpha_2\frac{\partial}{\partial t}\right) + \mu_0 H_0\right]\nabla^2 e - (3\lambda + 2\mu)\beta(\alpha_t\nabla^2\theta - \alpha_c\nabla^2) \tag{25}$$

The heat conduction equation, equation (8) can be written as:

$$k\nabla^2\theta = \left(\frac{\partial}{\partial t} + t_0\frac{\partial^{\alpha+1}}{\partial t^{\alpha+1}}\right)(\rho C_E\theta + (3\lambda + 2\mu)\alpha_t\beta T_0 e + aT_0 C) \tag{26}$$

where ∇^2 is Laplaces operator in spherical coordinates which is given by

$$\nabla^2 = \frac{1}{r^2}\frac{\partial}{\partial r}\left(r^2\frac{\partial}{\partial r}\right) + \frac{1}{r^2\sin\Theta}\left(\sin\Theta\frac{\partial}{\partial\Theta}\right) + \frac{1}{r^2\sin^2\Theta}\frac{\partial^2}{\partial\phi^2} \tag{27}$$

In case of dependence on only r, this reduce to

$$\nabla^2 = \frac{1}{r^2}\frac{\partial}{\partial r}\left(r^2\frac{\partial}{\partial r}\right) \tag{28}$$

Now, we will introduced the following non-dimensional variables:

$$r' = c\eta r, \quad u' = c\eta u, \quad P' = \frac{P}{(3\lambda + 2\mu)\alpha_c}, \quad t' = c^2\eta t,$$

$$\theta' = \frac{(3\lambda + 2\mu)\alpha_t}{\lambda + 2\mu}\theta, \quad t_0' = c^2\eta t_0, \quad C' = \frac{(3\lambda + 2\mu)\alpha_c}{\lambda + 2\mu}C,$$

$$t_1' = c^2\eta t_1, \quad \sigma_{ij}' = \frac{1}{\lambda + 2\mu}\sigma_{ij}, \quad q_r' = \frac{3\lambda_1 + 2\mu\alpha_2}{k'(3\lambda + 2\mu)c(\lambda + 2\mu)}q_r. \tag{29}$$

where $\eta = \frac{\rho C_E}{k'}$, $c = \sqrt{\frac{\lambda + 2\mu}{\rho}}$ is the speed of propagation of isothermal elastic waves, q_r is the heat flux in the radial direction.

Using these non-dimensional variables, equations (16-18) and (25-27) takes the form (dropping the primes for convenience):

$$\frac{\partial^2 e}{\partial t^2} = \beta_1\nabla^2 e - \beta\nabla^2\theta - \beta\nabla^2 C \tag{30}$$

$$\nabla^2\theta = \left(\frac{\partial}{\partial t} + t_0\frac{\partial^{\alpha+1}}{\partial t^{\alpha+1}}\right)(\theta + \varepsilon\beta e + \varepsilon\beta_2 C) \tag{31}$$

$$\beta_3\nabla^2 C = \beta\nabla^2 e + \beta_2\nabla^2\theta + \beta_4\left(\frac{\partial}{\partial t} + t_1\frac{\partial^2}{\partial t^2}\right)C \tag{32}$$

$$\sigma_{rr} = \left(1 + \frac{(\lambda\alpha_1 + 2\mu\alpha_2)^2}{\rho(\lambda + 2\mu)}\frac{\partial}{\partial t}\right)e - \frac{4\mu}{\lambda + 2\mu}\left(1 + \alpha_2\frac{\partial}{\partial t}\right)\frac{u}{r} - \beta\theta - \beta C \tag{33}$$

$$\sigma_{\theta\theta} = \left(1 - \frac{2\mu}{\lambda + 2\mu}\right)\left(1 + \alpha_1\frac{\partial}{\partial t}\right)e - \frac{2\mu}{\lambda + 2\mu}\left(1 + \alpha_2\frac{\partial}{\partial t}\right)\frac{u}{r} - \beta\theta - \beta C \tag{34}$$

$$P = \beta_3 C - \beta e - \beta_2\theta \tag{35}$$

here

$$\beta_1 = 1 + \frac{\mu_0^2 H_0^2}{\rho(\lambda + 2\mu)} + \frac{(\lambda\alpha_1 + 2\mu\alpha_2)^2}{\rho(\lambda + 2\mu)}\frac{\partial}{\partial t},$$

$$\beta_2 = \frac{a\rho c^2}{(3\lambda + 2\mu)^2\alpha_t\alpha_c}, \varepsilon = \frac{(3\lambda + 2\mu)^2\alpha_t^2 T_0}{\rho C_E(\lambda + 2\mu)},$$

$$\beta_3 = \frac{b\rho c^2}{(3\lambda + 2\mu)^2\alpha_c^2}, \quad \beta_4 = \frac{\rho c^2}{(3\lambda + 2\mu)^2\alpha_c^2\eta D}$$

(vii) The initial and regularity conditions:

$$u = 0 = \frac{\partial u}{\partial t}, \text{at } t = 0 \tag{36}$$

$$\theta = 0 = \frac{\partial\theta}{\partial t}, \text{ at } t = 0 \tag{37}$$

$$C = 0 = \frac{\partial c}{\partial t} \text{ at } t = 0 \tag{38}$$

The homogeneous indictional conditions are supplemented by the following boundary conditions:
• The cavity surface is traction free:

$$\sigma_{rr} = 0 \quad \text{at r = R} \tag{39}$$

• The cavity surface is subjected to a thermal shock:

$$\theta = \theta_0 H(t) \quad \text{at } r = R \tag{40}$$

• The chemical potential is also assumed to be a known function of time at the cavity surface

$$P = P_0 H(t) \quad \text{at } r = R \tag{41}$$

where θ_0 and P_0 are constants and $H(t)$ is heaviside unit step function.

3. Solution in the Laplace Transform Domain
Apply the Laplace transform defined by the relation.

$$\bar{f}(r,s) = L[f(r,t)] = \int_0^\infty e^{-st} f(r,t) dt \tag{42}$$

to equation (30) to (35) under the initial conditions given in equation (36) to (38) we obtain

$$(\nabla^2 - \beta_5 s^2)\bar{e} = \beta_6 s \nabla^2 \bar{\theta} + \beta_6 s \nabla^2 \bar{C} \tag{43}$$

$$\left(\nabla^2 - (s + t_0 s^{\alpha+1})\right)\bar{\theta} = \beta_7 \varepsilon s (s + t_0 s^{\alpha+1})\bar{e} \\ + \beta_2 \varepsilon (s + t_0 s^{\alpha+1})\bar{C} \tag{44}$$

$$\beta_3 \nabla^2 \bar{C} = \beta_8 \nabla^2 \bar{e} + \beta_2 \nabla^2 \bar{\theta} + \beta_4 (s + t_0 s^2)\bar{C} \tag{45}$$

$$\bar{\sigma}_{rr} = \beta_9 \bar{e} - \frac{4\mu(1+\alpha_2 s)}{\lambda + 2\mu}\frac{\bar{u}}{r} - \beta_8 \bar{\theta} - \beta_8 \bar{C} \tag{46}$$

$$\bar{\sigma}_{\theta\theta} = 1 + \frac{2\mu}{\lambda+2\mu}(1 + \alpha_1 s)\bar{e} + \frac{2\mu(1+\alpha_2 s)}{\lambda+2\mu}\frac{\bar{u}}{r} - \beta_6 \bar{\theta} - \beta_6 \bar{C} \tag{47}$$

$$\bar{P} = \beta_3 \bar{C} - \beta_8 \bar{e} - \beta_2 \bar{\theta} \tag{48}$$

here,

$\beta_5 = \frac{\rho(\lambda+2\mu)}{\rho(\lambda+2\mu)+\mu_0^2 H_0^2+(\lambda\alpha_1+2\mu\alpha_2)^2}$,

$\beta_6 = \frac{\rho(\lambda+2\mu)[(3\lambda+2\mu)+(3\lambda\alpha_1+2\mu\alpha_2)]}{(3\lambda+2\mu)[\rho(\lambda+2\mu)+\mu_0^2 H_0^2+(\lambda\alpha_1+2\mu\alpha_2)^2]}$, $\beta_7 = \frac{(3\lambda\alpha_1+2\mu\alpha_2)}{3\lambda+2\mu}$,

$\beta_8 = 1 + \frac{3\lambda\alpha_1+2\mu\alpha_2}{3\lambda+2\mu}s$, $\beta_9 = 1 + \frac{\mu_0^2 H_0^2}{\rho(\lambda+2\mu)} + \frac{(\lambda\alpha_1+2\mu\alpha_2)^2 s}{\rho(\lambda+2\mu)}$

Eliminating $\bar{e}$, $\bar{C}$ between equations (43)-(45), one obtained six-order partial differential equation satisfied by $\bar{\theta}$ in the form

$$(\nabla^6 - C_1\nabla^4 + C_2\nabla^2 - C_3)\bar{\theta} = 0 \tag{49}$$

here,

$C_1 = \frac{b_2 a_2 + b_1 a_3 - \xi b_3 - a_1 b_4}{b_1 a_2 - a_1 b_3}$,

$C_2 = \frac{b_2 a_3 - \xi b_4 - a_1 b_2}{b_1 a_2 - a_1 b_3}$, $C_3 = \frac{-\xi b_2}{b_1 a_2 - a_1 b_3}$,

in which,

$a_1 = 1 + \frac{[\rho(\lambda+2\mu)][(3\lambda+2\mu)+(3\lambda\alpha_1+2\mu\alpha_2)s]s\alpha_t\alpha_c}{a\rho c^2[\rho(\lambda+2\mu)+\mu_0^2 H_0^2+(\lambda\alpha_1+2\mu\alpha_2)^2]}$,

$a_2 = \frac{[\rho(\lambda+2\mu)][(3\lambda+2\mu)+(3\lambda\alpha_1+2\mu\alpha_2)s](3\lambda+2\mu)\alpha_t\alpha_c}{a\varepsilon\rho c^2[\rho(\lambda+2\mu)+\mu_0^2 H_0^2+(\lambda\alpha_1+2\mu\alpha_2)^2]}$,

$a_3 = \frac{[\rho(\lambda+2\mu)][(3\lambda+2\mu)+(3\lambda\alpha_1+2\mu\alpha_2)s][(s+t_0 s^{\alpha+1}) \\ ((3\lambda+2\mu)^2\alpha_t\alpha_c - a\varepsilon\rho c^2)]}{a\varepsilon\rho c^2[\rho(\lambda+2\mu)+\mu_0^2 H_0^2+(\lambda\alpha_1+2\mu\alpha_2)^2](3\lambda+2\mu)}$,

$b_1 = 1 + \frac{s(3\lambda\alpha_1+2\mu\alpha_2)(a+b\alpha_t)}{a(3\lambda+2\mu)}$,

$b_2 = \frac{\varepsilon s \alpha_t(s+t_0 s^{\alpha+1})(3\lambda\alpha_1+2\mu\alpha_2)}{a\varepsilon\eta D(3\lambda+2\mu)}$,

$b_3 = \frac{b\alpha_t}{a\varepsilon\alpha_c(s+t_0 s^{\alpha+1})}$,

$b_4 = \frac{a\rho c^2}{\varepsilon\alpha_t\alpha_c(3\lambda+2\mu)^2} + \frac{\alpha_t}{a\varepsilon\alpha_c\eta D} + \frac{b\alpha_t\lambda(1+\alpha_1 s)}{a\varepsilon\alpha_c(s+t_0 s^{\alpha+1})(\lambda+2\mu)}$,

$\xi = \frac{\rho(\lambda+2\mu)s^2}{\rho(\lambda+2\mu)+\mu_0^2 H_0^2+(\lambda\alpha_1+2\mu\alpha_2)^2}$

Similarly, we can show that $\bar{e}$ and $\bar{C}$ satisfy the equations

$$(\nabla^6 - C_1\nabla^4 + C_2\nabla^2 - C_3)\{\bar{e}, \bar{C}\} = 0 \tag{50}$$

Introducing k_i, $i = 1,2,3$ into equation (49), one obtained

$$(\nabla^2 - k_1^2)(\nabla^2 - k_2^2)(\nabla^2 - k_3^2)\bar{\theta} = 0 \tag{51}$$

where, k_1, k_2 and k_3 are the positive roots for the characteristic equation

$$k^6 - C_1 k^4 + C_2 k^2 + C_3 = 0 \tag{52}$$

The roots k_1, k_2 and k_3 are

$$k_1 = \sqrt{\frac{1}{3}[2p\,\sin(q) + C_1]},$$

$$k_2 = \sqrt{\frac{-p}{3}[\sqrt{3}\,\cos(q) + \sin(q)] + \frac{C_1}{3}},$$

$$k_3 = \sqrt{\frac{p}{3}[\sqrt{3}\,\cos(q) - \sin(q)] + \frac{C_1}{3}}$$

Where

$$p = \sqrt{C_1^2 - 3C_2}, \quad q = \frac{1}{3}\sin^{-1}(\chi),$$

$$\chi = -\frac{2C_1^3 - 9C_1 C_2 + 27C_3}{2p^3}$$

The solution of equation (52), which is bounded at infinity, is given by

$$\bar{\theta}(r,s) = \frac{1}{\sqrt{r}}\sum_{i=1}^3 B_i(s)K_{1/2}(k_i r) \tag{53}$$

where B_i are parameters depending on s and $K_{1/2}(.)$ are the half order modified Bessel function of the second kind.
Similarly,

$$\{\bar{e}(r,s), \bar{C}(r,s)\} = \frac{1}{\sqrt{r}}\sum_{i=1}^3 \{B_i'(s), B_i''(s)\}K_{1/2}(k_i r) \tag{54}$$

Where

$$B_i' = \frac{b_3 k_i^4 - b_4 k_i^2 + b_2}{b_1 k_i^2 - b_2}B_i = E_i B_i$$

$$B_i^{''} = \frac{(b_1 - a_5 b_3)k_i^4 - (b_1 a_4 + b_4 - b_4 a_5)k_i^2 + a_4 b_2 - a_5 b_2}{w_6(y_1 k_i^2 - y_2)} B_i$$
$$= G_i B_i$$

in which

$$a_4 = s + t_0 s^{\alpha+1}, \qquad a_5 = \epsilon(s + t_0 s^{\alpha+1})\frac{(3\lambda\alpha_1 + 2\mu\alpha_2)s}{3\lambda + 2\mu}$$

Substituting equation (40) into equations (30)-(34), one obtains

$$\{\bar{e}(r,s), \bar{C}(r,s)\} = \frac{1}{\sqrt{r}}\sum_{i=1}^{3} \{E_i, G_i\}B_i K_{1/2}(k_i r) \tag{55}$$

Using the relation between $\bar{u}$ and $\bar{e}$, one gets the solution for the dimensionless form of displacement assuming that $\bar{u}$ vanishes at infinity as:

$$\bar{u} = -\frac{1}{\sqrt{r}}\sum_{i=1}^{3} \frac{E_i}{k_i} B_i K_{3/2}(k_i r) \tag{56}$$

Thus, from equations (55) and (56), one obtains

$$\bar{\sigma}_{rr}(r,s) = \frac{1}{\sqrt{r}}\sum_{i=1}^{3}\left((\beta_9 E_i - \beta_8 - \beta_8 G_i)K_{\frac{1}{2}}(k_i r) + \right.$$
$$\left. \frac{4\mu(1+\alpha_2 s)}{\lambda+2\mu}\frac{E_i}{k_i r}K_{3/2}(k_i r)\right)B_i(s) \tag{57}$$

$$\bar{\sigma}_{\theta\theta}(r,s) = \frac{1}{\sqrt{r}}\sum_{i=1}^{3}\left(\left(\left(1 + \frac{2\mu}{\lambda+2\mu}\right)(1 + \alpha_1 s)E_i - \beta_8 - \beta_8 G_i\right)\right.$$
$$\left. K_{\frac{1}{2}}(k_i r) - \frac{2\mu(1+\alpha_2 s)}{\lambda+2\mu}\frac{E_i}{k_i r}K_{3/2}(k_i r)\right)B_i(s) \tag{58}$$

$$\bar{P}(r,s) = \frac{1}{\sqrt{r}}\sum_{i=1}^{3}(\beta_3 G_i - \beta_2 - \beta_8 E_i)K_{1/2}(k_i r)B_i(s) \tag{59}$$

The transformed boundary conditions become

$$\bar{\sigma}_{rr} = 0, \ \bar{\theta} = \frac{\bar{\theta}_0}{s}, \ \bar{P} = \frac{\bar{P}_0}{s}, \ \text{ at } r = R \tag{60}$$

Apply the boundary conditions given in equation (60) together with equations (55) and (57-59) is used. we obtains:

$$\sum_{i=1}^{3} B_i(s)K_{1/2}(k_i R) = \frac{\theta_0\sqrt{R}}{s} \tag{61}$$

$$\sum_{i=1}^{3}\left((\beta_9 E_i - \beta_8 - \beta_8 G_i)K_{\frac{1}{2}}(k_i R) + \right.$$
$$\left. \frac{4\mu(1+\alpha_2 s)}{\lambda+2\mu}\frac{E_i}{k_i R}K_{3/2}(k_i R)\right)B_i(s) = 0 \tag{62}$$

$$\sum_{i=1}^{3}(\beta_3 G_i - \beta_2 - \beta_8 E_i)K_{1/2}(k_i R)B_i(s) = \frac{P_0\sqrt{R}}{s} \tag{63}$$

Equations (61)-(63) is a system of linear equations with $B_i(s)$ as unknown parameters. On solving these equations, we get the complete solution of the problem in the Laplace transform domain.

4. Numerical Inversion of the Laplace Transforms

Laplace transformation of the continuous f(t) function is presented

$$\bar{f}(s) = \int_0^\infty e^{-st}f(t)dt \tag{64}$$
for t > 0 and s = x + iy.

The inversion integral is utilized to identify the actual function f(t) when the solution is provided in the Laplace domain.

$$f(t) = \int_{\gamma-i\infty}^{\gamma+i\infty} e^{-st}\bar{f}(s)ds \tag{65}$$

Where, contour should be placed to the right of all $\bar{f}(s)$ singularities. The direct Equation (65) integration is usually challenging and sometimes not feasible analytically. We use a numerical inverse approach based on the Stehfest for ultimate solution of the stress distribution, displacement temperature in the time domain [29]. In the given approach, the inverse f(t) of Laplace $\bar{f}(s)$ is estimated by the relationship.

$$f(t) = \frac{\ln 2}{t}\sum_{j=1}^{N} V_j \ F\left(\frac{\ln 2}{t}j\right) \tag{66}$$

Where the following equation is presented V_j:

$$V_j = (-1)^{((N/2)+1)} \sum_{k=(i+1)/2}^{\min(i,N/2)} \frac{k^{((N/2)+1)}(2k)!}{(N/2-k)! \ k! \ (i-k)! \ (2k-1)!} \tag{67}$$

The N parameter is the summation number (63) of terms and must be maximized by trial and error. Rising N improves the result accuracy to a point and subsequently decreases accuracy due to increased round-off errors. All parameters' solutions in the space time domain are therefore provided with

$$\theta(r,t) = \frac{\ln 2}{t}\sum_{j=1}^{N} V_j \ \bar{\theta}\left(r,\frac{\ln 2}{t}j\right) \tag{68}$$

$$u(r,t) = \frac{\ln 2}{t}\sum_{j=1}^{N} V_j \ \bar{u}\left(r,\frac{\ln 2}{t}j\right) \tag{69}$$

$$\sigma_{rr}(r,t) = \frac{\ln 2}{t}\sum_{j=1}^{N} V_j \ \bar{\sigma}_{rr}\left(r,\frac{\ln 2}{t}j\right) \tag{70}$$

$$\sigma_{\theta\theta}(r,t) = \frac{\ln 2}{t}\sum_{j=1}^{N} V_j \ \bar{\sigma}_{\theta\theta}\left(r,\frac{\ln 2}{t}j\right) \tag{71}$$

$$P = \frac{\ln 2}{t}\sum_{j=1}^{N} V_j \ \bar{P}\left(r,\frac{\ln 2}{t}j\right) \tag{72}$$

5. Numerical Results and Discussion

The copper material was chosen for purposes of numerical evaluations and the constants of the problem were taken as following Table 1.

The numerical calculation and graphs are carried out with the help of computational mathematical software PTC Mathcad Prime-7.0.0.0

Figure 2-6 shows the variation of the temperature field, displacement and stresses vary with different values of times, t = 0.25, 0.50, 0.75, 1 with fractional-order parameter $\alpha = 1$. Figure 2 has been plotted to illustrate the variation of temperature field in radial direction with different time parameters. The temperature filed start with the maximum value (in magnitude) and then gradually decreases with increase the radius. Figure 3 shows that the displacement increases as time t increases for r $\leq$ 0.2 and its remains constant for r $\geq$ 0.2. Figure 4 shows that variation of radial stress in radial direction, it is clear that initially radial stresses decreases within region 0 $\leq$ r $\leq$ 0.1 and increases within the region 0.1 $\leq$ r $\leq$ 1 with increases time. Figure 5

shows that the value of angular stress increases with an increase in time t along the radial direction.

Physical constants	Value
Reference uniform temperature (T_0)	293 K
Thermal diffusivity (c)	84.18 m^2/s
Thermal conductivity (k')	386 W/(m. K)
Density (ρ)	8954 kg/m^3
Lame's constants (μ)	3.86×10^{10} kg/(m. s^2)
Lame's constants (λ)	7.76×10^{10} kg/(m. s^2)
Coefficients of linear thermal expansion (α_t)	1.78×10^{-5} K^{-1}
Coefficients of linear diffusion expansion(α_c)	1.98×10^{-4} m^3/kg
Specific heat at constant strain (C_E)	383.1 J/(kg. K)
Magnetic permeability (μ_0)	$4\pi \times 10^{-7}$ H/m
Applied Magnetic field (H_0)	10^7/ 4π H/m
Coefficient describing the measure of thermoelastic diffusion effects (a)	1.2×10^4 m^2/(K. s^2)
Coefficient describing the measure of thermoelastic diffusive effects (b)	0.9×10^6 m^5/(kg. s^2)
Diffusion coefficient (D)	0.85×10^{-8} kg/m^3.s
Thermal relaxation time (t_0)	0.2 s
Diffusion relaxation time (t_1)	0.02 s
Component of thermoviscoelastic relaxation time (α_1)	0.06 s
Component of thermoviscoelastic relaxation time (α_2)	0.09 s

Figure 6-9 shows the variation of the temperature, displacement and stress with different values of fractional-order parameter α at time t = 0.5. Figure 6 depicts the variation of temperature distribution along radial direction with t = 0.5 for different values of parameter α. Also, it be seen that, the fractional parameter has an increasing effects on the magnitude of this field. The profile of displacement distribution at t = 0.5 for different values of fractional-order parameter α is displaced in figure 7. The fractional-order parameter is found to have decreasing effects on this distribution. The radial and angular stresses $\sigma_r r$ and $\sigma_{\theta\theta}$ are presented in figure 8 and 9 respectively, to investigate the effects of fractional parameter α. It is noticed that the stresses σ_{rr} and $\sigma_{\theta\theta}$ increases with decreasing the fractional-order parameter α.

Figure 3. Displacement distribution at α = 0.5 and different values of t.

Figure 4. Radial stress distribution at α = 0.5 and different values of t.

Figure 2. Temperature distribution at α = 0.5 and different values of t.

Figure 5. Angular stress distribution at α = 1 and different values of t.

Figure 6. Temperature distribution at t =0.5 and different values of α.

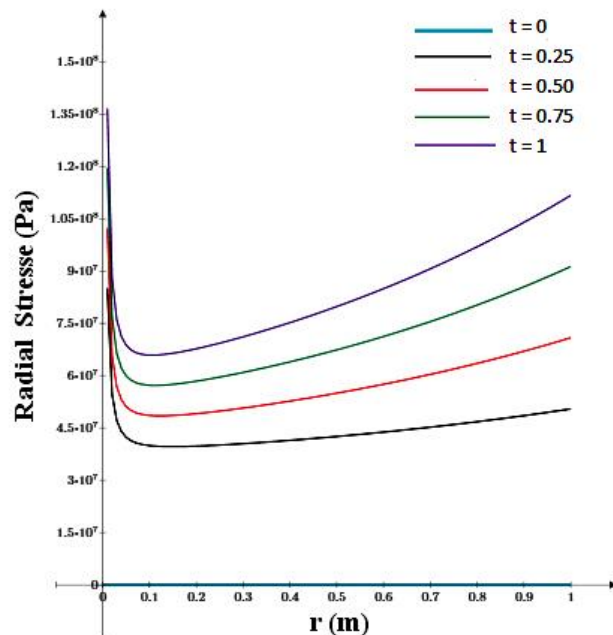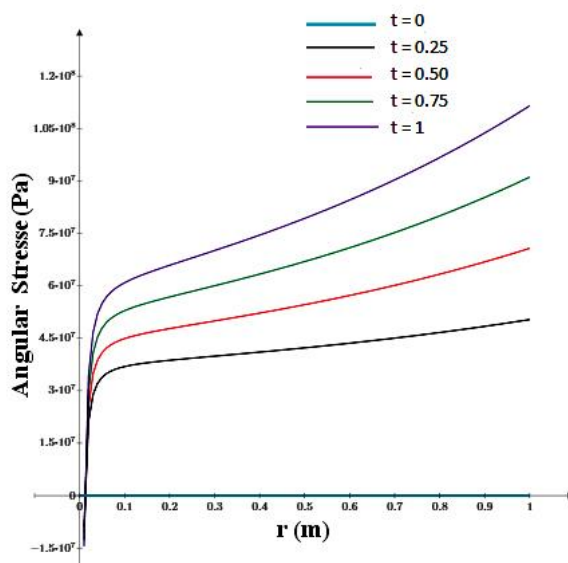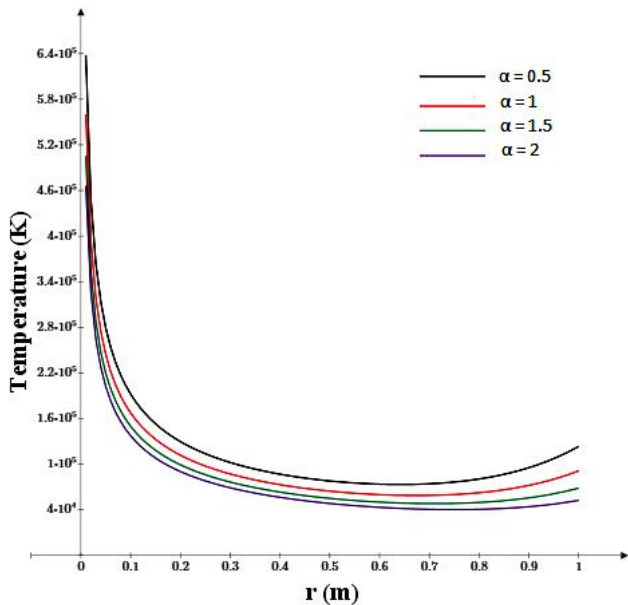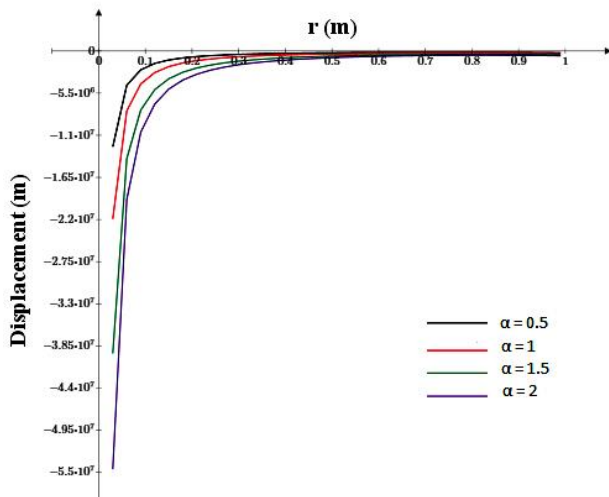Figure 7. Displacement distribution at t =0.5 and different values of α.
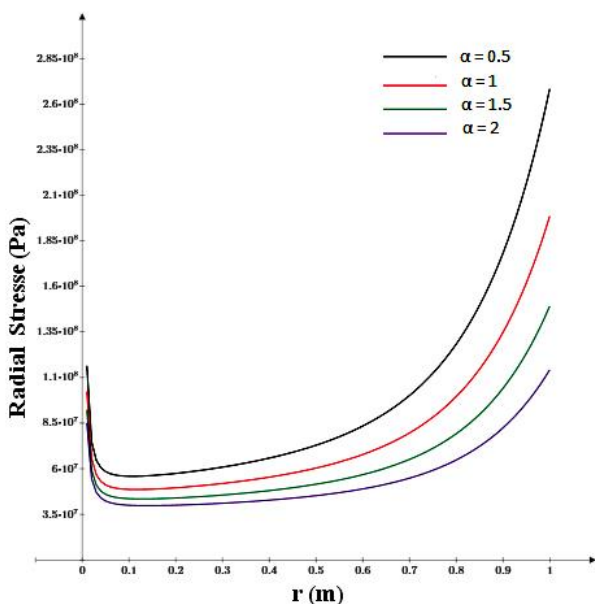

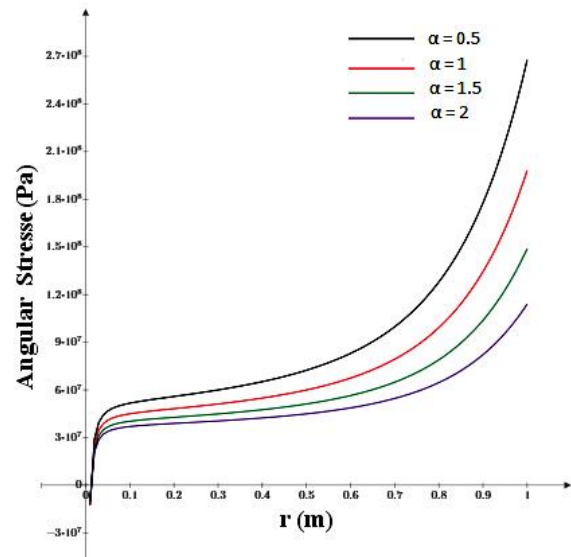Figure 8. Radial stress distribution at t =0.5 and different values of α.

Figure 9. Angular stress distribution at t = 0.5 and different values of α.

5. Conclusion

A two-dimensional boundary value problem based on the theory of generalised magneto-thermo-viscoelasticity for a spherical cavity with one relaxation time based on a fractional order model is solved. The spherical cavity of a solid surface is taken to be traction free with subject to both heating and an external magnetic field. Theoretical and numerical results reveal, that all the fractional-order parameters and time have a salient effect on the considered physical variables. The following concluding remakes can be considered according to the results of the present study.

1. In figure 2–5, the effect of time is quite pertinent on all the fields and can easily be noticed from the figures. The increase in the values of time results in increases in the numerical values of the physical variables. Hence, it has a increasing effect.

2. In figure 6–9, we observe that the, the fractional-order parameter strongly affects the physical quantities. It has a decreasing effect (in terms of magnitude) a profile of temperature, displacement and stresses.

3. The fractional order parameter 0 < α < 1, 1 < α < 2 and α = 1 indicates the weak, strong and normal conductivity respectively. For a normal conductivity α = 1 the results coincide with all the previous of application that are taken in the context of the generalised thermoelasticity with one relaxation time in the various field.

4. The results presented in this paper will be very helpful for researchers concerned with martial science, and designers of new materials, etc.

Nomenclature (List of Symbols):

J current density vector (A/m^2)

E induced electric field (V/m)

H_0 applied Magnetic field (N.s/C.m)

h the perturbation occurred in the total magnetic field by induction (Tesla)

u_i components of displacement vector (m)

T absolute temperature (K)

T_0 reference uniform temperature (K)

C concentration of the diffusive material in the elastic body (m^2/s)

α_t coefficients of linear thermal expansion (K^{-1})

α_c coefficients of linear diffusion expansion (K^{-1})

k' thermal conductivity (W/m.K)

C_E specific heat at constant strain (J/Kg.K)

e cubical dilation (K^{-1})

t_0 thermal relaxation time (s)

t_1 diffusion relaxation time (s)

F_i component of Lorentz force (Tesla)

P chemical potential (J/kg)

D diffusion coefficient (kg/m^3.s)

c speed of propagation of isothermal elastic waves

q_r heat flux in the radial direction(W/m^2)

a coefficient describing the measure of thermoelastic diffusion effects

b coefficient describing the measure of thermoelastic diffusive effects

α_1, component of thermoviscoelastic relaxation time(s)

α_2 component of thermoviscoelastic relaxation time(s)

$\theta = T - T_0$ temperature increment such that $|\theta/T_0| = 1$ (K)

Greek symbols

λ , μ Lame's constants (GPa)

μ_0 magnetic permeability (H/m)

ρ density (kg/m^3)

δ_{ij} Kronecker's delta tensor

σ_{ij} components of stress tensor

Abbreviations

$1D$ one-dimensional (m)

$2D$ two-dimensional (m)

References:

[1] M. A. Biot, "Thermoelasticity and Irreversible Thermodynamics," *J. Appl. Phys.,* 27, 240-253, 1956.

[2] H. W. Lord, Y. Shulman, "A Generalized Dynamical Theory of Thermoelasticity," *J. Mech. Phys. Solids.,* 15, 299-307, 1967.

[3] M. Caputo, "Vibrations on an Infinite Viscoelastic Layer With a Dissipative Memory," *J. Acoust. Soc. Amer.*, 56, 897-904, 1974.

[4] M. A. Ezzat, " Generation of generalized magnetothermoelastic waves by thermal shock in a perfectly conducting half-space," *J. Therm. Stress.*, 20, 617-633, 1997.

[5] M. A. Ezzat, "Magneto-thermoelasticity with thermoelectric properties and fractional derivative heat transfer," *Phys. B.*, 406, 30-35, 2011.

[6] S. K. Roychoudhuri, S. Banerjee, " Magnetothermoelastic interactions in an infinite viscoelastic cylinder of temperature rate dependent material subjected to a periodic loading," *Int. J. Eng. Sci.*, 36, 635-643, 1998.

[7] S. K. Roychoudhuri, S. Mukhopadhyay, " Effect of rotation and relaxation times on plane waves in generalized thermo-viscoelasticity," *Int. J. Math. Math. Sci.*, 23, 497-505, 2000.

[8] H. H. Sherief, A. El-Sayed, A. A. El-Latief, " Fractional order theory of thermoelasticity," *Int. J. Solids Struct.*, 47, 269-275, 2010.

[9] Y. Z. Povstenko, " Thermoelasticity that uses fractional heat conduction equation," *J. Math. Sci.*, 162, 296-305, 2009.

[10] S. Deswal, K. K. Kalkal, " A two-dimensional generalized electro-magneto-thermo-viscoelastic problem for a half-space with diffusion," *Int. J. Therm. Sci.*, 50, 749-759, 2011.

[11] A. M. Zenkour, D. S. Mashat, A. E. Abouelregal, "Generalized thermodiffusion for an unbounded body with a spherical cavity subjected to periodic loading," *J. Mech. Sci. Tech.*, 26, 749-757, 2012.

[12] K. R. Gaikwad, K. P. Ghadle, "Quasi-static thermoelastic problem of an infinitely long circular cylinder," *Journal of the Korean Society for Industrial and Applied Mathematics.*, 14, 141-149, 2010.

[13] K. R. Gaikwad, K. P. Ghadle, "On a certain thermoelastic problem of temperature and thermal stresses in a thick circular plate," *Australian Journal of Basic and Applied Sciences.*, 6,34-48, 2012.

[14] K. R. Gaikwad, K. P. Ghadle, " Nonhomogeneous heat conduction problem and its thermal deflection due to internal heat generation in a thin hollow circular disk," *Journal of Thermal stresses.*, 35, 485-498, 2012.

[15] K. R. Gaikwad, "Analysis of thermoelastic deformation of a thin hollow circular disk due to partially distributed heat supply," *Journal of Thermal stresses.*, 36, 207-224, 2013.

[16] H. Sherief, A. M. Abd El-Latief, "Application of fractional order theory of thermoelasticity to a 1d problem for a half-space," *ZAMM.*, 2, 1-7, 2013.

[17] W. Raslan, "Application of fractional order theory of thermoelasticity to a 1D problem for a cylindrical cavity," *Arch. Mech.*, 66, 257-267, 2014.

[18] K. K. Kalkal, S. Deswal, "Analysis of vibrations in fractional order magneto-thermoviscoelasticity with diffusion," *J. Mech*., 30, 383-394, 2014.

[19] E. M. Hussain, "Fractional order thermoelastic problem for an infinitely long solid circular cylinder," *Journal of Thermal Stresses.*, 38, 133-145, 2015.

[20] W. Raslan, "Application of fractional order theory of thermoelasticity in a thick plate under axisymmetric temperature distribution," *Journal of Thermal Stresses.*, 38, 733-743, 2015.

[21] K. R. Gaikwad, "Two-dimensional steady-state temperature distribution of a thin circular plate due to uniform internal energy generation," *Cogent Mathematics.*, .3, 1-10, 2016.

[22] J. J. Tripathi, G. D. Kedar, K. C. Deshmukh, "Dynamic problem of fractional order thermoelasticity for a thick circular plate with finite wave speeds," *Journal of Thermal Stresses*, 39, 220-230, 2016.

[23] K. R. Gaikwad, "Axi-symmetric thermoelastic stress analysis of a thin circular plate due to heat generation," *International Journal of Dynamical Systems and Differential Equations.*, 9, 187-202, 2019.

[24] K. R. Gaikwad, S. G. Khavale, "Time fractional heat conduction problem of a thin hollow circular disk and its thermal deflection," *Easy Chair Preprint.*, 1672, 1-11, 2019

[25] S. G. Khavale, K. R. Gaikwad, "Generalized theory of magneto-thermo-viscoelastic spherical cavity problem under fractional order derivative: state space approach," *Advances in Mathematics:Scientific Journal.*, 9, 9769-9780, 2020.

[26] K. R. Gaikwad, Y. U. Naner, "Analysis of transient thermoelastic temperture distribution of a thin circular plate and its thermal deflection under uniform heat generation," *journal of thermal stress.*, 44(1),75-85, 2021.

[27] K. R. Gaikwad, V. G. Bhandwalkar, " Fractional order thermoelastic problem for finite piezoelectric rod subjected to different types of thermal loading - direct approach," *Journal of the Korean Society for Industrial and Apllied Mathematics.*, 25, 117–131, 2021.

[28] K. R. Gaikwad, S. G. Khavale, "Fractional order transient thermoelastic stress analysis of a thin circular sector disk," *International Journal of Thermodynamics.*, 25(1), 1–8, 2022.

[29] I. Podlubny, *Fractional Differential Equation*, Academic Press, San Diego, 1999.

[30] H. Stehfest, *Communication of the ACM*, 13, 47, 1970.

[31] PTCMathcad Prime-7.0.0.0, [Online]. Available: https://support.ptc.com/help/mathcad/r7.0/en/ (accessed Dec. 1, 2021).

Enhancing the Thermal Performance of a Double Pipe Heat Exchanger in Turbulent Flow Conditions

Manish Sanserwal[1,2], Devendra Yadav[1*], and Mayank Bhardwaj[3], Gurjeet Singh[4]

[1]Department of Mechanical Engineering, Galgotias College of Engineering and Technology, Greater Noida 201308, Uttar Pradesh, India
[2]Department of Mechanical Engineering, Delhi Technological University, Delhi, India
[3]University Institute of Engineering and Technology, Kurukshetra University, Kurukshetra, Haryana, India
[4]Department of Mechanical Engineering, PEC University of Technology, Chandigarh, India
E-mail: [1*]ydevendra393@gmail.com

Abstract

Heat exchangers with high thermal performance are required for industrial applications. Using heat transfer methodology in conjunction with simple design changes and assembly functions of heat exchangers could be an effective way to accomplish this. An experimental analysis was performed in this study to improve the heat transfer performance of a double pipe heat exchanger by implanting a flat strip spring turbulator (FST) within the heat exchanger's inner tube. The experimental investigation of the Double pipe heat exchanger in conjunction with three sets of FST turbulators (pitch: 15 cm, 10 cm, and 5 cm) for turbulent flow (Re 9000-38000) was carried out. The Nusselt number, friction factor ratio, and thermal performance factor of heat exchangers with FST at various pitches are found to be between 60 and 170, 1.44 and 1.76, and 0.94 and 1.06, respectively. The highest heat transfer achieved by using a flat spring turbulator is 20% for a pitch value of 5cm. In comparison to other sets of FST, a double pipe heat exchanger with FST pitch value of 10 cm has greater thermohydraulic performance. When compared to previous research, the experimental results obtained from this work at higher Reynolds numbers the friction factor are within a well-accepted range.

Keywords: Heat exchanger; spring turbulator; thermal performance factor; heat transfer coefficient; Wilson plot.

1. Introduction

The heat exchanger allows heat to be transferred from the hotter fluid to the cooler fluid. There are essentially two types of categories: direct and indirect. In comparison to direct heat exchangers, indirect heat exchangers are more commonly used in industries since they eliminate fluid mixing during operation. In the current context, designing a heat exchanger is not an easy task because it still has scale and fluid flow rate constraints depending on the application. To obtain high heat transferability in heat exchangers, more attention on size reduction is required. The numerous techniques used in the heat exchanger to improve the rate of heat transfer [1]–[4], can be categorized as active, passive, and combined techniques (Fig. 1). Mechanical aids, injection, suction, electrostatic fields, and surface and fluid vibration all demand more power (external power) than the power used to run the heat exchanger. In contrast, in passive approaches, specially engineered geometries or turbulent circulation generators or turbulators are employed to impede the fluid flow with the purpose of enhancing heat transfer without the use of an external (additional) power source [5]. Multiple heat transfer improvement approaches, such as the use of twisted strips and tapes, coil or helical wire, polished surfaces, rough surfaces, stretched surfaces, perforated conical rings, conical springs, and so on, are included in the passive approach. However, the compound strategy combines passive and active methods to improve the thermo-

hydraulic performance of a heat exchanger. Hence, heat transfer enhancement in a heat exchanger can also be procured by creating turbulence in the fluid flow and at last, considering this concept as a motivation for literature. Therefore, the literature study was carried out to investigate how much higher the heat transfer rate in the heat exchanger with turbulators can be achieved. For the improvement in heat transfer rate with a full width twisted tape under laminar flow and steady wall temperature condition, Dasmahapatra & Rao [6] utilizes a viscous non-Newtonian fluid. Al-Fahed & Chakroun [7] experimentally investigated the heat transfer enhancement in a fully developed turbulent flow with a tube-tape clearance under constant heat flux condition. Whereas, an experimental study on twisted tape turbulator in a horizontal tube under viscous flow conditions were carried out by Manglik & Bergles [8]. Zamankhan [9] studied an improvement in the heat transfer rate in a heat exchanger with a helical metal wire turbulator using a glycol-water solution as a working fluid with varying concentrations. The 3D mathematical model, also developed for the confirmation of experimental data and the comparison of numerical findings with experimental results, concluded that actual system behaviors could be predicted by the LES model. [10] investigate conical spring turbulators in different configurations (convergent, divergent, and convergent-divergent conical rings CR, DR, and CDR) at different cone angles of 30°, 45°, 60° in a concentric double pipe heat
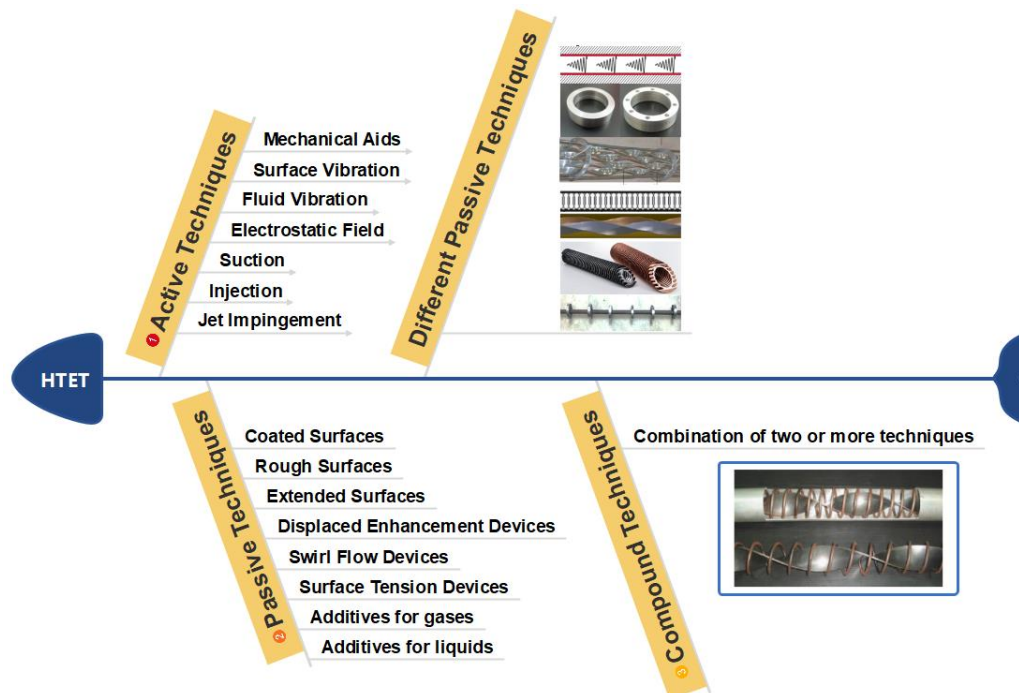
Figure 1. Techniques for heat transfer enhancement (HTET).

exchanger at different Reynolds number (10000-34000). Yadav et al. [11], [12] designed and fabricated a trio tube heat exchanger setup which has the better heat transfer capability and also compact in size. This heat exchanger requires ≈ 58% smaller in pipe length for the same amount of heat transfer as of double pipe heat exchanger. Sheikholeslami et al. [13]–[15] conducted an experimental investigation on a double pipe air to water heat exchanger with discontinuous helical turbulators (typical plane and perforated) at different Reynolds numbers, pitch and open area ratio for estimating the behaviour of heat transfer and pressure drop. For finding the optimal design of heat exchanger, Non-dominated Sorting Genetic Algorithm II (NSGA II) is used for having high efficiency and ANSYS FLUENT14 for better numerical simulation.

Later on, in the same scenario, the investigation was conducted typical and perforated circular-ring (TCR and PCR) turbulators. Nanan et.al. [16] carried out a comparative investigation in a heat exchanger between different turbulators designs: twisted and straight cross-baffles, twisted-baffles, alternate twisted and straight alternate-baffles and last one is straight baffles and with different pitch ratios (P/D = 1 to 2) and Reynolds number (6000 to 20000). For better comparison, a numerical simulation also is done with all types of turbulator for a better understanding of heat transfer enhancement and friction factor. Mashoofi et. al. [17] investigated tube in tube helically coil (TTHC) heat exchange with and without helical wire turbulator in four ways: TTHC heat exchanger a) with turbulator inside the inner tube b) with turbulator inside the annulus c) with turbulator inside both tube d) without turbulator, for evaluating the effect on heat transfer and frictional factor. The use of turbulator only in the annulus (containing hot water) and turbulator only in an inner tube (containing air) enhance the airside Nusselt number by 8-32% and 52-82%, respectively. Later, a helical wire turbulator (only inside the tube) in the shell and tube helically coiled heat exchanger was investigated by Panahi et al. [18]. Sandeep et al. [19] experimentally and numerically investigated a novel turbulator (aluminum small plate placed in the cross-type

arrangement) act as airflow divider at a different pitch to tube diameter ratios varying from 0.54 to 1.09 at a 90° angle of twist. For evaluating the Nusselt number enhancement at a different angle of twist (45° and 30°), a CFD simulation was conducted and find out 1.33 to 1.46 times and 1.43 to 1.60 times of enhancement at 45° and 30°, respectively. Khorasani et al. [20] investigated the effect of a spiral wire turbulator with four different-different spring pitches and wire diameter in a helical tube with constant heat flux. Further, each arrangement was conducted for five types of flow rates of water. It is found that, with the increase in spring pitch and wire diameter of the spiral wire turbulator, Nusselt number also increases up to 70% and 73% respectively. Zohiret. al. [21] utilize a coiled wire turbulator upon the outer surface of the inner tube of double pipe heat exchanger and achieve convective heat transfer coefficient enhancement of 400% and 450% in parallel (same direction) and counterflow (opposite direction) respectively. Budaket. al. [22] numerically analyzes the four geometries of turbulators in concentric pipe heat exchanger located inside the inner pipe and considering both parallel flow and counter flow condition at different flow rates. Also, formed an ANSYS 12.0 fluent program code to analyses pressure and thermal characteristics. Kumar et. al. [23] included the effect of perforation index (PI = 8% to 24%) and found, 4 and 1.47 times of heat transfer enhancement at PI=8% & d/D=0.6 and PI=24% & d/D=0.8 condition, respectively when compared with the plain tube. Singh et. al. [24] experimentally investigated circular solid ring turbulator with multiple twisted tape arrangements inside the core. Later, Kumar et al.[25] utilized both solid and perforated circular-ring turbulator with twisted tape for investigation. Results revealed improvement in both, heat transfer and thermal performance factor over the smooth pipe in a range of around 2.2-3.54 and 1.18- 1.64 times, respectively. Whereas, Dattet. al. [26] investigated a solid circular ring turbulator with a number (ranges 1 to 4) of square wing twisted tape. Akpinar [27] experimentally studied the effect of helical spring turbulator inside the inner pipe of a double pipe heat exchanger on heat transfer and friction factor. Nusselt

number and dimensionless exergy loss increment found to be 2.64 and 1.16 times, respectively as compared to the heat exchanger not using turbulator. Maradiya et. al. [28] revealed that twisted tape as turbulator not performed well with air as compare to water as a working fluid due to large density of liquid. Also, in case of air heating application, ribs or deflector and vortex generators, whereas, in case of liquids, swirl producing devices are more useful in thermal performance factor improvement.

According to the literature and recent review papers [29]–[31], passive turbulators perform better in the water medium than in the air medium in the double concentric pipe heat exchanger. In most cases, turbulators clearly increase the heat transfer rate to a significant level at a high Reynolds number. The majority of the researches concentrated on disturbing the fluid not only in the centre but also along the wall of the heat exchanger tube (where turbulators are inserted) in order to disturb the laminar sub-layer. The current study used a flat strip spring turbulator (FST) to alleviate the disadvantages associated with earlier investigations, namely the higher value of the friction factor. This FST design advantage of less material use and to expect the maximum possible increase in heat transfer at the lowest pressure drop. So far, no experimental work on flat metal strip springs has been published; this is a novel design consisting of circular rings, springs, and twisted tape to provide better distribution of fluid streams with lower frictional loss. This research also focuses on the employment of several sets of FST turbulator to obtain the best FST value for maximum thermohydraulic performance.

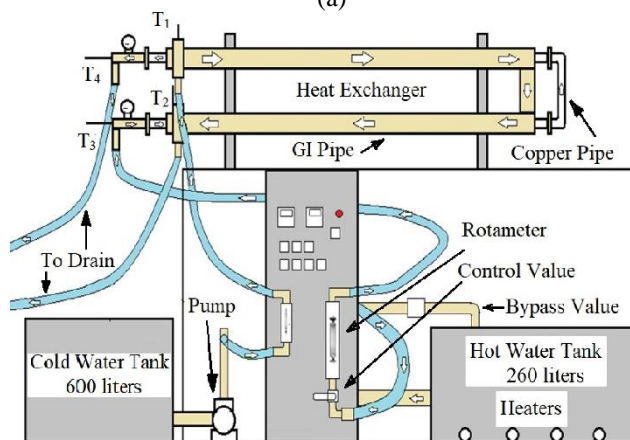## 2. Experimental
2.1 Fabrication of Experimental Setup
The theoretical analysis of the double pipe heat exchanger helped to develop the final size of the heat exchanger. Well before its mountings and attachments, the new apparatus underwent primary calibration. The construction of the experimental setup is made of mild steel to make the apparatus stable and sturdy. The experimental setup consists of housing for hot water tanks, cold and hot water pumps, display boards and test pipes. Two cold water tanks were used, one for the supply of fresh low-temperature cold water and the other for the storage of high-temperature cold water from the test section. Coldwater (at room temperature) and hot water (at set point 76 ±1°C) were allowed to flow through the annulus and inner pipe section, respectively, in the counter-flow direction. A schematic diagram of the experimental setup is shown in Fig. 2.

The test section consists of smooth inner copper tubes of 4432 mm length and outer (OD) and inner (ID) diameters of 24.5 mm and 21.5 mm respectively. The tubes were brought in, three separate parts of 2m+2m and a bend of 0.232 m. The outer G.I. pipes were selected accordingly so that there remains an effective inside diameter sufficient enough to maintain adequate flow and not to alter the original flow rate having an outer and inner diameter of 45mm and 50 mm respectively. The U-bend section is made detachable by providing flange couplings on both ends of individual lengths of copper tubes. This detachable portion was utilized to insert a full-length FST setup (when mounted on rods) easily. Two rotameters (glass tube flow meter) i.e. a cold water side small and a hot water side large were employed, with a maximum range of 100 to 1500 and 100 to 2000 LPH (liters per hour) respectively. The cold water (at room temperature) is drawn from a cold water tank (capacity of

600 liters) using a 0.5 Horsepower pump. The flow was controlled with the help of a bypass value to set the required flow rate in a small range rotameter. For a set of readings, mass flow rates for cold & hot water were kept equal. Both flow rates (cold, hot water) start from 400 LPH and end at 1500 LPH with an increase of 100 LPH for every reading. Two pressure gauges (bourdon tube) were used of a range of 0-2 kg/cm^2 and a least count of 0.001kg/cm^2. One was installed at the entry of the test section and the other just at the exit of the test section. Four PT100 RTDs (Resistance temperature detector) sensors were used for measuring the inlet &outlet temperatures of hot (T_3, T_4) & cold water (T_1, T_2). The detailed overview of the various aspects of the experimental setup is listed in Table 1.

(a)

(b)

Figure 2. (a) Experimental setup, (b) Schematic of double pipe heat exchanger experimental setup.

Table 1. A detailed description of different components of the experimental setup.

Name	Specification	Dimension
Outer G.I. pipe	Outer Diameter	50mm
	Inner Diameter	45mm
	Length	4232mm
Inner copper pipe	Outer Diameter	24.5mm
	Inner Diameter	21.5mm
	Length	4432mm
Flat strip spring insert	Width	2.5mm
	Thickness	1mm
	Inner Diameter	21.5mm
	Length	150mm

2.2 Accretion Techniques Utilized in Current Work

An overview investigation of different types of turbulence generation devices has been conducted in a wide range of Reynolds numbers. A spring turbulator perform better for turbulent flow with conical shape and different arrangements of converging, diverging and converging and diverging. In turbulent flow, conical converging spring shows lower friction factor and disturbance to boundary layer as compared to diverging spring in circular cross-section pipe within range of 10,000 to 34,000 [10]. In contrast, the performance of helical spring tubulators inside the inner pipe of a double pipe heat exchanger. Nusselt number increases as the pitch of helical spring increases at higher Reynold number [27]. The perforated solid metal ring was tested with different open area ratio (0 to 0.0833) in the range of Reynolds numbers 6000 to 12,000 Additionally, it was noted that the friction factor decreased as the perforations increased in the metal ring inserts when liquids used as working fluid [15]. The combined performance of metal rings and twisted tape turbulaors with different pitch ratios (1 and 2) and twist ratios (2,3 and 4) was investigated and found higher heat transfer enhancement but at a cost of higher friction factors in the ranges of Reynold number from 6000 to 24000 [24]. A triple twisted tape utilised as swirl flow generator inserts with four type of twist ratio (1.92 to 6.97) under the condition of constant heat flux. As the twist ratio decreases, values of different parameter (Nu, friction factor and efficiency) increases within the range Reynold number of 7200 to 50,200 [32]. The performance of helical spring tubulators was not as good as that of conical spring tabulators. The perforated metal ring turbulators have close to half the Nusselt number values of conical spring turbulators. Single twisted tape turbulators are found to perform better in flow with a low Reynolds number as opposed to one with a higher Reynolds number because they block the flow, which results in an increased friction factor.

Compared to the other swirl inserts, Nusselt number performance of metal rings and twisted tape turbulaors was found to be the best but with higher friction factor value. Hence thermohydraulic performance of twisted tape not better at higher values of Reynold number of turbulent flow. Therefore, it may be estimated that, for double pipe heat exchanger, flat plate turbulator perform well in the turbulent flow because its having all essential benefits of conical spring, metal rings and twisted tape.

In current work, a double pipe heat exchanger is used as a standard configuration. The passive heat transfer enhancement technique was predictable in order to increase the efficiency of the current heat exchanger without affecting the surface area necessary for heat transfer. Flat strip spring turbulators as shown Fig. 3 were used as swirl generators. Diameter of FST was 21.4mm which was only adequately large enough to get fit inside the inner copper tube so that, once inside and after initiation of hot water flow any undue movement or shivering could be prohibited. FST was fabricated in Mohits springs Pvt. Ltd. located in Meerut Utter Pradesh who are specialized in the manufacturing of springs. The FSTs were visualized mounted simultaneously on thin high carbon steel at certain specific gaps known as Pitch. Rods of varying pitches were prepared to insert them in inner copper tubes. The idea behind this concept was to create an obstruction to hot water flow which consequently enhances the turbulence and swirl flow thereby augmenting the rate of heat transfer.

FSTs were mounted by brazing on high carbon steel rod to prevent any flickering when inserted in inner copper tubes and with hot water flow commenced. Several pitches were decided in advance depending upon which the brazing was done. The U bend section was detached by opening the flange couplings, and hence, the FST of P = 15cm was inserted followed by 10cm and 5cm pitches.

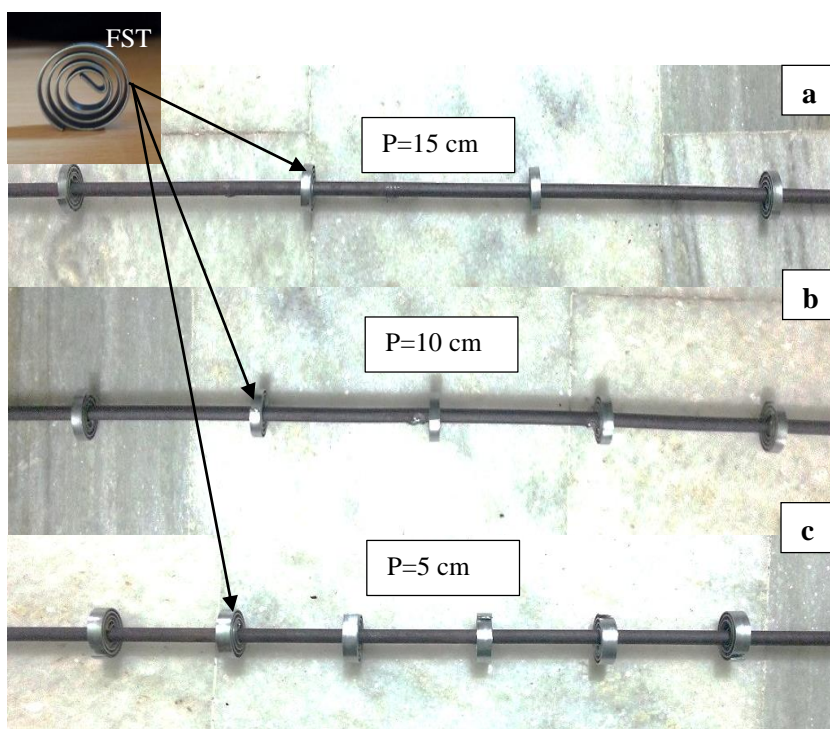*Figure 3. Flat spring tabulator (FST) mounted on rod having (a) 15 cm pitch, (b) 10cm Pitch, (c) 5cm Pitch.*

3. Methodology
3.1 Problem Formulation
During the experiments, some numerical investigations constraints/assumptions were taken;
1) Flow is assumed to be steady, non-uniform and incompressible. 2) Neglecting the heat losses in all directions by maintaining isothermal condition 3) the inner side coefficient of thermal expansion and outer side coefficient of thermal contraction of the inner pipe in the concentric pipe of heat exchanger negates each other. 4). the inner surface of the pipe is assumed to be smooth.

3.2 Standardization of the Heat Exchanger Set-up
Calibration of RTD and rotameter is an important task for getting the idea of the accuracy of the experimental setup. For the calibration of RTDs, all of them were dipped (at the same depth) in a water tank maintained at a constant temperature. By taking the reference of one of the RTD (T_4) temperature readings, other RTDs reading values (T_1 to T_3) were corrected accordingly and after taking 8 number of observations, calibration found to be ±1. In the case of rotameter calibration, initially, two buckets (25 kg each) were used for collecting and measuring the weight of water. A flow rate of the small rotameters was varied from 300 LPH to 700 LPH. Each observation was taken for 180 seconds and

ound percentage in error ranging from 1.307 to 1.774. And three observations were done for each mass flow rate of cold water rotameters. Similarly, large rotameters calibration was done by varying its mass flow rate from 800-1200 LPH for the same amount of time and observed percentage in error ranging from 1.715 to 2.614.

Before commencing the experimentation earthing of the apparatus was done. Friction factor and pressure drop readings were attained for the plane tube to verify the results with the existing standard equation for friction factor. This procedure was to eliminate the chances of deviation that could occur by repeated insertion and extraction of FSTs, which induce certain scratches (wall roughness) on the inner side of the copper tube. The readings hence obtained were compared with the Blasius equation to verify the plane tube results. This whole procedure was done at a normal temperature.

3.3 Thermal Performance Result and Repeatability
The complete experiment was re-conducted for thermal performance result and repeatability check (shown in Tables 2,3 & 4). For calculating the equivalent Reynolds number, water and pumping power was kept constant.

Table 2. Experimental data for repeatability Heat transfer versus Re for FST having pitch 15 cm.

$\dot{m}_{cw}, \dot{m}_{hw}$ (Kg/s)	T1 (°C)	T2 (°C)	T3 (°C)	T4 (°C)	Re_{hw}	Trail 1 Nu_{Exp}	Trail 2 Nu_{Exp}	%diff
0.113	35.9	57	75.8	57.1	9712.452	63.044	59.067	-6.732
0.141	35.8	56.2	75.8	57.9	12043.41	74.622	73.314	-1.783
0.17	35.8	55.8	75.9	58.6	14457.88	87.217	88.222	1.138
0.198	35.9	55.7	75.9	59.6	17115.7	98.551	97.270	-1.317

Table 3. Experimental data for repeatability heat transfer versus Re for FST having pitch 10 cm.

$\dot{m}_{cw}, \dot{m}_{hw}$ (Kg/s)	T1 (°C)	T2 (°C)	T3 (°C)	T4 (°C)	Re_{hw}	Trail 1 Nu_{Exp}	Trail 2 Nu_{Exp}	%diff
0.113	36.2	58.1	76.3	57.1	9643.40	64.32	62.770	-2.482
0.141	36.2	57.7	76.2	57.6	12043.41	78.90	77.715	-1.534
0.17	36.3	56.9	76.2	58.6	14457.88	91.31	92.489	1.269
0.198	36.3	56.7	76.1	59.6	17115.7	107.66	103.88	-3.642

Table 4. Experimental data for repeatability heat transfer versus Re for FST having pitch 5 cm.

$\dot{m}_{cw}, \dot{m}_{hw}$ (Kg/s)	T1 (°C)	T2 (°C)	T3 (°C)	T4 (°C)	Re_{hw}	Trail 1 Nu_{Exp}	Trail 2 Nu_{Exp}	%diff
0.113	36.3	58.7	76.9	57.1	9643.4	68.56	67.28	-1.902497
0.141	36.2	58.3	76.8	57.7	12043.41	83.18	82.11	-1.30313
0.17	36.2	57.6	76.7	58.5	14457.88	95.43	96.76	1.374535
0.198	36.4	57.2	76.5	59.3	17115.7	110.79	106.5	-4.028169

3.4 Factors Affected by Varying Pitch Between Consecutive FST

Pitch over here refers to the distance between two consecutive FST mounted on a brass rod. Apart from the enhancement in heat transfer and thermal performance installation of FST leads in the increase in pumping power requirement. The minimum pitch of the turbulators allows more turbulators on the given length which leads to more friction to the flow, more back pressure generates and all these leads to more pumping power requirement. This arrangement also separates the boundary layer commencing earlier as the pitch between two consecutive turbulators going to be decrease. Fig. 4 represents the effect of FST over variation in pitch ratio
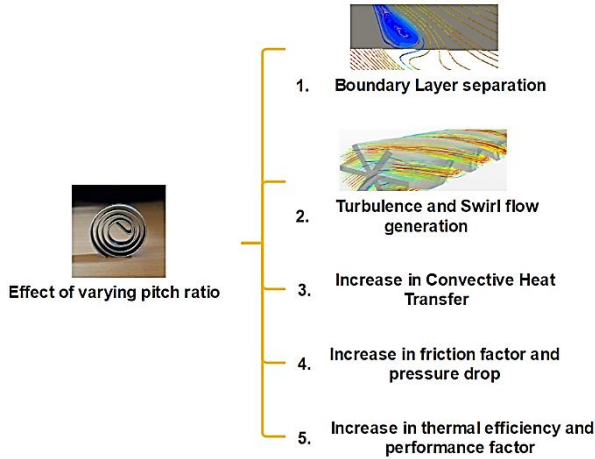
Figure 4. Repercussion by varying pitch value of FST.

4. Data Reduction

Water is taken as a working fluid for all the experiments conducted with a parametric study of the effects of variation in mass flow rate for turbulent case. Installation of FST with varying pitch ratio influences the flow conditions including an adverse effect i.e. increment of friction factor. Different equations required for the basis of such experiments are summed as follows:

Quantity of heat flow [33] for hot and cold water loops can be calculated from Eqn. (1) and (2)

$$\dot{Q}_c = \dot{m}_c \times C_{pc} \times (T_{ce} - T_{ci}) \tag{1}$$

$$\dot{Q}_h = \dot{m}_h \times c_{ph} \times (T_{hi} - T_{he}) \tag{2}$$

The arithmetic average of heat exchange from the hotter and colder fluid streams is

$$Q_{ave.} = \frac{Q_h + Q_c}{2} \tag{3}$$

The overall heat transfer coefficient can be calculated as

$$U = \frac{Q_{ave.}}{A \times lmtd} \tag{4}$$

$$lmtd = \frac{(T_{hi} - T_{ce}) - (T_{he} - T_{ci})}{\ln\left((T_{hi} - T_{ce})/(T_{he} - T_{ci})\right)} \tag{5}$$

Where A is the circumferential area of the inner pipe.

4.1 Standard Equation

The non-dimensional numbers; Nu, Re and Pr calculated from Eqn:

$$Nu = \frac{hD}{k} \tag{6}$$

$$\text{Re} = \frac{\rho V D}{\mu} \tag{7}$$

$$\text{Pr} = \frac{\mu c_p}{k} \tag{8}$$

$$\lambda = \frac{\Delta P}{\left(\dfrac{l}{d}\right)\left(\dfrac{\rho V^2}{2}\right)} \tag{9}$$

$$V = \frac{\dot{m}}{\rho A_c} \tag{10}$$

4.2 Heat Transfer and Friction Factor Calculation

For the heat transfer calculations, some standard equations from the literatures were used for the experimental flow conditions.
DittusBoelter Equation [34]

$$Nu = 0.023 \text{Re}^{0.8} \text{Pr}^{0.3} \tag{11}$$

Friction factor for the different flow arrangements were calculated from Blasius Equation and Darcy-weisbach equations [33]

$$\lambda = \frac{0.3164}{\text{Re}^{0.25}} \tag{12}$$

$$\lambda = \frac{\Delta P}{\dfrac{L}{D}\dfrac{\rho V^2}{2}} \tag{13}$$

Thermal performance factor calculation at constant pumping power

$$\left(\lambda \text{Re}^3\right)_{PT} = \left(\lambda \text{Re}^3\right)_T \tag{14}$$

The thermal performance factor and performance evaluation criteria is the key parameter in designing effective heat exchanging devices [35]. The thermal performance factor (η) is the ratio of the Nusselt number ratio (Nu_T/Nu_{PT}) to the friction factor ratio (λ_T/λ_{PT}) considering constant pumping powerand can be represented as

$$\eta = \frac{Nu_T / Nu_{PT}}{\left(\lambda_T / \lambda_{PT}\right)^{1/3}} \tag{15}$$

4.3 Uncertainty Calculation

Mass flow rate, pressure (at inlet and exit), and temperature distribution were the variables measured by the test rig. Before being used in the experimental setting, all variable measuring equipment were calibrated. The two crucial factors, Nusselt number and Reynolds number, were going to be used to understand the experiment's measured variables. Temperature and pressure drop are the most effect-causing variables for Nusselt number, while flow rate is the greatest effect-causing variable for Reynold number. Fluid thermo-physical properties, on the other hand, had a significant impact on both of them.

The root sum square equation, which combines the effects of each distinct input as proposed by Kline and McClintock [36], could be used to determine the uncertainties in the computed findings with improved precision. The uncertainties in the aforementioned equations are caused by inaccuracies in the primary parameters, as indicated in Table 5. The highest computed uncertainty in heat transfer coefficient, Prandtl number, and friction factor obtained from all experiments are 4%, 2.5%, and 5%, respectively. The computed uncertainty in the results is calculated from Eq. 16.

$$R = \pm \sqrt{\left(\frac{\delta R}{\delta x_1}\delta x_1\right)^2 + \left(\frac{\delta R}{\delta x_2}\delta x_2\right)^2 + \ldots + \left(\frac{\delta R}{\delta x_n}\delta x_n\right)^2} \quad (16)$$

Where δx is the uncertainty of the independent individual variables and $\frac{\partial R}{\partial x}$ is sensitivity.

Table 5. Uncertainties in the main parameters.

Parameter	Uncertainty (%)
Annulus-side Reynolds number	± 1.77**
Tube-side Reynolds number	± 2.61**
Thermocouple	± 0.1 °C*
Pressure transducer	± 0.35*
Heating wire	± 0.15*

* Based on manufacturer claim.
** Based on calibration.

4.4 Preparation of Wilson Chart and Standard Equations

The calculation of the film heat transfer [37], [38] can be estimated by the very popular technique known as the Wilson plot. This plot is based on the overall thermal resistance in the total heat transfer in the form of convection. For all sets of experiment, except the first term, all other resistance is constant on the RHS of Eq. 17.

$$\frac{1}{U_i} = \frac{1}{h_i} + \frac{h_i}{d_o h_o} + \frac{x_w d_i}{k_w d_i} \quad (17)$$

As a flow on inner waterside is turbulent and the variation in thermal properties are negligible, for a smooth tube with a flow rate of more than 10000 Reynold number, the Seider Tate equation is of the form

$$h_i = A\,Re^{0.8} \quad (18)$$

Therefore, from Eq. 17 and Eq. 18, it can be written as

$$\frac{1}{U_i} = \frac{1}{A\,Re^{0.8}} + K \quad (19)$$

Here, K is a constant and its value is to be estimated on the intercept of the y-axis of the Wilson chart (1/U_i vs. 1/$Re^{0.8}$). This value was put in Eq. 17 to obtain the value of h_i. This expression is in the form of the exponent of Reynold number.

The same procedure as was done for the plane tube was repeated for whole pitches of FST. Heat transfer results were obtained by preparing Wilson Charts between Reynolds number (Re) and overall heat transfer coefficient (U) it can be seen in section 5.3.

5. Result and Discussion

In this analysis effect of Flat Strip Spring Turbulator (FST) installed inside the double pipe heat exchanger in the counter-current flow arrangement was analysed. Friction factor increment means a decrease in the pitch ratio of turbulators used in the experiment, which ultimately affects the pressure drop i.e. pumping power. But, for maintaining higher value of Reynolds number, a constant (high) pumping power is required. Hence, it is desired to maintain an optimum condition i.e. balance between pitch ratio, friction factor, pressure loss, and ultimately in pumping power. The main function of a turbulator is to generate detachment and reattachment of flow around them and as a result of this, reduces the effect of the boundary layer (when heat is transferred through the laminar effect). This separation of flow generates proper mixing regions (with large turbulence energy) which ultimately destroy the eddies and vortex formation for heat transfer enhancement.

5.1 Plain Tube Experimentation

For hot water, heaters were used to heat the water to 76°C, as this temperature lied within the limits of the heating capacity of heaters and could be easily maintained in the working conditions. A temperature regulator is used for maintaining constant temperature. The tank is connected to pump (centrifugal type) for circulation of hot water inside the inner pipe of the heat exchanger and for controlling the flow rate a bypass valve is used (recirculation the hot water back into the tank). This hot water allowed to pass through the inner tube of heat exchanger at a desired mass flow rate and simultaneously cold water flow was initiated and this set up was left continued for at least 20 minutes to attain a steady-state condition. Now that a steady state was achieved, the main experimentation was commenced by adjusting the mass flow rates by using rotameters of both cold water and hot water side at desired values. The readings from RTDs were obtained only when a steady condition is achieved. This procedure was repeated at various flow rates (0.1134-0.425 Kg/s) of cold and hot water. Under the assumption of uniform heat flux, the calculation of Nusselt numbers is done and compared with the fundamental Eqn. 11 (provided by Dittus and Boelter) for validating the current plane tube.

The Nusselt number variation with Reynolds number for plain tube experiment are shown in the Fig.5(a).Whereas, it was noted that the variation of Nusselt number within the acceptable range of Dittus– Boelter equation correlation [34]. Before beginning any heat exchanger related experiment utilizing turbulator, measurement of friction factor as a secondary parameter is necessary. So, verifying (under similar test conditions) the current plain inner copper tube for the friction factor parameter by comparing of the current data obtained with those obtained from the Blasius correlation. This variation of friction factor with the Blasius equation is show in Fig.5(b).
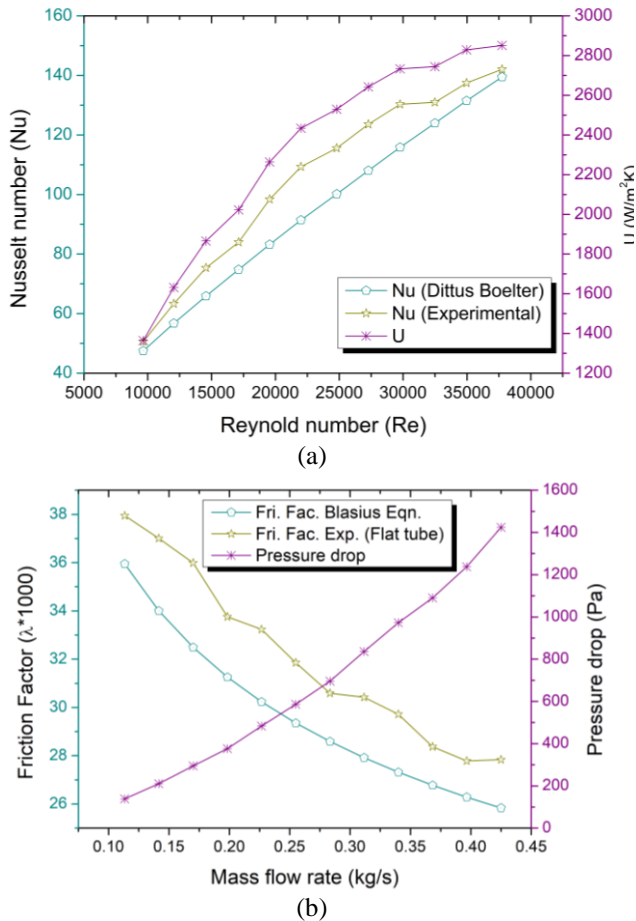
Figure 5. (a) Nusselt number and overall heat transfer coefficient for plane tube, (b) Variation in friction factor and pressure drop for plane tube.

5.2 Effect of FST Turbulator on Nusselt Number

Effect on tubes with FST at different pitches (PR=15, 10, and 5cm) on the heat transfer rate (Nu) is demonstrated in Fig. 6. For all values of Reynolds number, the heat transfer rate for FST is higher than those of the plain tube and this is due to the destruction of the thermal boundary layer present near the inner tube wall. In different turbulator arrangements, it is found that with the decrease of pitch the heat transfer rate increases. This is because since, FST with a smaller PR of 5cm, create more intervention in the generation of thermal as well as hydrodynamic boundary layer with a greater degree of turbulence than that of higher PR of 15cm. The quantitative analysis reveals that the percentage heat transfer rate in the tube with FST of P =15cm, P=10cm, P= 5cm is 7.93%, 13.09%, and 14.26% higher than those in the plain tube at Re =17115.70.

Fig. 6. (b) Indicate the Nusselt number ratio variation with respect to Reynolds number. From the graph, it is evident that Nusselt number values decrease with increasing Reynolds number or its having higher rate of heat transfer at lower values of Reynolds number. This occurs primarily because at low Reynolds numbers the thermal boundary layer thickness is higher near the surface of the pipe, limiting heat transfer, while after putting the FST in place, the boundary layer effect is no longer noticeable. It is evident that, 10 cm pitch FST has a higher value of Nusselt number ratio as compared to 15cm pitch. In all three cases, the values attained were greater than unity, demonstrating the advantage of using FST as an insert in heat exchangers as compared to a plan tube. It is found that the highest and lowest values of the Nusselt number ratio are in between 1.20 and 1.13 for FSTs with a pitch of 5 cm, whereas in case of pitch 15 cm it is between 1.10 and 1.05 for FSTs.
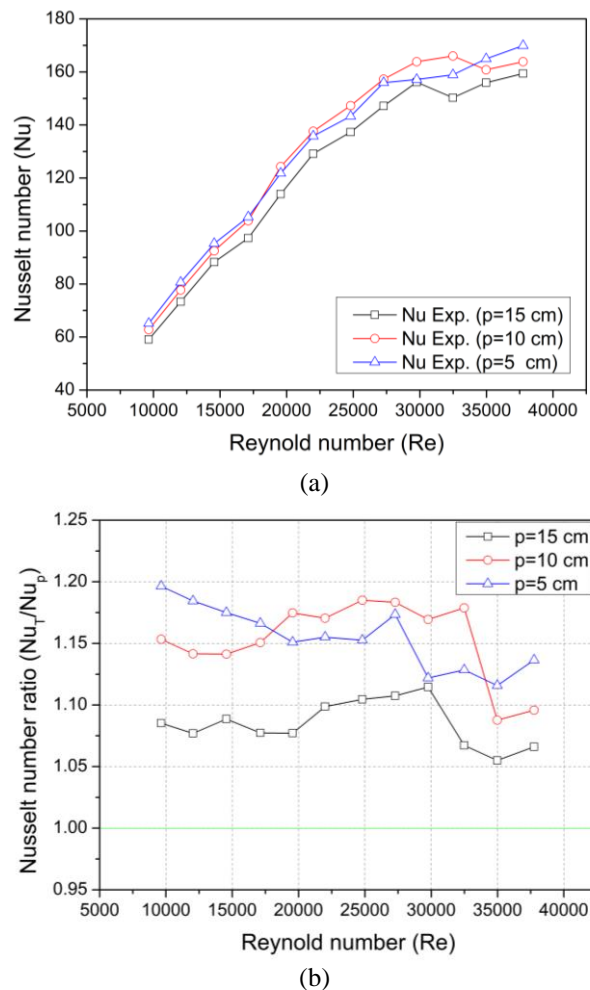

Figure 6. (a) Heat transfer enhancement by FST, (b) Effect of pitch values on Nusselt number.
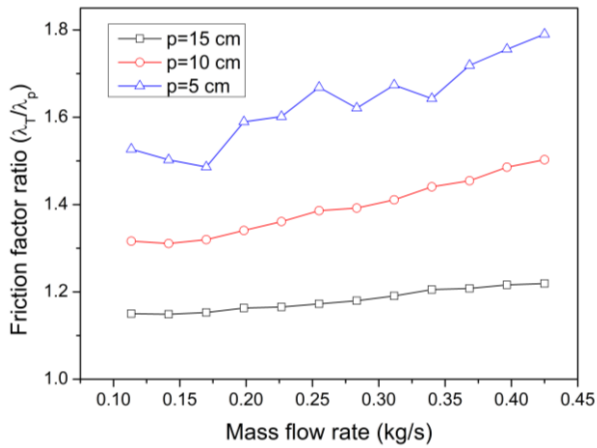
5.3 Effect of FST Turbulator on Friction Factor

The friction factor is one of the important parameters for improving the thermal performance factor in heat exchangers. Across the test section, friction factor value varies directly with the pressure drop values and inversely with the square of fluid velocity values. Whereas, by considering Reynolds number increment, friction factor decreases but pressure drop increases. So, as the turbulator used in the heat exchanger, the friction factor will increase because of the obstruction in the flow. Therefore, it is very important to find out a turbulator that imparted the lowest friction factor.

From the scenario of Fig. 7 (a&b), It is concluded that the value of friction factor increases as the pitch ratio decreases for the same Reynold number. The reason behind this trend is smaller the distance between FSTs, and more obstructions faced by the flow which ultimately causes an increase in friction factor. The simple fact is that, when the distance between two consecutive FSTs is less, more space is available for mounting the FSTs on the cylindrical rod inside the inner copper tube, thus the more obstruction against the flow stream of hot water. Hence, more turbulence results in a high-pressure drop.
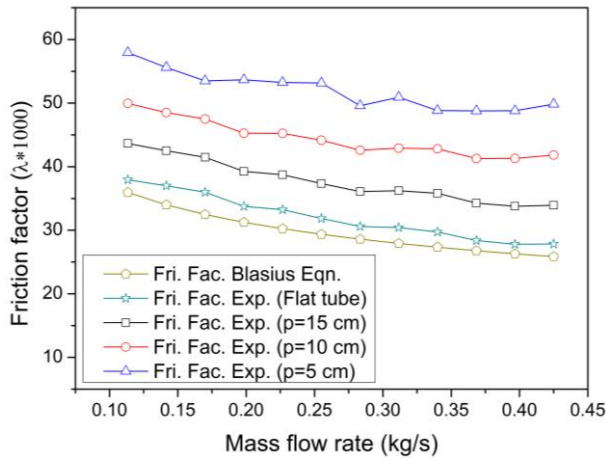
(a)

(b)
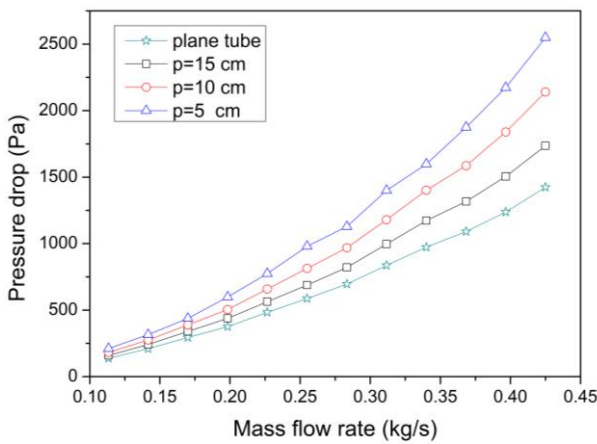
(c)

Figure 7. (a) Influence of different pitch value on (a-b) turbulator on friction factor, (c) Pressure drop.

The turbulator acts as an obstruction, as the difference between two consecutive FST increases, local flow velocity quantity also increases (which means local Reynolds number increase). The occurrence of these events may generate lots of vortexes and these vortexes when faces centrifugal force due to secondary flows cause pressure drop as compare to plan tube. As shown in Fig. 7(c) that as the FST pitch decreases pressure drop increases for the constant value of the Reynolds number. FST pitch increment means that obstruction located at larger distances and as a result of this decrement in Reynolds number and generation of vortexes is observed with an increment in hydraulic diameter. All these phenomena together cause the decrement in pressure drop.

5.4 Effect of FST Turbulator on the Thermal Performance Factor

Only thermal aspects cannot be set as the final criteria for the selection of FST. Here, an optimal value of pitch should be selected which has better heat transport capability and also have a lower value of frictional loss (pumping power). The thermal performance factor is also one of the important factors to count both the effect in the heat exchanger. A significant increment in Nusselt number and friction factor is always observed for various types of turbulators. So, designing the geometry of turbulator is an important task with a view of obtaining maximum thermal performance factors. As can be seen in Fig. 8(a) at constant pumping power, it is evident from the graph that Reynold number and thermal performance factor are in inverse relation with each other. Also, this can be concluded that because of improved thermal and hydraulic performance, the FSTs at P = 10 cm (having the same pumping power) are most efficient.

As can be seen from Fig. 8(b) there occur a significant change in heat gain and heat drop trends at different mass flow rate. It was observed that at higher mass flow rate heat drop and heat gain become approximately equal and the general trend was the heat drop rate decreases with increase in mass flow rate and rate of heat gain increases with increase in mass flow rate.
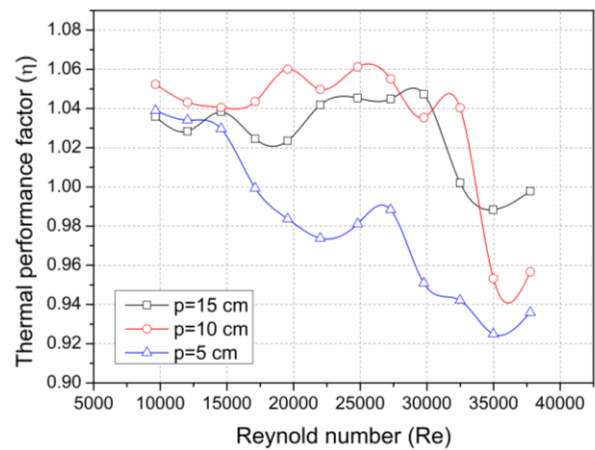
(a)
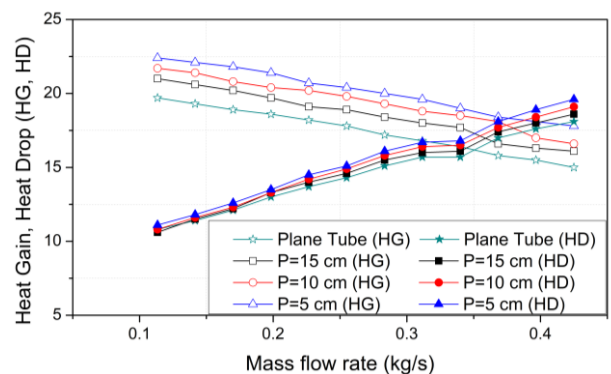
(b)

Figure 8. (a) Variation in thermal performance factor with Reynold number, (b) HT characteristics at constant $\dot{m}_{hw}$ & $\dot{m}_{cw}$.

5.5 Experimental Results Conjugated to Wilson Plot

Wilson plot is a very important tool that is utilized to check the performance of different types of heat exchangers [42]. Through this approach, the overall heat transfer coefficient value can directly be calculated which is not

easier indirect calculation from the experimental results due to inaccessible surface temperature values. The experimental results obtained from the experiment on double pipe heat exchanger experimental setup with flat strip spring Turbulator insert were analyzed with Wilson chart (having variation between overall heat transfer coefficient (U) and Reynold number). The results were plotted between $10000/U_i$ and $10000/Re^{0.8}$, which is presented in Fig. 9. The variation of $10000/U$ follows the linear trend as of the Wilson plot. However, the experimental values are slightly lesser than that of the straight-line of the Wilson plot.
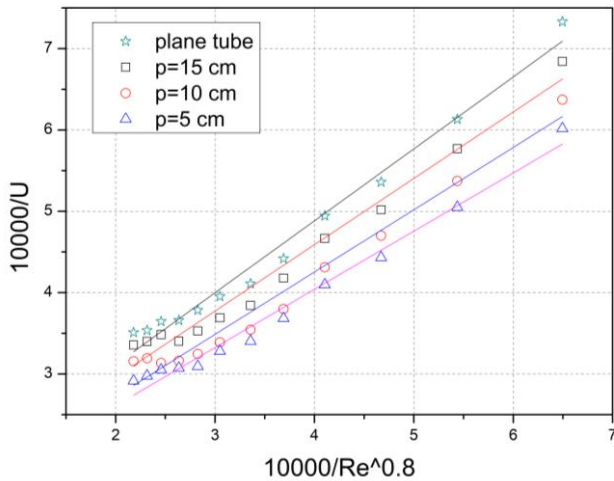

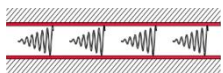*Figure 9. Visualization of overall heat transfer coefficient with Wilson plot.*

5.6 Comparison of Performance Parameters of Different Turbulators

In the Table 6, the term "Nusselt number ratio" (Nu_{max}/Nu_p) is the ratio of maximum Nusselt number after augmentation to Nuseelt number of the plane tube, and "friction factor ratio" (λ_{max}/λ_p) is the ratio of maximum friction factor after augmentation to friction factor of the plan tube. In current work, the Nusselt number ratio comes only 1.2 at the expense of friction factor ratio of 1.44 in a range of Reynolds no. (9000–38,000). Whereas, maximum increment in Nusselt number ratio is claimed by Singh et. al. [24] i.e. 4.6 but at a higher value of friction factor ratio of 36.07 in a range of Reynolds no. (6300– 22500) and as it is well known that, with the increment in Reynolds number friction factor also increases which further increases required pumping power and makes the heat exchange process uneconomical. So, in the present study even at a higher value of Reynolds number friction factor obtaining well-accepted range as compared to the previous studies.

6. Conclusion

The present experimental study presents the potential application of FST to enhance the heat transport performance of a concentric double tube heat exchanger. The experimental objectives investigation was successfully carried out with the insertion of FST at various pitch values at varying cold and hot water flow rate of 500 to 1500 LPH and 500 to 2000 LPH, respectively. All the time, the experiment was in turbulent flow with Reynold number ranging from 9000 to 38000, which significantly influences the different parameter of heat exchanger (Nusselt number, friction, and thermal performance factor). The most remarkable conclusions drawn after conducting this experiment are:

Table 6. Comparison of performance parameters of different turbulators.

Author	Turbulator used	Parameters	Reynolds Number	Nusselt Number ratio	Friction factor ratio	Image
Karakaya et. al. [10]	Conical spring turbulators	different cone angle (30°, 45°, 60°)	10,000 to 34,000	$Nu_{max} \approx 3.33\ Nu_p$	$\lambda_{max} \approx 1.72\ \lambda_p$	
Sheikholeslami et. al. [15]	typical and perforated circular turbulators	open area ratio (0 to 0.0625), pitch ratio (1.83 to 5.83)	6000 to 12,000	$Nu_{max} \approx 2.12\ Nu_p$	$\lambda_{max} \approx 11.40\ \lambda_p$	
Singh et. al. [24]	solid ring tubular (SRT) with Number of twisted tapes (TT): 1, 2, 3, 4	Pitch ratios (1 and 2_, twist ratios (2, 3, and 4)	6300 to 22500	$Nu_{max} \approx 4.6\ Nu_p$	$\lambda_{max} \approx 36.07\ \lambda_p$	
Akpinar[27]	helical (spring shaped)		6500 to 13,000	$Nu_{max} \approx 2.64\ Nu_p$	$\lambda_{max} \approx 2.74\ \lambda_p$	
Bhuiya et al. [39]	Triple twisted tape	Twist ratio-1.92–6.79	7200 to 50,200	$Nu_{max} \approx 3.85\ Nu_p$	$\lambda_{max} \approx 4.2\ \lambda_p$	
Present study	Flat strip spring turbulator	At different pitch ratio of 5, 10 &15	9000 to 38000	$Nu_{max} \approx 1.2\ Nu_p$	$\lambda_{max} \approx 1.44\ \lambda_p$	

- The enhancement of heat transfers with flat spring inserts of P =15cm, P=10cm, P= 5cm is 7.93%, 13.09%, and 14.26% higher than those in the plain tube at Re =17115.69 and flow rates at 0.19839 kg/s. Over the range investigated, the maximum heat transfer rise was about 20% for FST at pitch 5cm.
- The heat transfer rate and friction factor of FSTs increase with decreasing pitch due to the number FSTs present on the cylindrical rod was high inserted in the copper tube. However, the thermal performance factor increases with decreasing pitch
- The friction factor obtained from using the PCR with pitch 15, 10, and 5cm are found to be respectively, 17%, 30%, and 39%, over the plain tube at Reynolds number of 17997.71. An increase in the pitch of FSTs causes a reduction in Nusselt numbers as well as friction factors. The maximum friction factor rise was about 44% for Reynolds number of 22497.1.
- The maximum heat gain & heat drop-in plan tube is 19.7 & 18.1. On 15cm pitch, Maximum heat gain& heat drop is 21 & 18.6. On 10cm pitch, Maximum heat gain & heat drop was 21.7 & 19.1. On 5cm pitch, Maximum heat gain & heat drop is 22.4 & 19.6.

As the pitch between two consecutive FSTs decreases not only heat transfer rate increase but also an adverse effect increases i.e. friction factor. An optimal pitch value is suggested from this study because increasing the turbulator is not only the solution for heat transfer enhancement, a downside of this arrangement is the increasing pressure drop which leads to more power requirement and this should be considered for optimization to the maximum performance of heat exchanger.

Nomenclature

L	Total length of pipe
D	Hydraulic diameter
V	Velocity of water
ΔP	Frictional pressure drop
c	Specific heat
d	Diameter of inner pipe
Nu	Nusselt Number
Re	Reynold Number
P	Pitch
$\dot{m}$	Mass flow rate
c	Specific heat
T	Turbultor
A	Area
PT	Plane Tube
λ	Friction factor
ρ	Density of fluid
η	Thermal performance factor
LMTD	Log Mean Temperature Difference
RTD	Resistance temperature detector
HG	Heat Gain
HD	Heat Drop

Subscript	
i	Inner
o	Outer
c	Cross sectional
max	Maximum

References:

[1] A. E. Bergles, R. L. Bunn, and G. H. Junkhan, "Extended performance evaluation criteria for enhanced heat transfer surfaces," *Letters in Heat and Mass Transfer*, vol. 1, no. 2, pp. 113–120, Nov. 1974, doi: 10.1016/0094-4548(74)90147-7.

[2] W. M. Rohsenow, J. P. Hartnett, E. N. Ganic, and P. D. Richardson, *Handbook of Heat Transfer Fundamentals (Second Edition)*, vol. 53, no. 1. 1986.

[3] D. B. Berkowitz, *Handbook on Syntheses of Amino Acids: General Routes for the Syntheses of Amino Acids*, vol. 132, no. 50. 2010.

[4] H. S. Dizaji and S. Jafarmadar, "Experiments on New Arrangements of Convex and Concave Corrugated Tubes through a Double-pipe Heat Exchanger," *Experimental Heat Transfer*, vol. 29, no. 5, pp. 577–592, Sep. 2016, doi: 10.1080/08916152.2015.1046015.

[5] H. M. Şahin, E. Baysal, and A. R. Dal, "Experimental and numerical investigation of thermal characteristics of a novel concentric type tube heat exchanger with turbulators," *International Journal of Energy Research*, vol. 37, no. 9, pp. 1088–1102, Jul. 2013, doi: 10.1002/er.2919.

[6] J. K. Dasmahapatra and M. R. Rao, "Laminar flow heat transfer to generalised power law fluids inside circular tubes fitted with regularly spaced twisted tape elements for uniform wall temperature condition," in *American Society of Mechanical Engineers, Heat Transfer Division, (Publication) HTD*, 1991, vol. 174, pp. 51–58.

[7] S. Al-Fahed and W. Chakroun, "Effect of tube-tape clearance on heat transfer for fully developed turbulent flow in a horizontal isothermal tube," *International Journal of Heat and Fluid Flow*, vol. 17, no. 2, pp. 173–178, Apr. 1996, doi: 10.1016/0142-727X(95)00096-9.

[8] R. M. Manglik and A. E. Bergles, "Heat transfer enhancement and pressure drop in viscous liquid flows in isothermal tubes with twisted-tape inserts," *Wärme- und Stoffübertragung*, vol. 27, no. 4, pp. 249–257, Apr. 1992, doi: 10.1007/BF01589923.

[9] P. Zamankhan, "Heat transfer in counterflow heat exchangers with helical turbulators," *Communications in Nonlinear Science and Numerical Simulation*, vol. 15, no. 10, pp. 2894–2907, Oct. 2010, doi: 10.1016/j.cnsns.2009.10.025.

[10] H. Karakaya and A. Durmuş, "Heat transfer and exergy loss in conical spring turbulators," *International Journal of Heat and Mass Transfer*, vol. 60, no. 1, pp. 756–762, May 2013, doi: 10.1016/j.ijheatmasstransfer.2013.01.054.

[11] D. Yadav, Z. Upadhyay, A. Kushwaha, and A. Mishra, "Analysis Over Trio-Tube with Dual Thermal Communication Surface Heat Exchanger [T.T.H.Xr.]," in *Lecture Notes in Mechanical Engineering*, 2020, pp. 1–13.

[12] D. Yadav, A. Kushwaha, and A. Mishra, "Design and Fabrication of Trio Tube Heat Exchanger Experimental Setup," *SSRN Electronic Journal*, 2020, doi: 10.2139/ssrn.3576468.

[13] M. Sheikholeslami and D. D. D. Ganji, "Heat transfer enhancement in an air to water heat exchanger with discontinuous helical turbulators; experimental and numerical studies," *Energy*, vol. 116, pp. 341–352, Dec. 2016, doi: 10.1016/j.energy.2016.09.120.

[14] M. Sheikholeslami, M. Gorji-Bandpy, and D. D. D. Ganji, "Effect of discontinuous helical turbulators on heat transfer characteristics of double pipe water to air heat exchanger," *Energy Conversion and Management*, vol. 118, pp. 75–87, Jun. 2016, doi: 10.1016/j.enconman.2016.03.080.

[15] M. Sheikholeslami and D. D. D. Ganji, "Heat transfer improvement in a double pipe heat exchanger by means of perforated turbulators," *Energy Conversion and Management*, vol. 127, pp. 112–123, Nov. 2016, doi: 10.1016/j.enconman.2016.08.090.

[16] K. Nanan, C. Thianpong, M. Pimsarn, V. Chuwattanakul, and S. Eiamsa-ard, "Flow and thermal mechanisms in a heat exchanger tube inserted with twisted cross-baffle turbulators," *Applied Thermal Engineering*, vol. 114, pp. 130–147, Mar. 2017, doi: 10.1016/j.applthermaleng.2016.11.153.

[17] N. Mashoofi, S. M. Pesteei, A. Moosavi, and H. Sadighi Dizaji, "Fabrication method and thermal-frictional behavior of a tube-in-tube helically coiled heat exchanger which contains turbulator," *Applied Thermal Engineering*, vol. 111, pp. 1008–1015, Jan. 2017, doi: 10.1016/j.applthermaleng.2016.09.163.

[18] D. Panahi *et al.*, "Heat transfer enhancement of shell-and-coiled tube heat exchanger utilizing helical wire turbulator," *Applied Thermal Engineering*, vol. 115, no. 2–3, pp. 607–615, Mar. 2017, doi: 10.1016/j.applthermaleng.2016.12.128.

[19] S. P. Nalavade, C. L. Prabhune, and N. K. Sane, "Effect of novel flow divider type turbulators on fluid flow and heat transfer," *Thermal Science and Engineering Progress*, vol. 9, pp. 322–331, Mar. 2019, doi: 10.1016/j.tsep.2018.12.004.

[20] S. Khorasani, S. Jafarmadar, S. Pourhedayat, M. A. A. Abdollahi, and A. Heydarpour, "Experimental investigations on the effect of geometrical properties of helical wire turbulators on thermal performance of a helically coiled tube," *Applied Thermal Engineering*, vol. 147, pp. 983–990, Jan. 2019, doi: 10.1016/j.applthermaleng.2018.09.092.

[21] A. E. Zohir, M. A. Habib, and M. A. Nemitallah, "Heat Transfer Characteristics in a Double-Pipe Heat Exchanger Equipped with Coiled Circular Wires," *Experimental Heat Transfer*, vol. 28, no. 6, pp. 531–545, Nov. 2015, doi: 10.1080/08916152.2014.915271.

[22] N. Budak, H. L. Yucel, and Z. Argunhan, "Experimental and Numerical Investigation of the Effect of Turbulator on Heat Transfer in a Concentric-type Heat Exchanger," *Experimental Heat Transfer*, vol. 29, no. 3, pp. 322–336, May 2016, doi: 10.1080/08916152.2014.976723.

[23] A. Kumar, S. Chamoli, M. Kumar, and S. Singh, "Experimental investigation on thermal performance and fluid flow characteristics in circular cylindrical tube with circular perforated ring inserts," *Experimental Thermal and Fluid Science*, vol. 79, pp. 168–174, Dec. 2016, doi: 10.1016/j.expthermflusci.2016.07.002.

[24] V. Singh, S. Chamoli, M. Kumar, and A. Kumar, "Heat transfer and fluid flow characteristics of heat exchanger tube with multiple twisted tapes and solid rings inserts," *Chemical Engineering and Processing: Process Intensification*, vol. 102, pp. 156–168, Apr. 2016, doi: 10.1016/j.cep.2016.01.013.

[25] A. Kumar, S. Singh, S. Chamoli, and M. Kumar, "Experimental Investigation on Thermo-Hydraulic Performance of Heat Exchanger Tube with Solid and Perforated Circular Disk Along with Twisted Tape Insert," *Heat Transfer Engineering*, vol. 40, no. 8, pp. 616–626, May 2019, doi: 10.1080/01457632.2018.1436618.

[26] R. Datt, M. S. Bhist, A. D. Kothiyal, R. Maithani, and A. Kumar, "Effect of square wing with combined solid ring twisted tape inserts on heat transfer and fluid flow of a circular tube heat exchanger," *International Journal of Green Energy*, vol. 15, no. 12, pp. 663–680, Sep. 2018, doi: 10.1080/15435075.2018.1525552.

[27] E. K. Akpinar, "Evaluation of heat transfer and exergy loss in a concentric double pipe exchanger equipped with helical wires," *Energy Conversion and Management*, vol. 47, no. 18–19, pp. 3473–3486, Nov. 2006, doi: 10.1016/j.enconman.2005.12.014.

[28] C. Maradiya, J. Vadher, and R. Agarwal, "The heat transfer enhancement techniques and their Thermal Performance Factor," *Beni-Suef University Journal of Basic and Applied Sciences*, vol. 7, no. 1, pp. 1–21, Mar. 2018, doi: 10.1016/j.bjbas.2017.10.001.

[29] M. Sheikholeslami, M. Gorji-Bandpy, and D. D. Ganji, "Review of heat transfer enhancement methods: Focus on passive methods using swirl flow devices," *Renewable and Sustainable Energy Reviews*, vol. 49, pp. 444–469, Sep. 2015, doi: 10.1016/j.rser.2015.04.113.

[30] M. Omidi, M. Farhadi, and M. Jafari, "A comprehensive review on double pipe heat exchangers," *Applied Thermal Engineering*, vol. 110, pp. 1075–1090, Jan. 2017, doi: 10.1016/j.applthermaleng.2016.09.027.

[31] H. Li *et al.*, "A comprehensive review of heat transfer enhancement and flow characteristics in the concentric pipe heat exchanger," *Powder Technology*, vol. 397, p. 117037, Jan. 2022, doi: 10.1016/j.powtec.2021.117037.

[32] M. M. K. Bhuiya, M. S. U. Chowdhury, M. Shahabuddin, M. Saha, and L. A. Memon, "Thermal characteristics in a heat exchanger tube fitted with triple twisted tape inserts," *International Communications in Heat and Mass Transfer*, vol. 48, pp. 124–132, Nov. 2013, doi: 10.1016/j.icheatmasstransfer.2013.08.024.

[33] C. Ringsted, K. Eliasen, I. H. Gøthgen, and O. Siggaard-Andersen, *Positive correlation between "the arterial oxygen extraction tension" and mixed venous po2 but lack of correlation between "the oxygen compensation factor" and cardiac output in 38 patients*, vol. 50, no. S203. 1990.

[34] F. W. Dittus and L. M. K. Boelter, "Heat transfer in automobile radiators of the tubular type," *International Communications in Heat and Mass Transfer*, vol. 12, no.

1, pp. 3–22, 1985, doi: 10.1016/0735-1933(85)90003-X.

[35] R. L. Webb, "Performance evaluation criteria for use of enhanced heat transfer surfaces in heat exchanger design," *International Journal of Heat and Mass Transfer*, vol. 24, no. 4, pp. 715–726, Apr. 1981, doi: 10.1016/0017-9310(81)90015-6.

[36] S. Kline and F. McClintock, "Describing uncertainties in single-sample experiments," *Mechanical Engineering*, vol. 75, pp. 3–8, 1953.

[37] D. Wilkie, "Wilson Plot," in *A-to-Z Guide to Thermodynamics, Heat and Mass Transfer, and Fluids Engineering*, Begellhouse, 2011.

[38] J. Fernández-Seara, F. J. Uhía, J. Sieres, and A. Campo, "Experimental apparatus for measuring heat transfer coefficients by the Wilson plot method," *European Journal of Physics*, vol. 26, no. 3, pp. N1–N11, May 2005, doi: 10.1088/0143-0807/26/3/N01.

[39] M. M. Bhunia, K. Panigrahi, S. Das, K. K. Chattopadhyay, and P. Chattopadhyay, "Amorphous graphene – Transformer oil nanofluids with superior thermal and insulating properties," *Carbon*, vol. 139, pp. 1010–1019, Nov. 2018, doi: 10.1016/j.carbon.2018.08.012.